Spring 2019

The dynamical state of a young stellar cluster

Timothy Sullivan

Department: Physics

THE DYNAMICAL STATE OF A YOUNG STELLAR CLUSTER

by

TIMOTHY SULLIVAN

A DISSERTATION

Presented to the Graduate Faculty of the

MISSOURI UNIVERSITY OF SCIENCE AND TECHNOLOGY

and

UNIVERSITY OF MISSOURI – ST. LOUIS

In Partial Fulfillment of the Requirements for the Degree

DOCTOR OF PHILOSOPHY

in

PHYSICS

2019

Approved by

Dr. Bruce Wilking, Advisor
Dr. Paul Parris, Co-Advisor
Dr. Tom Greene
Dr. Erika Gibb
Dr. Alexey Yamilov

ABSTRACT

The dynamical state of the young star-forming cluster Rho Ophiuchi is considered, with emphasis on the L1688 cloud. Radial velocities are derived for 32 YSOs, with some being multi-epoch, using Markov-Chain Monte Carlo routines based upon the package *emcee*. Sources are chosen based upon their spectral index to focus on the earlier stages of star formation, in this case, Class I and Flat spectrum objects, and compared with a sample of Class II and III objects from the same embedded cluster. It is found that the radial velocity dispersion for these younger objects is $\Delta v = 2.8 \pm 0.6$ km s^{-1} which is about 2σ higher than the dispersion for Class II and III objects. The implication is that there are either small number statistics at play, or the cluster's dispersion is being increased as an inverse function of the distance from the center of the cluster due to a collapse-and-rebound phase that has been proposed in recent simulations.

ACKNOWLEDGMENTS

This dissertation would not have been possible had I worked alone, and there are many people that I would like to thank. First and foremost, my adviser, Dr. Bruce Wilking, has been instrumental in helping me learn all that I have in my time at the University of Missouri - St. Louis. He has continued to push me in the right direction and kept me on track throughout the entire process.

Dr. Tom Greene has also provided a lot of help working on some of the finer details of the project. He has always made himself available to help answer whatever questions I might have and has been excited to do so. I would also like to thank the rest of my committee for taking their valuable time to give me feedback along the way and finally to ensure that my work is the best it can be. In particular, Dr. Erika Gibb was very supportive when it came to our data collection. She ensured that we got the most out of our telescope time and was able to teach me many of the ins and outs of observing. I would also like to thank a few of my fellow students, Chemeda Ejeta and Lindsey Lisalda, for helping with the data reduction process.

Thank you to the staff at the NASA Infrared Telescope Facility for being incredibly supportive during our time observing, both on site and remotely. Michael Connelly and Michael Cushing helped with the observations as well as the data reduction.

Thank you to all the organizations that funded me along the way, including the University of Missouri - St. Louis, The University of Missouri of Science and Technology, and the NASA Missouri Space Grant Consortium.

Finally, thank you to my family. Thank you to my parents, Ted and Sue Sullivan, for always believing in me and encouraging me to want to learn something new every day. And thank you to my brother, Ben Sullivan, for inspiring me to take an interest in science so early in life.

TABLE OF CONTENTS

Page

LIST OF ILLUSTRATIONS

LIST OF TABLES

Table Page

1. INTRODUCTION

Stars are among the oldest astronomical objects to be studied by scientists. While there has been a significant amount of information learned about their nature, especially in the last century, there are still many details that are not yet known about the life cycles of stars. While we now know that the majority of stars form out of molecular clouds of gas and dust in what are called embedded clusters (Lada and Lada, 2003), there are still many details regarding the formation and early evolution of stars that need to be filled in. Understanding stars and the environments in which they form in is critical to fully understand how the universe works, as the specifics of these processes have implications for both planet and galaxy formation. This section will broadly cover the current ideas behind the mechanisms responsible for both the birth of individual stars as well as the formation and evolution of star clusters. In addition, recent observations of specific, nearby star clusters will be discussed and how those studies led to the motivation for the research presented here regarding the Rho Ophiuchi embedded cluster.

1.1. STAR FORMATION AND EVOLUTION

Since individual stars are some of the most basic building blocks of galaxies and of the universe, it is important to understand how a singular star comes to be. The material that goes into creating a star is almost entirely hydrogen and helium. These elements comprise over 99% of the interstellar medium. While in most places the interstellar medium has a very low density of approximately one atom per cubic centimeter, there are areas of denser clouds of molecular gas and dust that form. Within these environments it is possible that the density becomes high enough ($> 10^6$ cm^{-3}) for this gas and dust to begin to collapse into a star (Shklovskii, 1978). Specifically, the amount of mass that will result in a molecular cloud collapsing is called the Jeans Mass (Jeans, 1902). This is the point at which the

gravitational forces of the cloud have overcome the internal gas pressure and is given by

$$M_J = 1.0\mathrm{M}_\odot(\frac{T}{10K})(\frac{n_{H_2}}{10^4\mathrm{cm}^3})^{-\frac{1}{2}} \tag{1.1}$$

where T is the temperature of the cloud and n_{H_2} is the number density of molecular hydrogen. It is clear then that either a higher temperature or lower density will result in the need for a higher mass in order to start the collapse of the cloud. Once the collapse begins, there will inevitably be regions of the molecular cloud that are significantly denser than others. These areas are referred to as dense cores. A subset of these dense cores will be gravitationally bound tightly enough that they will undergo the star forming process and are called prestellar cores (Ward-Thompson *et al.*, 2007). At this stage of evolution, there is still no centralized hydrostatic protostellar object within the core. The lifetime of a typical prestellar core is on the order of millions of years, with those cores with higher densities having shorter lifetimes (André *et al.*, 2000).

Between the formation of a prestellar core and a star triggering nuclear fusion (the main sequence phase where it spends most of its life) there are four general stages of evolution of a young stellar object (YSO) with a mass less than about 3 times the Sun's mass. These are classified based on the YSO's spectral energy distribution and are known as Class 0, Class I, Class II, and Class III. While these stages of evolution are, from a theoretical standpoint, distinct, the classification of real protostars can be imprecise. This is because of the fact that direct observation of these objects is often difficult, and so indirect indicators are relied upon when attempting to categorize them. It has only been with relatively recent developments in infrared astronomy that it has been possible to observe the characteristics of some of the more deeply embedded, and therefore younger, protostars.

The end of the prestellar core stage is marked by the condensation of a protostellar object within the core, referred to as a Class 0 protostar. These objects are defined as having their mass less than the envelope of material surrounding it. They can be detected

observationally by looking for three different signatures: a centimeter radio continuum source or CO outflow indicating the possible presence of a protostar, extended submillimeter continuum emission due to a spheroidal cloud, or a high ratio of submillimeter to bolometric luminosity, since the surrounding cloud should be cooler than the protostar itself (André *et al.*, 1993). The spectral energy distribution (SED) of a Class 0 object should resemble a single temperature blackbody at about 10-30 K. Class 0 objects have lifetimes on the order of about 10^5 years (Dunham *et al.*, 2014). This stage of protostellar evolution is also known as the main accretion phase, as this is when most of the mass collapses onto the YSO at the center of the dense core. The time scale for this phase can be estimated by the free-fall time for a cloud to collapse under its own self-gravity, given by

$$\tau_{ff} = (\frac{3\pi}{32G\rho})^{\frac{1}{2}} \tag{1.2}$$

where ρ is the cloud density. For a cloud with $n_{H_2} = 10^6$ cm^{-3}, $\tau_{ff} = 3 \times 10^4$ years.

After the majority of the matter has centralized, the YSO is considered to be a Class I object. Physically, the main differences between Class 1 and Class 0 objects is that the remaining cloud of gas and dust around the central object is a much smaller fraction of the total mass since most of the mass has been accreted onto the star, and that this material is starting to form into a protoplanetary disk due to the conservation of angular momentum. The result is that the temperature of the YSO at the center of the cloud is much higher than it was during the Class 0 phase, and there is a much larger range of temperatures observed since photons from the YSO are absorbed by dust and re-radiated at longer infrared wavelengths. Therefore, it is no surprise that the SED for a Class I source is also much broader and the energy radiated by the dust over that of the central blackbody is called an infrared excess. Observationally, these objects should also produce a CO outflow, but the outflow should be

significantly broader and slower in nature than Class 0 sources (André, 1994). The typical lifetime of the Class I stage of evolution is on the order of 5×10^5 years (Barsony and Kenyon, 1992; Dunham *et al.*, 2014).

As an object transitions from Class I to Class II, it is now that a protostar is nearly finished accreting matter. The infalling envelope that had surrounded the younger Class I object is dispersed by the outflow or collapses into a circumstellar disk. At this intermediate stage, the infrared excess is reduced and the spectral energy distribution no longer rises into the far-infrared but appears flat. YSOs in this phase are referred to as Flat-spectrum, or Class F, sources. As the envelope is finally dispersed, an optically-thick disk surrounds the central object, but this has only a small fraction of the total mass, on the order of 0.01 $M_\odot$. Objects in this phase display Class II SEDS and include the classical T Tauri Stars. These types of objects were first observed a few decades before the introduction of the current classification system because this stage of stellar evolution is one of the earliest that is potentially observable in the visible spectrum, assuming it is not obscured by its own disk and the molecular cloud that it is embedded in. Lifetimes for this stage of stellar evolution are on the order of 2×10^6 years, however, the transitional phase between Class II and Class III objects appears to be fast since there are a relatively small number of transition objects detected between these two stages.

Once this circumstellar disk has all but completely dissipated, the object is classified as a Class III source. A Class III object is nearly a fully formed main sequence star. It is no longer self-embedded and its circumstellar disk is either non-existent or very thin. The faint presence of a disk has been detected in these types of objects before, but this is usually in cases very favorable for detection, i.e.; the source is somewhat close and the disk is being viewed edge on. The lifetime of this stage of stellar evolution is on the order of 10^7 years (André and Montmerle, 1994). The SED for a Class III YSO closely resembles that of a single temperature blackbody. The timescale for the overall length of the Class II and Class

III phases together is given by the Kelvin-Helmholtz contraction time

$$\tau_{K-H} = \frac{GM^2}{RL} \tag{1.3}$$

where R is the radius of the star and L the luminosity. For a 1 $M_\odot$ star it takes about 30 million years to reach the main sequence . Higher mass stars will take a shorter time, and lower mass stars will take a longer time. At this point, the star has reached temperatures and pressures high enough to begin the fusion of hydrogen into helium within its core, and it is considered to be on the main sequence.

The classification scheme derived above was first developed by Lada (1987) and has been refined by several others since. While the different classes themselves are qualitative descriptions of a continuous process, there is a quantitative observational basis for distinguishing one class from another. This is done by defining a spectral index as the slope of the near- to mid-infrared SED for a given object. The reason this works is that the infrared excess for a YSO will change as the shape, structure, and mass of the circumstellar material surrounding it changes and evolves over time. The spectral index is given by

$$\alpha = \frac{d\log(\lambda F_\lambda)}{d\log(\lambda)} \tag{1.4}$$

where λ is the wavelength and F_λ is the flux density at λ. The wavelength region measured for this index is between 1 and 20 microns. Class 0 sources have $\alpha > 1.5$, for Class I sources $1.5 > \alpha > 0.3$, for Flat-spectrum sources $0.3 > \alpha > -0.3$, for Class II sources $-0.3 > \alpha > -1.6$, and for Class III sources $\alpha < -1.6$ (André and Montmerle, 1994; Greene *et al.*, 1994; White *et al.*, 2007). Figure 1.1 shows qualitative illustrations of the stages of YSO evolution next to an example of what the corresponding SED might look like.

Again, a protostar is said to transition to a fully formed star once nuclear fusion begins to take place within the core. Within the cores of stars is where nearly all elements heavier than hydrogen and helium and up to iron are produced, depending on the size of the

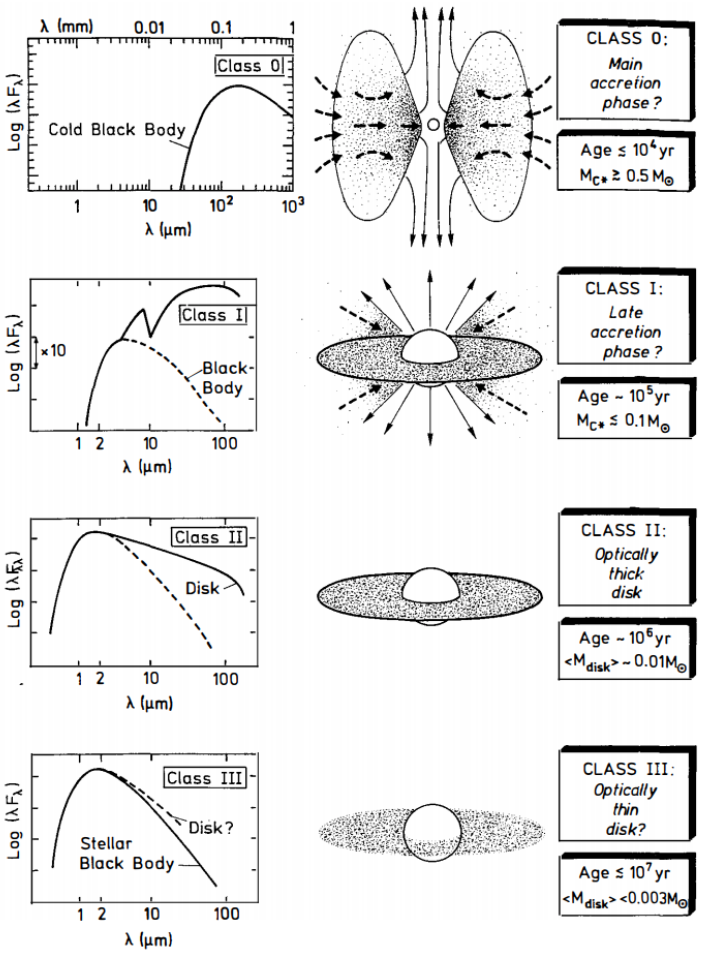

Figure 1.1 Conceptual drawings of the various phases of protostellar evolution (André, 1994).

star, and there are many different nuclear reactions that take place to make this happen. The two most important and most common processes, however, are the proton-proton chain, and the CNO (carbon-nitrogen-oxygen) cycle. The proton-proton chain starts with two protons fusing to create deuterium. Then the deuterium fuses with another proton to create ^{3}He. Finally, two ^{3}He nuclei will collide to produce one ^{4}He nucleus and two protons. The carbon-nitrogen cycle starts with a proton fusing with a ^{12}C nucleus and creating the nitrogen isotope ^{13}N. This isotope then undergoes beta decay, leaving behind ^{13}C to fuse

with another proton, resulting in ^{14}N. Another proton will then fuse with the ^{14}N nucleus and create ^{15}O. ^{15}O will then beta decay into ^{15}N. Ultimately, this ^{15}N nucleus will fuse with another proton, resulting in ^{12}C and ^{4}He being produced. In each step of each process, a large amount of energy is released. It is this energy from the nuclear fusion reactions that pushes outward, and opposes the force of gravity. While the protostar had been collapsing for its whole life, these reactions within the core of the star stop this process, finally bringing it to near equilibrium (Shklovskii, 1978).

Not surprisingly, the main sequence is where a star will spend the majority of its life. The amount of time that a star will spend on the main sequence and its subsequent evolution vary greatly and depend almost solely upon the star's mass. The relationship between lifetime and mass is inversely proportional ($M^{-2.5}$), so while higher mass stars have more material to fuse, the higher temperatures and pressures within these stars means that they burn through it much more quickly. On the other hand, low mass stars will burn their fuel much more slowly, and are able to stay on the main sequence for much longer than their high mass counterparts. In particular, some of the smallest and most abundant stars in our galaxy, red dwarf stars ($M \approx 0.08 - 0.4$ M$_\odot$), will remain physically small for their entire life, slowly becoming smaller and hotter and evolving into what are sometimes called blue dwarfs. While they will eventually run out of hydrogen to fuse, the main sequence could last as long as a few trillion years, at which point they will likely start to fade and contract to become a white dwarf, meaning that it will be electron degeneracy pressure, instead of thermal gas pressure, that is pushing against gravity and preventing further collapse. Obviously, this has never been observed since the universe is only about 13.7 billion years old (Adams *et al.*, 2005).

For intermediate mass stars ($M \approx 0.4 - 8.0$ M$_\odot$) it is common that they will evolve into the red giant category of stars after spending somewhere on the order of a few billion years on the main sequence. These stars are characterized as having relatively low surface temperatures while being very large in size, sometimes having a radius on the order of a few

hundred or even thousand times larger than the Sun. Internally, these stars have exhausted the hydrogen in their cores, and now have a shell of hydrogen fusion taking place around the helium core. As the red giant phase continues, the star pushes its outer layers further and further away, eventually leaving a white dwarf surrounded by a large cloud of the ejected material known as a planetary nebula. The various elements and chemical compounds that formed within the star throughout its life can then go on and influence the chemical evolution of the interstellar medium, and potentially future embedded clusters (Iben, 2013; Laughlin *et al.*, 1997; Maciel *et al.*, 1991).

For more massive stars ($M > 8.0\ \mathrm{M}_{\odot}$) there are several different possible outcomes. Depending on just how massive these stars are, it is possible that their time spent on the main sequence may be on the order of only a few million years or even just a few hundred thousand years. The most interesting outcome for these most massive stars is when they become supernovae. There are a few different mechanisms by which this can happen, including thermal runaway and core collapse. For a massive star at the end of its life, core collapse is the mechanism that will drive the supernova explosion. This happens when the remaining core that would normally produce a white dwarf exceeds the Chandrasekhar mass limit of about $1.4\ \mathrm{M}_{\odot}$. When this happens the electron degeneracy pressure is not strong enough to sustain the white dwarf, and it collapses and subsequently explodes. Supernovae can often be bright enough to outshine the total luminosity of the rest of the galaxy that they are in. This obviously pushes out an incredible amount of highly energetic material. The rate of supernovae is approximately one per galaxy per century, and these massive explosions are thought to be one possible mechanism that triggers the collapse of nearby molecular clouds, thus setting off the star formation process once again. In addition to the shockwaves they create, supernovae also manufacture and release large amounts of heavy elements, including silicon, which helps create more interstellar dust, which then helps

create more molecular clouds. In this way, the deaths of some of the largest stars could be the catalyst to the star formation process beginning again (Heger *et al.*, 2017; Krebs and Hillenbrandt, 1983).

1.2. CLUSTER FORMATION AND EVOLUTION

In the previous section, the focus was on the formation and evolution of a single star, following it from the collapse of a gas cloud and inception as a protostellar object, all the way to the end of its life. It should come as no surprise, however, that this process does not often happen in isolation. When there is enough gas and dust to begin to collapse into one star, there is usually enough to form several stars. When multiple stars are forming and evolving together and gravitationally interacting with one another in the same region, it is called a star cluster. Specifically, they are defined as groups of stars whose observed stellar mass volume density is sufficiently large enough to render the group stable against tidal disruption by the galaxy (Bok, 1934) and by passing interstellar clouds (Spitzer, 1958). It is now clear that the majority of stars form within clusters. The three main types of clusters that are observed are (from youngest to oldest) embedded clusters, open clusters, and globular clusters. The youngest of these, the embedded clusters, have only been observed relatively recently, that is, since the advent of infrared astronomy. Before this, embedded clusters were just that: deeply embedded within gas and dust, causing most of their members to be unobservable at visible wavelengths. Technological advancements have allowed these types of environments to be studied in much greater detail than before and as a result have helped reveal many details about the early life of clusters themselves, as well as the individual members that make them up (Lada and Lada, 2003).

As stated before in Equation (1.1), the Jeans Mass is the condition that needs to be met in order to start the collapse of a molecular cloud. But one aspect of the star formation process that still isn't entirely clear is what causes this condition to be met in the first place. Two different mechanisms that have been proposed for this are turbulent fragmentation of

the molecular cloud due to gravity, and, as mentioned at the end of the previous section, some type of external triggering event that could condense the cloud and start the collapse. It is known that giant molecular clouds that form from the interstellar medium are highly turbulent, and it seems that on a global scale, this turbulence might serve to stabilize the cloud against collapse. However, locally, numerical simulations suggest that turbulent flows can collide and dissipate energy, causing a subsection of the cloud to become gravitationally unstable and begin to collapse (Klessen *et al.*, 2000). If a large enough segment of the cloud becomes gravitationally unstable, this could lead to the production of an embedded cluster. There have also been observations of OB associations (groups of very large, hot, short-lived stars) that suggest that star formation can occur in sequential bursts. Since there appear to be spatially separate subgroups of OB stars within several associations where the age of the OB stars correlates with the distance from the associated molecular cloud that form them, the implication is that some sort of shockwave traveled through the region, triggering the formation of these stars as it went. Hence the idea has been forwarded that the shockwaves produced by supernovae could compress otherwise stable sections of molecular clouds and start their collapse (Elmegreen and Lada, 1977).

Once a cluster begins forming stars, it has usually set a fairly short lifetime for itself. Despite the fact that there is an incredibly large range of masses of stars that can form out of these embedded clusters (a range spanning a few orders of magnitude) the time in which these clusters exist only spans about 5×10^6 years. This is because the star formation process itself is inherently a destructive one for the cluster. Stellar winds, radiation pressures, and, most importantly, jets and outflows produced by embedded protostars work together to disperse the gas out from the cluster. This happens before most of the mass of the cluster has gone into forming stars, and as such, much of the binding mass of the cluster gets dispersed along with it. The result is that the star formation process is an incredibly inefficient one. Typically, less than 10% of the mass of the original molecular cloud actually goes into creating new stars. Once the gas has been dispersed after a few million years, most

clusters will no longer be gravitationally bound, and the members will expand and disperse into the general population of the galaxy (Matzner and McKee, 2000; Whitworth, 1979). When comparing the birthrate of embedded clusters to the observed numbers of bound and open clusters, it appears as though roughly 95% of embedded clusters do not survive the gas removal phase. It is only the most massive 5% that are potentially able to stay bound after this happens, and even in these cases, they are likely to lose a significant number of their members (Lada and Lada, 1991, 2003). Constraining the time it takes for the gas in a given cluster to disperse is important because it is usually also tied to the lifetime of the cluster itself. Thus, the time to remove the gas, τ_{gr}, gives an estimate for how long the members of a given cluster are both forming and dynamically interacting with one another. Based on observations, the upper limit of τ_{gr} is approximately five million years. However, there is certainly a lot of variance in this number, depending upon the size of the cluster and the types of stars that are forming. If there are O stars forming within the cluster, τ_{gr} could even be on the order of only about 10^4 years (Lada and Lada, 2003).

For those clusters massive enough to maintain some structure after the gas removal phase and evolve into open clusters, it is possible they do not fit the strict definition of a star cluster that was mentioned earlier. This means that some clusters that survive the gas removal may only be weakly gravitationally bound. They could be broken apart by external gravitational forces, if not from the tidal forces of the galaxy itself, but from other nearby clusters or molecular clouds. Open clusters can contain anywhere from a few dozen to a few thousand members, and are typically smaller than a few parsecs in diameter. The observed ages of open clusters currently range from about 1 million years up to a few billion years, implying that these types of clusters are still being formed, which is consistent with the idea that they evolve from embedded clusters (Binney and Merrifield, 1998).

Studying various properties of clusters can also help explain properties of stars as well. For instance, it is important to study the internal structure and physical distribution of stars within clusters, and especially within embedded clusters. In addition to learning

about the present conditions of the cluster, their structure can shed light on the types of processes that created them in the first place. In particular, the fact that some clusters show signs of mass segregation while others do not is important for understanding how clusters evolve and how their members interact. Essentially, if a cluster is mass segregated, it just means that the higher mass objects are distributed differently than lower mass objects. The most basic explanation for how this structure could arise is that over time, as all of the cluster members interact gravitationally with one another, the lower mass objects end up with higher velocities, and the higher mass objects with lower velocities. This would cause the lower mass objects to be generally found towards the edges of the cluster, while the higher mass objects would reside more centrally. However, there are questions as to whether or not embedded clusters have lifetimes long enough for this to happen through dynamic interactions (Bonnell and Davies, 1998). This is related to the ratio of a cluster's crossing time, τ_{cross}, to τ_{gr}. The crossing time is given by

$$\tau_{cross} = \frac{2R}{v} \tag{1.5}$$

where R is the radius of the cluster and v the typical speed of cluster members as measured by the velocity dispersion. Typically, τ_{cross} is on the order of one million years, and as mentioned before, τ_{gr} is almost always less than five million years. Given the variance in τ_{gr}, it is possible that some embedded clusters could live long enough to dynamically mass segregate, whereas others could not. Another issue is that observed mass segregation could have been present in the dense molecular cores as the embedded cluster was forming, in which case it would be observed no matter how young the cluster was. Currently there are very young clusters that have been observed to show signs of mass segregation (Elmegreen *et al.*, 2000; Hillenbrand and Hartmann, 1998), some clusters that have shown no signs of mass segregation (Carpenter *et al.*, 1997), and some that show the higher mass stars found towards the edges of the cluster, as well as the center (Herbig and Dahm, 2002).

The environments in which embedded clusters form must also have a significant impact on the initial mass function (IMF). The IMF is simply the distribution of the initial masses at which stars form and given by $\frac{dN}{d\log M_*}$. This is important to study since the birth mass of a star is the single most important parameter when it comes to determining the life of a star. Understanding the distribution of masses at which stars form is critical to understanding how clusters and galaxies form and evolve over time. By studying the IMF of individual clusters, it is possible to begin to build a picture of the "universal" IMF. Traditionally, there have been two methods for measuring an IMF. The first is by measuring directly the luminosity function of a cluster, and then deriving the mass function from that, via the equation

$$\frac{dN}{dm_k} = \frac{dN}{d\log M_*} \times \frac{d\log M_*}{dm_k} \tag{1.6}$$

where m_k is the apparent (near-infrared) stellar magnitude and M_* is the mass. The second is by obtaining spectra of many different sources and placing those individual objects on a Hertzsprung-Russell Diagram (HRD) and comparing their locations to a set of theoretical mass tracks and isochrones. The first method was originally used by Salpeter (1955) when deriving the IMF of field stars, but the method is not as simple when deriving the IMF of embedded clusters. This is because, for pre-main sequence objects, $\frac{d\log M_*}{dm_k}$ is time dependent and therefore much more difficult to model. In order to use the second technique for measuring a cluster's IMF, the luminosity and effective temperature of each cluster member must be known. With this knowledge it is possible to place each member on the HRD and get a snapshot of the current distribution of objects within the cluster as well as estimates for their mass. While the end result is a very detailed picture of the cluster, the practical issue with this method is simply telescope time. Obtaining detailed photometric and spectroscopic data for each object within a cluster is incredibly time consuming. Both techniques, despite being complex, have been used successfully in the past to yield reasonable estimates for a cluster's IMF (Erickson *et al.*, 2011; Muench *et al.*, 2000).

It is clear that in order to form a complete picture of the star formation process, there must also be in-depth study of cluster formation and evolution. It is not possible to completely decouple one from the other. Since stars do not form in isolation, formulating a theory of star formation requires that embedded star clusters are studied as well.

1.3. MOTIVATIONS AND OBJECTIVES

The main focus of this project is to estimate the velocity dispersion of YSOs (Class I-III objects) within the Rho Ophiuchi embedded cluster. Velocity dispersions can be computed in the plane of the sky using long time-baseline astrometric observations or along the line of sight from the Doppler shift of absorption lines in very high-resolution spectra. The goal is to investigate the possible role of dynamical interactions between YSOs during the star formation process. These interactions could play a role in determining several observed properties of star formation, such as shaping the IMF through competitive accretion and ejection (Bonnell *et al.*, 2007), determining the fraction of stars in multiple systems (Reipurth *et al.*, 2014), influencing the formation and evolution of circumstellar disks through disk truncation, and ultimately, the formation of planetary systems (Clarke and Pringle, 1993; Kobayashi and Ida, 2001).

The main reason for choosing the Rho Ophiuchi cluster and, specifically, the L1688 cloud (Figure 1.2), is that it is one of the closest active star- forming regions, making it one of the best places to study both star formation and embedded cluster evolution. It is estimated to be 137 ± 1.2 pc away (Loinard *et al.*, 2008; Lombardi *et al.*, 2008; Mamajek, 2008; Ortiz-León *et al.*, 2017) and is located near the Sco-Cen OB association. This embedded cluster appears to have started its star formation via an external trigger about two million years ago (De Geus, 1992; Erickson *et al.*, 2011). The trigger itself seems to be the passage of an expanding shell from a nearby subgroup of massive OB stars. There are over 300 known YSOs within the cluster covering the whole range from Class 0 to Class III objects, and in addition to this, there have been about 55 starless cores identified within the cloud

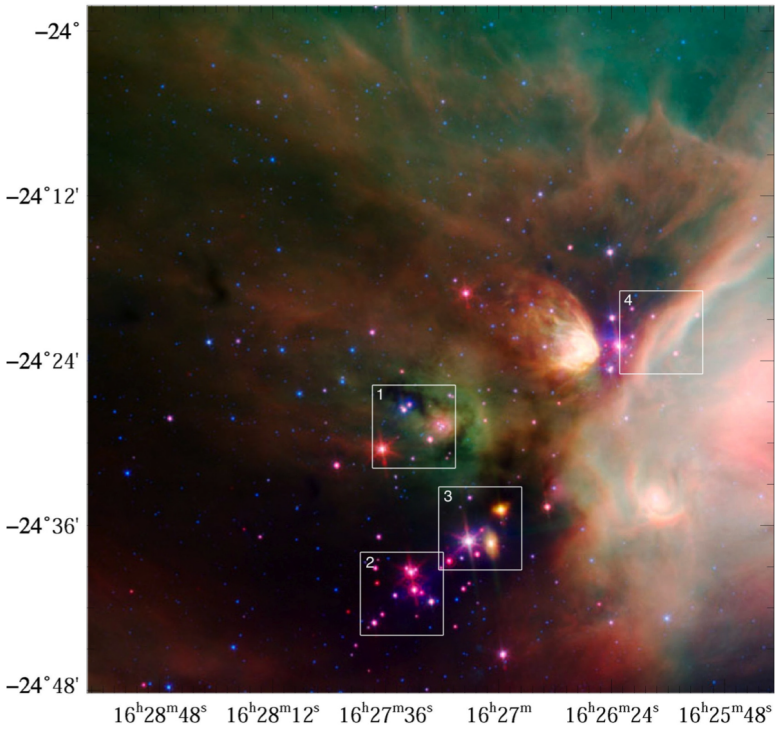

Figure 1.2 A combined Spitzer IRAC/MIPS image of L1688 with red representing emission in the 24 μm band, green the IRAC 8 μm band, and blue the IRAC 4.5 μm band (image by Robert Hurt) (Wilking *et al.*, 2008). Boxes have been added to indicate fields observed for the proper motion study.

that could be in the process of collapsing. The Rho Ophiuchi star-forming region is also known for its population of very low mass objects and brown dwarf candidates. A brown dwarf is essentially a failed star; it formed from a dense core within a molecular cloud, but never accreted enough material to become massive enough and hot enough to start burning hydrogen into helium. This makes Rho Ophiuchi a great place to study how and why these objects form and what the implications are for the IMF (Wilking *et al.*, 2008). Since this region has almost only low mass stars forming within it, it necessarily means that this project is focused specifically on the formation and evolution of low mass stars. The sources studied and properties derived may only apply to stars of about 1 $M_{\odot}$ or less, which is the case for most objects in Rho Ophiuchi.

There have also been recent studies of several nearby star-forming regions, including Rho Ophiuchi, regarding the velocity dispersions of dense cores. Studies of the Rho Ophiuchi, NGC 1333, and NGC 2264 molecular clouds by Peretto *et al.* (2006), André *et al.* (2007), and Kirk *et al.* (2010) have shown that the dense cores in these regions have velocity dispersions between 0.4 and 0.8 km s^{-1} and are most likely subvirial. The virial theorem states that for a stable, self-gravitating distribution of objects

$$2T = -V \tag{1.7}$$

where T is the total kinetic energy and V is the gravitational potential energy. In other words, the velocities of these dense cores are lower than expected for a self-gravitating distribution of objects and are perhaps restrained by magnetic fields. However, for some of these same star-forming regions, it has been shown that the velocity dispersions of YSOs are significantly higher than that of the dense cores. This would imply that sometime after the cores have collapsed, these YSOs were dynamically interacting with one another and converting some potential energy into kinetic energy (Foster *et al.*, 2015). Indeed, this idea has theoretical backing as some simulations of cloud collapse indicate a higher rate of stellar interactions while the objects are still embedded (Bate, 2009; Bate *et al.*, 2003; Proszkow and Adams, 2009). If stellar interactions are responsible for the higher velocity dispersions of the YSOs relative to the dense cores, then one might expect to observe a steady increase in velocity dispersion as YSOs emerge from the dense cores and evolve toward hydrogen burning.

For this project, radial velocity and proper motion data of Rho Ophiuchi members have been collected from infrared telescopes or archival data with the goal of measuring the velocity dispersion. Data have been acquired from the US Naval Observatory (USNO) in Flagstaff, Arizona (Wilking *et al.*, 2015), the Near-Infrared Spectrometer (NIRSPEC) (Doppmann *et al.*, 2005) on the Keck telescope in Hawaii, the Cryogenic High-Resolution

Infrared Echelle Spectrograph (CRIRES) on the Very Large Telescope (VLT) in Chile from Viana Almeida *et al.* (2012) and Cottaar (2012, unpublished data; Program ID 089.C-0753(A)), the Cryogenic Near-Infrared Facility Spectrograph (CSHELL, this study) on the Infrared Telescope Facility (IRTF) in Hawaii, and the Immersion Grating Echelle Spectrograph (iSHELL, this study) also on the IRTF. The focus for the radial velocity sample was the least evolved YSOs, Class I/Flat spectrum sources, while the proper motion sample was not biased by evolutionary state.

The proper motion study played a large part in the initial motivation for this study. As mentioned before, proper motion data was acquired by Fred Vrba from 2001–2006 and then again from 2011–2012 using ASTROCAM on the USNO 1.55 m telescope. This instrument was able to produce proper motions on the order of mas yr^{-1}. As well as producing proper motions, the images from ASTROCAM also allowed for infrared photometry to be performed on all the objects observed in order to check for variability in the infrared. In total, 111 objects over four different fields of view within the L1688 cloud as indicated in Figure 1.2 were observed. Using a straightforward χ^2 analysis, 18 sources were identified with possible variability in the infrared that had not been included in previous surveys, four of which had not been previously identified as YSOs and are likely cluster members.

The results of the proper motion study (Table 1.1, Figure 1.3) then started to show some evidence of a dispersion that varies as a function of evolutionary state. Velocity dispersions were obtained for 65 YSOs by measuring their relative proper motions, meaning that a background reference frame was unable to be established and the average proper motion in each field for each direction (R.A. and Dec.) was defined to be zero. This sample was then split into the more evolved (Class II/III) and less evolved (Class I/F) objects. Two velocity dispersions were obtained for each group: one for motion in right ascension (RA) and one for their motion in declination (Dec). While the dispersions were nearly identical in RA, there was a significant difference between the two groups in Dec. The dispersion for the Class I/F objects was found to be $\Delta v = 0.71 \pm 0.09$ km s^{-1} while for Class II/III objects it was

Table 1.1. Velocity Dispersion from Relative Proper Motions

Sample	No. of Sources	$\Delta v_{\mathrm{R.A.}}$ (km s^{-1})	$\Delta v_{\mathrm{Dec.}}$ (km s^{-1})
Fields 1 and 2	44	0.82 ± 0.10	0.97 ± 0.10
All Fields	65	0.88 ± 0.10	0.96 ± 0.09
SED Class I/F	29	0.84 ± 0.11	0.71 ± 0.09
SED Class II/III	28	0.88 ± 0.08	1.28 ± 0.26

$\Delta v = 1.28 \pm 0.26$ km s^{-1}. This is a preliminary indication that there could be a relationship between the velocity dispersion and evolutionary state for low mass YSOs. In addition to this, a radial velocity dispersion recently derived for 47 Class II/III objects in Rho Ophiuchi has been obtained by Rigliaco *et al.* (2016) and was measured to be 1.14 ± 0.35 km s^{-1}. In other words, the radial velocity dispersion is in agreement with that for objects from the proper motion study. This value was found to be consistent with the sources being in virial equilibrium.

Since the Class I/Flat sources are more deeply embedded, it is necessarily more difficult to obtain precise radial velocities for them, so the sample of these objects will inevitably be smaller than any sample of Class II/III objects because there is no multi-object infrared spectrograph capable of the necessary precision. The goal is to use the radial velocities found for the Class I/F objects to compare to that of Class II/III YSOs. Then one can investigate if there is any evidence that the velocity dispersion is a function of the evolutionary state. A velocity dispersion that changes significantly with how evolved these YSOs are would indicate that they are undergoing dynamical interactions while also undergoing their initial formation and accretion of mass.

Alternatively, a velocity dispersion that does not vary with how evolved the YSOs are could indicate that stellar encounters are occurring very early on, possibly even before the Class I phase, and therefore on a very short timescale. Given the disparity between

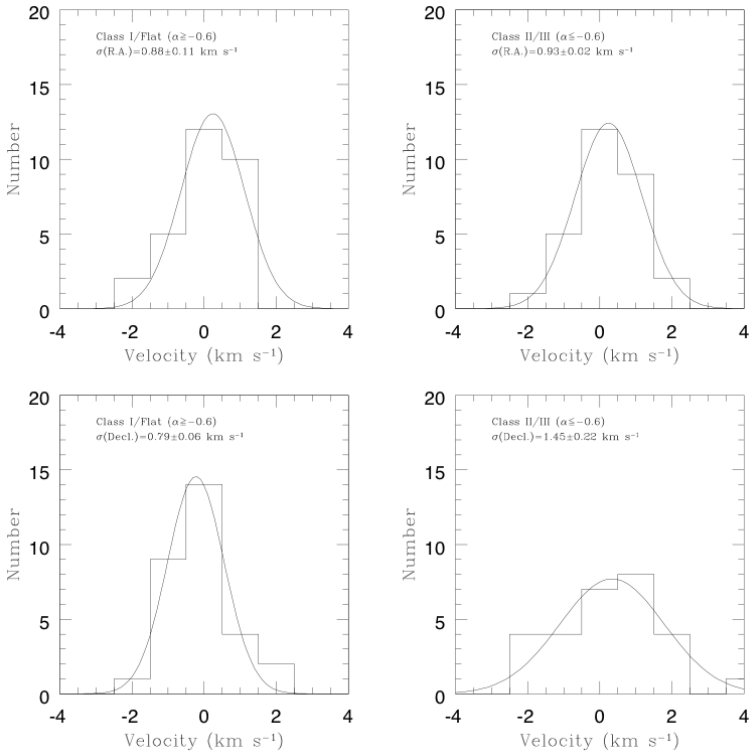

Figure 1.3 Velocity dispersion for proper motion samples separated by both SED (Class I/F on left, Class II/III on right) and also in RA (top) and Dec (bottom) (Wilking *et al.*, 2015).

the velocity dispersions of the dense cores and that of the Class II/III protostars, it seems that these interactions must be taking place at some point between the two stages of star formation. Figuring out when this might be happening could provide evidence for the many ideas regarding observed properties of star-formation that are dependent upon dynamical interactions.

The rest of this dissertation will be organized as follows: Section 2 will cover all the relevant observations made regarding this project, including the rationale for source selection, specific telescopes and instruments used, all the objects and standards that were observed, and the data reduction procedures. Section 3 will explain the analysis done on these sources, including details regarding the Markov-Chain Monte Carlo technique being used to simultaneously fit various observed parameters for all of the objects studied. Section

4 will present the results of this analysis and the measured radial velocities and velocity dispersions. Section 5 will include a discussion of the results and their implications. Section 6 will summarize the entire work and discuss options for continuing this research in the future.

2. OBSERVATIONS

Four data sets were used to derive radial velocities for a collection of young stellar objects (YSOs) in L1688, most with Flat-spectrum or Class I spectral energy distributions. A few Class II sources were also observed along with radial velocity standards. A summary of the YSO observations is presented in Table 2.1 with source positions, dates of observation, wavelength coverage, integration times, and signal-to-noise estimates. Similar data for radial velocity standards are presented in Table 2.2.

2.1. SOURCE SELECTION

Sources were selected based upon their spectral index, α, as defined in Section 1, to be Class I, Flat, or Class II sources. The focus is primarily on as many Class I and Flat sources as possible, with some Class II sources. In addition to this, sources are biased by their K_{mag} (infrared magnitude at $\lambda = 2.2$ μm) depending on the instrument and telescope that was used for the observation. For NIRSPEC and CRIRES this resulted in sources with $K_{mag} \leq 11$; for CSHELL and iSHELL $K_{mag} \leq 10$. The sample presented here is assumed to be biased towards slightly more massive YSOs, since these objects will be brighter and easier to observe. Figure 2.1 shows the physical location of these objects within the Rho Ophiuchi cluster, showing that the sample is concentrated within the L1688 cloud in subclusters corresponding to cores A (northwest), B (northeast), and E/F (south).

2.2. CSHELL

Observations were made using CSHELL on NASA's 3 meter Infrared Telescope Facility (IRTF) on the summit of Mauna Kea in Hawaii. Seven first-half nights in 2016 June 23, 29, 30, and July 10, 11, 13, 14 were used to observe 10 YSOs and 5 radial velocity

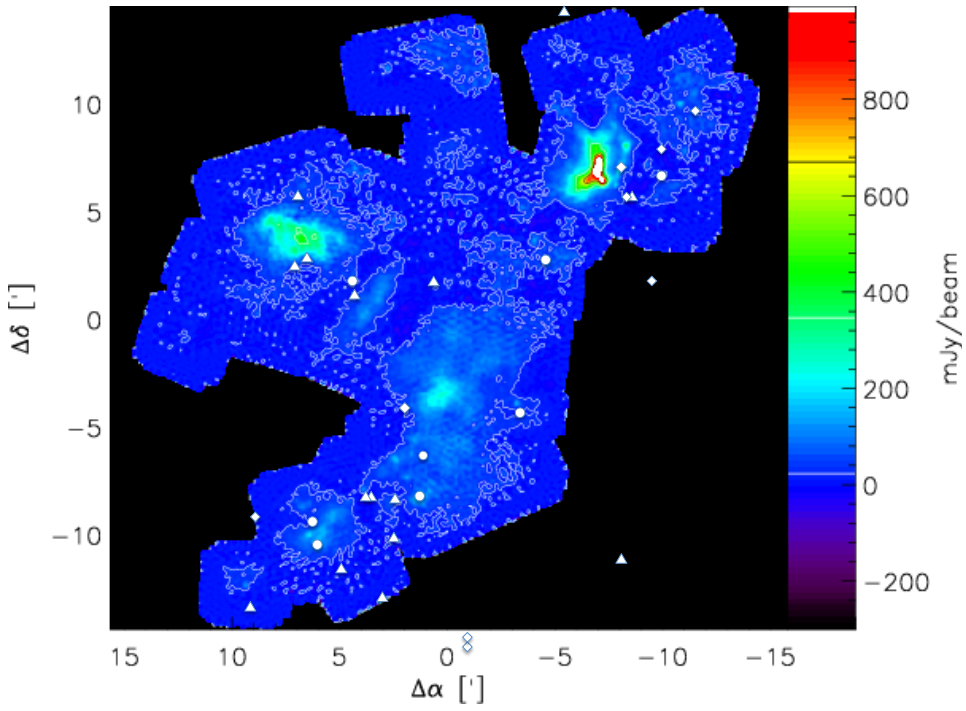

Figure 2.1 The location of YSOs for which radial velocities were derived is shown relative to the distribution of cold dust in L1688 as measured from the 1.3 mm continuum observations of Motte et al. (1998). The (0,0) position corresponds RA(2000) = 16h 27m and Dec(2000) = -24d 30'. The source symbols represent their SED class: circles, Class I; triangles, Flat Spectrum; diamonds, Class II. The figure is adapted from Ossenkopf *et al.* (2008).

standards. Observations from June 29 and 30 were made through some cirrus cloud cover. CSHELL was an infrared echelle spectrograph with a 256 spectral by 160 spatial pixel array (Greene *et al.*, 1993). The 1.0 arcsecond wide slit was used providing a spectral resolving power of 21,500. Seven YSOs were observed at a central wavelength of 2.298 μm, three at 2.2935 μm, and one at both. Each setting covered a wavelength range of approximately 50 Å. The 2.298 μm setting was chosen to detect nine prominent absorption lines from the CO $v = 2 - 0$ bandhead. The 2.2935 μm setting was chosen to detect the bandhead itself in sources where the longer wavelength absorption lines might be too faint to detect.

Exposures were taken at various integration times depending on the source, but in each case the objects were nodded 15 arcseconds along the slit in an ABBA pattern. Offset guiding was possible for most, but not all, sources. Telluric standards were taken every time the airmass had changed by approximately 0.2.

Data reduction was performed using Image Reduction and Analysis Facility (IRAF[1]). Master flats were made using dark-subtracted frames, and the data were then flat-fielded before being corrected for bad pixels. Due to the nodding, data images were subtracted in their AB pairs and this subtraction ensured that dark current as well as the sky background in the data images themselves was removed. Spectra were then extracted, normalized, and divided by the telluric standards. The final step was to wavelength calibrate the spectra using 10 telluric methane lines identified from the HITRAN database (Gordon *et al.*, 1992).

2.3. iSHELL

Further observations were conducted using the new instrument iSHELL on NASA's 3 meter IRTF the following year (Rayner *et al.*, 2016). Three second-half nights in 2017 April 26-28 were used to observe twelve YSOs and 4 radial velocity standards, focusing on a different group of slightly fainter objects than what was possible using CSHELL. iSHELL is a $1.1 - 5.3$ μm cross-dispersed high-resolution echelle spectrograph. For these observations a 0.75 arcsecond slit was used yielding a spectral resolving power of $R = 35,000$. The K2 setting was selected for each object and covered a wavelength range of $2.09 - 2.38$ μm over 32 orders, ensuring that once again, the CO $v = 2 - 0$ bandhead as well as the $3 - 1$ and $4 - 2$ bandheads were observed plus various atomic absorption lines (Rayner, 2017).

[1]IRAF is distributed by the National Optical Astronomy Observatory, which is operated by the Association of Universities for Research in Astronomy, Inc., under cooperative agreement with the National Science Foundation.

Total integration times on sources brighter than K_{mag} = 9 were 30 minutes, while fainter sources were observed for 60 minutes. The slit used was only 5 arcseconds long and therefore no nodding was done. Flats, calibration lamps, and telluric standards were observed at regular intervals. Observing efficiency was aided by guiding with an infrared slit viewing camera.

Data reduction was performed using iSHELL Tool, a program developed by Michael Cushing for the specific purpose of reducing iSHELL data based on an earlier program for a cross-dispersed spectrograph (Cushing *et al.*, 2004). The first step in this process was to create master darks and flats. The program would then generate a wavelength calibration solution using Thorium-Argon arc lamp images that were taken as close in time to the data as possible. Following identification of the apertures for spectral extraction, dark subtraction, flat-fielding, background subtraction, spectral extraction, and wavelength calibration would all be performed automatically. The next step was to apply these same steps to the telluric standards, divide out the telluric lines, and clean up any bad pixels. It should be noted that during the telluric division, a small shift was applied to the telluric based on the cross-correlation of the YSO spectrum and the telluric in order to improve telluric division. This implies a small uncertainty in the wavelength calibration solution that varies for each source. The shift was always less than 0.5 pixels and was recorded for the spectrum of each source.

2.4. NIRSPEC

In addition to our own observations, high-resolution infrared spectra were generously provided by Dr. Thomas Greene from the 10-meter Keck II telescope on Mauna Kea, Hawaii, using the NIRSPEC multi-order cryogenic echelle facility spectrograph (McLean *et al.*, 1998). Observations were made on 2000 May 30, 2001 July 7, 8, and 10, and, 2003 June 20-21 and published by Doppmann *et al.* (2005). Fifteen Class I and Flat-spectrum YSOs within the L1688 region were observed, usually having $K_{mag} \geq 10$. The

0.58 arcsecond slit was used, providing a spectral resolving power of $R = 16,400$. Several orders were obtained in the original data, but for this project, only order 33, containing the CO $v = 2 - 0$ bandhead, was analyzed. This covered a wavelength range of $2.270 - 2.303$ μm.

All data were reduced by Doppmann *et al.* (2005) using IRAF. Images were cleaned of bad pixels and cosmic rays, flat-fielded, and sky-subtracted. Extracted spectra were then wavelength calibrated and co-added with spectra at the same slit position and similar airmasses. Integration times varying from 6 minutes to 120 minutes were used depending upon the brightness of each object. High SNR (typically > 100) was achieved for nearly all objects. Further details can be found in the original paper.

2.5. CRIRES

Data for seven YSOs were also reduced from the European Southern Observatory archive taken with the Cryogenic Infrared Echelle Spectrograph (CRIRES), which is an adaptive optics assisted spectrograph mounted on the 8 meter VLT UT1 (Antu) located at Paranal Observatory, Chile (Käufl *et al.*, 2004). Data were from Viana Almeida *et al.* (2012) (Program ID 081.C-0395(A)), Viana Almeida (2012, unpublished data; Program ID 089.C-0539(A)), and Cottaar (2012, unpublished data; Program ID 089.C-0753(A)). CRIRES is capable of delivering a spectral resolving power of up to 100,000 in the $960 - 5200$ nm wavelength range. Light is projected onto four detectors that are each 4096×512 pixels. Viana Almeida *et al.* (2012) chose to cover a wavelength range of $2.2542 - 2.3047$ μm using a 0.3 arcsecond slit to achieve a resolution of 60,000. This put the CO $v = 2 - 0$ absorption bands on detector 4, but CO bands were placed on detectors 1 and 3 for other sets of observations. Spectra were collected in an ABBA nodding pattern allowing a very similar reduction process to that which was used for CSHELL as described above including wavelength calibration using telluric methane lines.

Table 2.1. Log of YSO Observations

Source Name[a]	Other Name	RA(J2000) (hhmmss.s)	DEC(J2000) (° ′ ″)	Date	$\lambda_{central}$ (μm)	λ_{range} (μm)	Int. Time (min)	SNR[b]
CSHELL								
WLY 2-3		16 25 39.6	-24 26 34.9	2016 Jul 10	2.2980	2.2956-2.3006	16	8
VSSG 1	EL 2-20	16 26 18.9	-24 28 19.7	2016 Jul 10	2.2980	2.2956-2.3006	32	35
				2016 Jul 13	2.2935	2.2906-2.2958	36	50
SR 24N	WSB 41	16 26 58.4	-24 45 31.9	2016 Jul 14	2.2935	2.2908-2.2959	48	45
SR 24S	WSB 42	16 26 58.5	-24 45 36.9	2016 Jul 14	2.2935	2.2908-2.2959	48	55
GY 235	WLY 2-32b	16 27 13.8	-24 43 31.7	2016 Jul 14	2.2935	2.2908-2.2959	64	15
WL 20W		16 27 15.7	-24 38 43.4	2016 Jul 11	2.2980	2.2956-2.3006	60	10
WL 20E		16 27 15.9	-24 38 43.4	2016 Jul 11	2.2980	2.2956-2.3006	60	9
WLY 2-42	GY 252	16 27 21.5	-24 41 43.1	2016 Jul 11	2.2980	2.2956-2.3006	68	7
VSSG 17	WLY 2-47	16 27 30.2	-24 27 43.4	2016 Jun 23	2.2980	2.2956-2.3006	64	25
GY 314	WSB 52	16 27 39.4	-24 39 15.5	2016 Jun 23	2.2980	2.2956-2.3006	24	100
WLY 2-51	GY 315	16 27 39.8	-24 43 15.1	2016 Jul 10	2.2980	2.2956-2.3006	44	30
iSHELL								
VSSG 1	EL 2-20	16 26 18.9	-24 28 19.7	2017 Apr 26	2.2916	2.2835-2.2997	30	100
GY 33		16 26 27.5	-24 41 53.5	2017 Apr 28	2.2916	2.2835-2.2997	60	90
SR 24N	WSB 41	16 26 58.4	-24 45 31.9	2017 Apr 26	2.2916	2.2835-2.2997	30	180
SR 24S	WSB 42	16 26 58.5	-24 45 36.9	2017 Apr 26	2.2916	2.2835-2.2997	30	100
GY 235	WLY 2-32b	16 27 13.8	-24 43 31.7	2017 Apr 27	2.2916	2.2835-2.2997	60	50
WL 20W		16 27 15.7	-24 38 43.4	2017 Apr 27-28	2.2916	2.2835-2.2997	60	70
WL 20E		16 27 15.9	-24 38 43.4	2017 Apr 28	2.2916	2.2835-2.2997	60	50
WL 4	GY 247	16 27 18.5	-24 25 05.9	2017 Apr 27	2.2916	2.2835-2.2997	30	30
WLY 2-42	GY 252	16 27 21.5	-24 41 43.1	2017 Apr 27	2.2916	2.2835-2.2997	60	50
GY 284		16 27 30.8	-24 24 56.0	2017 Apr 27-28	2.2916	2.2835-2.2997	60	20
WLY 2-51	GY 315	16 27 39.8	-24 43 15.1	2017 Apr 26	2.2916	2.2835-2.2997	30	90
WLY 2-54	GY 378	16 27 51.8	-24 31 45.5	2017 Apr 26	2.2916	2.2835-2.2997	30	90
CRIRES								
GSS 26		16 26 10.3	-24 20 54.8	2008 Apr 28	2.2998	2.2949-2.3047	8	20
GY 23	GSS 32	16 26 24.0	-24 24 48.1	2008 Apr 28	2.2998	2.2949-2.3047	2	50
WL 17	GY 205	16 27 06.8	-24 38 15.0	2012 Aug 30	2.3012	2.2948-2.3075	40	30
GY 224		16 27 11.2	-24 40 46.6	2008 May 11	2.2998	2.2949-2.3047	18	50
WLY 2-44	YLW 16A	16 27 28.0	-24 39 33.5	2012 Aug 31	2.3012	2.2948-2.3075	10	65
VSSG 18	WLY 2-45	16 27 28.4	-24 27 21.0	2008 Apr 28	2.2998	2.2949-2.3047	8	35
				2012 Aug 18	2.3010	2.2960-2.3060	4	30
VSSG 17	WLY 2-47	16 27 30.2	-24 27 43.4	2012 Aug 30	2.3012	2.2948-2.3075	10	70
NIRSPEC								
GSS 29		16 26 16.8	-24 22 23.3	2003 Jun 21	2.2867	2.2705-2.3029	4	200
CRBR 12	ISO-Oph 21	16 26 17.2	-24 23 45.4	2003 Jun 20	2.2867	2.2705-2.3029	50	50
GY 21		16 26 23.6	-24 24 39.5	2001 Jul 10	2.2865	2.2699-2.3032	16.7	170
GY 30		16 26 25.5	-24 23 01.6	2003 Jun 19	2.2866	2.2691-2.3040	120	50
ISO-Oph 51		16 26 36.8	-24 15 51.9	2001 Jul 10	2.2865	2.2699-2.3032	15	100
GY 91		16 26 40.5	-24 27 14.5	2003 Jun 21	2.2866	2.2705-2.3028	40	55
WL 12	GY 111	16 26 44.2	-24 34 48.4	2001 Jul 07	2.2871	2.2705-2.3037	87.3	215
WL 1	GY 192	16 27 04.1	-24 28 29.9	2000 May 30	2.2846	2.2685-2.3008	30	35
GY 197		16 27 05.3	-24 36 29.8	2003 Jun 21	2.2865	2.2691-2.3040	90	20
WL 17	GY 205	16 27 06.8	-24 38 15.0	2001 Jul 10	2.2865	2.2699-2.3032	30	140
WL 10	GY 211	16 27 09.1	-24 34 08.1	2003 Jun 20	2.2866	2.2692-2.3041	20	200
GY 224		16 27 11.2	-24 40 46.6	2001 Jul 10	2.2865	2.2699-2.3032	50	150
WL 19		16 27 11.7	-24 38 32.1	2000 May 30	2.2846	2.2671-2.3022	20	150
WL 3	GY 249	16 27 19.2	-24 28 43.8	2001 Jul 10	2.2865	2.2699-2.3032	40	95
WLY 2-43	GY 265	16 27 26.9	-24 40 50.8	2001 Jul 07	2.2869	2.2706-2.3032	73.3	330
WLY 2-44	YLW 16A	16 27 28.0	-24 39 33.5	2001 Jul 8	2.2871	2.2705-2.3037	38	170
VSSG 17	WLY 2-47	16 27 30.2	-24 27 43.4	2001 Jul 10	2.2865	2.2700-2.3030	6	160
WLY 2-51	GY 315	16 27 39.8	-24 43 15.1	2003 Jun 20	2.2870	2.2705-2.3035	4	330

[a]Sources names from optical studies by (SR) Struve and Rudkjobing (1949), (WSB) Wilking *et al.* (1987), and infrared studies by (GSS) Grasdalen *et al.* (1973), (VSSG) Vrba *et al.* (1975), (EL) Elias (1978), (WL) Wilking and Lada (1983), (YLW) Young *et al.* (1986), (WLY) Wilking *et al.* (1989), (GY) Greene and Young (1992), (CRBR) Comeron *et al.* (1993), (ISO-Oph) Bontemps *et al.* (2001).

[b]Central wavelengths, wavelength ranges, and SNRs for iSHELL are for order 226 which contains the CO $v = 0 - 2$ bandhead.

Table 2.2. Log of Radial Velocity Standards

Source Name	RA(J2000) (hhmmss.s)	DEC(J2000) (° ′ ″)	Date	λ_{range} (μm)	Sp. Ty.	RV (Pub.)[a] (km s^{-1})	RV (this study) (km s^{-1})
CSHELL							
HD 111631	12 50 43.6	-00 46 05.2	2016 Jun 29	2.2956-2.3006	M0.5 V	4.48±0.15	2.5±1.5
HD 122120	13 59 19.4	+22 52 11.1	2016 Jul 10	2.2956-2.3006	K5 V	-58.04±0.37	-57.1±1.5
HD 147776	16 24 19.8	-13 38 30.0	2016 Jul 13	2.2908-2.2959	K2 V	7.20±0.18	5.5±1.5
HD 156026	17 16 13.4	-26 32 46.1	2016 Jul 14	2.2908-2.2959	K5 V	-0.04±0.22	1.2±1.5
iSHELL							
HD 122120	13 59 19.4	+22 52 11.1	2017 Apr 26	2.2835-2.2997	K5 V	-58.04±0.37	-56.80±0.37
HD 156026	17 16 13.4	-26 32 46.1	2017 Apr 26	2.2835-2.2997	K5 V	-0.04±0.22	1.24±0.37
HD 165222	18 05 07.6	-03 01 52.7	2017 Apr 27	2.2835-2.2997	K4/5 V	32.26±0.19	32.36±0.37
HD 173818	18 47 27.2	-03 38 23.4	2017 Apr 28	2.2835-2.2997	K5 V	15.33±0.17	16.28±0.37
CRIRES							
HD 129642	14 45 09.7	-49 54 58.6	2008 Apr 28	2.2949-2.3047	K2 V	-6.47±0.20	-6.28±0.12
NIRSPEC							
GJ 806	20 45 04.1	+44 29 56.6	2003 Jun 19	2.2705-2.3029	M2 V	-24.84±0.31	-24.3±1.3
HD 201091	21 06 53.9	+38 44 57.9	2003 Jun 19	2.2705-2.3029	K5 V	-64.94±0.14	-65.8±1.3

[a]Radial velocities from the Gaia DR2 data release Soubiran *et al.* (2018)

3. MARKOV-CHAIN MONTE CARLO METHODS

In order to model much of the data for this project, a Markov-Chain Monte Carlo (MCMC) routine developed by Foreman-Mackey *et al.* (2013) was used to fit various physical parameters of the objects observed. This was achieved using synthetic spectra obtained from the Göttingen Spectral Library based on the PHOENIX stellar atmosphere code (Husser *et al.*, 2013), which were veiled, rotated, and Doppler shifted until they closely matched the observed spectra. The use of MCMC routines in astronomy is relatively new, however these techniques are becoming more and more common due to how powerful they can be. The reason these kinds of routines are used is because they are very good at exploring multi-dimensional parameter spaces with degeneracy, which is exactly the case for the problem of fitting models to spectra given the various ways these parameters can affect the shapes of absorption lines detected. This section will cover some of the general Bayesian statistics behind how these programs work and why they are so useful. It will then cover the specifics of the program used for this project (*emcee*) and how it was used to fit the parameters of interest for this study. The code used for this project was run in Python 2.7 using a Jupyter notebook and has been included as Appendix A.

3.1. BAYESIAN STATISTICS

Bayesian probability theory can be derived from the sum rule and product rule. The sum rule simply states that the probability of something being true plus the probability of it not being true must be one. The product rule is a little more complicated, but can be written as

$$p = (H, D|I) = p(H|D, I)p(D|I) = p(D|H, I)p(H|I). \tag{3.1}$$

In other words, the probability of H and D being true given I is true is equivalent to the probability of H being true given D and I multiplied by the probability of D being true given I, and vice versa. Rearranging this equation gives us Bayes's theorem:

$$p(H|D,I) = \frac{p(D|H,I)p(H|I)}{p(D|I)} \tag{3.2}$$

The first term on the right side of the equation, $p(D|H,I)$ is known as the likelihood, or as the probability of observing the data D, given that the hypothesis, H, is true. The second term, $p(H|I)$, is called the prior and represents any previous knowledge about H being true. The denominator, $p(D|I)$, is a constant and serves to normalize the distribution. The left side, $p(H|D,I)$, is called the posterior distribution and, conceptually, is the updated probability of the hypothesis being true given the data (Cox, 1946; Sharma, 2017).

3.2. BAYESIAN STATISTICS WITH MCMC

This theorem can be very useful when trying to fit a model to some data, which is exactly what needs to be done for this project. A relevant example for how Bayesian statistics can be utilized by MCMC routines is the problem of trying to fit a straight line given by the equation $y = mx + c$ to some data points (Foreman-Mackey, 2013). The goal is to construct the likelihood and priors to generate the posterior distribution. However, in many cases the posterior distribution is very large and multidimensional and so cannot be computed directly. This is where the MCMC routines come in so as to sample the distribution in a representative way, without the need to explore the entire distribution space. For a straight line we can write the likelihood as

$$p(y|x,\sigma,m,c) = \Sigma\frac{1}{2\pi\sigma^2}\exp[-\frac{(y_i - mx_i - c)^2}{2\sigma^2}] \tag{3.3}$$

This assumes that the uncertainty, σ, of each data point is the same value. To construct the prior it is possible to use what are called "uninformative" priors. It means that upper and lower boundaries are provided for the parameters to be fit, in this case m and c. Essentially this serves to just say what are and are not acceptable values of m and c to sample, otherwise there would be infinite possible options. With this information the MCMC routine is able to sample the posterior distribution and search for areas where the values of m and c have the highest probability, i.e., trying to find the line that most likely describes the data. In addition to this, the MCMC routines will also explore the areas of the distribution near, but not necessarily at, the most likely values, and in doing so can provide uncertainties on each parameter (Sharma, 2017).

3.3. *emcee* AND MCMC SAMPLING ALGORITHMS

The next question is then how exactly MCMC programs, and in particular *emcee*, are exploring this distribution space. Monte-Carlo simulations make use of random walkers to move about the distribution space, while MCMC routines put some constraints on these walkers and try to provide them with more direction. This direction comes from what is called a Markov-Chain. A Markov-Chain is a sequence of random variables where the probability of moving to the next state is only dependent upon the current state, and not any previous states. When combined with Monte-Carlo techniques, the result is that the random walkers are no longer purely randomly sampling the distribution space, but instead are more likely to go towards areas with higher probability, and less likely to walk towards areas with lower probability. The most commonly used MCMC algorithm is known as the Metropolis-Hastings Algorithm (Hogg *et al.*, 2010). In this algorithm, a given walker starting at position $X(t)$ samples a proposed position Y based upon $X(t)$. This proposed position is often drawn from a Gaussian distribution centered on $X(t)$. If this step is accepted then $X(t + 1) = Y$, otherwise $X(t + 1) = X(t)$. The probability of this step being accepted is based upon comparing the probabilities of the two positions within the distribution space. In other

words, the step is more likely to be accepted if the proposed position has a higher likelihood of matching the data than the current position. This ensures that as t approaches infinity, the algorithm will converge to a stationary set of samples from the posterior distribution.

While useful in its most basic form, the Metropolis-Hastings Algorithm can be improved upon and has been within the open source *emcee* program. Specifically, the authors of *emcee* have modified what they call the "stretch move" which was originally developed by Goodman and Weare (2010). In the stretch move, instead of sampling the proposed moves for walkers from some distribution around the current position of the walker itself, proposed moves are based upon the positions of other walkers and upon a random variable, Z, from a distribution, $g(z)$, that satisfies

$$g(\frac{1}{z}) = zg(z) \tag{3.4}$$

such that, for some walker at position X_k, and the position of another random walker X_j, the propose move Y is given by

$$Y = X_j + (Z(X_k(t) - X_j) \tag{3.5}$$

This proposed move is then accepted based upon the relative probability of Y and X_k and upon the random variable Z. The advantage of this algorithm is that it is affine invariant, meaning that it is not affected by covariances among parameters. The improvement to this method by Hogg *et al.* (2010) is that they were able to have this algorithm run in parallel by simultaneously updating the positions of half the walkers at a time, instead of one at a time, thus improving the overall efficiency of the program.

3.4. *emcee* APPLIED TO INDIVIDUAL HIGH-RESOLUTION SPECTRA

As mentioned above, for this project *emcee* is being used to modify and fit synthetic spectra to real spectra taken at various telescopes. This problem is actually very similar to the example of fitting data to a straight line that was covered earlier. Instead of trying to figure out the slope and intercept (m and c), the program is being used to try and find the most likely values for rotational velocity, veiling, radial velocity, and temperature of each object. In addition to this the surface gravity ($\log(g)$) is chosen before the program is run depending on whether the object in question is a YSO or radial velocity standard. The general procedure is to read in both the data and the synthetic as (x, y) pairs and then bin the synthetic to the same wavelength range and resolution as the data. Then the likelihood and priors are constructed. When using this program, however, instead of working with regular probabilities, computations are done with the log of the probabilities in order to ensure certain values remain positive. The log of the likelihood is then given by

$$\ln[\, p(y|\sigma, m)] \; = -\frac{1}{2} \sum [\, \frac{(y_i - m_i)^2}{\sigma^2} + \ln(2\pi\sigma^2)] \tag{3.6}$$

where now y_i represents a data point and m_i represents a point on the model, and σ is the value of the data point divided by the approximate SNR. The next step is to construct the priors, which is done by setting up acceptable ranges in which the walkers in *emcee* are allowed to go. This amounts to finding physically reasonable ranges for each parameter informed by physical constraints and by previous estimates in the literature when possible. For instance, the rotational velocity and veiling cannot be negative as they are defined, and the radial velocity is unlikely to be more than a few dozen km s^{-1} away from zero. With this information, the log of the probability can be calculated which is then used by *emcee* when sampling the distribution. The end result is then relative probability distributions for each of the four parameters being fit, as well as their 1σ uncertainties.

As mentioned previously, the four parameters being fit are the veiling, rotational velocity, radial velocity, and temperature. For the program being used to run correctly, the synthetic and object spectrum both need to be normalized and have the same resolution and number of channels. De-reddening the spectra was not necessary given the narrow wavelength range of each order. For the wavelength range covered by most of the data, the vast majority of lines being fit are CO bandheads and absorption lines from the $v = 2 - 0$ energy level transition. Physically, the veiling is a measure of the emission from circumstellar gas and dust. The effect on the spectra is that there is extra continuum emission of infrared light, resulting in shallower absorption lines when compared with an unveiled star. The way this is measured is through the veiling coefficient, r_k. The relation between an unveiled spectrum and the same spectrum veiled by an amount r_k is

$$F_v = \frac{F + r_k}{1 + r_k} \tag{3.7}$$

where F_v is the veiled spectrum, and F the unveiled spectrum. For example, for $r_k = 1$, the absorption line depth is half of that compared to $r_k = 0$ (Stahler and Palla, 2004). Due to the sensitivity of r_k to the normalization, the veiling coefficient returned by the program is only accurate to first order. That being said, it is not irrelevant, and it is still important that the program is able to vary the depth of the absorption lines of the synthetic as this helps fit the other parameters of interest. The rotational velocity, or $vsini$, of the synthetic is modified by using a simple rotational broadening kernel from the PyAstronomy package called $rotBroad()$. This function simply takes in an unrotated synthetic spectrum smoothed to the resolution of the spectrometer and a value of $vsini$ in km s^{-1}, and returns the broadened spectrum. A higher value of $vsini$ will result in the observation of broader and shallower absorption lines. This is because the difference in the Doppler shift of one edge of the star moving away from the observer and one edge moving towards the observer broadens the wavelength range able to be absorbed. The important point, however, is that

changing the $vsini$ does not change the area of the absorption lines, unlike r_k. The most important parameter for this study being fit is the radial velocity. The effect this has is to simply shift the spectrum to bluer or redder wavelengths, depending on how fast the object is moving towards or away from Earth. This is modeled as a simple fractional pixel shift, assuming that there is a linear variation in normalized flux between each pixel. Because the shift is measured in pixels, the radial velocity measurement is sensitive to the resolution of the instrument being used. For this reason, the uncertainties in the radial velocities being measured are directly correlated with the resolution of the instrument. CRIRES and iSHELL data produce the most precise results, with NIRSPEC data being the least precise. An equation describing the modeling of these parameters is given by

$$F_{model}[i] = \text{rotBroad}(\frac{F_{T_{avg},\log(g)}[i + dx] + r_k}{1 + r_k}, vsini) \tag{3.8}$$

where F_{model} is the broadened, veiled, and shifted synthetic spectrum, $F_{T_{avg},\log(g)}$ is the unbroadened, unveiled, and unshifted synthetic spectrum corresponding to a certain $\log(g)$ and T_{eff}, dx is the pixel shift, r_k is the veiling factor, $vsini$ is the rotational velocity in km s^{-1}, and the rotBroad() function is a convolution determined by $vsini$.

In addition to these parameters, the surface gravity ($\log(g)$) and effective temperature (T_{eff}) can also be constrained for this study. The effect of increasing $\log(g)$ on the spectrum of a star is to increase the pressure in the gas in the atmosphere, and therefore broaden the absorption lines. Increasing T_{eff} increases the velocity distribution of the gas and again causes the lines to broaden. For both of these parameters it is possible, although difficult, to model them continuously. For this project, the choice was made to vary T_{eff} continuously within the program, while $\log(g)$ was held constant. This was done by averaging together two synthetics from the library in order to estimate a synthetic with an intermediate temperature to the models. For instance, several synthetics were read into the program with varying temperatures, but all with the same $\log(g)$. The program was then

able to create weighted averages of these synthetics to fill in the gaps and better model the temperature of the spectra. It is possible to interpolate both $\log(g)$ and T_{eff} and allow the program to create synthetics of any combination of $\log(g)$ and T_{eff}, however, this was not done for this project. One reason is that first averaging spectra of a given $\log(g)$ to constrain the temperature and then averaging those together to constrain the $\log(g)$ results in less accurate synthetics, since the T_{eff} and $\log(g)$ are not allowed to change together. While the uncertainties introduced into the synthetics by this method would most likely be too small to significantly impact the results, it was found that for this program, *emcee* would not adequately explore both dimensions. Instead it would pick the highest available $\log(g)$ and then adjust the other parameters accordingly. For these reasons the decision was made to just let T_{eff} vary, while $\log(g)$ was fixed for a given run. For sources believed to be YSOs, it was assumed that $\log(g) = 3.5$ which is typical for YSOs. For radial velocity standards $\log(g) = 4.5$ which is characteristic for these main sequence stars.

As a check for errors associated with assuming a standard $\log(g)$, separate runs were made for a range of values in T_{eff} ($\pm$500 K) and $\log(g)$ ($2.5 - 4.5$) while not letting either be a free parameter in the program. For a given source, the derived $vsini$ would decrease as $\log(g)$ increased and r_k would decrease as T_{eff} increased and CO lines weakened. However, these variations had little effect on the pixel shift and derived radial velocity, making the most important parameter from the model fits the most reliable.

Because each of these parameters can change the size and shape of the absorption lines in various ways, there will be some degeneracy in the possible solutions. But it is because of this degeneracy that using a Markov-Chain Monte-Carlo routine, such as *emcee*, is so helpful. For a given $\log(g)$, the program is able to vary each of the above parameters and explore the full distribution space.

3.5. *emcee* APPLIED TO RADIAL VELOCITY DATASETS WITH VELBIN

In addition to using *emcee* to model individual sources, it was also used to analyze the entire sample in order to derive values for the mean velocity of the cluster, the intrinsic velocity dispersion, and the binary fraction. This is necessary because single epochs of radial velocity data are likely to have their results affected by the presence of binaries. If a source with a close binary companion happens to be observed in such a way that a component of the binary orbital motion is directed towards or away from Earth, then the observed radial velocity will be offset from the source's true motion through the cluster. The overall effect on the sample is to increase the measured radial velocity dispersion of the cluster. For clusters with higher intrinsic velocity dispersions, this effect may be small, however, for clusters with dispersions smaller than a few km s^{-1}, the effect can greatly increase the measured dispersion (Gieles *et al.*, 2010; Kouwenhoven and de Grijs, 2008, 2009; McConnachie and Côté, 2010). The way this has been accounted for in this project is by using the program Velbin (Cottaar *et al.*, 2012) in conjunction with *emcee*.

In order to use these two programs together, the following information is required: a set of N radial velocity observations ($v_{obs,i}$), each with the associated uncertainties ($\sigma_{obs,i}$) and mass estimates (m_i), and assumptions about the binary period, mass ratio, and eccentricity distributions. Velbin interprets the radial velocity observations as being randomly drawn from a dynamical model describing the intrinsic velocity distribution. Free parameters for the dynamical model include the mean velocity (v_{mean}) and the velocity dispersion (v_{disp}). The intrinsic distribution is assumed to be Gaussian. Then, for a certain subset of stars, a velocity offset is added to v_{obs} based upon the binary fraction (f_{bin}). This offset is labeled as v_{bin} since it is the velocity due to the binary motion. The likelihood function for observing a specific radial velocity for a given star can then be written as

$$L_i(v_{obs,i}) = (1 - f_{bin})L_{dyn,i}(v_{obs,i}) + f_{bin}\int_{-\infty}^{+\infty} L_{dyn,i}(v_{obs,i} - v_{bin})L_{bin,i}(v_{bin})dv_{bin} \qquad (3.9)$$

This results in fitting the three free parameters v_{mean}, v_{disp}, and f_{bin}. The dynamical model of Velbin takes into account all of the assumptions regarding the binary period, mass ratio, and eccentricity distributions, in addition to the mass estimates and errors for the individual stars and the likelihood of the added velocity due to binary motion being in the direction of line of the sight. The overall likelihood function for the entire sample can then be computed by multiplying the individual likelihood functions. From there, Velbin computes the log-likelihood function and then the process is very similar to using *emcee* as before. The log-likelihood function is combined with the priors to compute the probability and fed into *emcee* which then returns relative probability distributions for how likely the given radial velocity dataset is described by v_{mean}, v_{disp}, and f_{bin}.

4. RESULTS

In total, there are 34 different sources that have been observed for this study. Of these, 32 have yielded precise radial velocity measurements which are presented in Table 4.1. Twenty-three of these are classified as either Class I or Flat spectrum objects. The location of these YSOs in the L1688 cloud relative to the distribution of cold dust is shown in Figure 2.1. Eleven sources were observed using the instrument CSHELL on NASA's IRTF during the summer of 2016. Twelve sources were observed using iSHELL in the spring of 2017, eleven of which yielded precise radial velocity measurements. In addition to the data taken specifically for this project, data from previous studies were obtained and reanalyzed using the same technique developed for the CSHELL and iSHELL data outlined in Section 3. Data were obtained from Doppmann *et al.* (2005) who used NIRSPEC on the Keck telescope; radial velocities were derived from these data for fourteen sources. And finally, data obtained from the ESO archive taken by Viana Almeida *et al.* (2012) or Cottaar (2012 unpublished data) using CRIRES on the VLT resulted in radial velocity measurements for seven sources. Between all the instruments and data runs, there were five sources for which radial velocities were derived for two epochs.

4.1. MEASURING RADIAL VELOCITIES WITH *emcee*

To measure the radial velocities of the sources observed, all of the spectra obtained were run through the MCMC routine described in Section 3. It was found that to explore adequately the full four-dimensional parameter space (rotational velocity, veiling, radial velocity, and temperature) the program needed 100 walkers to run for 500 steps. The output for each run was then a corner plot of the positions of these walkers along their steps, resulting in relative probability distributions. The corner plots themselves show

Table 4.1. Best Fit YSO Parameters for $\log(g) = 3.5$

Source Name[a]	SED Class[b]	Instr.	T_{eff} (K)	V_{helio} (km sec^{-1})	*vsini* (km sec^{-1})	orders
GSS 26	II	CRIRES	4400±20	-7.58±0.14	19.0±0.1	1
GSS 29	II	NIRSPEC	4360±40	-6.7±1.4	36.6±0.4	1
CRBR 12	I	NIRSPEC	3460±20	-12.9±1.5	40.5±0.7	1
VSSG 1	II	iSHELL	4370±300	-3.26±0.64	15.0±0.4	2
GY 21	FS	NIRSPEC	4340±100	-7.9±1.5	20.3±1.0	1
GY 23	II	CRIRES	4120±20	-7.81±0.14	20.9±0.2	1
GY 30	I	NIRSPEC	3140±20	-7.5±1.5	33.5±1.1	1
GY 33	FS	iSHELL	4220±20	-3.67±0.81	13.1±0.7	3x2
ISO-Oph 51	FS	NIRSPEC	4500±180	-4.8±1.9	34.8±2.1	1
GY 91	I	NIRSPEC	3450±20	-7.8±1.4	9.6±0.2	1
WL 12	I	NIRSPEC	3420±140	2.3±2.3	31.6±2.7	1
SR 24N	II	iSHELL	3380±20	0.89±0.42	9.5±0.8	3
SR 24S	II	iSHELL	4900±80	-0.27±0.61	28.5±0.5	3
WL 1	FS	NIRSPEC	3420±20	-25.1±1.4	13.3±0.4	1
GY 197	I	NIRSPEC	3220±20	-7.7±1.5	49.8±1.1	1
WL 17	I	NIRSPEC	3360±60	-3.8±1.5	3.1±2.9	1
		CRIRES	3120±20	-3.87±0.18	14.56±0.08	1
WL 10	II	NIRSPEC	4580±140	-7.6±1.5	39.0±0.9	1
GY 224	FS	NIRSPEC	4400±210	-5.8±1.5	9.9±2.8	1
		CRIRES	5420±50	-5.54±0.39	23.0±0.8	1
WL 19	FS	NIRSPEC	3680±380	-27.4±1.7	22.7±1.9	1
GY 235	FS	iSHELL	3360±20	-5.4±1.2	12.1±0.1	2
WL 20W	FS	iSHELL	3380±20	-1.96±0.82	25.6±0.2	1
WL 20E	FS	iSHELL	4840±60	0.00±0.55	41.1±0.3	1
WL 4	FS	iSHELL	3260±20	0.33±0.38	17.0±0.2	1
WL 3	I	NIRSPEC	4320±30	-6.9±1.4	40.7±0.4	1
WLY 2-42	FS	iSHELL	4420±20	-5.46±0.37	22.1±0.2	1
WLY 2-43	I	NIRSPEC	4920±190	-8.0±3.2	47.0±3.6	1
WLY 2-44	I	NIRSPEC	4360±380	-8.3±1.8	28.9±1.6	1
		CRIRES	5300±60	-4.37±0.41	29.1±0.6	1
VSSG 18	FS	CRIRES (08)	3800±20	-4.85±0.14	23.61±0.05	1
		CRIRES (12)	4100±20	-3.37±0.15	22.2±0.1	1
VSSG 17	FS	NIRSPEC	4160±90	-6.2±1.5	41.2±0.5	1
		CRIRES	4040±40	-5.48±0.36	43.4±0.5	1
GY 284	FS	iSHELL	3440±20	-3.78±0.71	6.1±0.5	3x2
GY 314	II	CSHELL	3220±20	-5.5±1.5	16.9±0.5	1
WLY 2-51	FS	NIRSPEC	4660±230	-3.5±2.3	42.3±2.0	1

[a]Sources names same as Table 1

[b]Spectral energy distribution class as defined by the spectral index from 2.2-24 μm

the probability distribution for each parameter separately along the diagonal and the off-diagonal plots show correlations between each pair of parameters. Approximately the first 100 steps were excluded from the corner plots as this was found to be the "burn in" time for the program to settle on what it thought were the most likely values. This results in the corner plots themselves being approximately Gaussian distributions centered on the most likely values for each parameter. These center values were then exactly calculated by finding the value that was higher than 50% of the positions of the walkers and used to create a synthetic to plot over the original data to ensure that the program was returning physically meaningful results. A sample corner plot and overlay of GY 33 taken from iSHELL can be seen in Figures 4.1 and 4.2. Parameters derived for YSOs are presented in Table 4.1, and radial velocities for radial velocity standards are in Table 2.2.

Corner plots and overlays for each source observed can be found in Appendix B. When looking at the corner plots, the first two parameters ($vsini$ and r_k) correspond directly to the physical quantities of the rotational velocity and the veiling. However, dx corresponds to the shift in the spectrum measured in pixels, meaning that this value still needs to be converted to a heliocentric radial velocity via the dispersion of the instrument and detector, as well as corrected for the Earth's motion around the Sun depending on the date and time of the observation (as has been done in Table 4.1). The last parameter, T_{eff}, is a measurement of the effective surface temperature of the star, but the actual value of T_{eff} returned by the program corresponds to the weighted average of two synthetics represented by their array index, as discussed in Section 3. In case of GY 33, the T_{eff} of 5.8 corresponds to a temperature of about 4260 K. The uncertainties in the fit parameters quoted in Table 4.1 are from the 16th and 84th percentile of the marginalized distributions. While the veiling of each source was measured, and does correspond to a physical quantity, it was found to be a nuisance parameter for this study. Since the veiling affects the depths of the absorption lines, the value returned by *emcee* was found to be very sensitive to the normalization of the spectra. Since the exact location of the continuum is often poorly constrained for these

spectra, especially those with low SNRs or high rotational velocities, the measured veiling was found to have a wide variance for the sources that were observed multiple times, or even across multiple orders of the same spectrum for those sources observed using iSHELL. For this reason the veiling parameter has been left out of the results in Table 4.1.

With the radial velocities for each of these sources measured, a histogram of these velocities with 1.5 km s^{-1} bins (corresponding approximately to the largest uncertainty for a given radial velocity) has been constructed and is shown in Figure 4.2. This histogram would indicate a velocity dispersion of 2.9 ± 0.8 km s^{-1}. This is significantly higher than what was expected for this cluster based upon previous studies. However, at this point no correction for binaries has been made, which means this should be higher than the intrinsic velocity dispersion given the high binary fraction measured for younger stars. It is also clear from this figure that the distribution itself is rather non-Gaussian, making the calculation of a velocity dispersion much more difficult. As described in Section 3, the program Velbin was used to analyze these data and attempted to correct for the presence of binaries. The details of this analysis are discussed in Section 4.3.

4.2. ERROR ANALYSIS

As can be seen in Figure 4.1, one advantage of *emcee* is an estimation of the errors. However, the 1σ statistical error in the radial velocity returned by *emcee*, while related to the SNR of our spectrum, underestimates the total error of the radial velocities presented in Table 4.1. Since the program did not vary the surface gravity, there will be an uncertainty associated with assuming a surface gravity ($\log(g)$ = 3.5 for YSOs, $\log(g)$ = 4.5 for radial velocity standards). For several sources, we fixed the temperature and varied $\log(g)$ from 2.5 to 4.5 in steps of 0.5. Variations in $\log(g)$ resulted in slight variations on the best fit pixel shifts, and an error of 0.1 pixels was adopted for this effect. This means, of course, that this error is proportional to the resolution of the instrument. In addition to this, there

were several other contributions to the error which were dependent upon the instrument and all added in quadrature with the error from *emcee* and log(g) that are discussed in the following section.

In the case of CSHELL, there was only one YSO for which a radial velocity was derived, GY 314. The largest contribution to the error appears to be from the wavelength calibration arising from small shifts between the source and the telluric standard from which the calibration was determined. This error has been estimated to be 1.5 km s^{-1} based on comparisons between the four radial velocity standards that were observed with CSHELL (Table 2.2) and radial velocities measured for those same stars by the Gaia DR2 survey (Soubiran *et al.*, 2018). This is the dominant source of uncertainty for the CSHELL radial velocities.

For NIRSPEC, due to the lower spectral resolution, the error from *emcee* is larger than that from the other spectrographs. To estimate our systematic errors, radial velocity standards from NIRSPEC were used in place of the synthetics for a few sources. This allowed for a comparison of the pixel shift of a given YSO measured against the synthetics vs. the standards. It was found that the average difference was 0.3 pixels which corresponds to an uncertainty of about 1.3 km s^{-1}. This uncertainty is attributed to the wavelength calibration and noting that the spectra were calibrated using arc lamps available on NIRSPEC that do not contain very many bright lines near the CO bands. When this is added in quadrature with the uncertainties from the program itself and log(g), the typical error is around 1.5 km s^{-1}. This is nearly the same error that was quoted by Covey *et al.* (2006) for this data set obtained by comparing their derived radial velocities to 15 spectral standards with published values.

CRIRES has the highest spectral resolution of all the spectrographs used and yielded the smallest errors on average. This should not be a surprise since the *emcee* routine developed for this project is ultimately measuring pixel shifts, which are then converted into radial velocities. It is also the case that the wavelength calibration for CRIRES spectra,

using well-resolved telluric lines, was the most accurate out of all the instruments. The same method as described above, using a radial velocity standard in place of a synthetic and comparing the shifts, was used with CRIRES data as well. The difference in the shifts between the two methods was found to be, on average, less than 0.1 pixels. With the high resolution of CRIRES, this only corresponds to an uncertainty of about 0.1 km s^{-1}. Consequently, the main contributors to the radial velocity errors were the error returned by *emcee*, and the error due to the assumed value of $\log(g)$.

Finally for the iSHELL data, the errors quoted in Table 4.1 are mainly due to the wavelength calibration. During the reduction process, iSHELL Tool allows the user to have the program automatically shift the telluric by a very slight amount in order to minimize the presence of telluric lines in the final spectrum. The average shift was about 0.5 pixels and was always less than 1.0 pixel. A similar shift was seen from running *emcee* with a YSO and a radial velocity standard in place of the synthetic. As a check, it was possible to compare the difference in the radial velocities measured across multiple orders, across the course of a given night, and across multiple nights. For several sources the CO bands were strong enough to be seen in three orders. In the case of GY 33, it was observed at two different times on the same night at different air masses. And in the case of GY 284, it was observed on two successive nights. The derived radial velocities across multiple orders, multiple airmasses, and multiple nights are consistent within the errors computed considering contributions from *emcee*, the wavelength calibration, and $\log(g)$. This, and the agreement between the radial velocity standards in Table 2.2 with their published values, suggests that no major sources of error have been neglected.

4.2.1. Comparisons with Published Data. It should be pointed out, however, that many of the radial velocity measurements in Table 4.1 do not always agree with those published by Viana Almeida *et al.* (2012). Of the four sources retrieved from the ESO archive, only the radial velocity of GSS 26 is close to their published value. It is not clear why their results do not match up with the ones presented here, but, as a check, the one

available radial velocity standard in their data was again compared with the result obtained by the Gaia DR2 survey. As shown in Table 2.2, the result derived from *emcee* agrees very well the Gaia DR2 value but not with that derived by Viana Almeida *et al.* (2012).

When looking at the NIRSPEC data, the results presented here can also be compared to the results obtained by Doppmann *et al.* (2005) when the data were originally published and to the results published by Covey *et al.* (2006) when reanalyzing the data. Generally, the results presented here match up better with the results obtained by Covey *et al.* (2006) within the mutual uncertainties, although there are a few sources where this is not true. The largest discrepancy is regarding WL 12. The best explanation is that this source has a low SNR and is probably heavily veiled, leading to a very washed out and not well-defined CO $v = 2 - 0$ bandhead. This makes it difficult for the program to line up exactly where the bandhead should be, and with the low resolution of the instrument, these effects could lead to a large error. That being said, the radial velocity standards analyzed from the NIRSPEC data agree well with the results from the Gaia DR2 data release.

The only source with a derived radial velocity from CSHELL, GY 314, has been observed before by Prato (2007), and agrees well within the mutual errors.

4.2.2. Radial Velocity Variables. While most of the data here is single-epoch, there are seven sources with multi-epoch datasets. Within the stated uncertainties, GY 314, WL 17, GY 224, and VSSG 17 do not show evidence for radial velocity variability. In the case of WLY 2-44, VSSG 18, and SR 24S, there is reason to believe that these sources have variable radial velocities. For SR 24S, it is clear that it has a wide companion in SR 24N, which was also observed. However, there is evidence that this might be an even higher order star system. According to the measurements made from both the iSHELL data and the Rigliaco *et al.* (2016) dataset, SR 24S may have its own companion with subarcsecond separation. Rigliaco *et al.* (2016) measured the radial velocity in 2012 to be -8.2 ± 0.33 km s^{-1} while the iSHELL data taken from the spring of 2017 shows a radial velocity of -0.27 ± 0.61 km s^{-1}. This is a relatively bright source with high SNR data and so the

most likely explanation for this discrepancy would be that the radial velocity is variable. WLY 2-44 was observed by NIRSPEC in 2002 and CRIRES in 2008, and is known to have one, or perhaps two, subarcsecond companions (Plavchan *et al.*, 2013; Terebey *et al.*, 2001). The NIRSPEC data showed a radial velocity of -8.3 ± 1.8 km s^{-1}, while the CRIRES data indicated a radial velocity of -4.37 ± 0.41 km s^{-1}. Finally, VSSG 18 was observed by CRIRES in 2008 and again in 2012. In this case, the difference is small with the 2008 data indicating a radial velocity of -4.85 ± 0.14 km s^{-1} and the 2012 data a radial velocity of -3.37 ± 0.15 km s^{-1}. The higher precision of CRIRES and thorough error analysis indicates that these measurements are outside each other's uncertainties. Once again, the most likely explanation for this difference is that VSSG 18 does in fact have a variable radial velocity, implying the presence of a subarcsecond companion.

4.3. MEASURING CLUSTER PROPERTIES WITH VELBIN

After having established radial velocity measurements for 32 sources within the L1688 cloud, the next step is to try to learn about the properties of the cluster as a whole. To do this, the program Velbin was used in order to constrain the cluster's velocity dispersion, binary fraction, and mean velocity as outlined in Section 3. In order to use Velbin, the program requires a radial velocity, the error in the radial velocity measurement, and a mass estimate for each source. The radial velocities and errors have been presented in the previous section, which leaves the mass estimate for each source to still be determined. The way this is done for young stars is to model their mass depending upon their location in a Hertzprung-Russell diagram relative to theoretical pre-main sequence tracks and isochrones. This means that the accuracy of these mass estimates is dependent upon the accuracy of intrinsic luminosity and temperature measurements. Temperature estimates have been obtained from the *emcee* routine used to model all the sources and those have been used when estimating masses. However, luminosity measurements are much more difficult to obtain.

Due to the deeply embedded nature of these YSOs within the cloud, and the large infrared excesses (veiling), intrinsic luminosities are difficult to estimate. The excesses lead to overestimates of the luminosity and often imply ages younger than the earliest model isochrones. Nevertheless, for small infrared excesses, luminosity estimates can be made to within a factor of a few. (J-H) colors were available for 22 of our 32 sources from the 2MASS catalog (Cutri *et al.*, 2003) and de-reddened using the reddening law of Yuan *et al.* (2013) and intrinsic colors for main sequence stars from Pecaut and Mamajek (2013). Adding the appropriate bolometric correction to the dereddened absolute J magnitude yielded the intrinsic luminosity assuming a distance of 137 pc. There were three different theoretical models used to produce mass estimates including ones developed by D'Antona and Mazzitelli (1997), Palla and Stahler (1999), and Siess *et al.* (2000). When running Velbin, the estimates produced by the D'Antona & Mazzitelli model were used. While other, more recent models are seemingly more accurate, there is very little difference in the various models for stars that are near one solar mass or less (Herczeg and Hillenbrand, 2015). Published mass estimates for 8 objects from this study range from 0.2 – 1.7 $M_{\odot}$ and the mass estimates from this study agree with these to within a factor of two (Correia *et al.*, 2006; Erickson *et al.*, 2011; Ressler and Barsony, 2001; Rigliaco *et al.*, 2016; Simon *et al.*, 2017). As the mass estimates scale roughly with $\log T_{eff}$, for sources that could not be de-reddened we have assigned masses of 1.5, 1.0, 0.5, or 0.2 $M_{\odot}$ based on their $\log T_{eff}$. For the mass range in this sample, variations in mass do not have a large effect on the results of Velbin. As a check to this, Velbin was run several times, with various mass estimates. It was found that even assuming all the sources in this study were 1.5 $M_{\odot}$ the values returned by Velbin were nearly identical to the ones returned using the mass estimates from the models.

The corner plot from running Velbin on all 32 sources can be seen in Figure 4.3. In addition to this, because of the large uncertainties in mass estimates, Velbin was also run on the same dataset, but with the masses set to uniformly be 0.5 $M_{\odot}$, 1.0 $M_{\odot}$, or 1.5 $M_{\odot}$. The

Table 4.2. Velbin Results for Various Masses

Source Masses ($M_\odot$)	v_{mean} (km s^{-1})	v_{disp} (km s^{-1})	f_{bin}
From Models[a]	-4.9 ± 0.6	2.8 ± 0.6	0.7 ± 0.3
0.5	-4.8 ± 0.6	2.8 ± 0.6	0.7 ± 0.3
1.0	-4.9 ± 0.6	2.7 ± 0.6	0.6 ± 0.3
1.5	-4.9 ± 0.6	2.5 ± 0.6	0.6 ± 0.3
From Models[a]	-4.9 ± 0.6	2.5 ± 0.7	$f_{bin} = 1.0$[b]

[a]Mass Estimates for sources computed from models created by D'Antona and Mazzitelli (1997).

[b]For this run f_{bin} was not allowed to be a free parameter, but set to 1.0 to see how far down this would push the dispersion.

results of these runs can be seen in Table 4.2. The results from this program point towards a velocity dispersion of about $\Delta v = 2.8 \pm 0.6$ km s^{-1} and a binary fraction of $f_{bin} = 0.7 \pm 0.3$. It is clear that the mass estimates do have some effect on the results, with higher masses resulting in a lower velocity dispersion. But it can be seen that this effect is overall very small for masses within the range expected for these sources.

This same program was used by Rigliaco *et al.* (2016) to analyze their dataset of mostly Class III objects. The dispersion measured by this same program for those data is much smaller ($\Delta v = 1.14 \pm 0.35$ km s^{-1}) than what is found here for a different set of objects in the central regions of the cluster. Moreover, the binary fraction measured here is slightly larger than $f_{bin} = 0.56$ found by Rigliaco *et al.* (2016), although consistent within the 1σ errors. There are several potential reasons why these measured dispersions do not agree, including problems with sample size, error size, or miscalculated binary fractions, and these will be discussed in greater detail in Section 5.

4.4. ADDITIONAL INFORMATION REGARDING SPECIFIC SOURCES

While the main focus of this project was to derive precise radial velocities from the data, there is a wealth of information that can be obtained from the spectra. In particular, the iSHELL data covered a very large wavelength range that included 3 CO bandheads ($v = 2-0, 3-1, 4-2$), Brγ (2.166 μm), and a number of atomic lines. Brγ emission is of interest because it is associated with accretion; the Brγ luminosity is correlated with the accretion luminosity and can be used to estimate accretion rates for YSOs (Muzerolle *et al.*, 1998). Brγ emission was detected in the spectra of VSSG 1, SR 24S, GY 235, WLY 2-51, and WLY 2-54. In addition, emission from shocked molecular hydrogen at 2.12 μm was detected in SR 24S, GY 235, and WLY 2-54. This is usually associated with energetic mass outflows.

Another notable feature was found in the spectrum of WLY 2-54. The spectrum itself is basically devoid of any photospheric absorption lines, but along with Brγ and H_2 emission, there were very narrow interstellar absorption lines from the low R and P branch of the CO $v = 2-0$ transition. The source itself worked out to be a featureless template that allowed for the identification of these lines in 10 other YSOs in our sample. With this information, it should be possible to estimate the temperature and optical depth of the foreground gas, and a different group is already analyzing these data as an independent project.

There are further notes regarding individual sources that can be found in Appendix C.

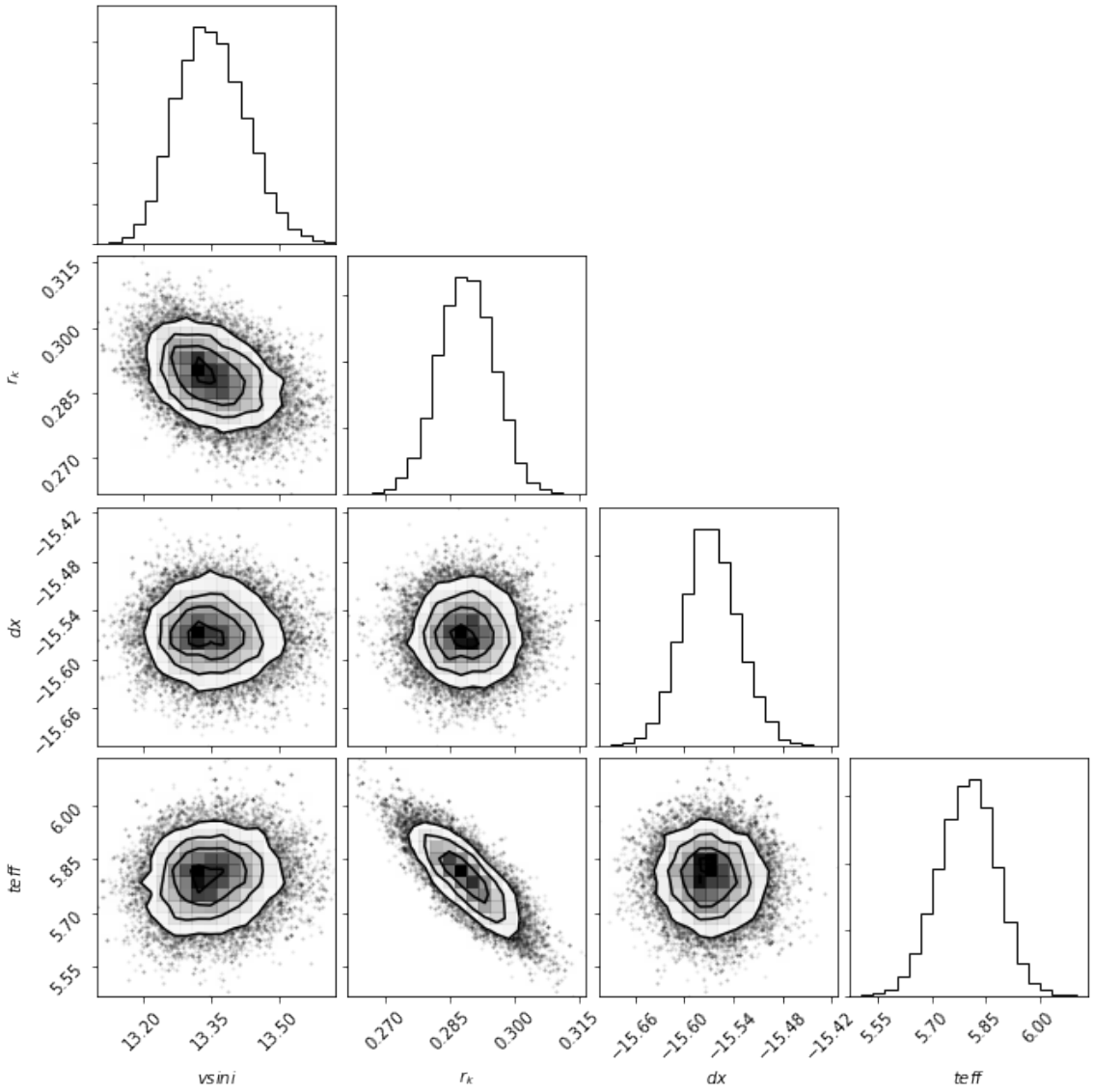

Figure 4.1 Relative probability distributions and correlations for the four fit parameters returned by *emcee* to best match the iSHELL spectrum of order 225 of object GY 33 corresponding to $T = 4260 \pm 20$ K, $vsini = 13.3 \pm 0.08$ km s^{-1}, $r_k = 0.29 \pm 0.02$, and $dx = -15.57 \pm 0.04$.

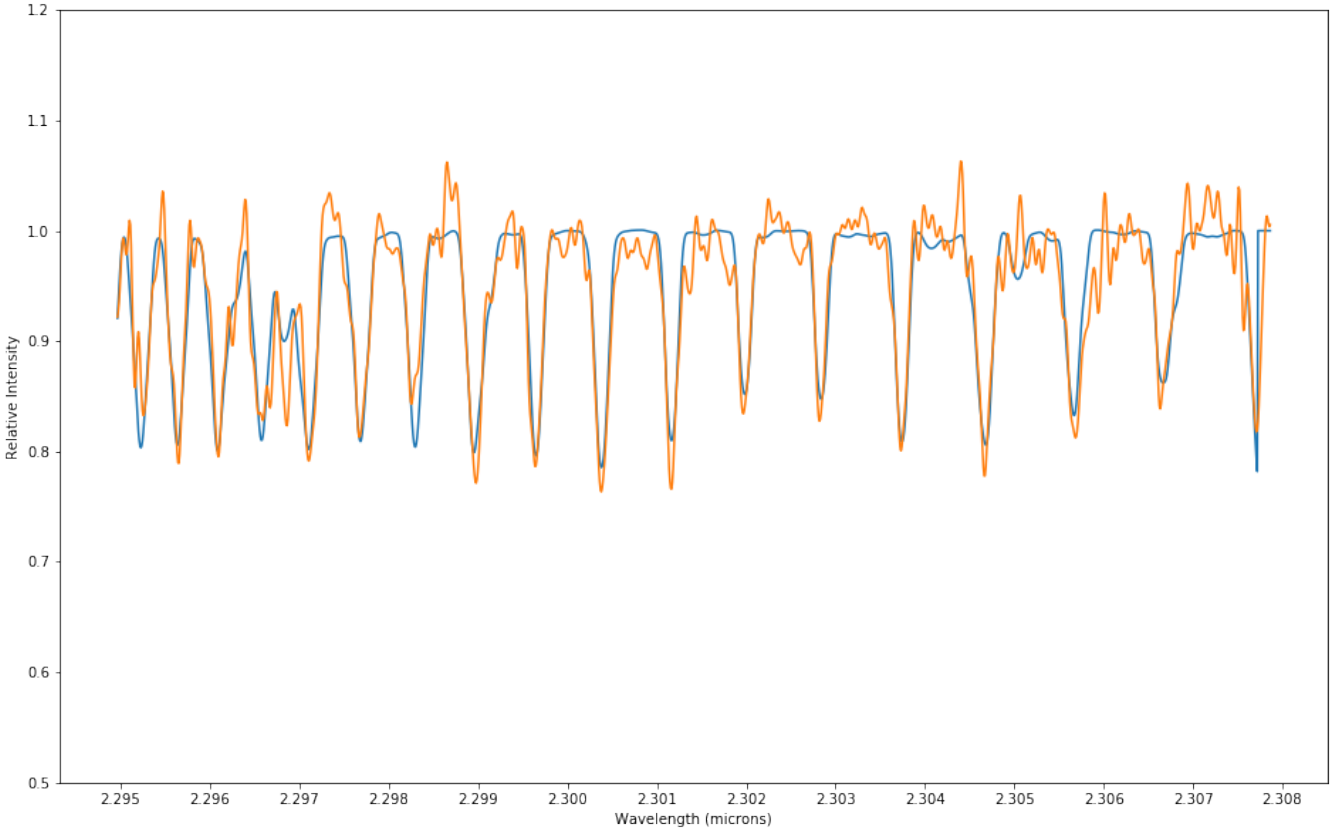

Figure 4.2 Synthetic overlay (blue) on top of the data (orange) for the four fit parameters returned by *emcee* to best match the iSHELL spectrum of order 225 of object GY 33 corresponding to $T = 4260 \pm 20$ K, $vsini = 13.3 \pm 0.08$ km s^{-1}, $r_k = 0.29 \pm 0.02$, and $dx = -15.57 \pm 0.04$.

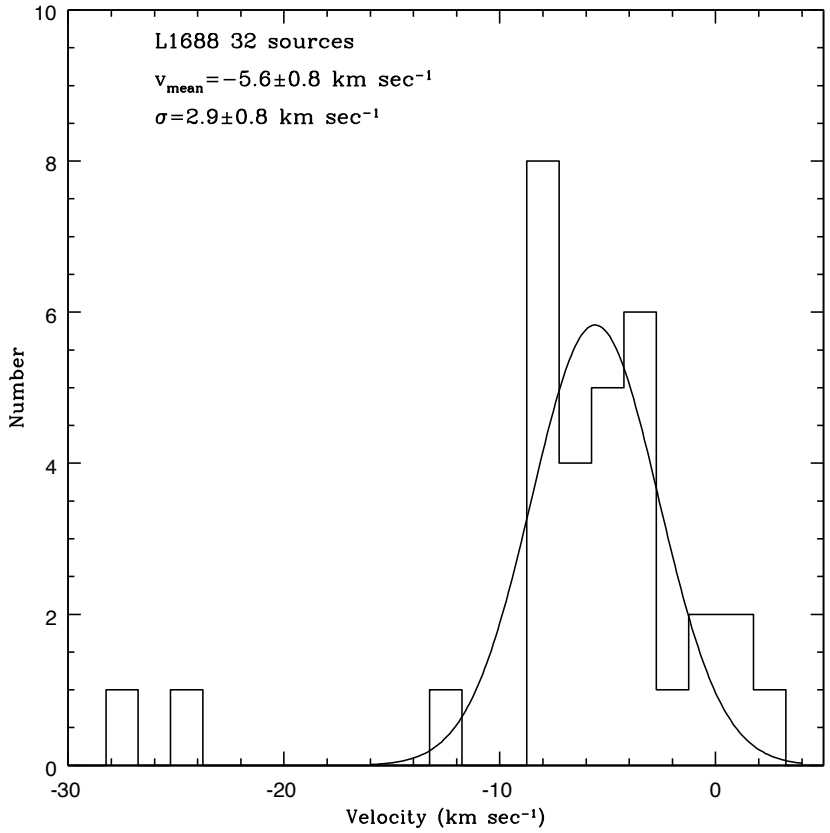

Figure 4.3 Histogram of 32 sources from the L1688 cloud with overlaid Gaussian fit of 30 sources. The two outliers between −25 and −30 km s^{-1} have been excluded from the fit.

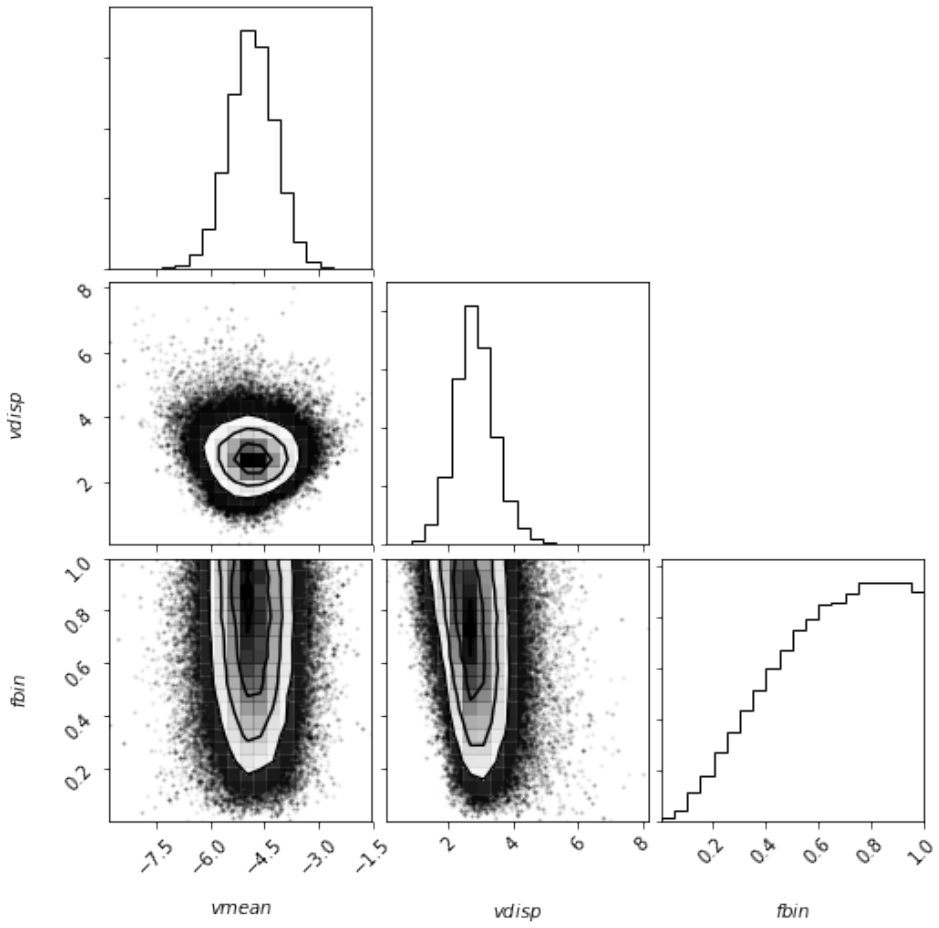

Figure 4.4 Corner plot showing the relative probability distributions of the fit parameters for the sample of 32 YSOs as measured by Velbin corresponding to $v_{mean} = -4.9 \pm 0.6$ km s^{-1}, $v_{disp} = 2.8 \pm 0.6$ km s^{-1}, $f_{bin} = 0.7 \pm 0.3$.

5. ANALYSIS AND DISCUSSION

The original motivation for this work was to attempt to learn more details about the environment in which low mass stars form. As discussed in Section 1, it is clear that the dense cores out of which these stars are forming are in a subvirial state (André *et al.*, 2007; Kirk *et al.*, 2010; Peretto *et al.*, 2006), while studies of more evolved Class II and III YSOs show signs of being near virial equilibrium (Rigliaco *et al.*, 2016). The initial hypothesis was that the less evolved Class I and Flat spectrum sources would show a velocity dispersion somewhere in between the dense cores and the more evolved sources as they had experienced fewer stellar encounters. As can be seen from the results in the previous section, this appears not to be the case.

In this section, a few ideas for how to interpret these results will be discussed. Since the results here do not match up with the results of the proper motion study by Wilking *et al.* (2015), it is important to discuss the differences between them. It is also important to discuss any possible biases in the sample itself. One way to end up with a higher than expected dispersion would be to have a sample that is biased towards low mass stars, which would have higher velocities. Another factor that must be taken into account is the limitations and assumptions made by Velbin when calculating the intrinsic dispersion. The program does not take into account higher order systems such as triple systems, of which there are at least a few in this sample. Velbin may also not be able to precisely determine the likelihood of a binary companion due to some of the larger errors for sources observed by NIRSPEC and CSHELL thus leading to a higher dispersion. If the binary fraction were higher than expected, it would also help explain the higher velocity dispersion. The age of this sample compared to the relaxation time could also affect the results, and push the dispersion higher or cause the distribution of velocities to be non-gaussian as the younger sources observed here have not had time to dynamically interact as often as some of the more evolved YSOs.

Finally, simulations suggest it is possible that as these objects evolve, they move from a subvirial state to a supervirial state, and then settle into a virial state (Kuhn *et al.*, 2018; Sills *et al.*, 2018). In this scenario, shortly after the YSOs form, subclusters would need to collapse towards one another and then rebound very quickly before settling into a virialized state in order to explain the both the results of the Rigliaco *et al.* (2016) study as well as this one. These ideas or some combination of them are almost certainly responsible for the results derived in Section 4 and will be discussed in this section.

5.1. COMPARISON WITH PROPER MOTION STUDY

In total, there are 32 YSOs for which radial velocities were derived for this study. In comparison, Rigliaco *et al.* (2016) had a sample size of 47. When looking at the difference between velocity dispersions derived between this study and that of Rigliaco $etal.$, the results are in agreement to within 2σ errors. Certainly, some of this discrepancy could be from the smaller sample size, however, the proper motion study (Wilking *et al.*, 2015) done before this project indicates that it is unlikely to explain the entire difference. The proper motion study had a larger sample, but it could be split up nearly evenly into two groups: a group of 29 Class I and Flat spectrum objects, and a group of 28 Class II/III objects. These groups then each had a relative 1-D velocity dispersion derived from their RA and Dec motions (Figure 1.3). The results from the proper motion study are similar to what was expected for this study, i.e., the dispersions are all at or around the dispersions of the more evolved objects. So there is already a sample of about 30 Class I and Flat spectrum objects within L1688 that has a 1-D velocity dispersion that appears to be consistent with the Rigliaco *et al.* (2016) radial velocity study but inconsistent with this study.

This contradiction implies a possible problem with the data in either the proper motion study or this one. The proper motion study was only able to derive relative proper motions by assuming the average proper motion in each of four fields in both RA and Dec was the same. Two fields were centered on the core E/F subcluster, one on core B, and one

on Core A. If this assumption is not correct, and the average proper motion for each field of view was different, then it would have the effect of underestimating the true dispersion. This could explain some of the discrepancy in the results between the studies.

One advantage of the proper motion study is that the effect of binaries on the dispersion is minimized. Since the proper motions are being derived over decade long baselines, any effects due to binaries would either be averaged out over several periods, or be too small to have a significant impact on the measured motion.

5.2. LOW MASS BIAS

Another possible explanation for a higher than expected dispersion would be that the sample in question is not unbiased. If the sample presented here is somehow biased towards lower mass objects within the cluster, then it is possible that these objects would have higher velocities than average due to interactions with higher mass objects, and as such, inflate the measured velocity dispersion. This explanation does not seem very likely, because while the sample here might be biased, it would more likely be biased towards higher mass objects, and any effect due to this would be to underestimate the velocity dispersion. The reason is simply because objects were chosen that were bright enough to observe and achieve a high SNR in order to resolve the number of lines necessary to produce precise radial velocities.

One caveat to this is that it is possible for lower mass YSOs to appear brighter due to emission from active accretion. In order for this to cause the sample to be biased towards low mass objects, these objects would require a high accretion rate and likely be heavily veiled, displaying weak or absent absorption lines. This would make deriving a radial velocity impossible or problematic. Another issue with this idea is that these objects may be too young to have gained a noticeably larger velocity by this time. The ages of these objects are all on the order of the crossing time calculated for Rho Ophuchi, which is about 1 Myr. In order to have higher velocities, they would need to have dynamically interacted with other objects.

Overall, it does not appear that there is a low mass bias in the sample. In addition to this, the mass range presented here is nearly identical to the mass range for the sample of Class II/III objects studied by Rigliaco *et al.* (2016), which is about $0.2 - 1.7$ $M_{\odot}$.

5.3. ASSUMPTIONS MADE WHEN USING VELBIN

Since Velbin is being used to calculate the intrinsic velocity dispersion, it is important to look at all the assumptions that go into this calculation. Since the errors for some sources are large (1.5 km s^{-1}) compared to the dispersion being measured, it is possible that these errors are increasing the measured dispersion. Velbin does attempt to account for the errors, but when the errors are about the same size as, or larger than, the dispersion being measured, it becomes much more difficult to learn the details of the dispersion itself.

Another possibility is that the assumed mass and period distributions of binaries provided by Velbin do not match up as well as with less evolved YSOs. The distributions for mass ratios (Reggiani and Meyer, 2011) and periods (Raghavan *et al.*, 2010) used in this study are the same used by Rigliaco *et al.* (2016), but these distributions have been derived for main sequence stars and may have better agreement with more evolved YSOs than with those less evolved. However, the most likely cause of any problems with Velbin would be the fact that Velbin does not consider any triple or higher order systems, only binaries. There are likely at least a few triple systems in this sample, with SR 24N having a known companion, and SR 24S seeming to have a subarcsecond companion. In fact, the fraction of binary systems that may be even higher order has been found to be relatively high. Stassun *et al.* (2014) found that six of thirteen pre-main sequence eclipsing binaries they studied were, in fact, triple systems. This would imply an overall fraction of triple systems for young stars to be on the order of 0.25.

Finally, Velbin makes its calculations by assuming that the intrinsic dispersion is Gaussian in nature. As can be seen from the histogram of velocities in Section 4 (Figure 4.2) this distribution is only vaguely Gaussian in shape. With a larger sample size, it is likely that

the distribution would appear to be more Gaussian. However, the apparent non-Gaussian sample provided to Velbin could at least introduce uncertainty and cause the program to either miscalculate the cluster properties or to assign larger errors and overestimate the dispersion. It should be noted that according to the Shapiro-Wilk test, this sample is likely Gaussian ($p - value = 0.11$) with the two outliers between -25 and -30 km s^{-1} left out. This is a simple statistical test to check whether or not a distribution is normal or not, but does not take into account the errors associated with each radial velocity.

5.4. RELAXATION TIME

The relaxation time for a cluster is defined as

$$\frac{\tau_{relax}}{\tau_{cross}} = \frac{N}{6ln(\frac{N}{2})} \tag{5.1}$$

where N is the number of stars in the cluster. For $N > 100$, $\frac{\tau_{relax}}{\tau_{cross}} \approx 4$. In the case of Rho Ophiuchi, τ_{relax} appears to be about 4 Myr. Estimates of the age of the cluster itself place it at about $2 - 3$ Myr old. The Class II and Class III objects within the Rigliaco *et al.* (2016) sample have most likely been around for nearly the entire age of the cluster, while the Class I and Flat spectrum sources have ages that are probably no more than 1Myr (Dunham *et al.*, 2014). The relaxation time is an estimate of how long the cluster will take to virialize, and so it can be seen that these younger YSOs are going to have had fewer dynamic interactions and this could contribute to the non-gaussian distribution seen in the results in Section 4. So while the possible lack of interactions may help explain the non-gaussian nature of the dispersion, it probably does not explain why the dispersion is so large, as a lack of dynamical interactions should result in a smaller dispersion.

5.5. UNDERESTIMATING THE BINARY FRACTION

It is currently thought that the binary fraction of YSOs is higher than for main sequence stars (Reipurth *et al.*, 2014), and this is what was found by Rigliaco *et al.* (2016). From that study, using Velbin, they measured the binary fraction to be $f_{bin} = 0.56$. For the data from this study, Velbin estimates a binary fraction of about $f_{bin} = 0.7 \pm 0.3$. Both of these results are in line with the results found by Reipurth *et al.* (2014) regarding the fraction of young stars that appear to be in multiple systems. Their estimates were that about $2/3$ of Class 0 protostars are multi-star systems, and that this multiplicity frequency slowly drops off as the objects evolve towards the main sequence. However, they also note that due to the difficulty in resolving very close protobinaries, it is possible that the fraction is nearly 1. This could be part of what is being observed in this study. Obviously there are no Class 0 protostars in the sample, but it is not unreasonable to think that the binary fraction could be significantly closer to 1 than the Rigliaco *et al.* (2016) sample, which would increase the observed dispersion. However, since the dispersion measured here is still about 2σ away from agreement with the Rigliaco *et al.* (2016) sample, it would seem that a high binary fraction probably does not account for the entire difference. Running Velbin while setting the binary fraction to 1 results in a slight smaller dispersion of $v_{disp} = 2.5 \pm 0.7$ km s^{-1} as seen in Table 4.2. This then implies that while an underestimation of the binary fraction could account for some of the increased dispersion, it probably does not account for all of the difference.

5.6. SUPERVIRIAL STATE

It is also possible that the observed velocity dispersion is pointing towards a supervirial state for the cluster. It has been calculated that for this cluster to be in virial equilibrium the velocity dispersion should be about 1 km s^{-1}. Assuming that there are not unaccounted for affects artificially increasing the measured dispersion, these data suggest

a picture whereby these YSOs formed from subvirial cores, quickly became supervirial during the Class I/F phase, and settled back down into a virial state as they continued to evolve. Past simulations have shown that during the first crossing time of a cluster, it could become slightly supervirial as the objects begin to fall towards the center (Proszkow and Adams, 2009). However, more recent studies and simulations have shown that these effects may be greater than first thought. Kuhn *et al.* (2018) and Sills *et al.* (2018) have shown through simulations that it is possible that clusters start to collapse very quickly after they begin to form stars. According to these simulations, by the time a cluster is 3 Myr old it has collapsed and rebounded, greatly changing the velocity dispersion as it undergoes this process. The dispersion can start out relatively small, then increase rapidly until peaking after about 2 Myr, before decreasing nearly as quickly over the next 1 Myr, until finally settling into a nearly virialized state. In addition to this, they were able to show that the velocity dispersion is the greatest towards the center of the cluster, and smaller towards the edges. This would imply a process of collapse towards one another and speeding up by the YSOs shortly after they form, then passing by each other and slowing down until they virialize. All of these results are broadly in agreement with both the results found by this study and with the results found by Rigliaco et al. This is clear when looking at the spatial distribution of this sample compared to the Rigliaco et al. sample, as can be seen in Figure 5.1. The Rigliaco et al. sample of more evolved YSOs lies at the periphery of L 1688 with a dispersion consistent with virial equilibrium.

Finally, it needs to be noted that Rigliaco *et al.* (2016) measured a velocity gradient in their sample corresponding to increasing velocities from the northwest towards the southeast of the cluster. This gradient was calculated to be about 1 km s^{-1} pc^{-1}. This gradient is not attributed to the rotation of the cluster, but is thought to be a real gradient such that the northwest section of the cluster is moving towards the Earth, while the southeast section is moving away from the Earth. To check this for the sample presented here, the YSOs can be roughly split up into subgroups of 8 sources that lie in the northwest quadrant of Figure

2.1, 15 that lie in the southeast quadrant, and 5 that lie in the northeast. The average radial velocity in the northwest quadrant is $v_{avg,NW} = -7.4 \pm 2.6$ km s^{-1}, the average velocity for the southeast quadrant is $v_{avg,SE} = -3.6 \pm 3.3$ km s^{-1}, and the average velocity for the northeast quadrant is $v_{avg,NE} = -4.3 \pm 2.8$ km s^{-1}. The separation of the northwest and southeast subgroups is about 1 pc. Certainly these samples are much smaller, but there is a definite trend of increasing velocity towards the southeast. This would suggest that the velocity gradient of this sample is potentially significantly larger than the gradient of the Rigliaco *et al.* (2016) sample, but in roughly the same direction. According to the simulations of Proszkow and Adams (2009), a real velocity gradient will only be observed when there is either collapse or expansion happening in a non-spherical cluster that is tilted at some angle relative to the Earth. It is clear from the shape of the L1688 cloud that the cluster is elongated in roughly the same direction as the velocity gradient measured by Rigliaco *et al.* (2016). Distance measurements to different parts of the L1688 cloud have been made by Ortiz-León *et al.* (2017), but this was only done for 11 sources, and there is no orientation of the cloud that is discernible from these data. Nevertheless, all of the results derived by this study regarding less evolved YSOs lying towards the center of the cluster and the study performed by Rigliaco *et al.* (2016) regarding more evolved YSOs located radially outward from the center are consistent with the results of simulations by both Proszkow and Adams (2009) and the studies and simulations of Kuhn *et al.* (2018) and Sills *et al.* (2018). This interpretation of the data provides the best physical explanation for the observed results without assuming there is something wrong with the data itself. This could indicate that L1688 may be on either side of a collapse-and-rebound process during the first $2 - 3$ Myr of its life.

While these simulations generally agree with the results, there are some issues that need to be considered. The main difference between the simulations by Kuhn *et al.* (2018) and Sills *et al.* (2018) and the Rho Ophiuchi cloud complex is the number of cluster members. Kuhn and Sills ran simulations for clusters that consist of thousands of stars,

while Rho Ophiuchi only has > 300 members. With fewer members and less total mass involved, the collapse-and-rebound may not be as pronounced as it is in larger clusters. Small number statistics could again be playing a role in the data on a larger scale than just the sample size provided, in that this collapse-and-rebound process may look different for clusters with only a few hundred members.

5.7. DISCUSSION

While there are several reasons why this measured dispersion is higher than anticipated, it is likely a combination of several effects. The results of the simulations from Kuhn and Sills are very compelling regarding the observed velocity dispersion and gradient. But it is also clear that the binary fraction is probably underestimated. It is also important to not say that these results confirm the simulation results because the observed distribution of radial velocities is not very gaussian to begin with. This could mean that measuring a dispersion from the data is not very meaningful without a larger sample. Nevertheless, the collapse-and-rebound idea has merit, and can help explain the small gap in dispersions being measured at various parts of the cluster. Further study is needed to definitively say whether or not this is a real effect being observed.

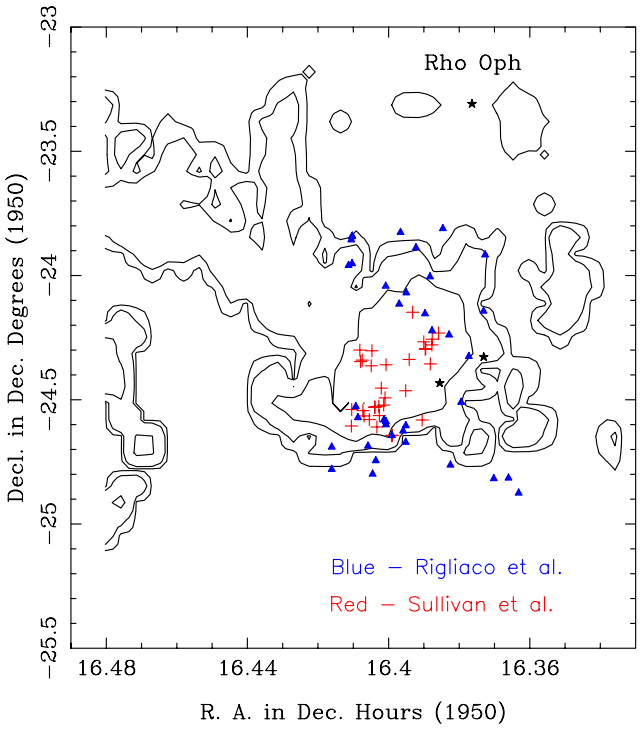

Figure 5.1 Map of the L1688 cloud with the Rho Ophiuchi cluster showing the locations of the sources in the Sullivan sample (red crosses) compared with the locations of the sources in the Rigliaco sample (blue triangles). Contours represent the ^{13}CO column density computed from Loren (1989) assuming LTE and T_{eff} = 25 K and are in units of cm^{-2} with 6×10^{14}, 3×10^{15}, and 1.5×10^{16} from lowest to highest. Visible stars including SR 3, HD 147889, and Rho Ophiuchi can be seen as well (black stars).

6. SUMMARY AND FUTURE WORK

This section will briefly summarize the work and explain what the next steps should be to continue this project.

6.1. SUMMARY

The majority of stars form within embedded star clusters (Lada and Lada, 2003). It is then clear that in order to form a full picture of star formation, the dynamics and evolution of these clusters must be studied. This project has focused on the nearby (137 ± 1.2 pc) star forming cluster Rho Ophiuchi, which is thought to be about 2 – 3 Myr old and actively forming relatively low mass stars (De Geus, 1992; Erickson *et al.*, 2011; Loinard *et al.*, 2008; Lombardi *et al.*, 2008; Mamajek, 2008; Ortiz-León *et al.*, 2017; Wilking *et al.*, 2008)

Radial velocities were derived for 32 sources within the Rho Ophiuchi cluster, all located in or near the L1688 cloud from data taken on the instruments CSHELL, iSHELL, CRIRES, and NIRSPEC. In addition, the majority of these sources are Class I/F objects and are thought to be less than 1 Myr old (Dunham *et al.*, 2014). Radial velocities were derived using a Markov-Chain Monte Carlo routine developed by using the Python package *emcee*. The velocity dispersion was derived using the program Velbin. This dispersion was measured to be $\Delta v = 2.8 \pm 0.7$ km s^{-1}. This was found to be significantly higher than both the dispersion of the dense cores from which these stars have formed (André *et al.*, 2007; Kirk *et al.*, 2010; Peretto *et al.*, 2006) and the dispersion of the more evolved Class II/III objects located within this same cluster (Rigliaco *et al.*, 2016).

Possible explanations for the discrepancy between the velocity dispersions include small number statistics, incorrect assumptions about YSO and embedded cluster properties (mass ratios, binary fractions, etc.), a low mass bias, and relaxation time considerations.

However, the most compelling explanation would be that the dispersion is real, and corresponds to a collapse-and-rebound phase described by Kuhn *et al.* (2018) and Sills *et al.* (2018) in their recent simulations.

6.2. FUTURE WORK

This study alone is unable to definitively answer key questions regarding the dynamical state of the Rho Ophiuchi cluster and the star formation process in general. The results presented here do provide some early observational evidence of the collapse-and-rebound proposed by the simulations of Sills et al. but more work must be done to shed more light on this idea. A study similar to the initial proper motion study that motivated this work (Wilking *et al.*, 2015) would be very helpful. This proper motion study included infrared astrometric observations of several different fields of view in Rho Ophiuchi. The main limitation of that study was that these fields were too include background stars as an astrometric frame of reference. This only allowed for relative proper motions to be derived, and thus less robust measurements of the velocity dispersion. The solution to this is to use an instrument that allows for very precise infrared astrometric observations over a much wider field of view, that can cover at least the entire L1688 cloud, and possibly more. Doing this over a sufficiently long baseline of time would yield a two-dimensional dispersion of about 400 YSOs. In addition to the dispersion, the relative directions of these objects could be determined, which would yield information as to whether or not this cluster is collapsing, rebounding, or neither. In the short term, it is possible to use the GAIA DR2 database which has proper motions for about 100 objects thought to be in the cloud. These are mostly Class II/III objects, but would provide a larger sample. Longer term, the best option for this is to wait for the Wide Field Infrared Survey Telescope (WFIRST) to launch in the mid 2020s. WFIRST will have Hubble Space Telescope resolution with an infrared imager that covers 22.5×45 arcminutes. This telescope will be able to do exactly what was described previously, and do so with a very high precision over a much shorter baseline

of time than many proper motion studies to date. Another option would be to continue to increase the radial velocity sample size for Rho Ophiuchi sources. This could even be done by reobserving some of the NIRSPEC sources presented here using CRIRES on the Very Large Telescope in order to reduce some of the errors. A larger and more precise sample size will allow the dispersion to be constrained much better, and help answer any questions about the current dynamics of the cluster. These steps are not just applicable to the Rho Ophiuchi star forming cluster, but can be be applied to many other young embedded clusters in order to continue progress towards a complete theory of star formation.

APPENDIX A.

PYTHON SOURCE CODE

1. SOURCE CODE FOR DERIVING RADIAL VELOCITIES

```
#Procedure for Deriving Radial Velocities from iSHELL Data Order 225
#Different Synthetics are used depending on the instrument, otherwise
#program works nearly the same across various instruments. Code was
#based upon a different MCMC routine developed and provided by Tom Greene
```

```
#Import necessary packages
%matplotlib inline
import matplotlib
import matplotlib.pyplot as plt
from matplotlib.ticker import MultipleLocator
import numpy as np
import scipy.optimize as op
from astropy.convolution import Gaussian1DKernel, convolve
from astropy import units as u
from astropy.analytic_functions import blackbody_lambda
from PyAstronomy import pyasl
import emcee
import corner
import math
```

```
##### Read data in from a text file as columns for x and y and plot
data = np.loadtxt('ishell/errorchecks/gy284/o225/gy284.o225.2n.n.txt',
    usecols=(0,1))
data[:,0] = data[:,0]/1.0
ndata = len(data)
x = data[:,0]
y = data[:,1]
yerr = y/100

#data2 = np.loadtxt('nirspec/wl17/wl17.co.crnbh.txt', usecols=(0,1))
#data2[:,0] = data2[:,0]/10000.0
#ndata2 = len(data2)
#x2 = data2[:,0]
#y2 = data2[:,1]

fig, ax = plt.subplots(figsize=(16,10))
majorLocator = MultipleLocator(0.001)
minorLocator = MultipleLocator(0.01)
ax.set_xlabel("Wavelength (microns)")
ax.set_ylabel("Relative Intensity")

ax.set_ylim([.5, 1.5])
ax.xaxis.set_major_locator(majorLocator)
ax.xaxis.set_minor_locator(minorLocator)
ax.get_xaxis().get_major_formatter().set_useOffset(False)
```

```
# matplotlib inline
ax.plot(x,y)
#ax.plot(x2,y2)

print ndata
```

```
#Create a function to bin the synthetic to the same wavelength solution as
    the spectra
def binnedsynth(synthfile):
    fstar = open(synthfile, 'r')
    header1 = fstar.readline()
    header1 = header1.strip()
    columns = header1.split()
    Teff = int(columns[0])
    logg = float(columns[1])
    Metals = float(columns[2])
    print Teff, logg

    header2 = fstar.readline()
    header2 = header2.strip()
    columns = header2.split()
    npoints= int(columns[0])

    nlambdalines = npoints
    nfluxlines = npoints

    listlambda = []
    listflux = []
    for i in range(0, npoints):
        line = fstar.readline()
        currentline = line.split()
        listlambda.append(float(currentline[0]))
        listflux.append(float(currentline[1]))

    wavelen = np.array(listlambda)/1000.0

    F_lam = np.array(listflux)

    fstar.close()

    model_wavelen = np.copy(wavelen)
    model_F_lam = np.copy(F_lam)
    nmodel = len(model_wavelen)

    i = 0
    ndata = len(data)
    mod_flux = np.empty(ndata)
    wavelen = data[0,0]
```

```
    dlam = data[1,0] - data[0,0]
    while (wavelen < data[(ndata-1),0]):
        mod_flux[i] = 0.0
        j = 0
        for k in range(0, nmodel):
            if (abs(model_wavelen[k] - wavelen) <= dlam/2):
               mod_flux[i] = model_F_lam[k] + mod_flux[i];
               j+=1
        if (j == 0):
            print 'ACK! - Model sampling is too low'
        mod_flux[i] = mod_flux[i] / (j * 1.0)
        wavelen = wavelen + dlam
        i+=1
        if (wavelen < data[(ndata-1),0]):
           dlam = data[i,0] - data[i-1,0]

    return mod_flux
```

```
#Read in grid of synthetics based on T and Log(g)
synthgrid = np.empty((12,ndata))
synthgrid[0] =
    binnedsynth('synthetics/ishell/k2sm5/o225/ishell.o225.3100.35.sm5.txt')
synthgrid[1] =
    binnedsynth('synthetics/ishell/k2sm5/o225/ishell.o225.3300.35.sm5.txt')
synthgrid[2] =
    binnedsynth('synthetics/ishell/k2sm5/o225/ishell.o225.3500.35.sm5.txt')
synthgrid[3] =
    binnedsynth('synthetics/ishell/k2sm5/o225/ishell.o225.3700.35.sm5.txt')
synthgrid[4] =
    binnedsynth('synthetics/ishell/k2sm5/o225/ishell.o225.3900.35.sm5.txt')
synthgrid[5] =
    binnedsynth('synthetics/ishell/k2sm5/o225/ishell.o225.4100.35.sm5.txt')
synthgrid[6] =
    binnedsynth('synthetics/ishell/k2sm5/o225/ishell.o225.4300.35.sm5.txt')
synthgrid[7] =
    binnedsynth('synthetics/ishell/k2sm5/o225/ishell.o225.4500.35.sm5.txt')
synthgrid[8] =
    binnedsynth('synthetics/ishell/k2sm5/o225/ishell.o225.4700.35.sm5.txt')
synthgrid[9] =
    binnedsynth('synthetics/ishell/k2sm5/o225/ishell.o225.4900.35.sm5.txt')
synthgrid[10] =
    binnedsynth('synthetics/ishell/k2sm5/o225/ishell.o225.5100.35.sm5.txt')
synthgrid[11] =
    binnedsynth('synthetics/ishell/k2sm5/o225/ishell.o225.5300.35.sm5.txt')
```

```
#Remove the last pixel of each binned synthetic to remove unrealistic
    binning artifact, and plot
#the synthetics as a sanity check
ndata = ndata - 1
```

```
x = np.delete(x,ndata)
y = np.delete(y,ndata)
synthgrid = np.delete(synthgrid, ndata, 1)
yerr = np.delete(yerr, ndata)

fig, ax = plt.subplots(figsize=(16,10))
majorLocator = MultipleLocator(0.001)
minorLocator = MultipleLocator(0.01)
ax.set_xlabel("Wavelength (microns)")
ax.set_ylabel("Relative Intensity")

ax.set_ylim([.4, 1.1])
ax.xaxis.set_major_locator(majorLocator)
ax.xaxis.set_minor_locator(minorLocator)
ax.get_xaxis().get_major_formatter().set_useOffset(False)

for i in range(0,12):
    ax.plot(x,synthgrid[i])
\begin{lstlisting}
#Set initial "guesses" for each parameter
vsini0 = 10.0
rk0 = 0.0
dx0 = -16.0
teff0 = 1.0
```

```
#Define the model for the three parameters: veiling, rotational velocity,
    radial velocity (in pixels)
synth = [0.0]*(ndata)
veiled = [0.0]*(ndata)
broadened = [0.0]*(ndata)
shifted = [0.0]*(ndata)
def model(vsini, rk, dx, teff):
    #define temp variables for model
    dxfl = int(math.floor(dx))
    dxcl = int(math.ceil(dx))
    if teff < 0.0:
        tefffl = int(0)
        teffcl = int(0)
    elif teff > 11.0:
        tefffl = int(11)
        teffcl = int(11)
    else:
        tefffl = int(math.floor(teff))
        teffcl = int(math.ceil(teff))
    teffdec = teff - tefffl

    #average temperature dependent synthetics
    for i in range(0,ndata):
```

```
        synth[i] = synthgrid[tefffl][i]*(1-teffdec) +
            synthgrid[teffcl][i]*(teffdec)

    #veil the spectra
    for i in range(0, ndata):
        veiled[i] = (synth[i] + rk)/(1 + rk)

    #broaden the spectra
    broadened = pyasl.rotBroad(x, veiled, 0.6, abs(vsini))

    #shift the spectra
    if dx == 0.0:
        return broadened
    if dx > 0.0:
        dxdec = dx - float(dxfl)
        for i in range(dxcl, ndata):
            shifted[i] = broadened[i - dxfl] + (broadened[i - dxcl] -
                broadened[i - dxfl])*dxdec
        for i in range(0, dxcl):
            shifted[i] = 1.0
        return shifted
    if dx < 0.0:
        dxdec = float(dxcl) - dx
        for i in range(0, ndata + dxfl):
            shifted[i] = broadened[i - dxcl] + (broadened[i - dxfl] -
                broadened[i - dxcl])*dxdec
        for i in range(ndata + dxfl, ndata):
            shifted[i] = 1.0
        return shifted
```

```
#Then the likelihood function and initial params: use log
def lnlike(theta, x, y, yerr):
    vsini, rk, dx, teff = theta
    return -0.5* np.sum(((y-model(vsini, rk, dx, teff))/yerr)**2 +
        np.log(2.0 * np.pi * yerr**2))

nll = lambda *args: -lnlike(*args)
result = op.minimize(nll, [vsini0, rk0, dx0, teff0], args=(x, y, yerr))
vsini_ml, rk_ml, dx_ml, teff_ml = result["x"]
#result["x"] = vsini0, rk0, dx0, teff0

# Now define the priors: use log
def lnprior(theta):
    vsini, rk, dx, teff = theta
    if 0.0 < vsini < 100.0 and -0.5 < rk < 15.0 and -50.0 < dx < 30.0 and
        0.0 < teff < 11.0:
        return 0.0
    return -np.inf
```

```
# Combine likelihood & priors to get probability:
def lnprob(theta, x, y, yerr):
    lp = lnprior(theta)
    if not np.isfinite(lp):
        return -np.inf
    return lp + lnlike(theta, x, y, yerr)

print vsini_ml, rk_ml, dx_ml, teff_ml
```

```
#Set up and initialize walkers:
ndim, nwalkers = 4, 100
pos = [result["x"] + 1e-2*np.random.randn(ndim) for i in range(nwalkers)]
#Set up and run sampler
#100 walkers and 500 steps takes ~20 minutes for a 1000 channel spectrum

sampler = emcee.EnsembleSampler(nwalkers, ndim, lnprob, args=(x, y, yerr),
    threads =4)
sampler.run_mcmc(pos, 500)

samples = sampler.chain[:, 100:, :].reshape((-1, ndim))
#Display relative probablility distributions
fig = corner.corner(samples, labels=["$vsini$","$r_k$","$dx$","$teff$"])
    #take out truths
fig.savefig("Output.png")

#Print out most likely values for each parameter and one sigma uncertainty
vsini_mcmc, rk_mcmc, dx_mcmc, teff_mcmc = map(lambda v: (v[1], v[2]-v[1],
    v[1]-v[0]),
                          zip(*np.percentile(samples, [16,50,84],
                                             axis=0)))

print vsini_mcmc
print rk_mcmc
print dx_mcmc
print teff_mcmc

#Plot the modified synthetic against the original data to compare
fig, ax = plt.subplots(figsize=(16,10))
majorLocator = MultipleLocator(0.001)
minorLocator = MultipleLocator(0.01)

ax.set_ylim([.5, 1.2])
ax.xaxis.set_major_locator(majorLocator)
ax.xaxis.set_minor_locator(minorLocator)
ax.set_xlabel("Wavelength (microns)")
ax.set_ylabel("Relative Intensity")
ax.get_xaxis().get_major_formatter().set_useOffset(False)
```

```
ax.plot(x, model(vsini_mcmc[0], rk_mcmc[0], dx_mcmc[0], teff_mcmc[0]))
#Plot a modified synthetic by hand picking values to get approximate
    initial "guesses"
#ax.plot(x, model(10.95, 2.25, -13.46, 1.5, 4.0))
ax.plot(x,y)
```

2. SOURCE CODE FOR DERIVING DISPERSIONS WITH VELBIN

```
#Code provided by Elisabetta Rigliaco
```

```
#python libraries scipy, velbin, and emcee
import velbin
%matplotlib inline
import matplotlib
import matplotlib.pyplot as plt
from matplotlib.ticker import MultipleLocator
import numpy as np
import scipy as sp
import emcee
import corner
import math
```

```
##### load in data
data = np.loadtxt('MCMCResults/subclusters/MCMC_rv_err_mass.txt',
    usecols=(0,1,2))
data[:,0] = data[:,0]
ndata = len(data)
velocities = data[:,0]
sigvel = data[:,1]
mass = data[:,2]

sumv = 0
for i in range(0, ndata):
    sumv = sumv + velocities[i]

vmean0 = sumv/ndata
#vdisp0 = np.std(velocities)
vdisp0 = 1.1
fbin0 = 0.5

print vmean0, vdisp0, fbin0
print velocities
```

```
# initialize MCMC
p0 = [vmean0, vdisp0, fbin0]
prand = sp.randn(1000, 3) * 0.01 + p0
```

```
log_likelihood = lambda params: fitter(*params) if abs(params[-1] - 0.5) <
    0.5 and params[1] > 0.0 else -sp.inf # ensure binary fraction is
    between 0 and 1
# generate binaries
binaries = velbin.solar(1000000)
binaries.draw_mass_ratio('Reggiani13')
binaries.draw_period('Raghavan10')
binaries.draw_eccentricities('thermal')

# prepare calculation of log-likelihood
fitter = binaries.single_epoch(velocities, sigvel, mass)
# run MCMC
sampler = emcee.EnsembleSampler(1000, 3, log_likelihood)
sampler.run_mcmc(prand, 400)
samples = sampler.chain[:, 100:, :].reshape((-1, 3))
fig = corner.corner(samples, labels=["$vmean$","$vdisp$","$fbin$"]) #take
    out truths
fig.savefig("Rig_Velbin.png")

vmean_mcmc, vdisp_mcmc, fbin_mcmc = map(lambda v: (v[1], v[2]-v[1],
    v[1]-v[0]),
                        zip(*np.percentile(samples, [16,50,84],
                                           axis=0)))

print vmean_mcmc
print vdisp_mcmc
print fbin_mcmc
```

APPENDIX B.

CORNER PLOTS AND OVERLAYS OF INDIVIDUAL SOURCES

The following Appendix contains corner plots and overlays for all spectra analyzed in this study. They are organized first by instrument (NIRSPEC, CSHELL, CRIRES, iSHELL) and then alphabetically.

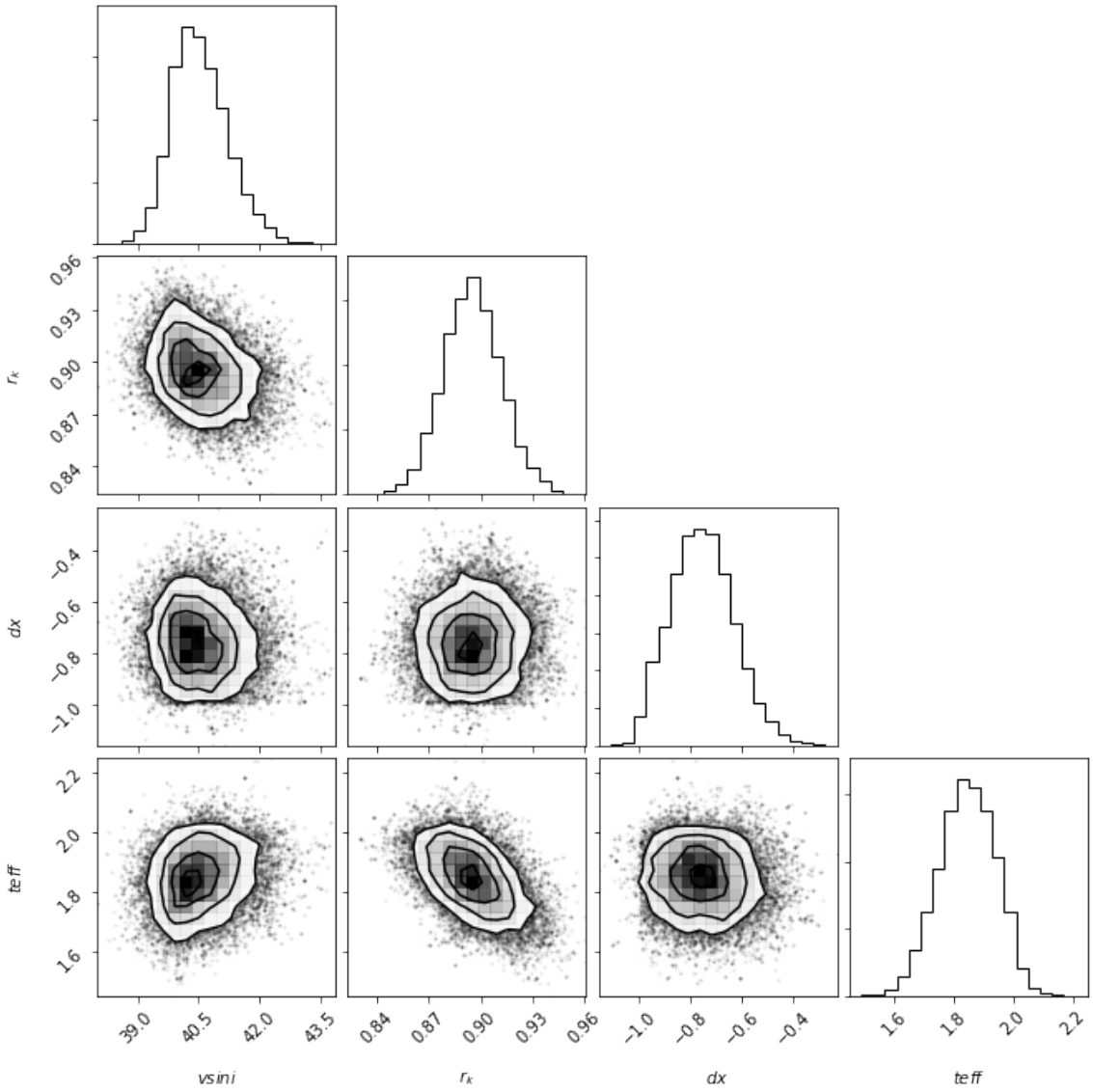

Figure 1 Relative probability distributions and correlations for the four fit parameters returned by *emcee* to best match the NIRSPEC spectrum of object CRBR 12 corresponding to $T = 3460 \pm 20$ K, $vsini = 40.5 \pm 0.7$ km s^{-1}, $r_k = 0.89 \pm .02$, and $dx = -0.76 \pm 0.13$.

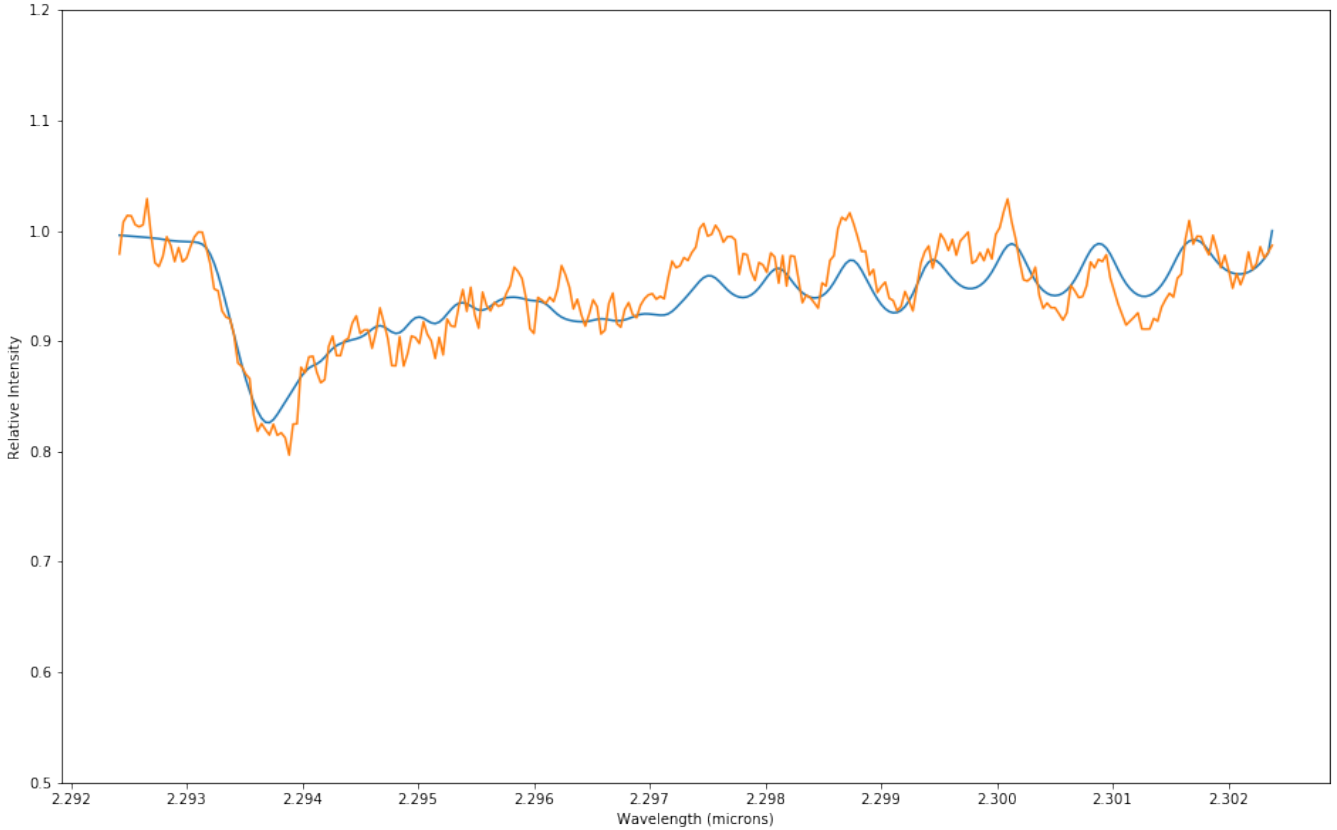

Figure 2 Synthetic overlay (blue) on top of the data (orange) for the four fit parameters returned by *emcee* to best match the NIRSPEC spectrum of object CRBR 12 corresponding to $T = 3460 \pm 20$ K, $vsini = 40.5 \pm 0.7$ km s^{-1}, $r_k = 0.89 \pm .02$, and $dx = -0.76 \pm 0.13$.

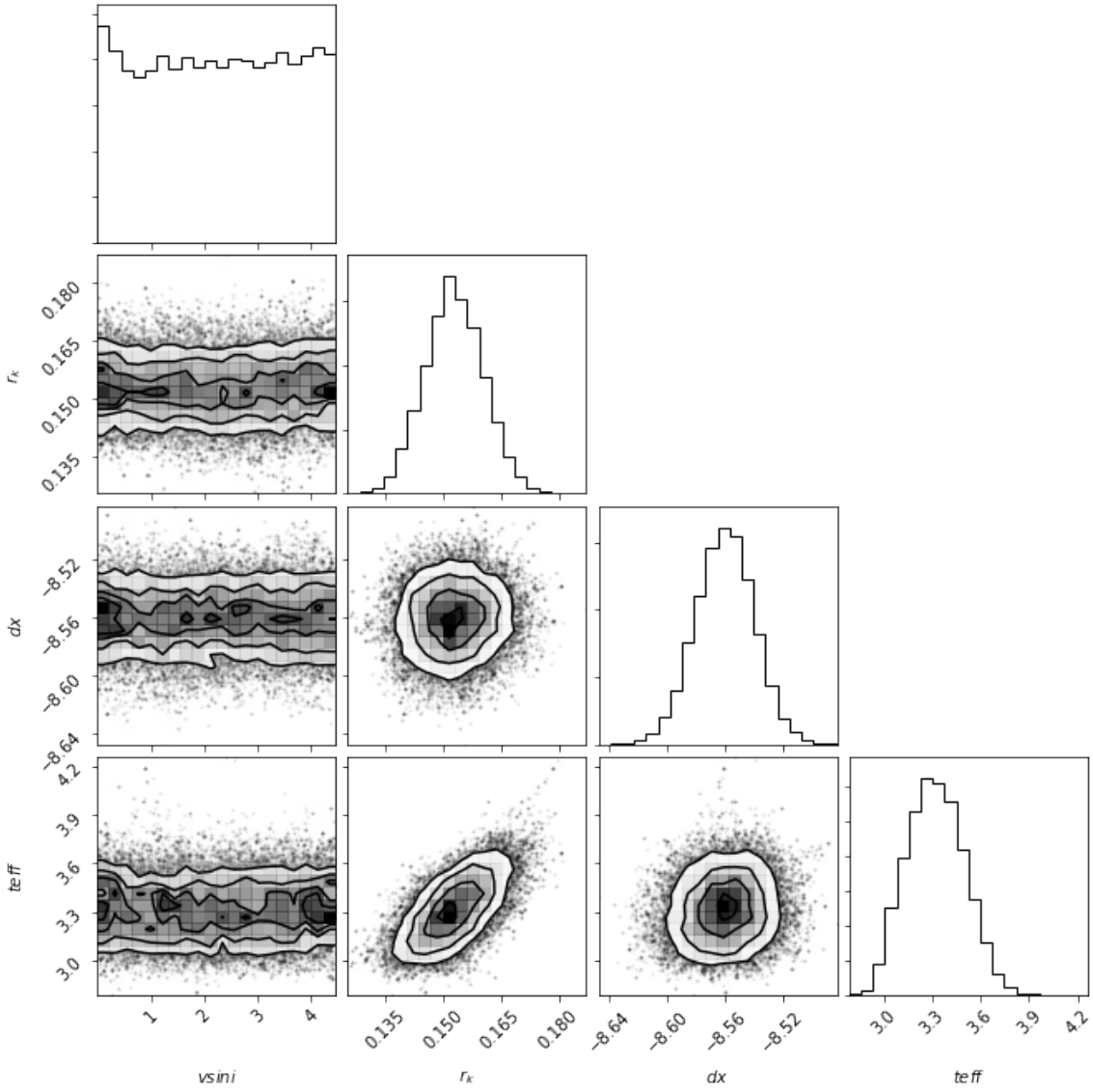

Figure 3 Relative probability distributions and correlations for the four fit parameters returned by *emcee* to best match the NIRSPEC spectrum of radial velocity standard GJ 806 corresponding to $T = 3760\pm40$ K, $vsini = 2.2\pm1.5$, $r_k = 0.15\pm0.01$, and $dx = -8.56\pm0.02$.

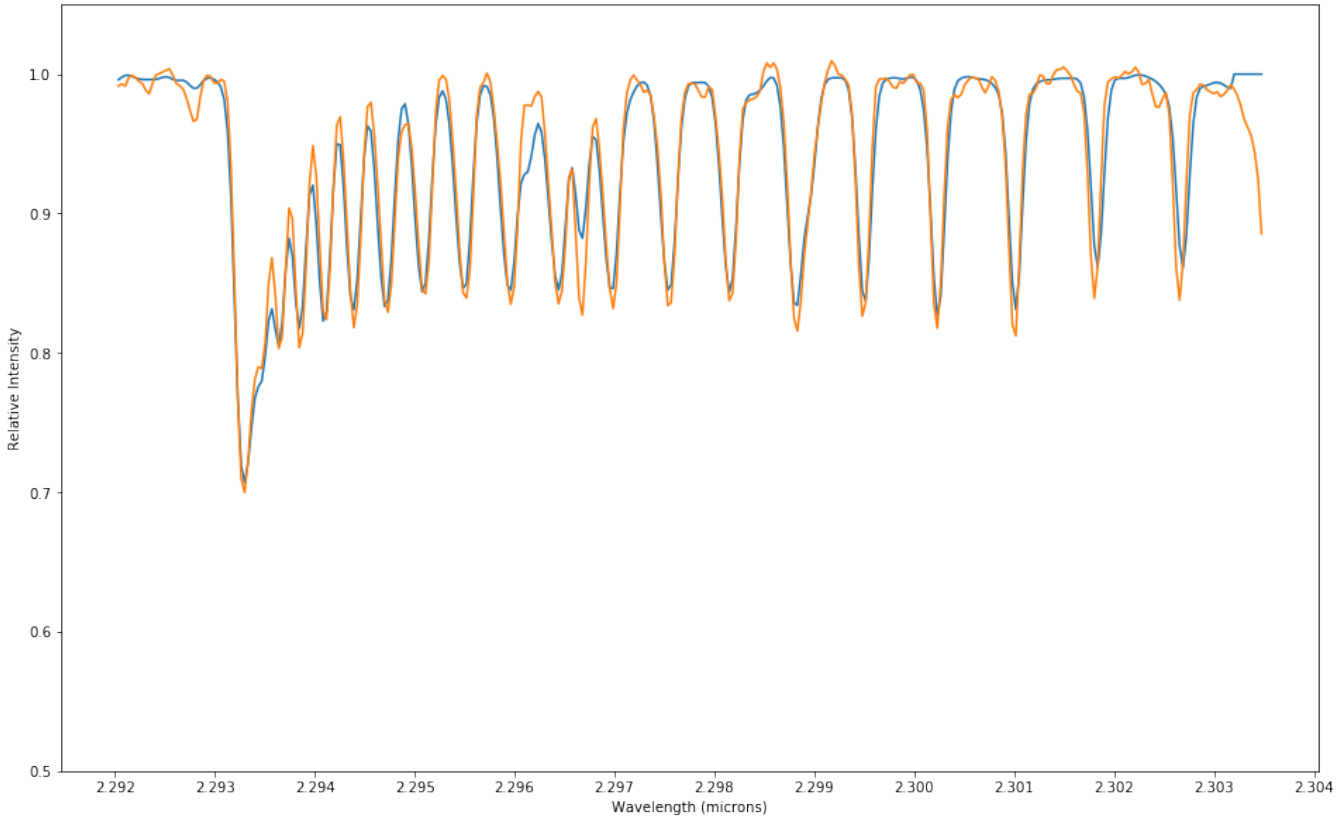

Figure 4 Synthetic overlay (blue) on top of the data (orange) for the four fit parameters returned by *emcee* to best match the NIRSPEC spectrum of radial velocity standard GJ 806 corresponding to $T = 3760 \pm 40$ K, $vsini = 2.2 \pm 1.5$ km s^{-1}, $r_k = 0.15 \pm 0.01$, and $dx = -8.56 \pm 0.02$.

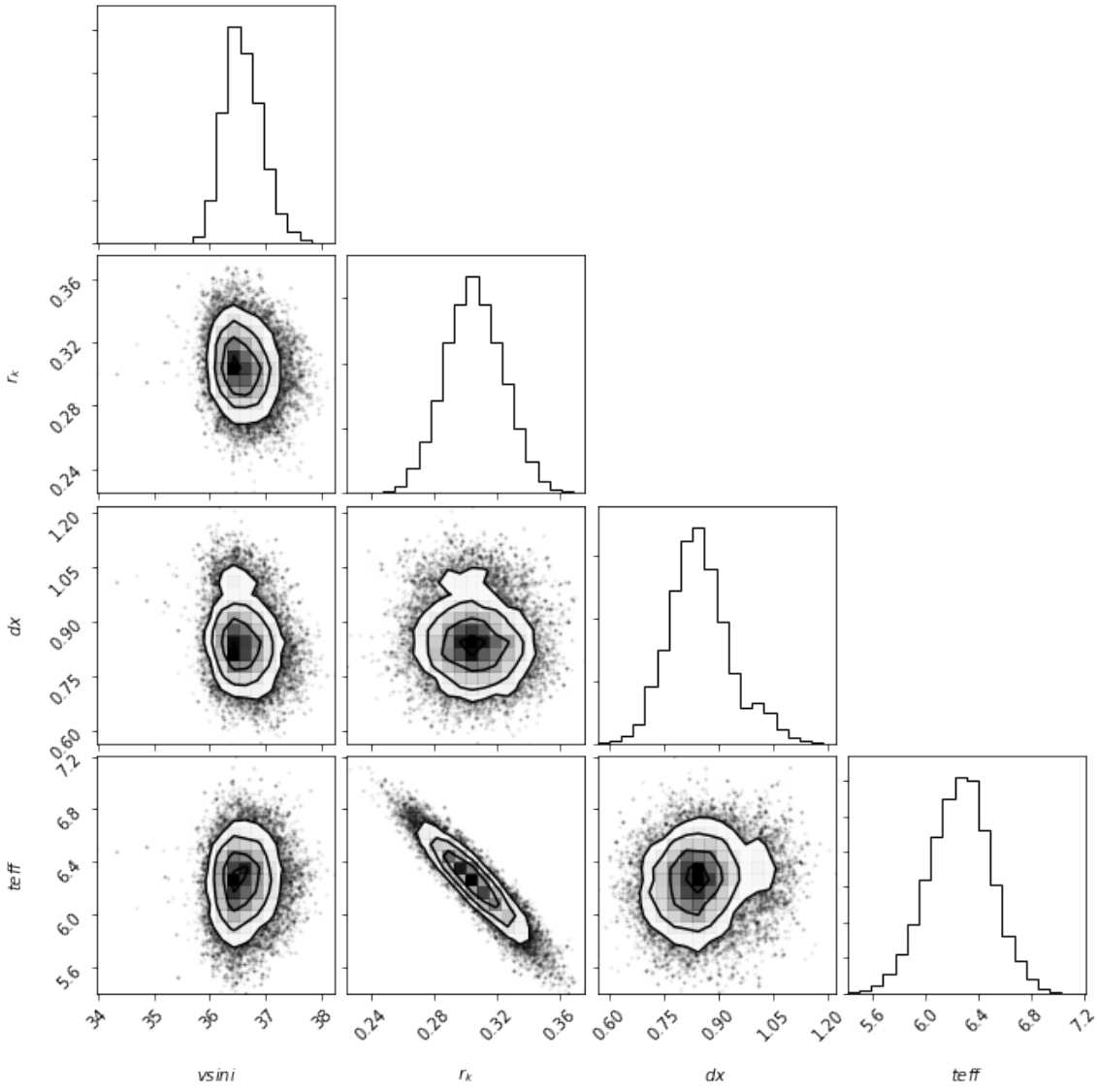

Figure 5 Relative probability distributions and correlations for the four fit parameters returned by *emcee* to best match the NIRSPEC spectrum of object GSS 29 corresponding to $T = 4360 \pm 40$ K, $vsini = 36.6 \pm 0.4$ km s^{-1}, $r_k = 0.3 \pm 0.02$, and $dx = 0.84 \pm 0.08$.

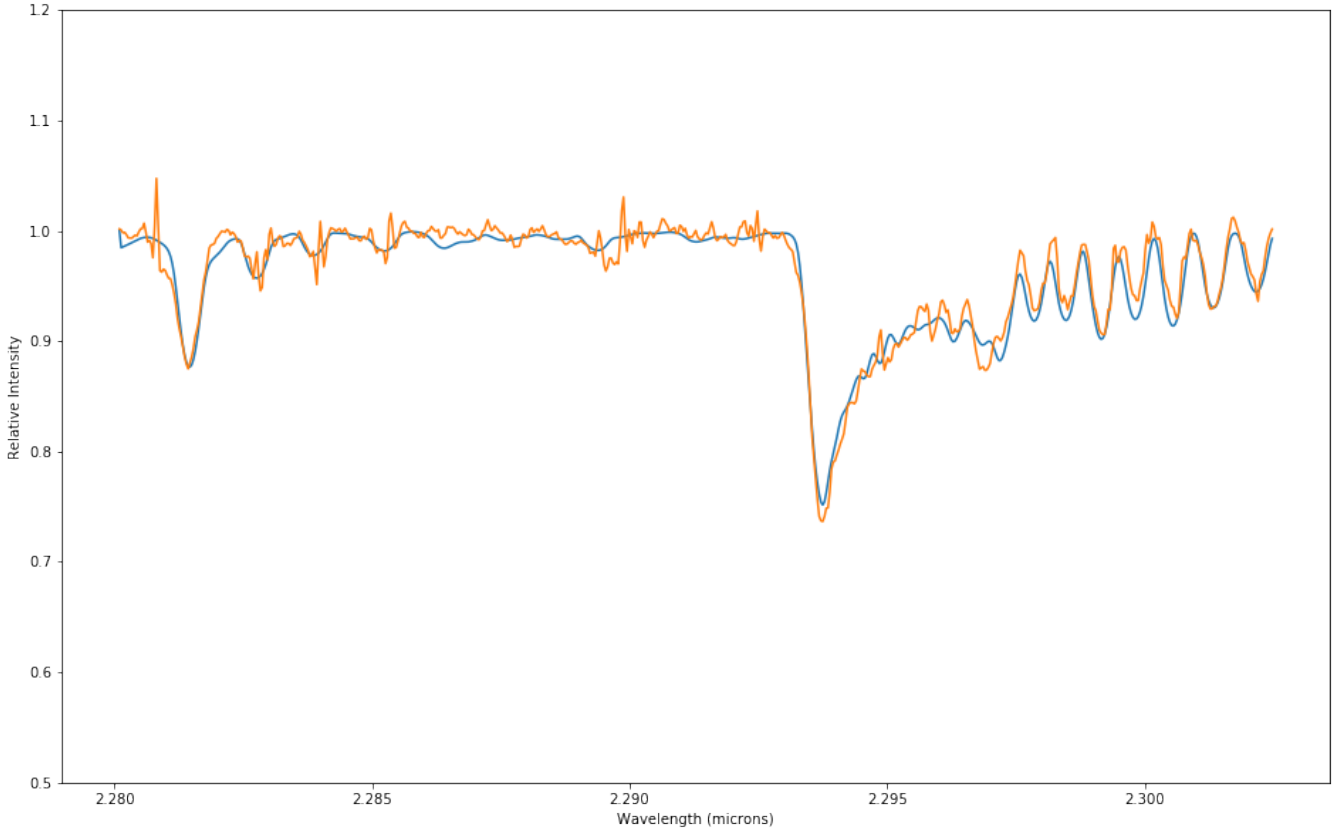

Figure 6 Synthetic overlay (blue) on top of the data (orange) for the four fit parameters returned by *emcee* to best match the NIRSPEC spectrum of object GSS 29 corresponding to $T = 4360 \pm 40$ K, $vsini = 36.6 \pm 0.4$ km s^{-1}, $r_k = 0.3 \pm 0.02$, and $dx = 0.84 \pm 0.08$.

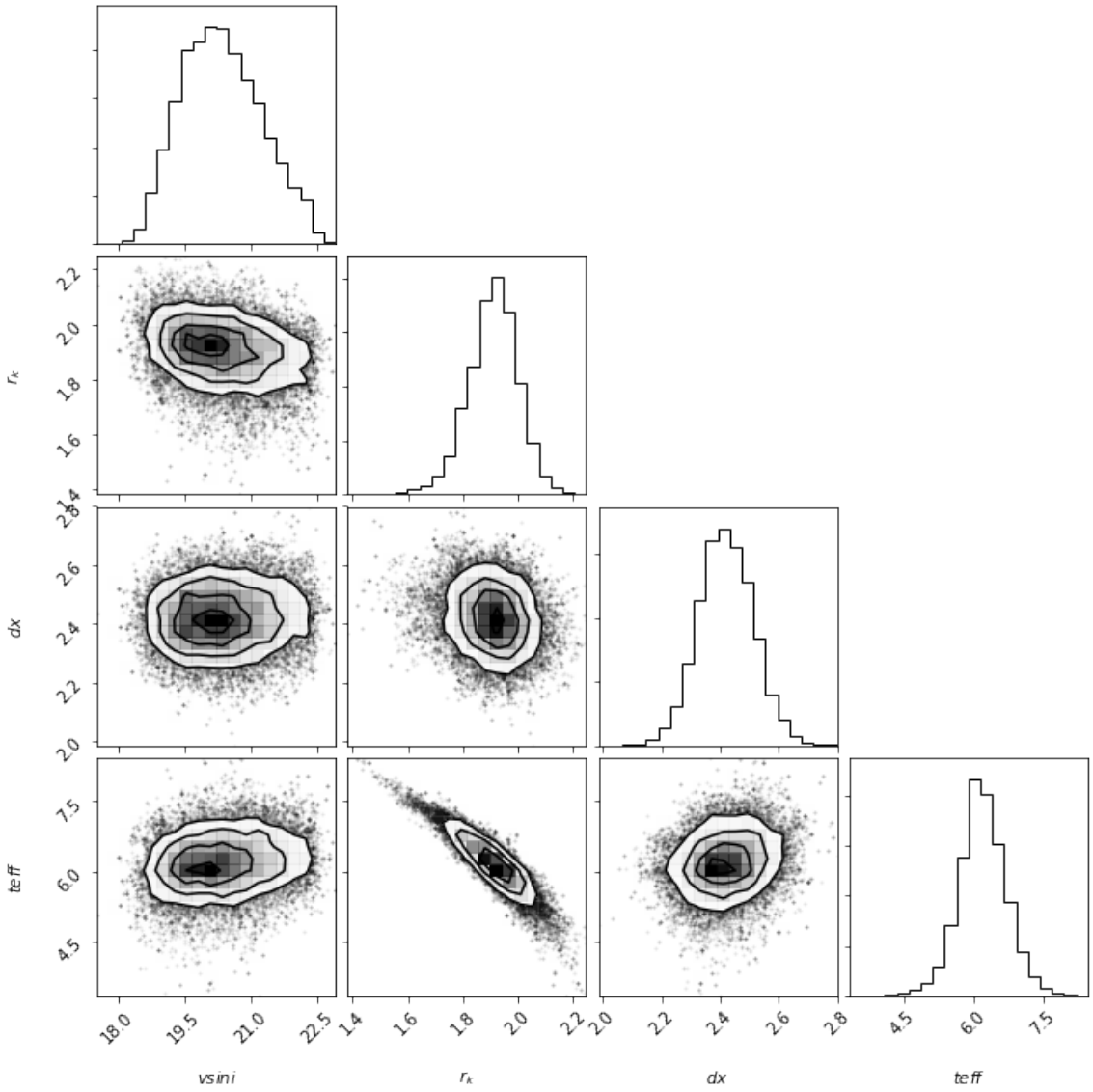

Figure 7 Relative probability distributions and correlations for the four fit parameters returned by *emcee* to best match the NIRSPEC spectrum of object GY 21 corresponding to T = 4340 ± 100 K, $vsini$ = 20.3 ± 0.9 km s^{-1}, r_k = 1.91 ± 0.09, and dx = 2.42 ± 0.09.

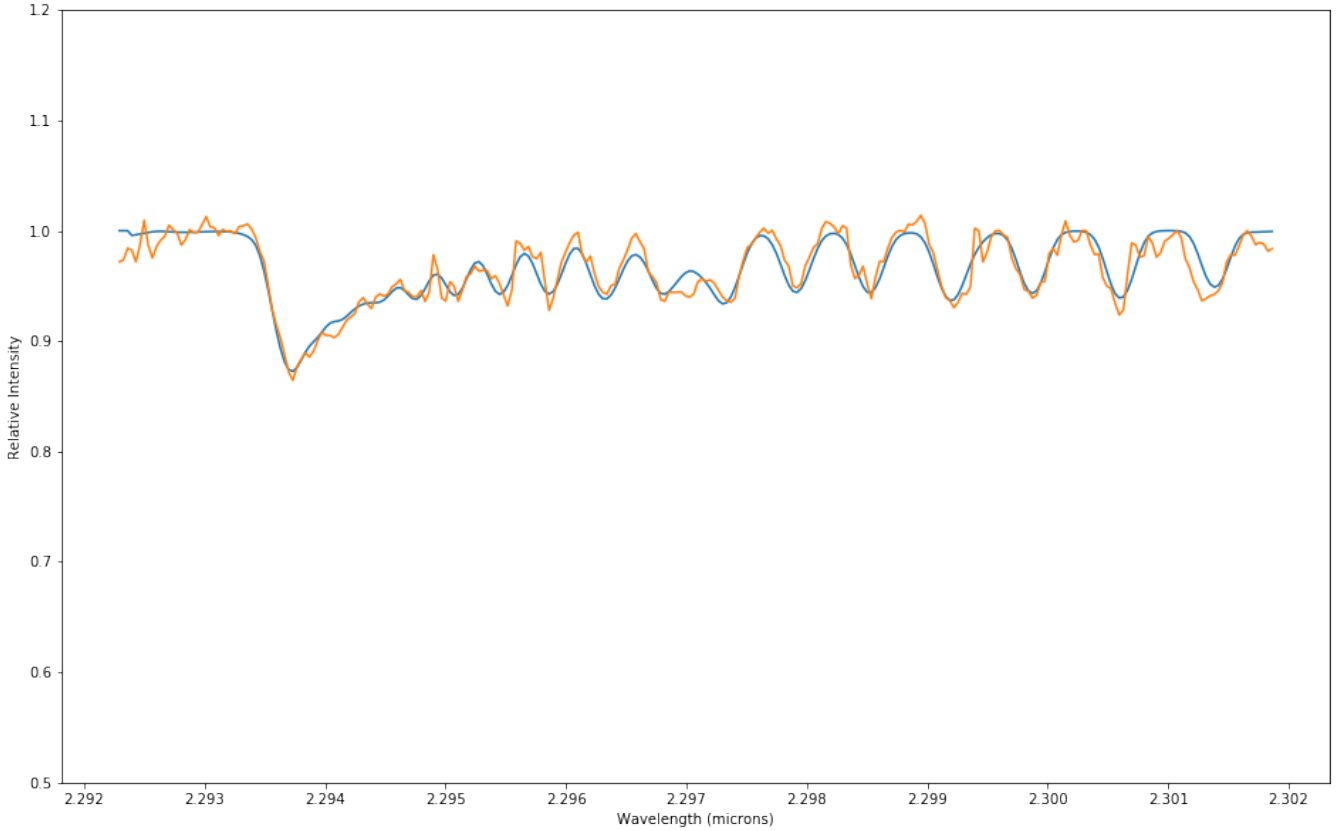

Figure 8 Synthetic overlay (blue) on top of the data (orange) for the four fit parameters returned by *emcee* to best match the NIRSPEC spectrum of object GY 21 corresponding to $T = 4340 \pm 100$ K, $vsini = 20.3 \pm 0.9$ km s^{-1}, $r_k = 1.91 \pm 0.09$, and $dx = 2.42 \pm 0.09$.

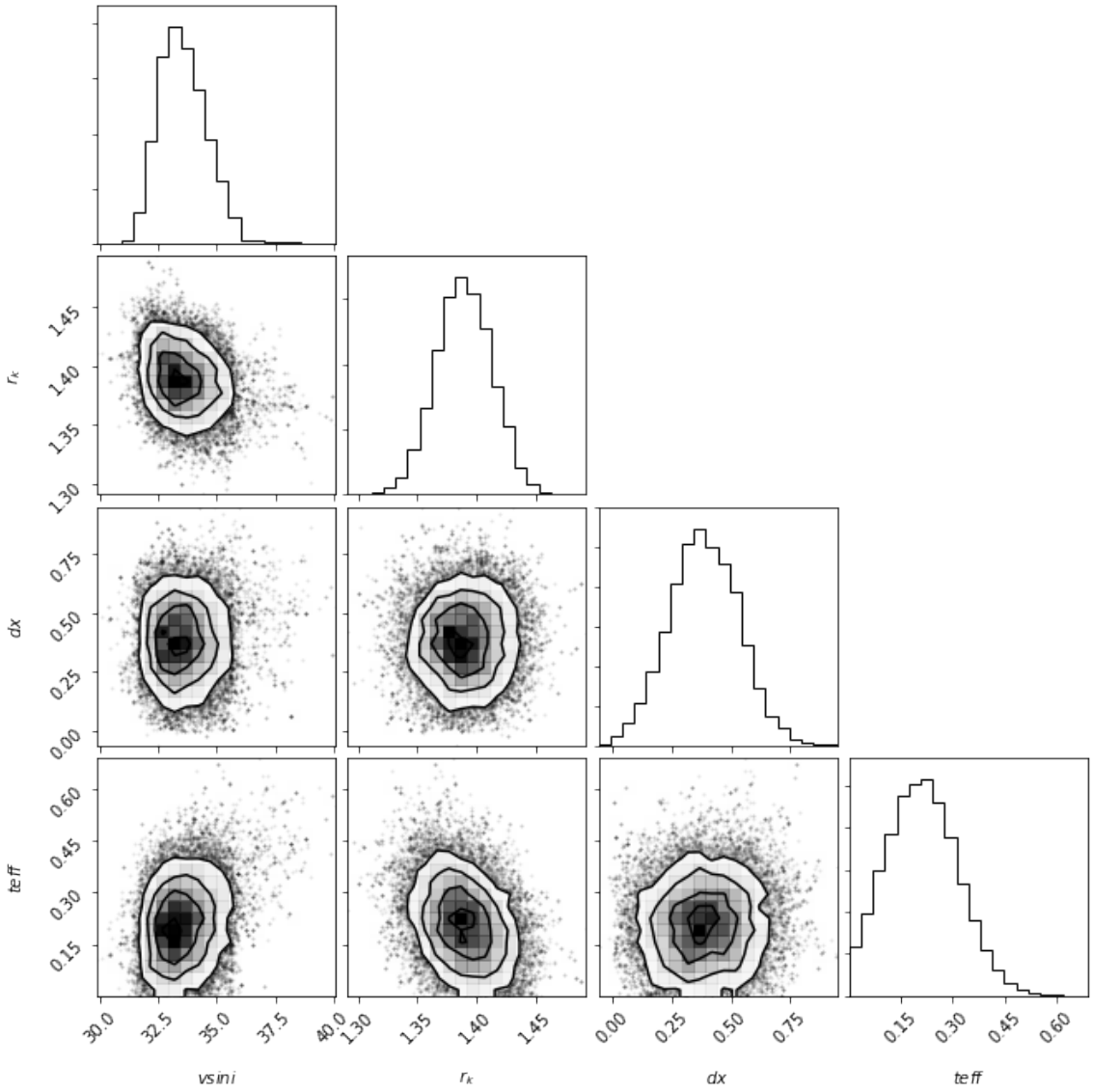

Figure 9 Relative probability distributions and correlations for the four fit parameters returned by *emcee* to best match the NIRSPEC spectrum of object GY 30 corresponding to T = 3140 ± 20 K, $vsini$ = 33.5 ± 1.1 km s^{-1}, r_k = 1.39 ± 0.02, and dx = 0.38 ± 0.15.

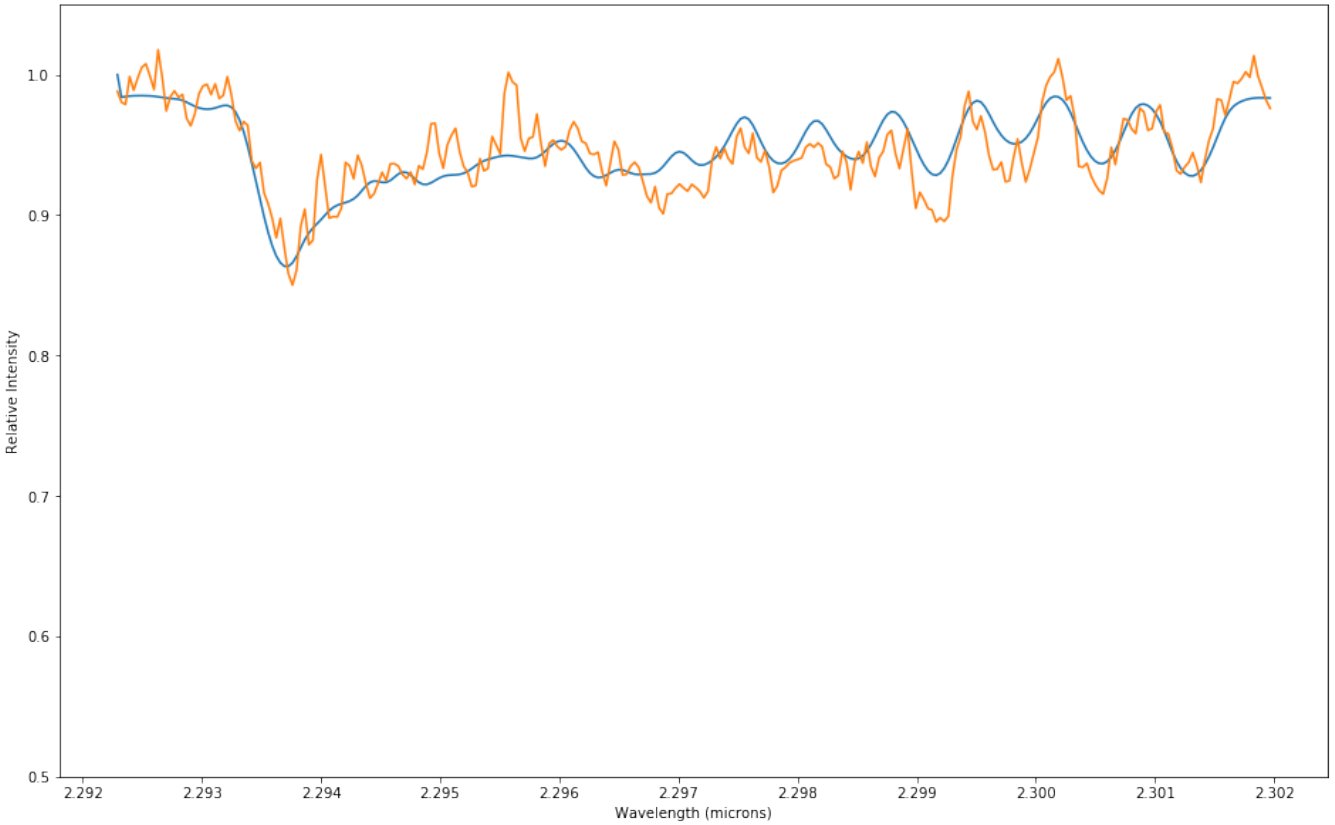

Figure 10 Synthetic overlay (blue) on top of the data (orange) for the four fit parameters returned by *emcee* to best match the NIRSPEC spectrum of object GY 30 corresponding to $T = 3140 \pm 20$ K, $vsini = 33.5 \pm 1.1$ km s^{-1}, $r_k = 1.39 \pm 0.02$, and $dx = 0.38 \pm 0.15$.

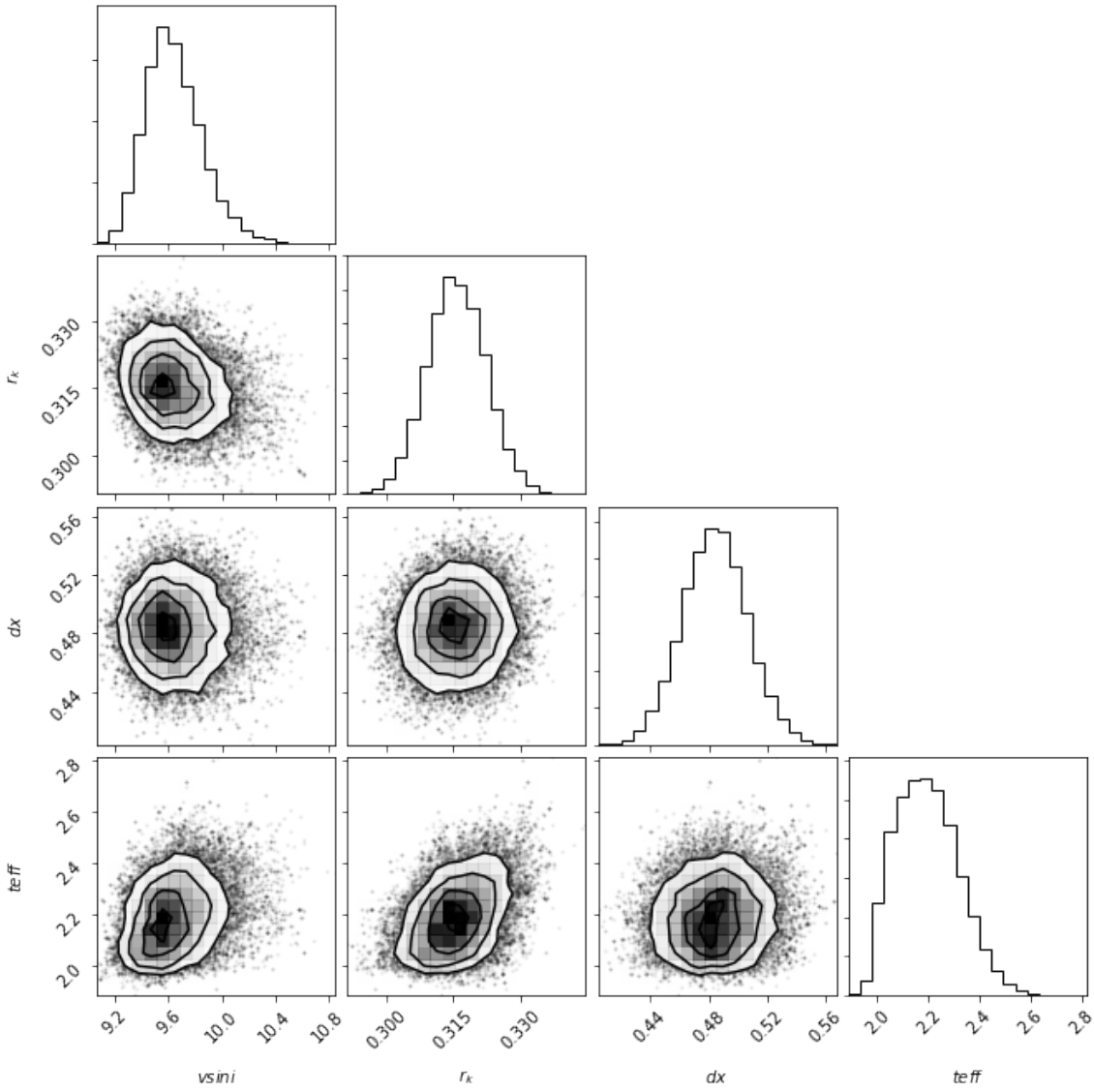

Figure 11 Relative probability distributions and correlations for the four fit parameters returned by *emcee* to best match the NIRSPEC spectrum of object GY 91 corresponding to $T = 3540 \pm 20$ K, $vsini = 9.6 \pm 0.2$ km s^{-1}, $r_k = 0.32 \pm 0.01$, and $dx = 0.48 \pm 0.02$.

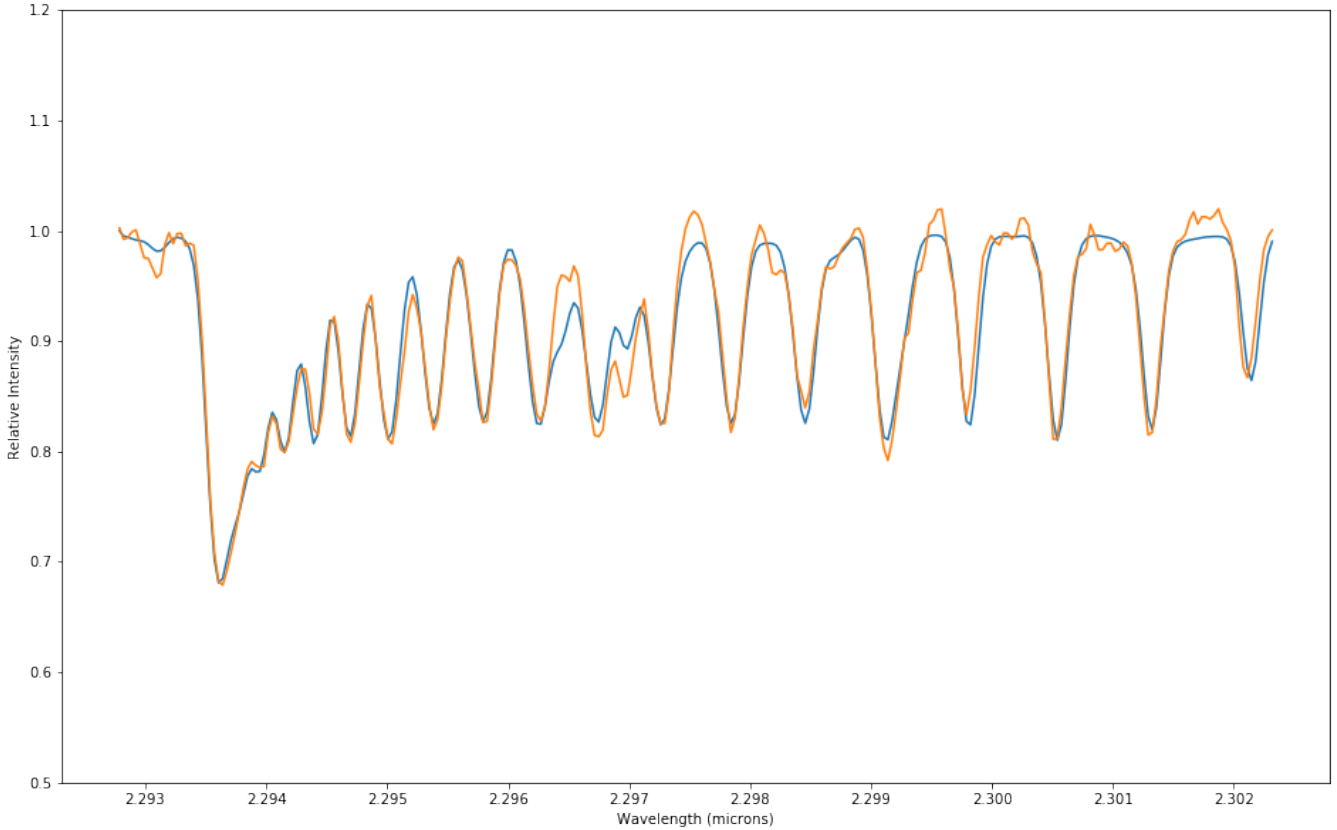

Figure 12 Synthetic overlay (blue) on top of the data (orange) for the four fit parameters returned by *emcee* to best match the NIRSPEC spectrum of object GY 91 corresponding to $T = 3540 \pm 20$ K, $vsini = 9.6 \pm 0.2$ km s^{-1}, $r_k = 0.32 \pm 0.01$, and $dx = 0.48 \pm 0.02$.

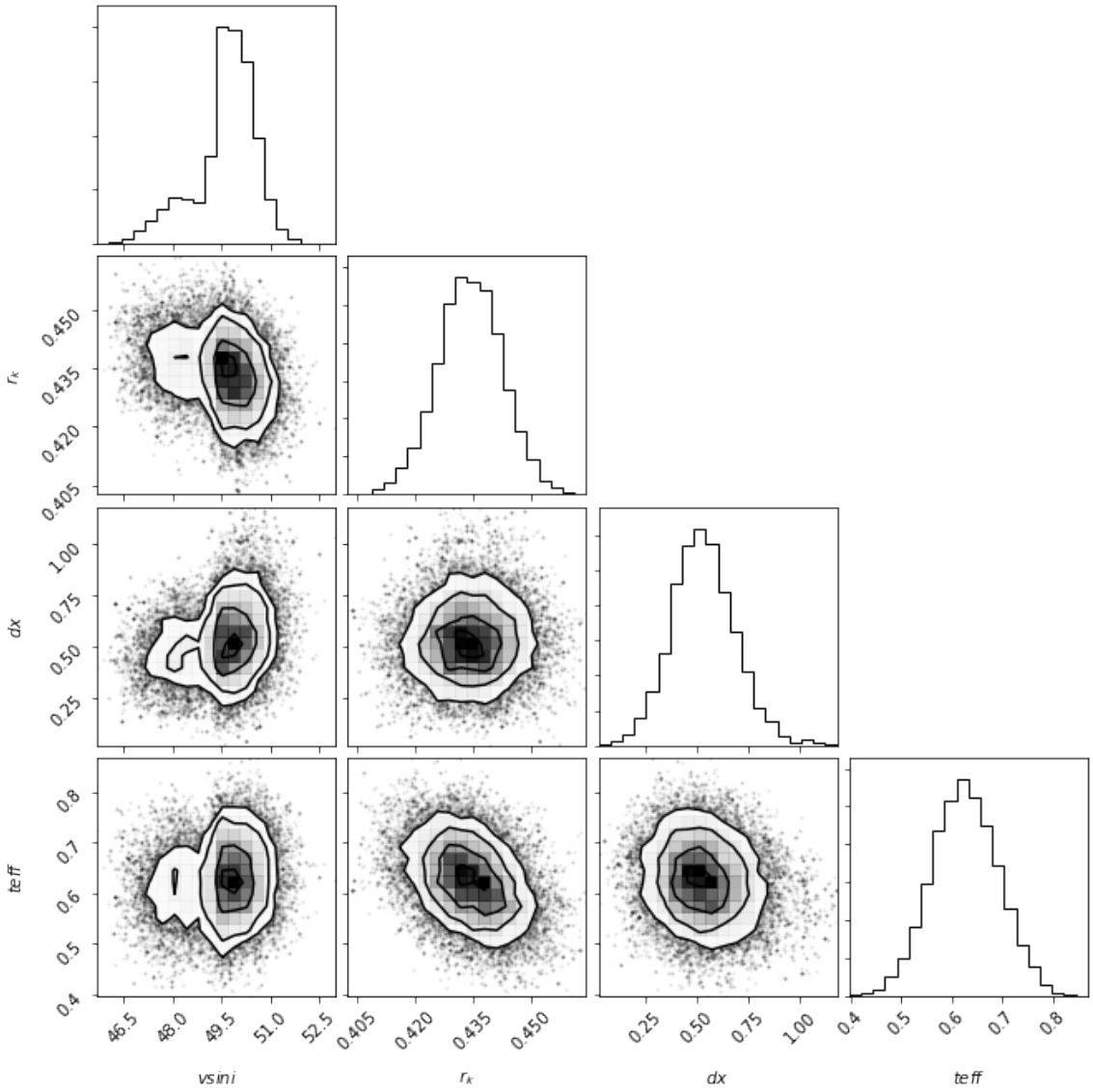

Figure 13 Relative probability distributions and correlations for the four fit parameters returned by *emcee* to best match the NIRSPEC spectrum of object GY 197 corresponding to $T = 3220 \pm 20$ K, $vsini = 49.8 \pm 1.1$ km s^{-1}, $r_k = 0.43 \pm 0.01$, and $dx = 0.52 \pm 0.15$.

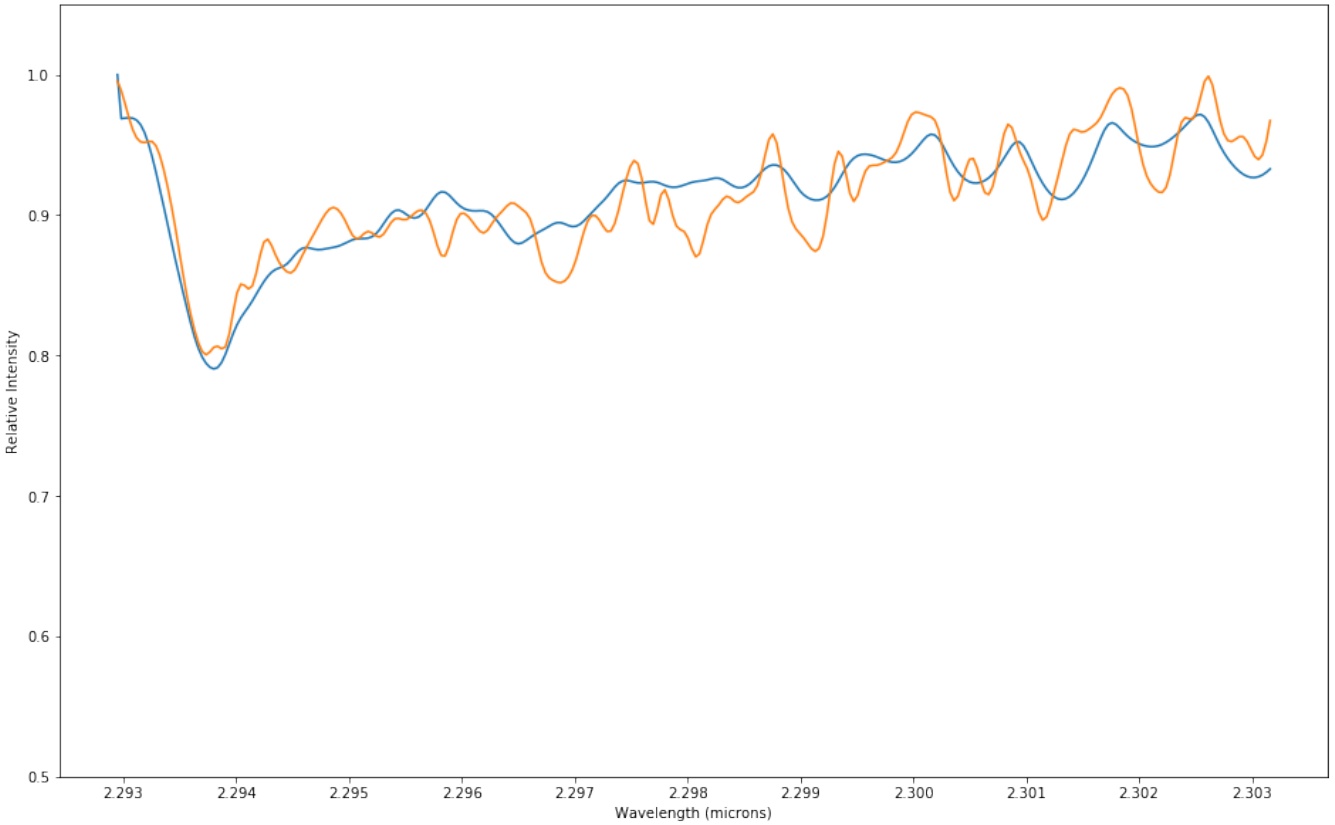

Figure 14 Synthetic overlay (blue) on top of the data (orange) for the four fit parameters returned by *emcee* to best match the NIRSPEC spectrum of object GY 197 corresponding to $T = 3220 \pm 20$ K, $vsini = 49.8 \pm 1.1$ km s^{-1}, $r_k = 0.43 \pm 0.01$, and $dx = 0.52 \pm 0.15$.

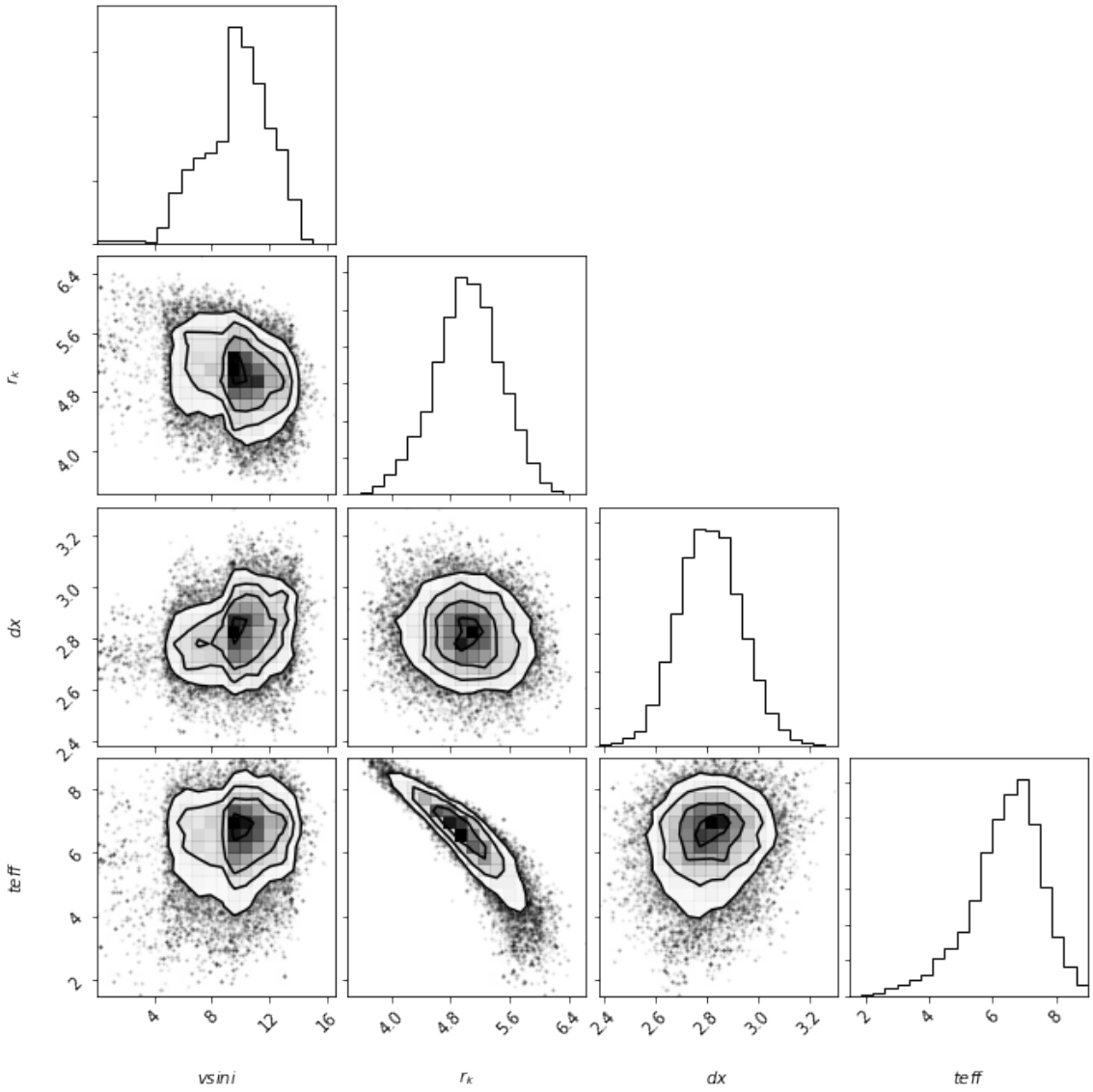

Figure 15 Relative probability distributions and correlations for the four fit parameters returned by *emcee* to best match the NIRSPEC spectrum of object GY 224 corresponding to $T = 4400 \pm 210$ K, $vsini = 9.9 \pm 2.8$ km s^{-1}, $r_k = 5.03 \pm 0.45$, and $dx = 2.81 \pm 0.12$.

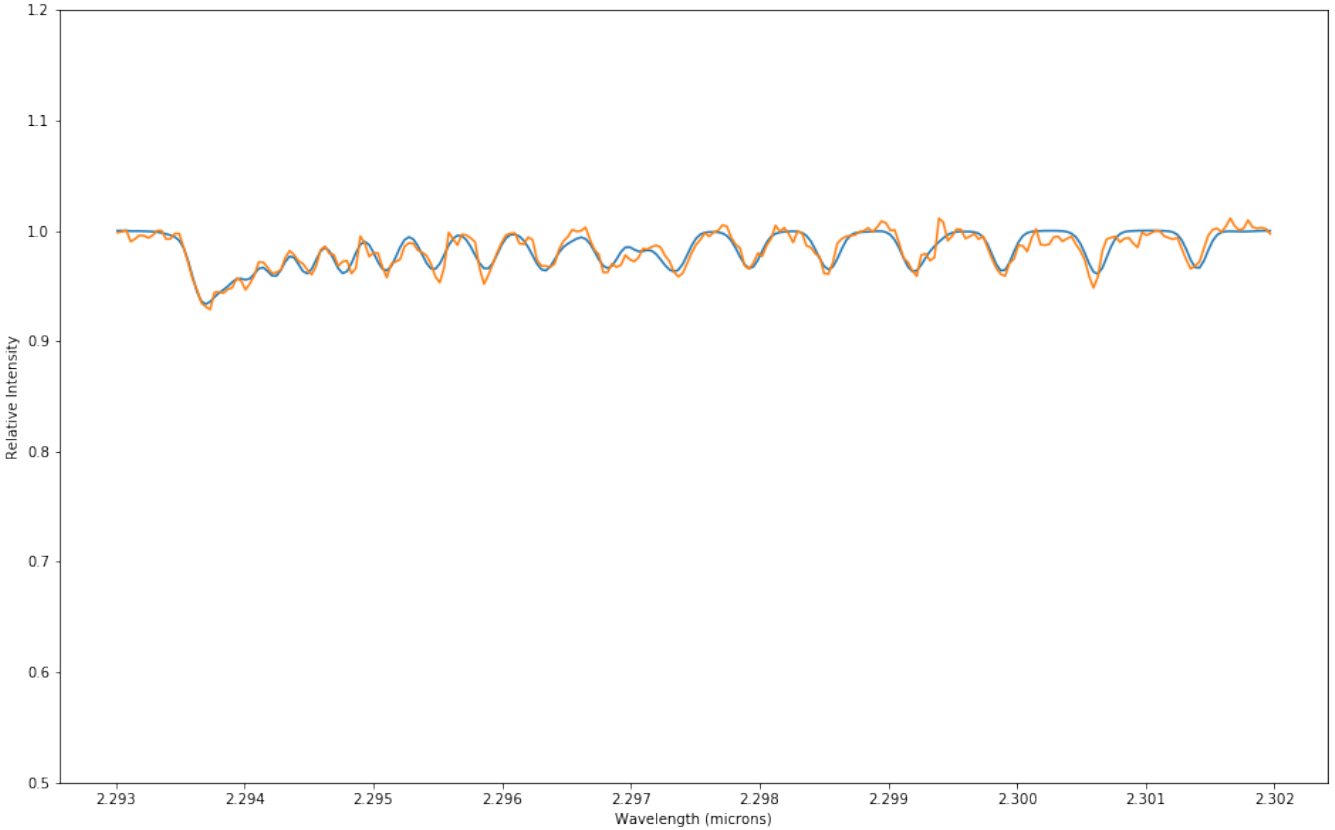

Figure 16 Synthetic overlay (blue) on top of the data (orange) for the four fit parameters returned by *emcee* to best match the NIRSPEC spectrum of object GY 224 corresponding to $T = 4400 \pm 210$ K, $vsini = 9.90 \pm 2.8$ km s^{-1}, $r_k = 5.03 \pm 0.45$, and $dx = 2.81 \pm 0.12$.

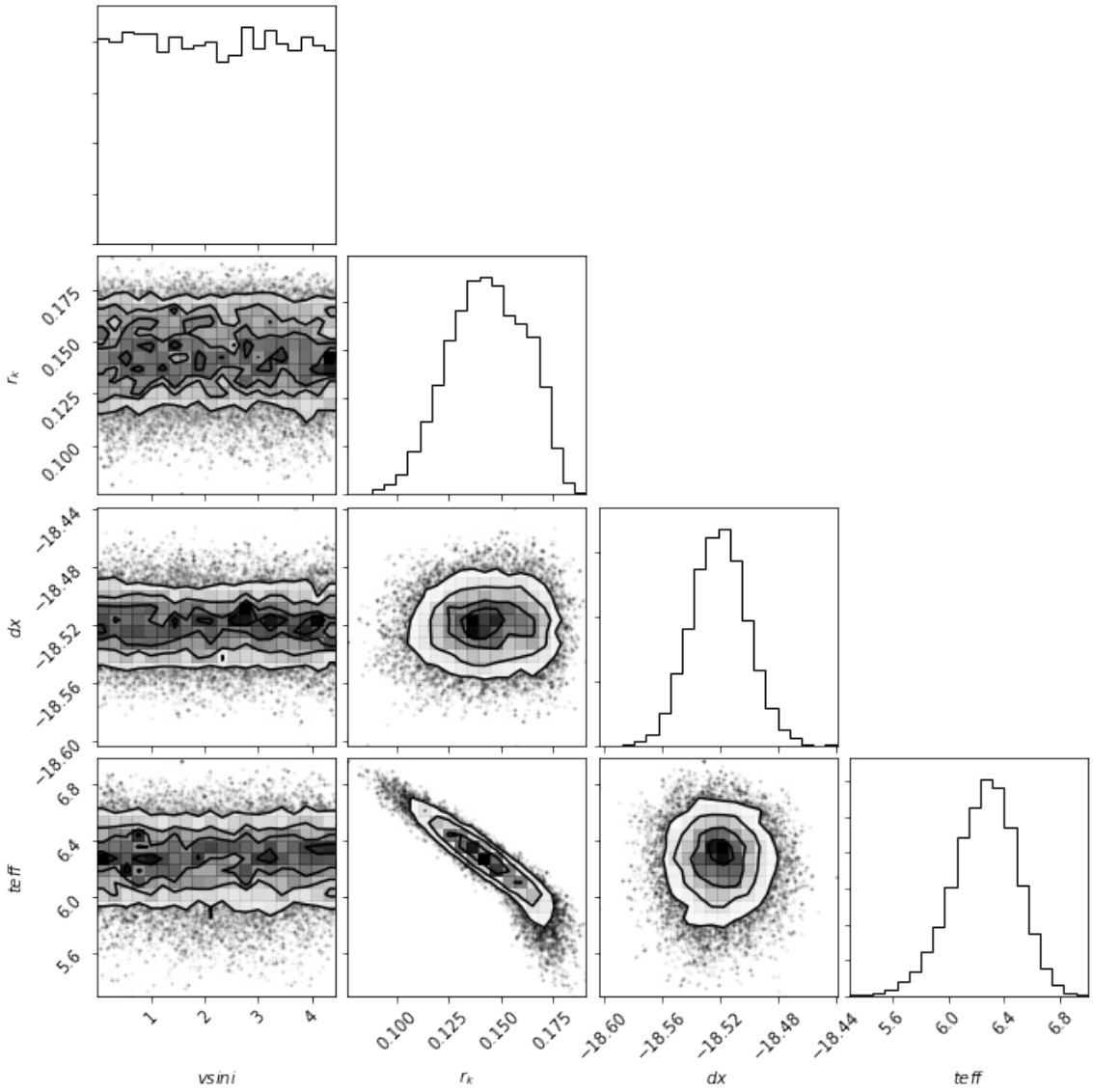

Figure 17 Relative probability distributions and correlations for the four fit parameters returned by *emcee* to best match the NIRSPEC spectrum of radial velocity standard HD 201091 corresponding to $T = 4360 \pm 40$ K, $vsini = 2.2 \pm 1.5$ km s^{-1}, $r_k = 0.14 \pm 0.02$, and $dx = -18.52 \pm 0.02$.

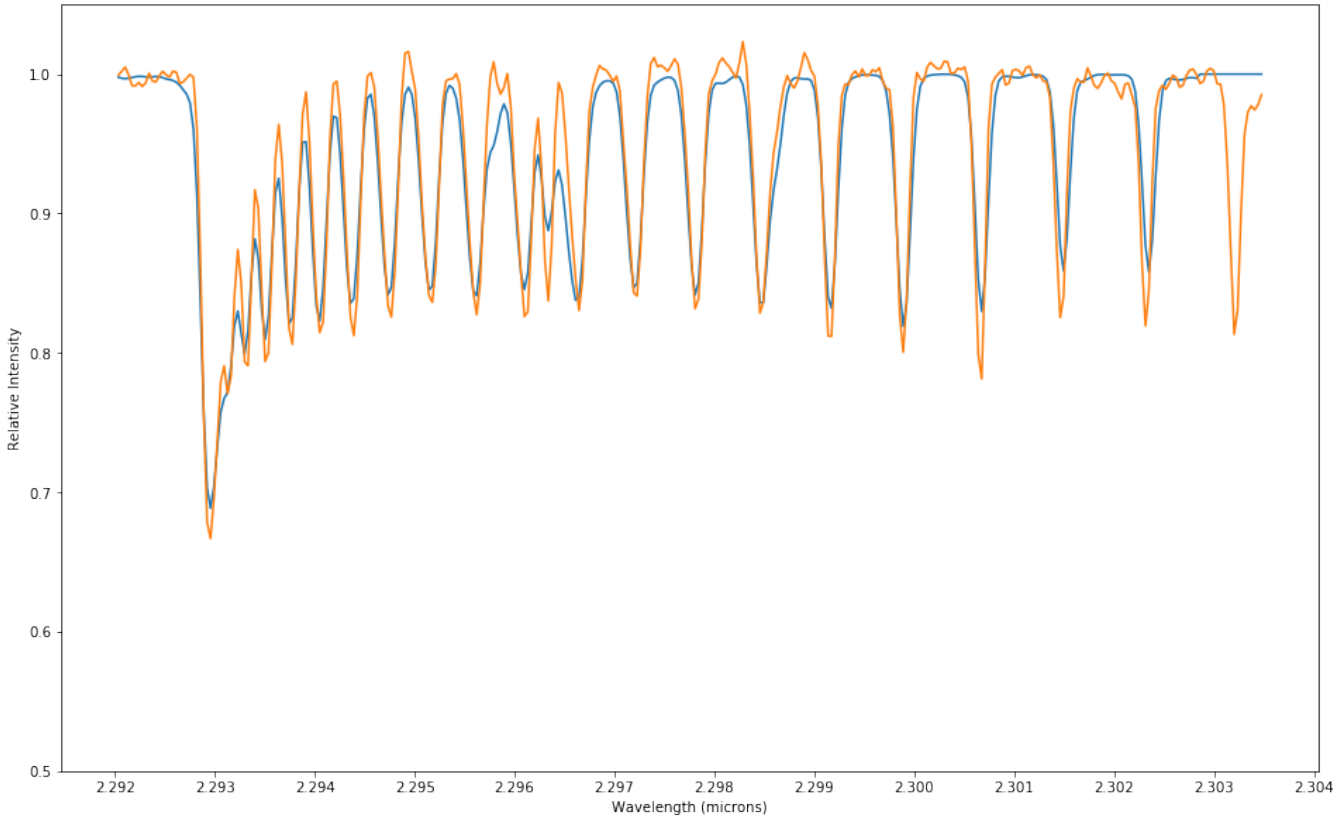

Figure 18 Synthetic overlay (blue) on top of the data (orange) for the four fit parameters returned by *emcee* to best match the NIRSPEC spectrum of radial velocity standard HD 201091 corresponding to $T = 4360 \pm 40$ K, $vsini = 2.2 \pm 1.5$ km s^{-1}, $r_k = 0.14 \pm 0.02$, and $dx = -18.52 \pm 0.02$.

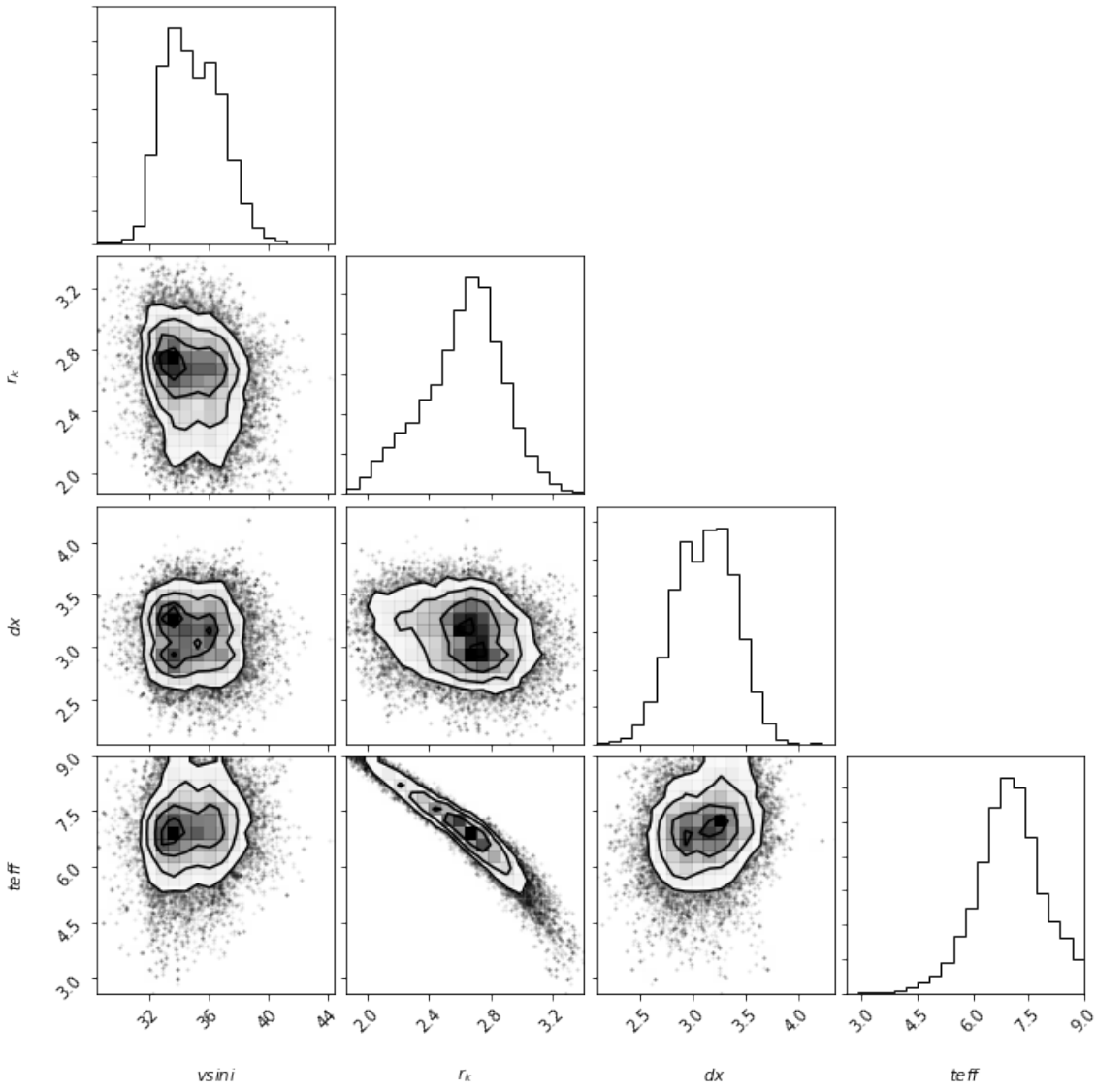

Figure 19 Relative probability distributions and correlations for the four fit parameters returned by *emcee* to best match the NIRSPEC spectrum of object ISO-Oph 51 corresponding to $T = 4500 \pm 180$ K, $vsini = 34.8 \pm 2.1$ km s^{-1}, $r_k = 2.65 \pm 0.26$, and $dx = 3.13 \pm 0.29$.

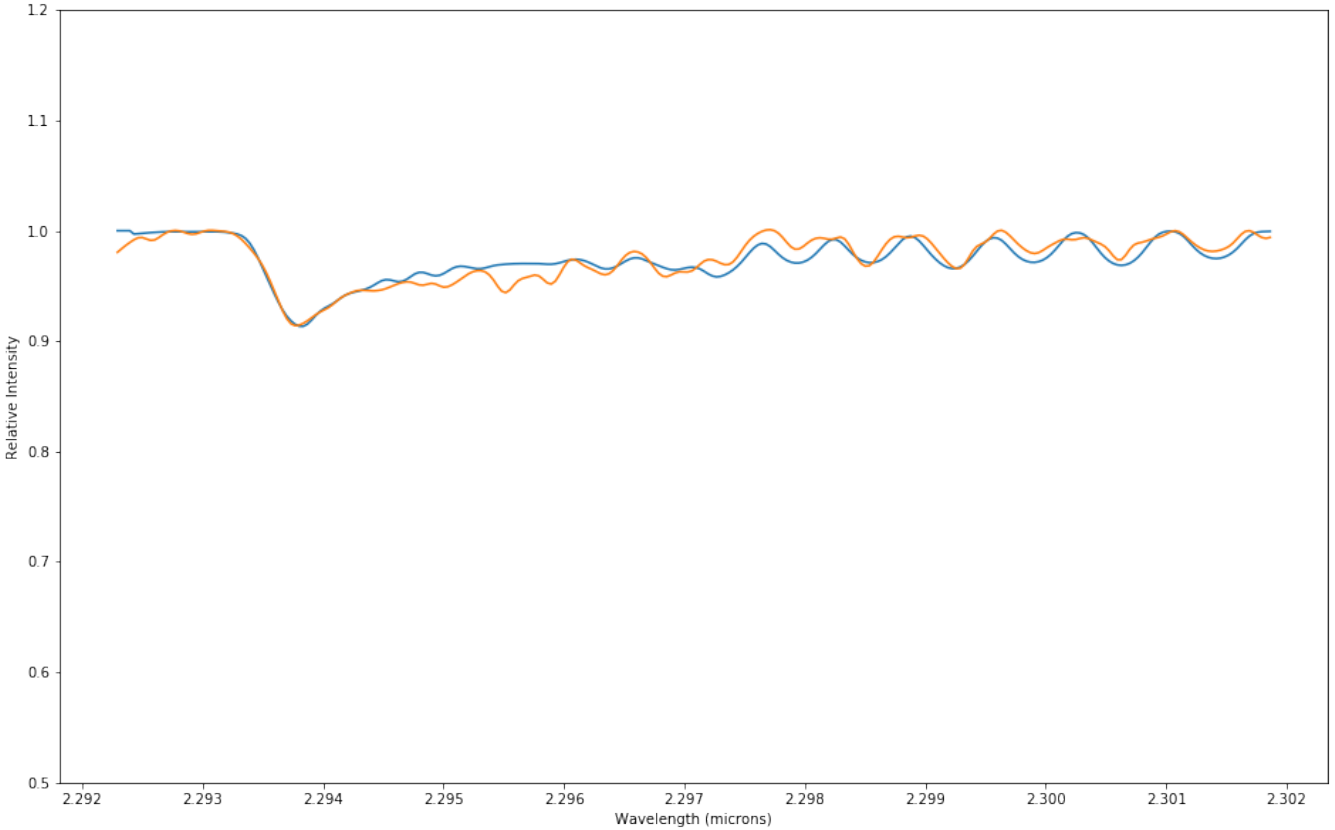

Figure 20 Synthetic overlay (blue) on top of the data (orange) for the four fit parameters returned by *emcee* to best match the NIRSPEC spectrum of object ISO-Oph 51 corresponding to $T = 4500 \pm 180$ K, $vsini = 34.8 \pm 2.1$ km s^{-1}, $r_k = 2.65 \pm 0.26$, and $dx = 3.13 \pm 0.29$.

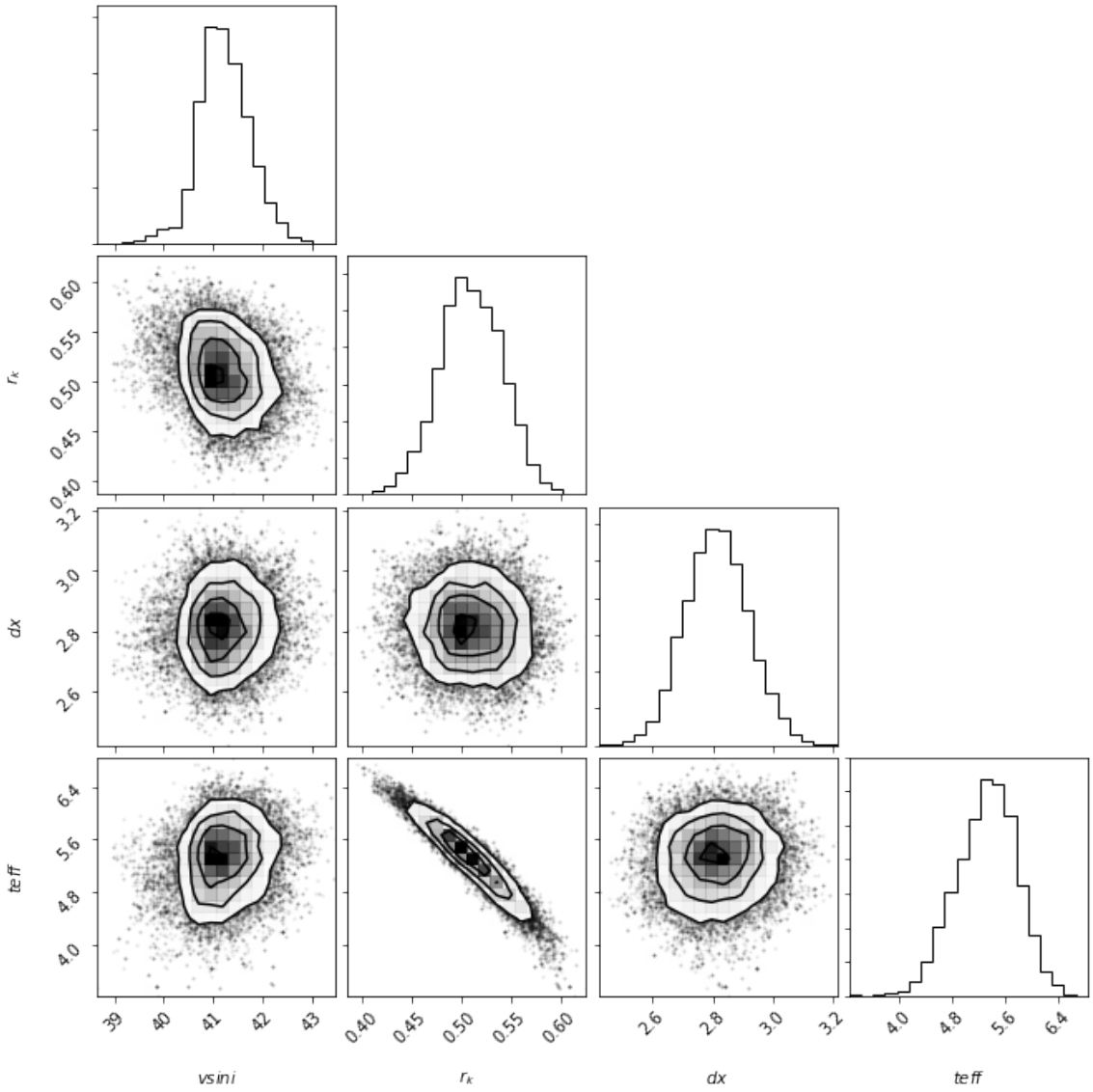

Figure 21 Relative probability distributions and correlations for the four fit parameters returned by *emcee* to best match the NIRSPEC spectrum of object VSSG 17 corresponding to $T = 4160 \pm 90$ K, $vsini = 41.2 \pm 0.5$ km s^{-1}, $r_k = 0.51 \pm 0.03$, and $dx = 2.81 \pm 0.10$.

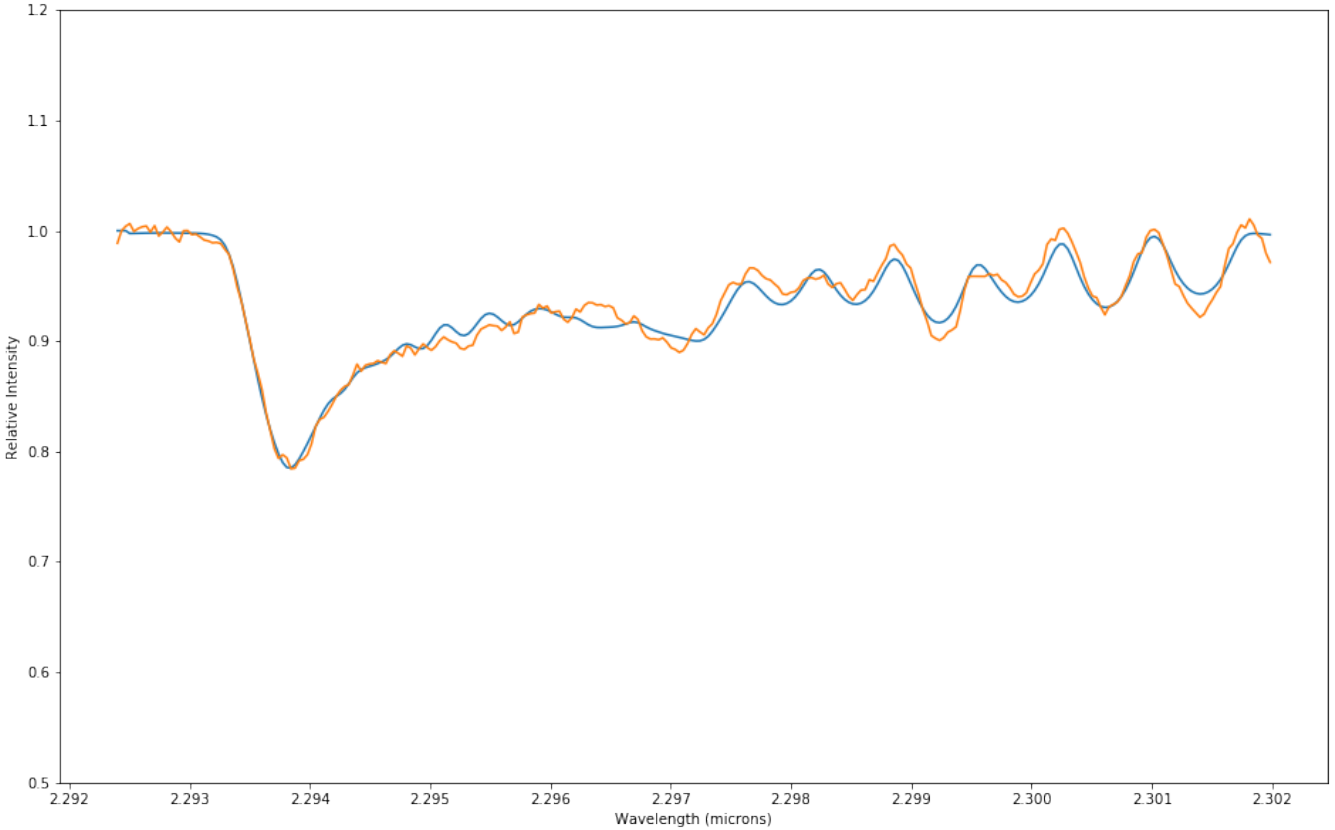

Figure 22 Synthetic overlay (blue) on top of the data (orange) for the four fit parameters returned by *emcee* to best match the NIRSPEC spectrum of object VSSG 17 corresponding to $T = 4160 \pm 90$ K, $vsini = 41.2 \pm 0.5$ km s^{-1}, $r_k = 0.51 \pm 0.03$, and $dx = 2.81 \pm 0.10$.

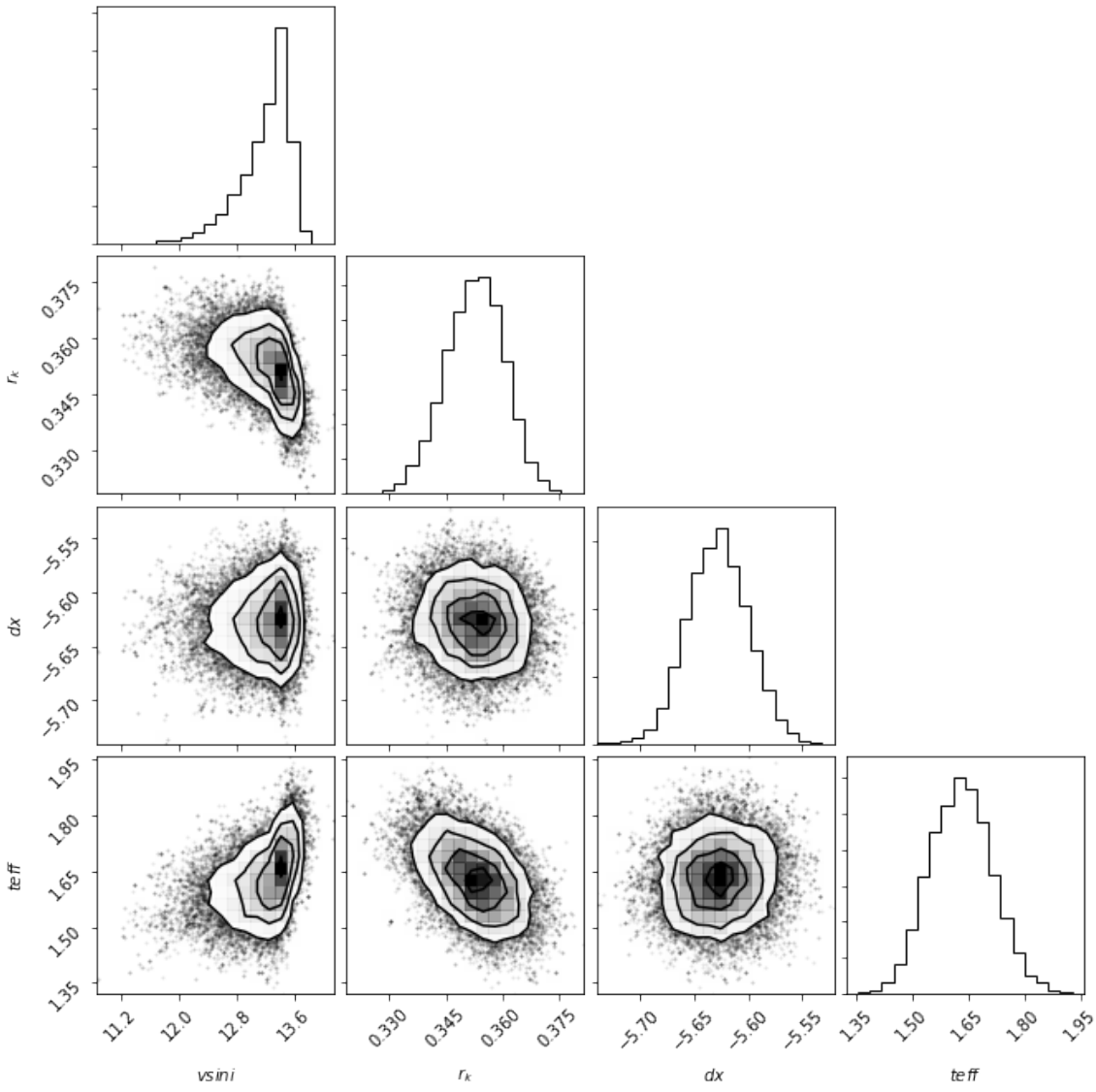

Figure 23 Relative probability distributions and correlations for the four fit parameters returned by *emcee* to best match the NIRSPEC spectrum of object WL 1 corresponding to $T = 3420 \pm 20$ K, $vsini = 13.3 \pm 0.4$ km s^{-1}, $r_k = 0.36 \pm 0.01$, and $dx = -5.63 \pm 0.03$.

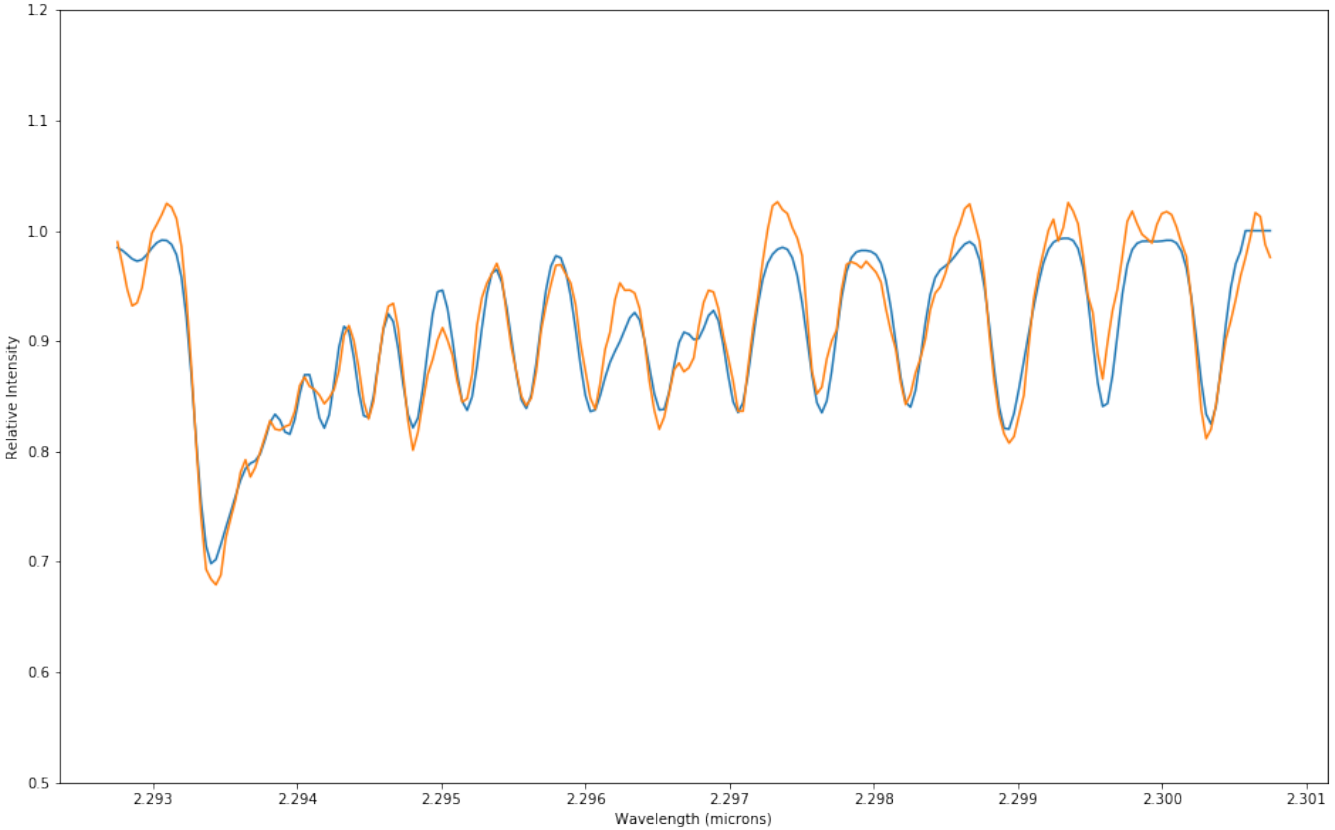

Figure 24 Synthetic overlay (blue) on top of the data (orange) for the four fit parameters returned by *emcee* to best match the NIRSPEC spectrum of object WL 1 corresponding to $T = 3420 \pm 20$ K, $vsini = 13.3 \pm 0.4$ km s^{-1}, $r_k = 0.36 \pm 0.01$, and $dx = -5.63 \pm 0.03$.

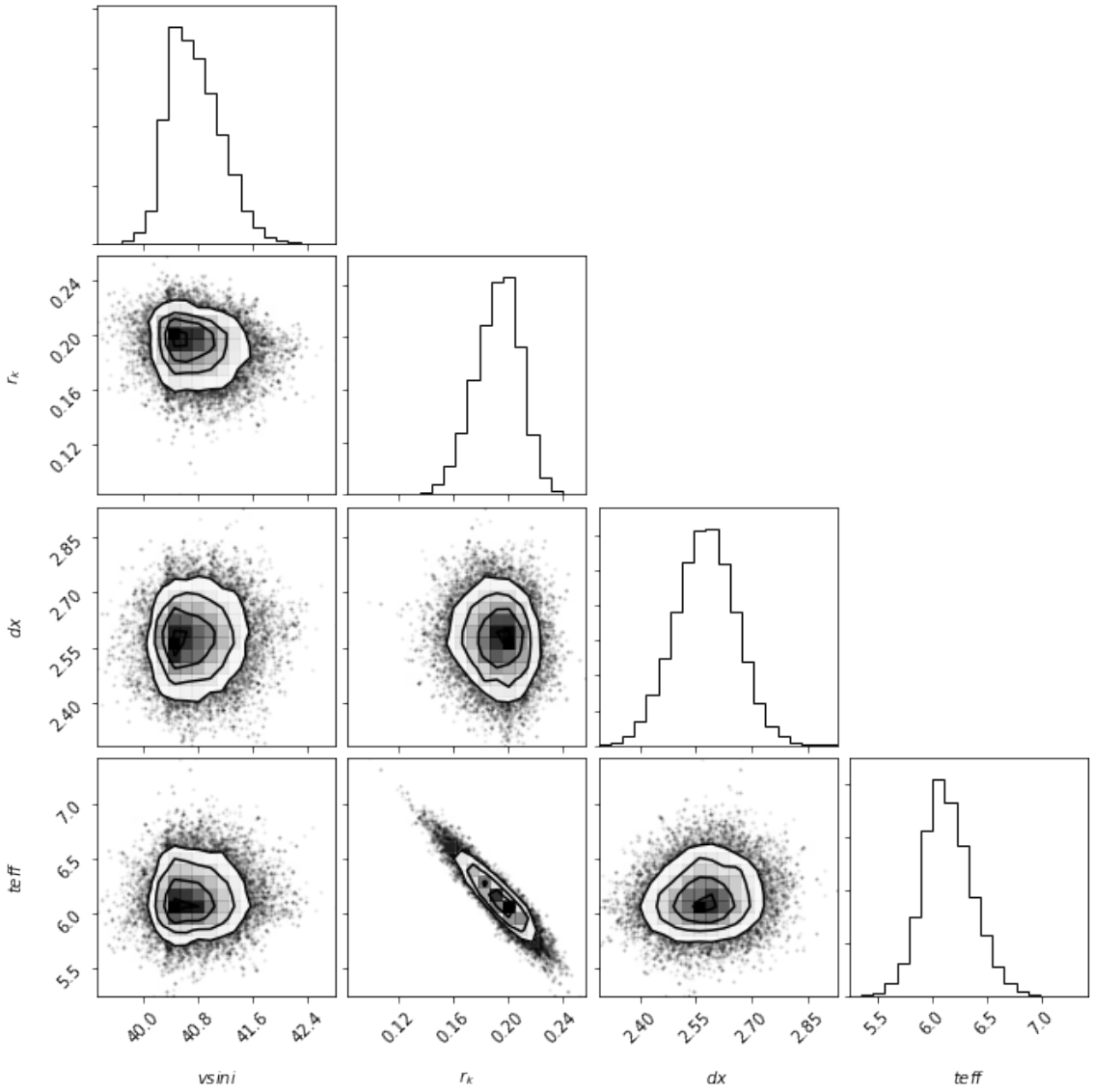

Figure 25 Relative probability distributions and correlations for the four fit parameters returned by *emcee* to best match the NIRSPEC spectrum of object WL 3 corresponding to $T = 4320 \pm 30$ K, $vsini = 40.7 \pm 0.4$ km s^{-1}, $r_k = 0.19 \pm 0.02$, and $dx = 2.58 \pm 0.08$.

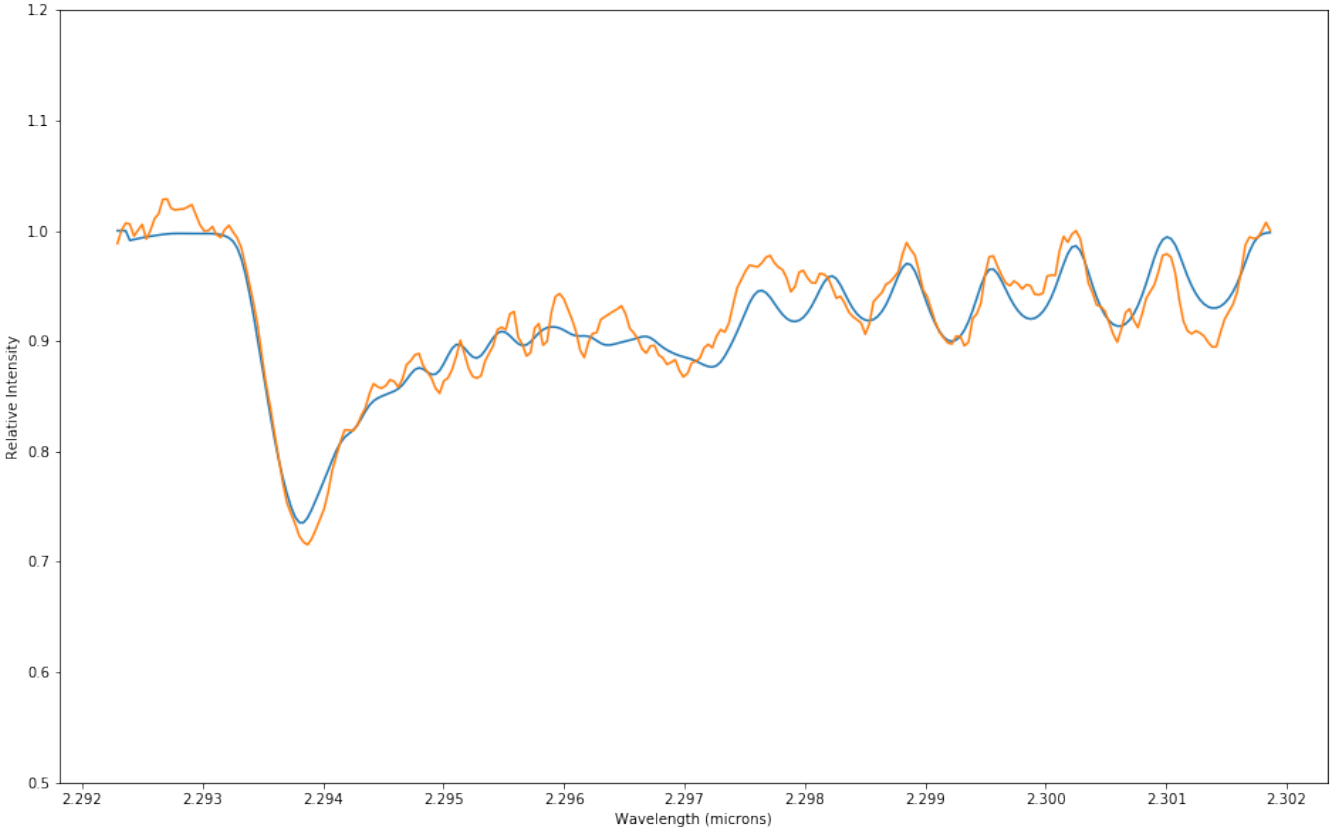

Figure 26 Synthetic overlay (blue) on top of the data (orange) for the four fit parameters returned by *emcee* to best match the NIRSPEC spectrum of object WL 3 corresponding to $T = 4320 \pm 30$ K, $vsini = 40.7 \pm 0.4$ km s^{-1}, $r_k = 0.19 \pm 0.02$, and $dx = 2.58 \pm 0.08$.

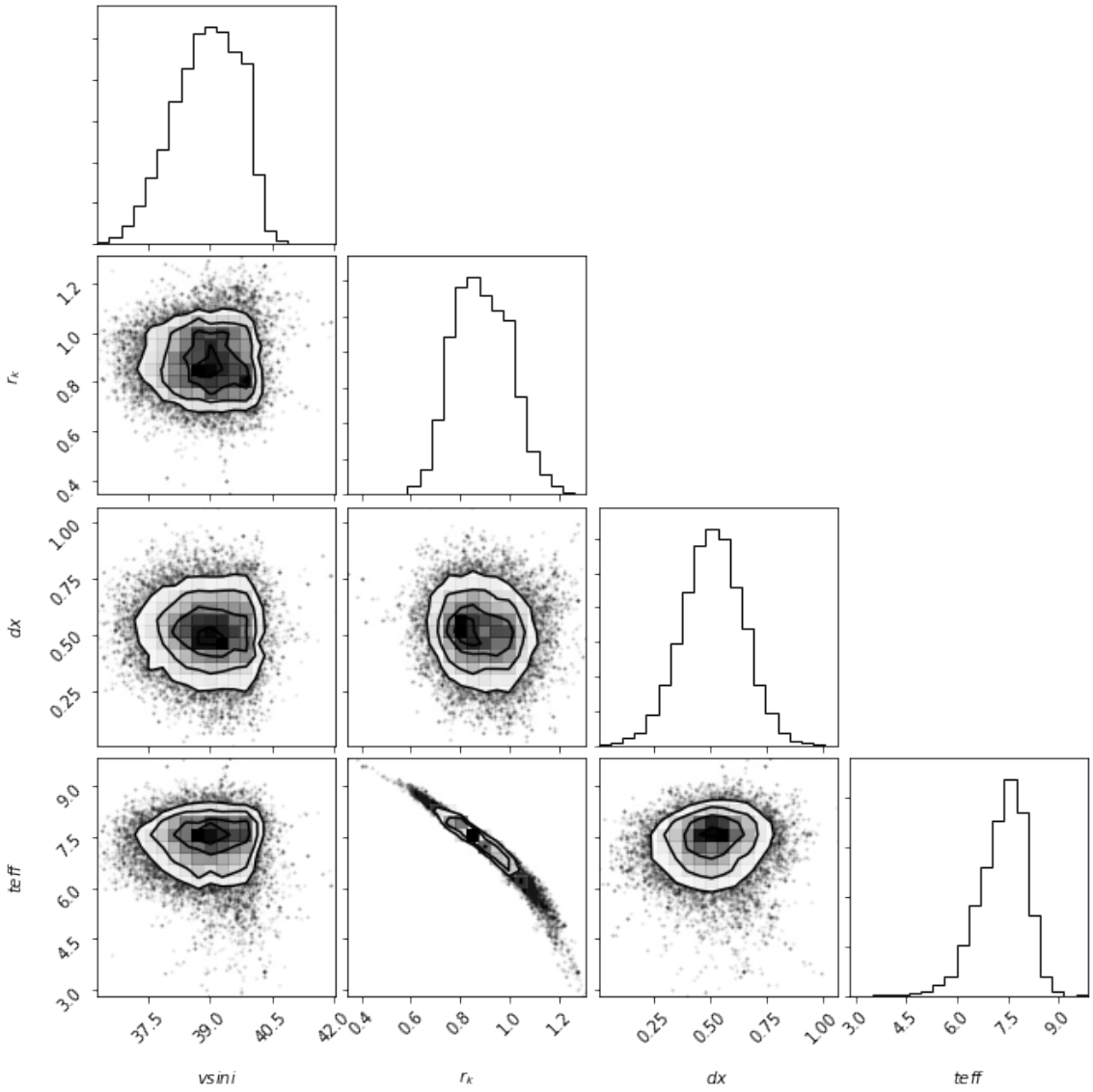

Figure 27 Relative probability distributions and correlations for the four fit parameters returned by *emcee* to best match the NIRSPEC spectrum of object WL 10 corresponding to $T = 4580 \pm 140$ K, $vsini = 39.0 \pm 0.9$ km s^{-1}, $r_k = 0.88 \pm 0.12$, and $dx = 0.51 \pm 0.13$.

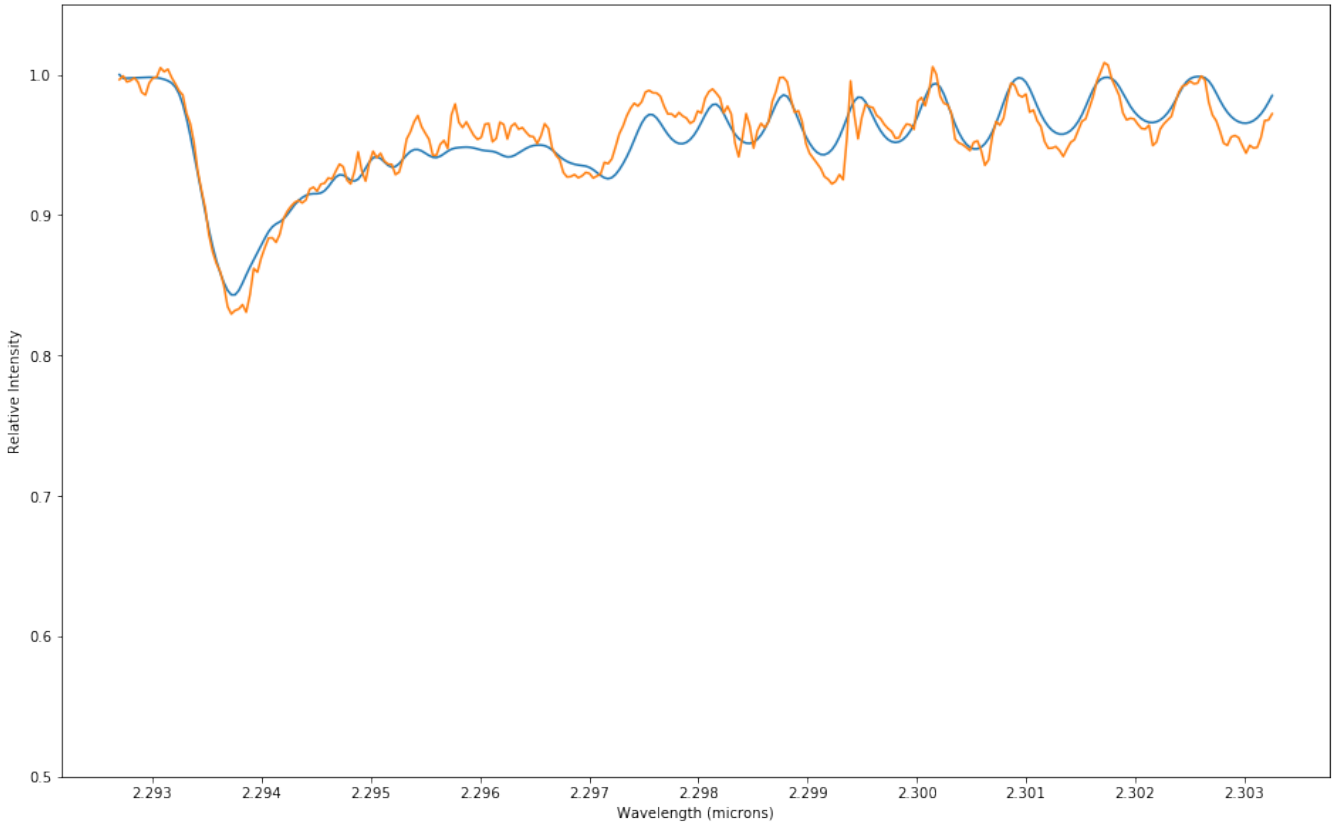

Figure 28 Synthetic overlay (blue) on top of the data (orange) for the four fit parameters returned by *emcee* to best match the NIRSPEC spectrum of object WL 10 corresponding to $T = 4580 \pm 140$ K, $vsini = 39.0 \pm 0.9$ km s^{-1}, $r_k = 0.88 \pm 0.12$, and $dx = 0.51 \pm 0.13$.

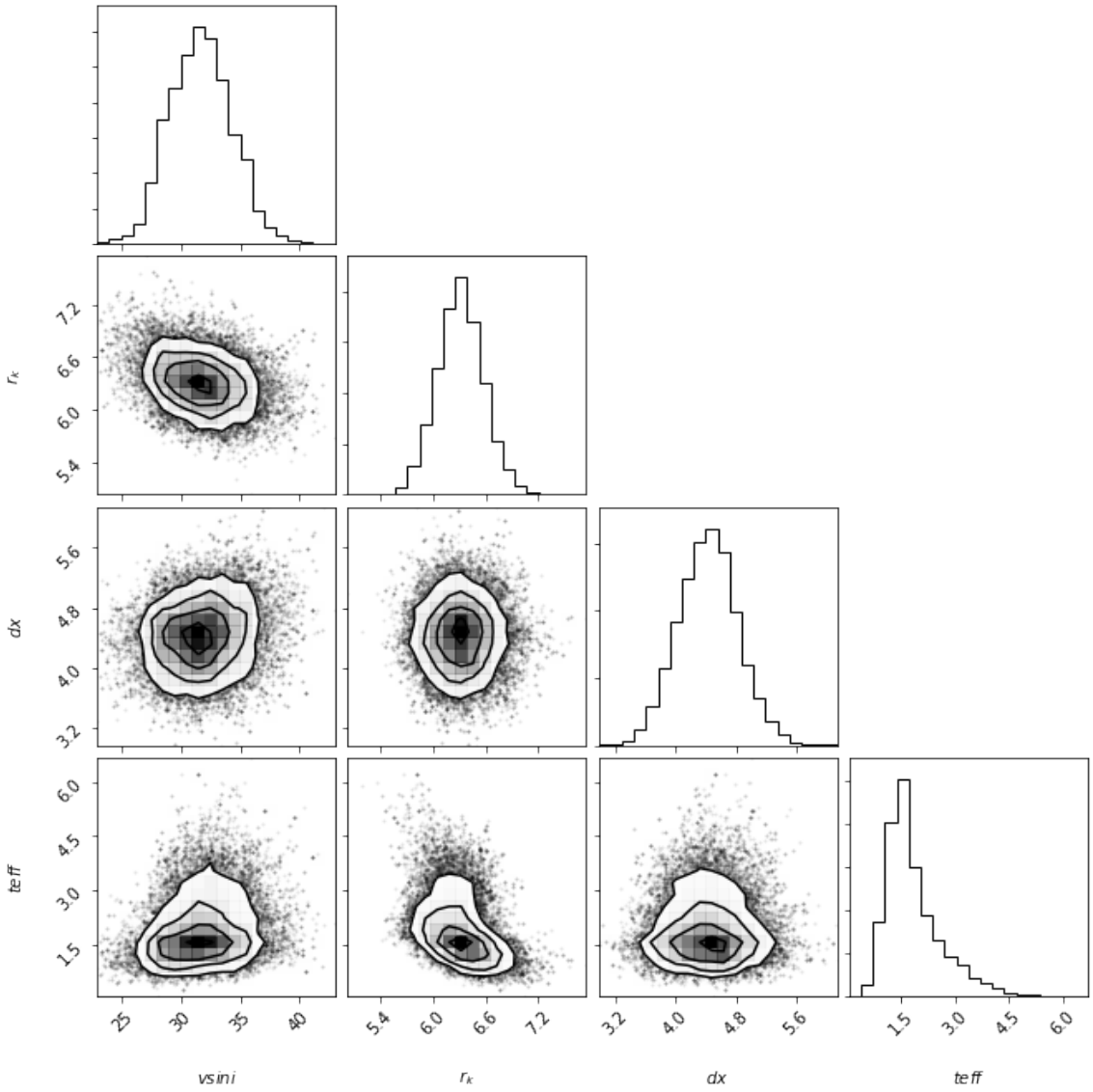

Figure 29 Relative probability distributions and correlations for the four fit parameters returned by *emcee* to best match the NIRSPEC spectrum of object WL 12 corresponding to T = 3420 ± 140 K, $vsini$ = 31.6 ± 2.7 km s^{-1}, r_k = 6.3 ± 0.26, and dx = 4.43 ± 0.40.

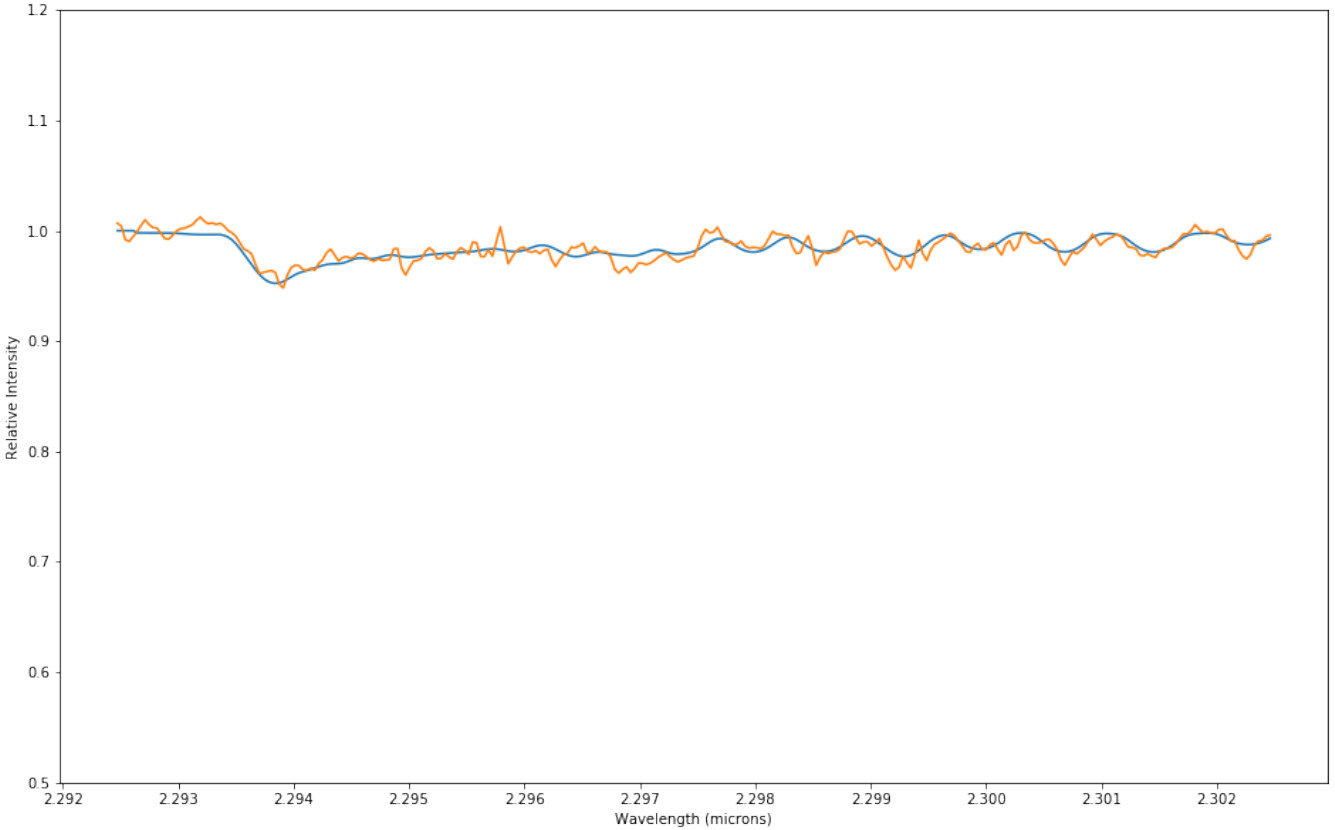

Figure 30 Synthetic overlay (blue) on top of the data (orange) for the four fit parameters returned by *emcee* to best match the NIRSPEC spectrum of object WL 12 corresponding to $T = 3420 \pm 140$ K, $vsini = 31.6 \pm 2.7$ km s^{-1}, $r_k = 6.3 \pm 0.26$, and $dx = 4.43 \pm 0.40$.

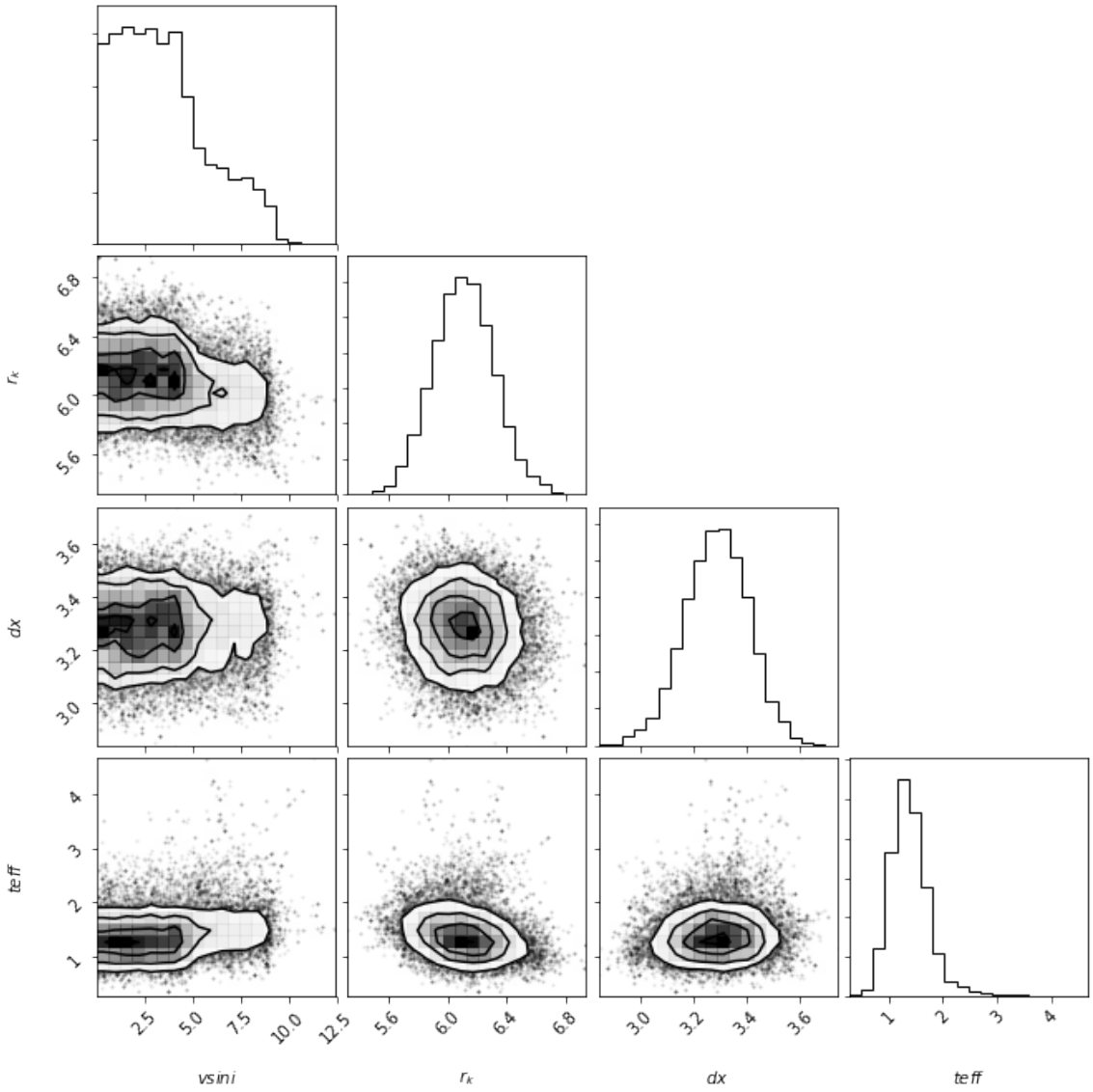

Figure 31 Relative probability distributions and correlations for the four fit parameters returned by *emcee* to best match the NIRSPEC spectrum of object WL 17 corresponding to T = 3360 ± 60 K, $vsini$ = 3.1 ± 2.9 km s^{-1}, r_k = 6.11 ± 0.21, and dx = 3.29 ± 0.12.

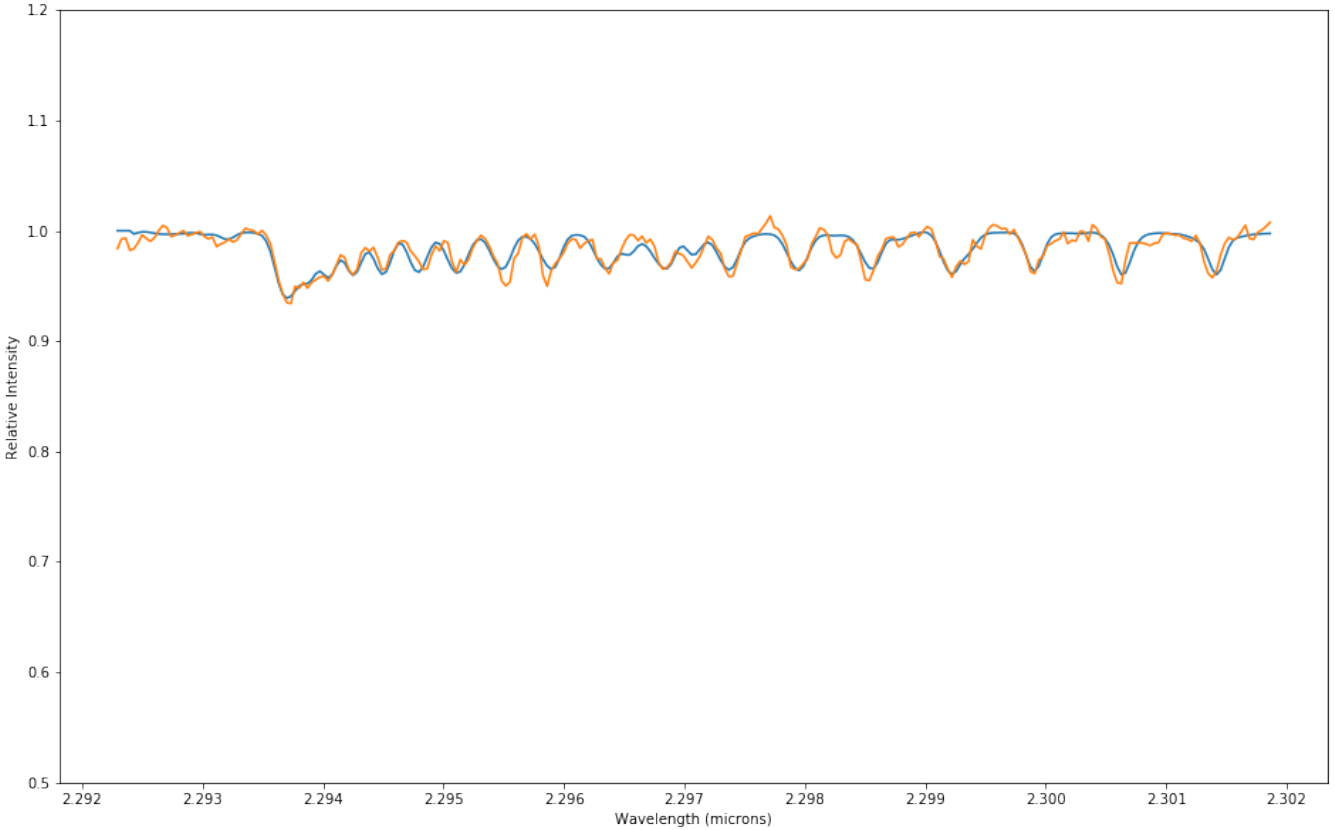

Figure 32 Synthetic overlay (blue) on top of the data (orange) for the four fit parameters returned by *emcee* to best match the NIRSPEC spectrum of object WL 17 corresponding to $T = 3360 \pm 60$ K, $vsini = 3.1 \pm 2.9$ km s^{-1}, $r_k = 6.11 \pm 0.21$, and $dx = 3.29 \pm 0.12$.

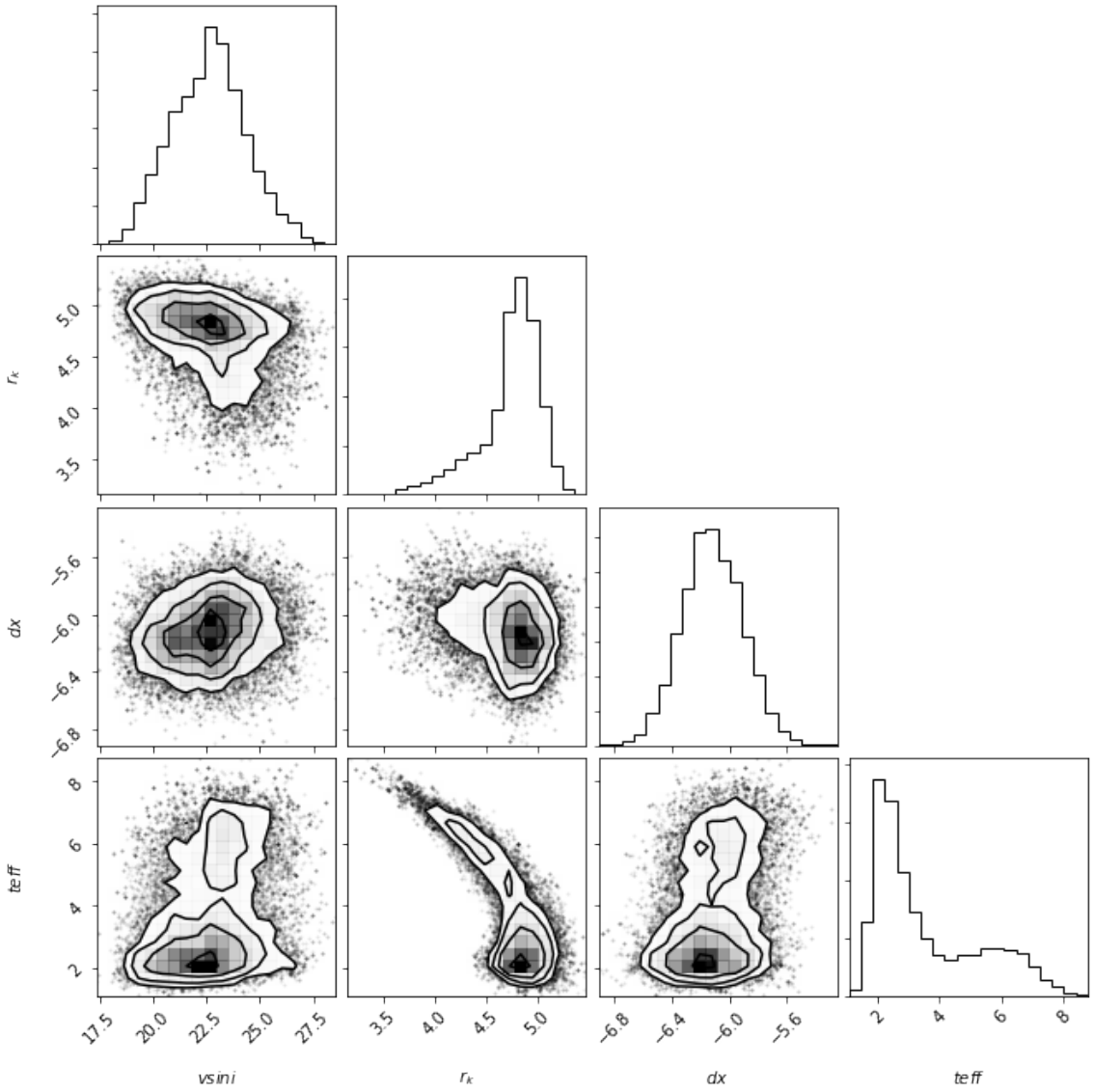

Figure 33 Relative probability distributions and correlations for the four fit parameters returned by *emcee* to best match the NIRSPEC spectrum of object WL 19 corresponding to $T = 3680 \pm 380$ K, $vsini = 22.7 \pm 1.7$ km s^{-1}, $r_k = 4.80 \pm 0.11$, and $dx = -6.12 \pm 0.21$.

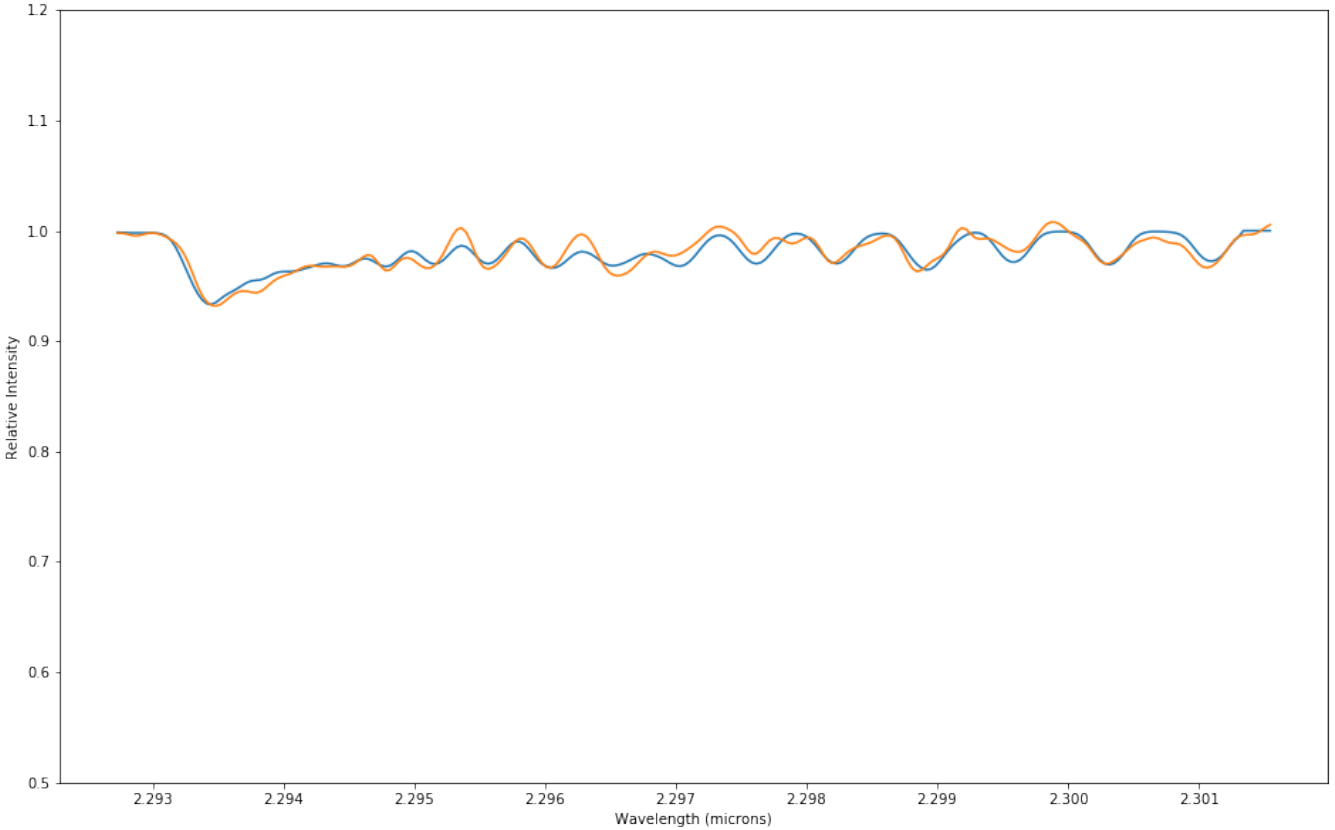

Figure 34 Synthetic overlay (blue) on top of the data (orange) for the four fit parameters returned by *emcee* to best match the NIRSPEC spectrum of object WL 19 corresponding to $T = 3680 \pm 380$ K, $vsini = 22.7 \pm 1.9$ km s^{-1}, $r_k = 4.80 \pm 0.11$, and $dx = -6.12 \pm 0.21$.

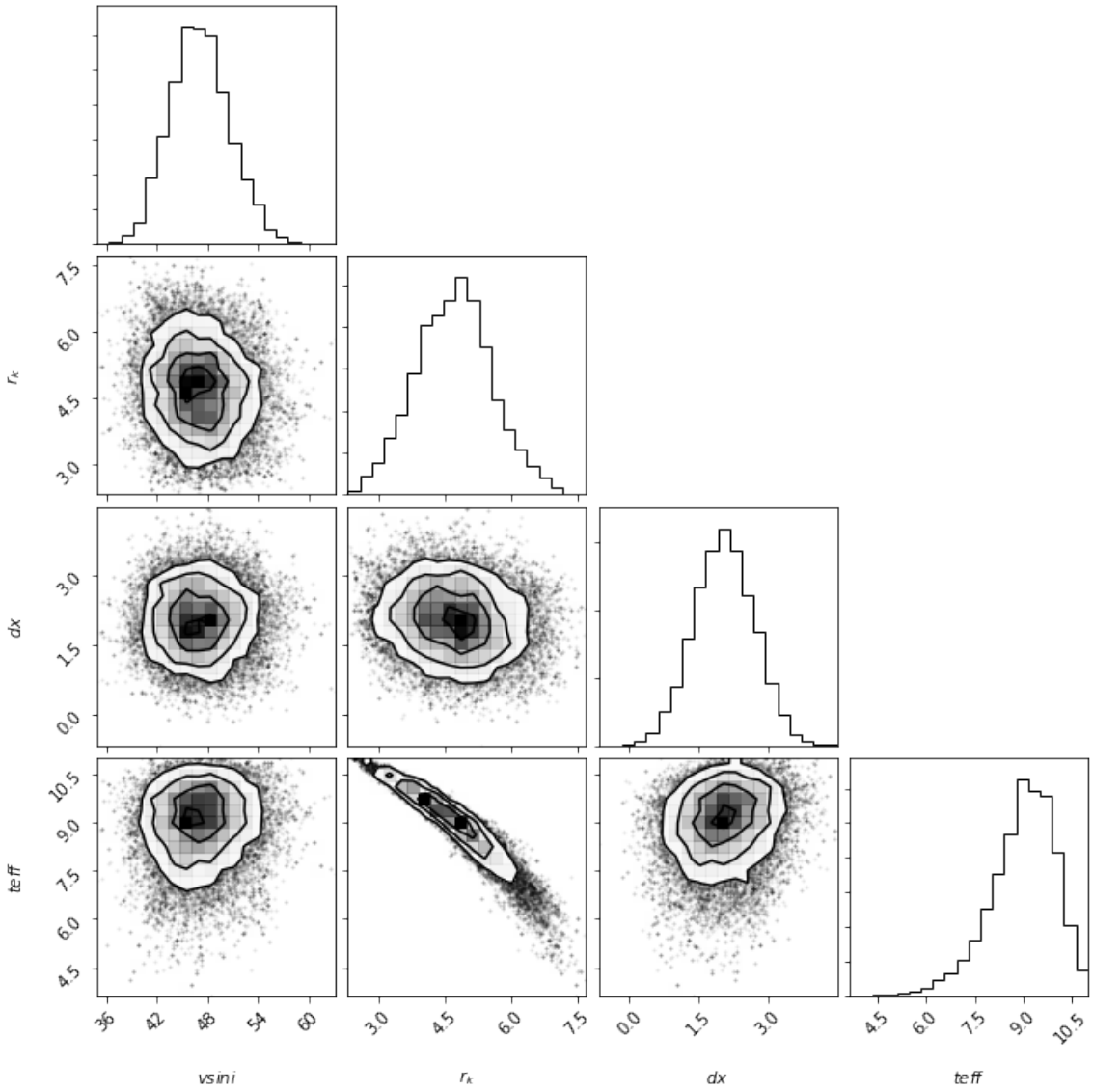

Figure 35 Relative probability distributions and correlations for the four fit parameters returned by *emcee* to best match the NIRSPEC spectrum of object WLY 2-43 corresponding to $T = 4920 \pm 190$ K, $vsini = 47.0 \pm 3.6$ km s^{-1}, $r_k = 4.71 \pm 0.85$, and $dx = 2.03 \pm 0.65$.

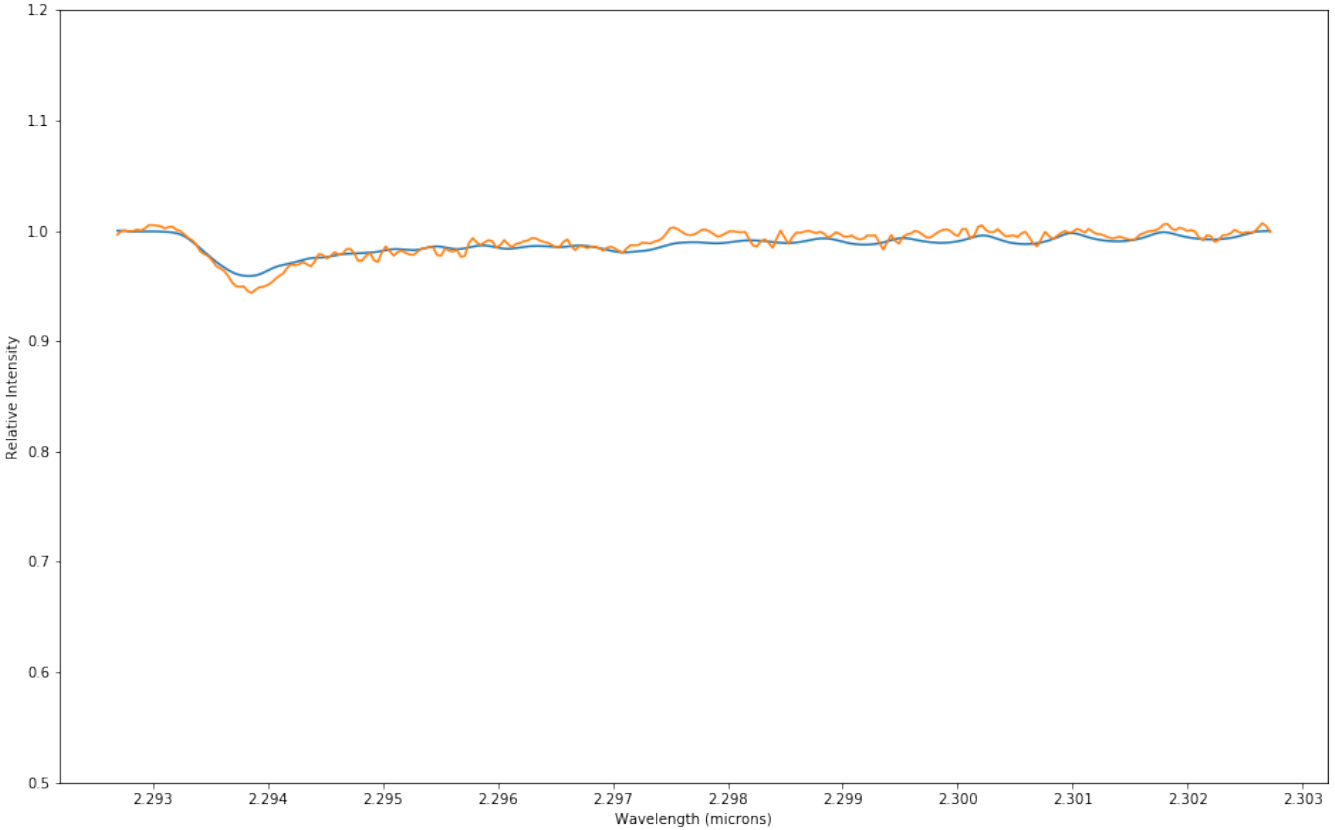

Figure 36 Synthetic overlay (blue) on top of the data (orange) for the four fit parameters returned by *emcee* to best match the NIRSPEC spectrum of object WLY 2-43 corresponding to $T = 4920 \pm 190$ K, $vsini = 47.0 \pm 3.6$ km s^{-1}, $r_k = 4.71 \pm 0.85$, and $dx = 2.03 \pm 0.65$.

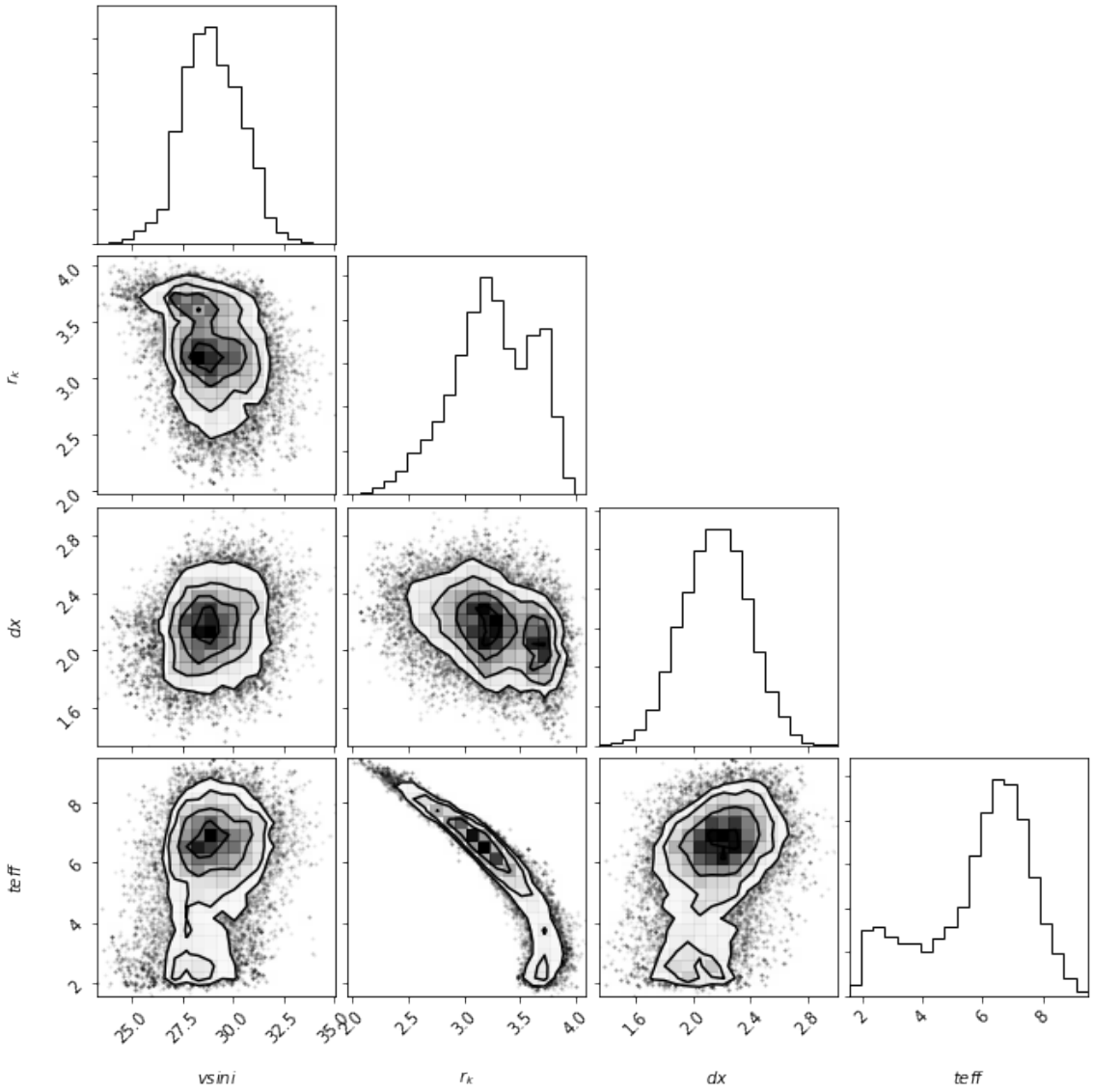

Figure 37 Relative probability distributions and correlations for the four fit parameters returned by *emcee* to best match the NIRSPEC spectrum of object WLY 2-44 corresponding to $T = 4360 \pm 380$ K, $vsini = 28.9 \pm 1.6$ km s^{-1}, $r_k = 3.25 \pm 0.39$, and $dx = 2.15 \pm 0.24$.

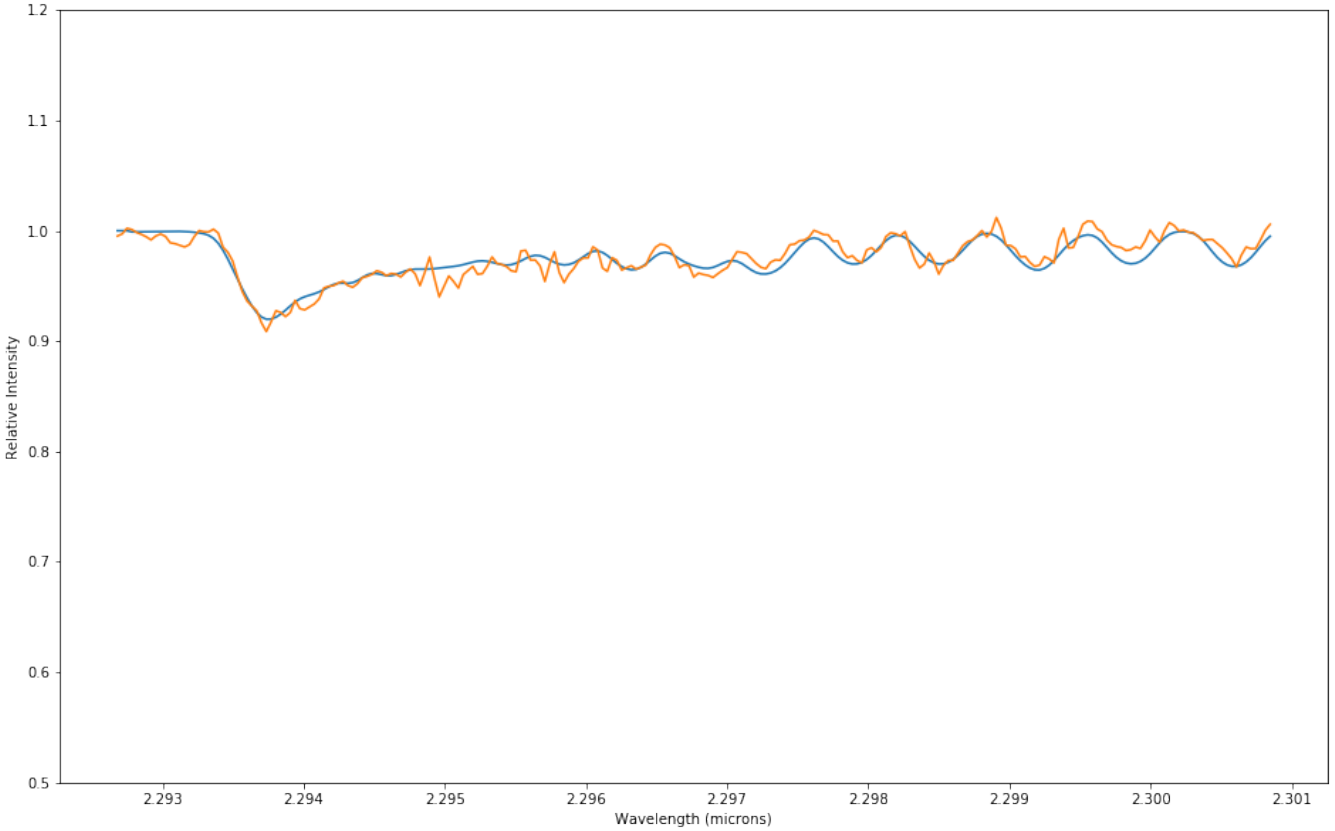

Figure 38 Synthetic overlay (blue) on top of the data (orange) for the four fit parameters returned by *emcee* to best match the NIRSPEC spectrum of object WLY 2-44 corresponding to T = 4360 ± 380 K, $vsini$ = 28.9 ± 1.6 km s^{-1}, r_k = 3.25 ± 0.39, and dx = 2.15 ± 0.24.

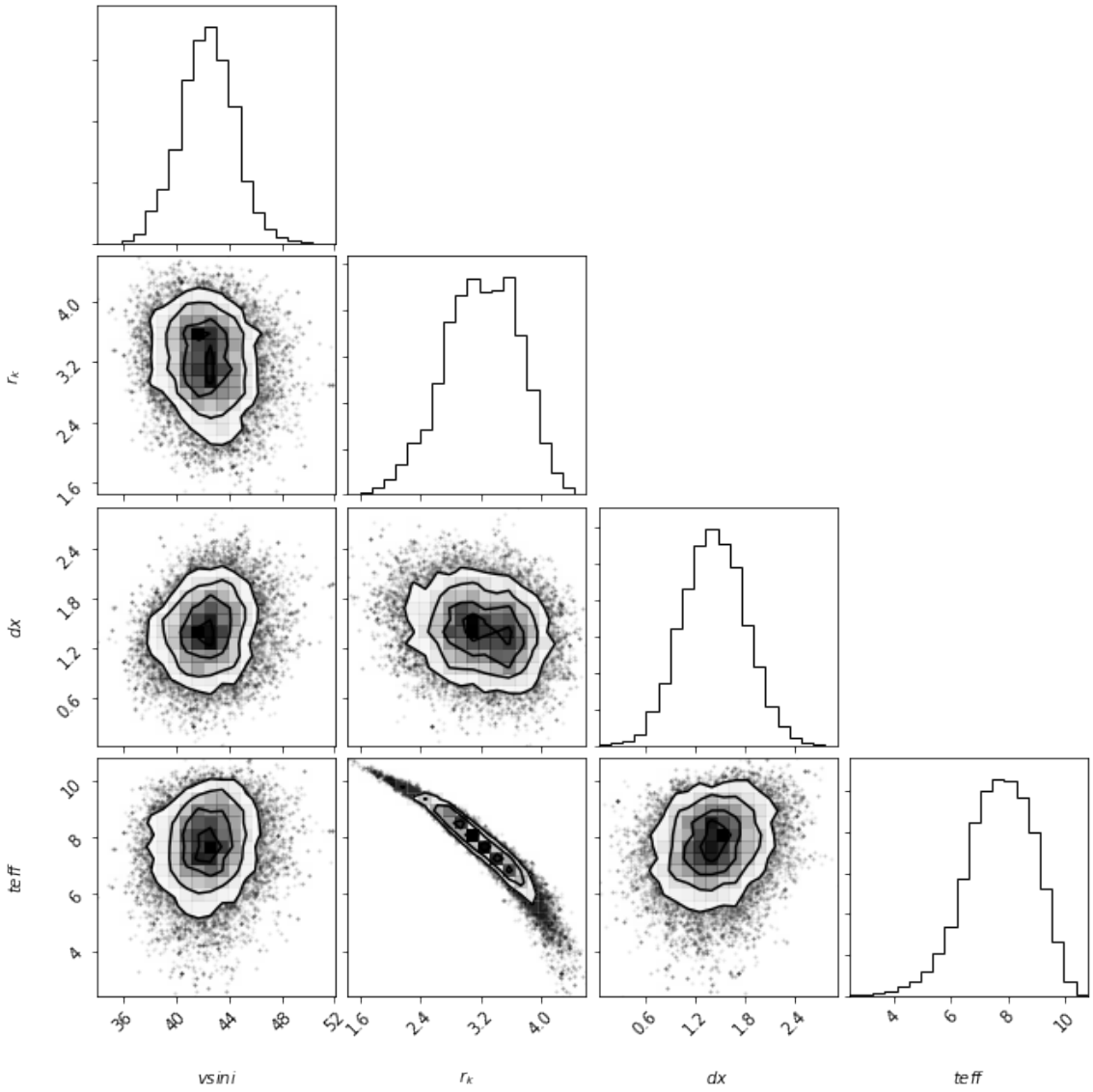

Figure 39 Relative probability distributions and correlations for the four fit parameters returned by *emcee* to best match the NIRSPEC spectrum of object WLY 2-51 corresponding to $T = 4660 \pm 230$ K, $vsini = 42.3 \pm 2.0$ km s^{-1}, $r_k = 2.32 \pm 0.49$, and $dx = 1.41 \pm 0.39$.

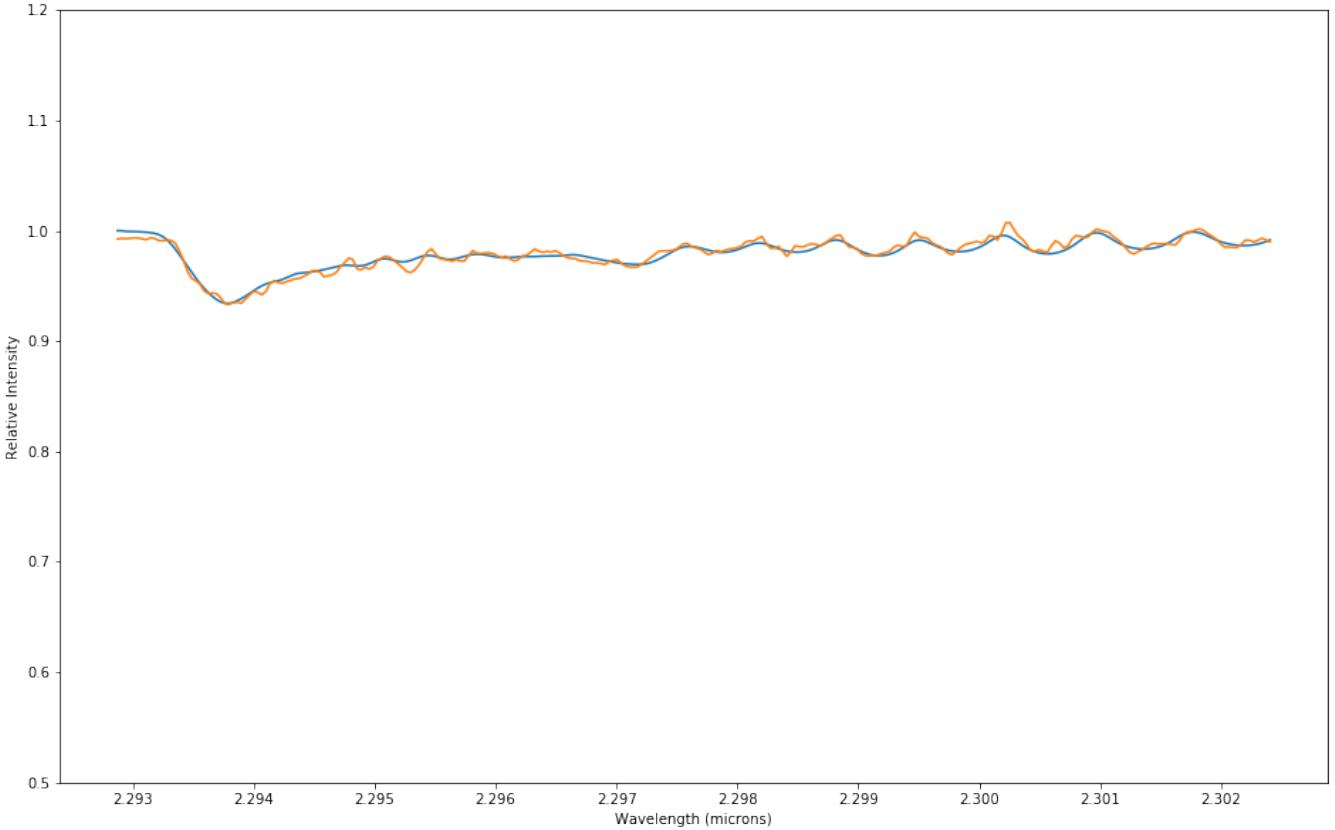

Figure 40 Synthetic overlay (blue) on top of the data (orange) for the four fit parameters returned by *emcee* to best match the NIRSPEC spectrum of object WLY 2-51 corresponding to T = 4660 ± 230 K, $vsini$ = 42.3 ± 2.0 km s^{-1}, r_k = 2.32 ± 0.49, and dx = 1.41 ± 0.39.

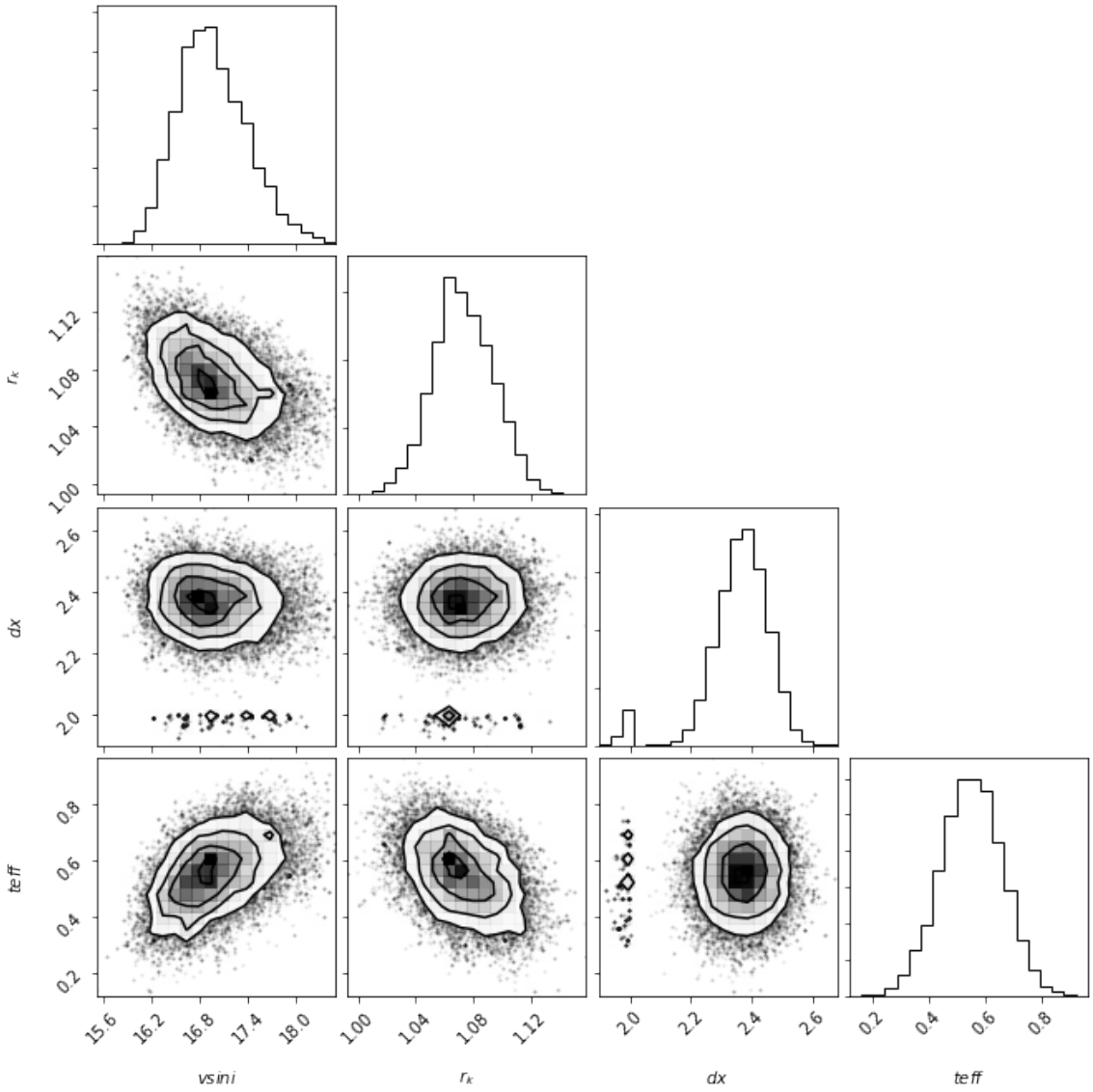

Figure 41 Relative probability distributions and correlations for the four fit parameters returned by *emcee* to best match the CSHELL spectrum of object GY 314 corresponding to T = 3220 ± 20 K, $vsini$ = 16.9 ± 0.5 km s^{-1}, r_k = 1.07 ± 0.02, and dx = 2.37 ± 0.09.

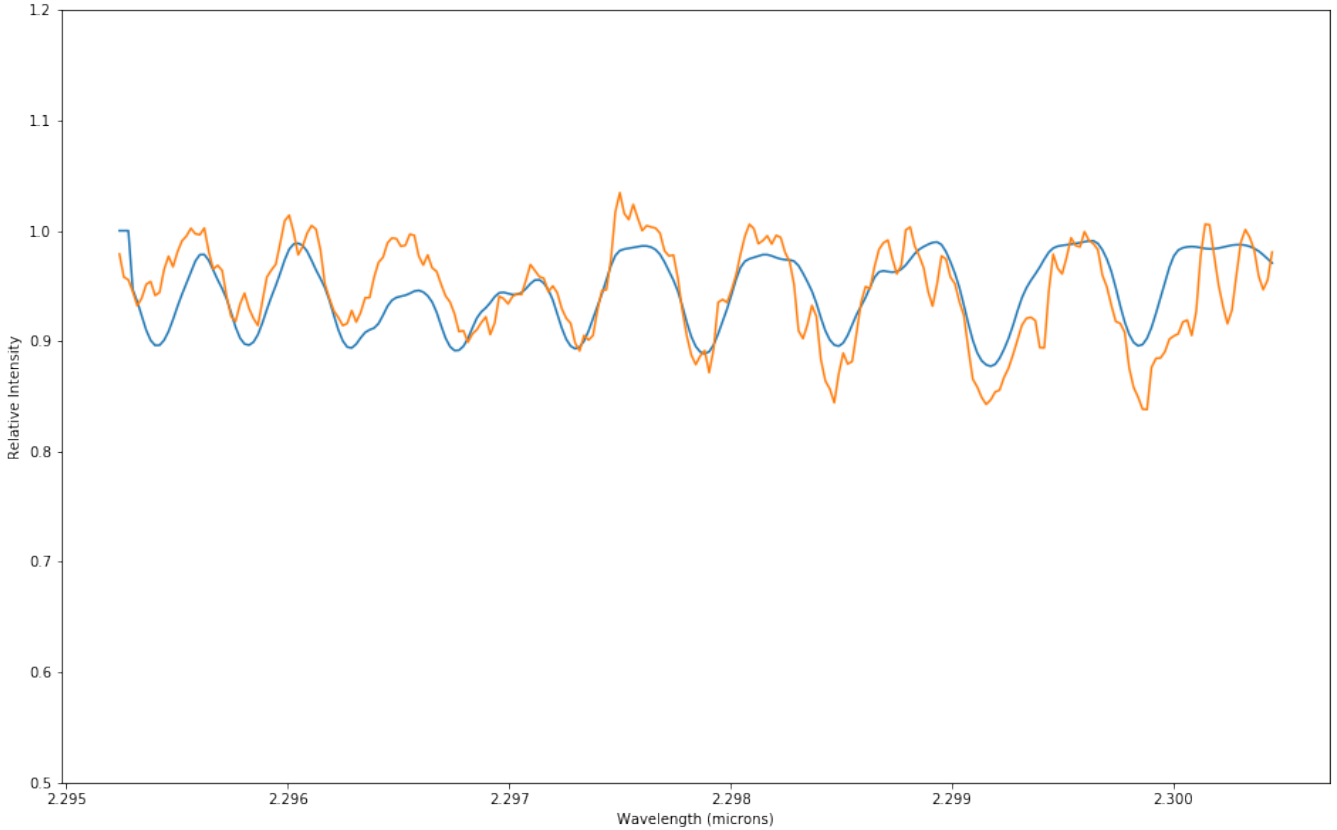

Figure 42 Synthetic overlay (blue) on top of the data (orange) for the four fit parameters returned by *emcee* to best match the CSHELL spectrum of object GY 314 corresponding to $T = 3220 \pm 20$ K, $vsini = 16.9 \pm 0.5$ km s^{-1}, $r_k = 1.07 \pm 0.02$, and $dx = 2.37 \pm 0.09$.

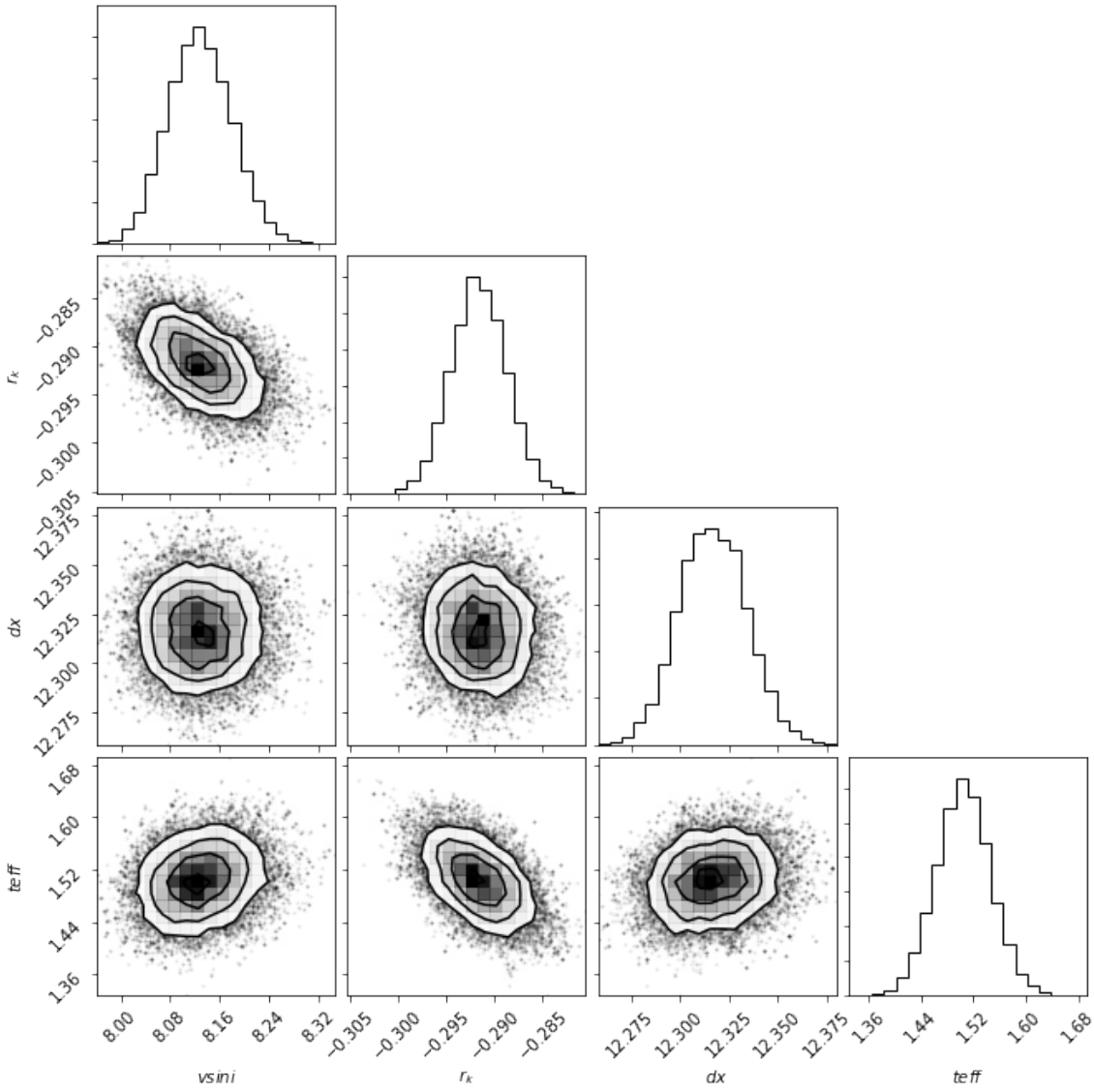

Figure 43 Relative probability distributions and correlations for the four fit parameters returned by *emcee* to best match the CSHELL spectrum of radial velocity standard HD 111631 corresponding to T = 3400 ± 20 K, $vsini$ = 8.1 ± 0. km s^{-1}, r_k = 0.00 ± 0.01, and dx = 12.32 ± 0.02.

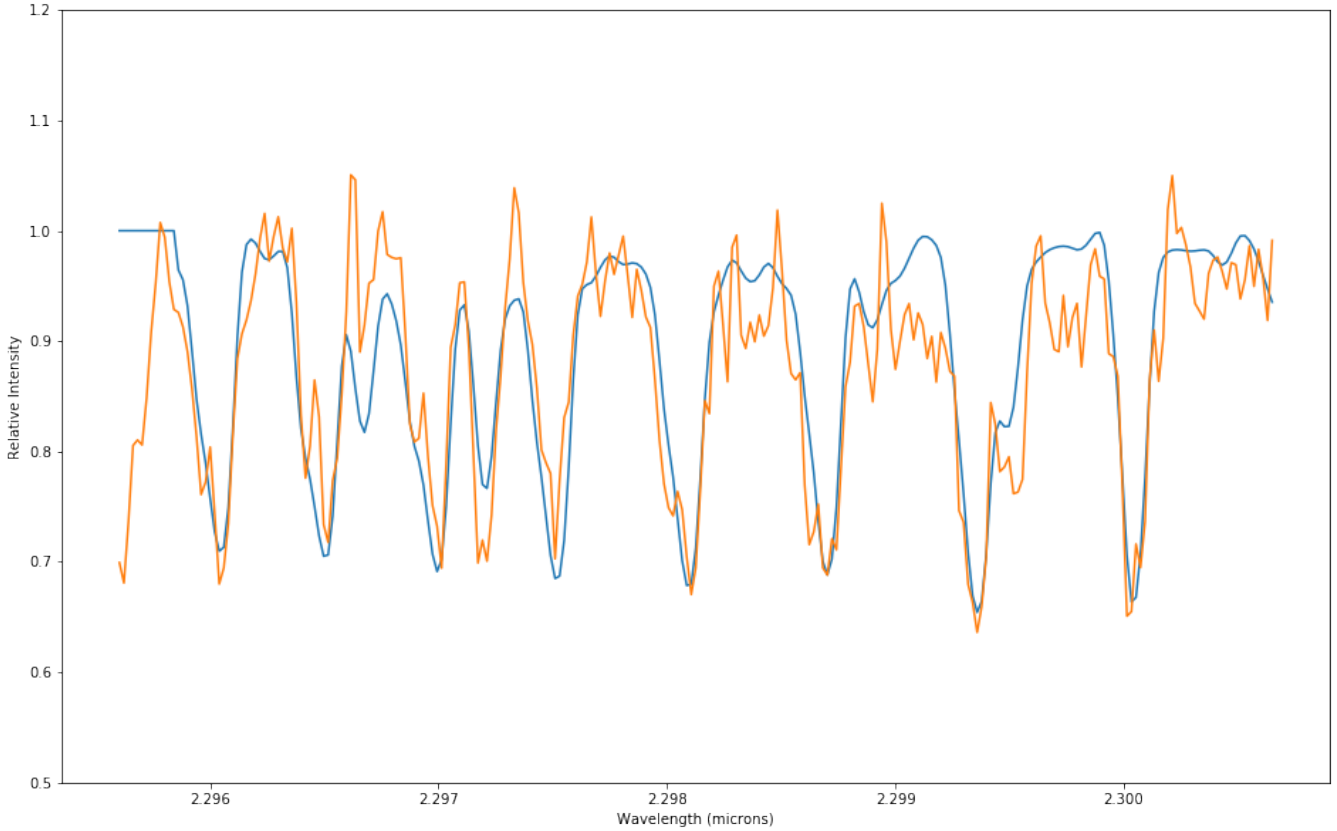

Figure 44 Synthetic overlay (blue) on top of the data (orange) for the four fit parameters returned by *emcee* to best match the CSHELL spectrum of radial velocity standard HD 111631 corresponding to $T = 3400 \pm 20$ K, $vsini = 8.1 \pm 0.1$ km s^{-1}, $r_k = 0.00 \pm 0.01$, and $dx = 12.32 \pm 0.02$.

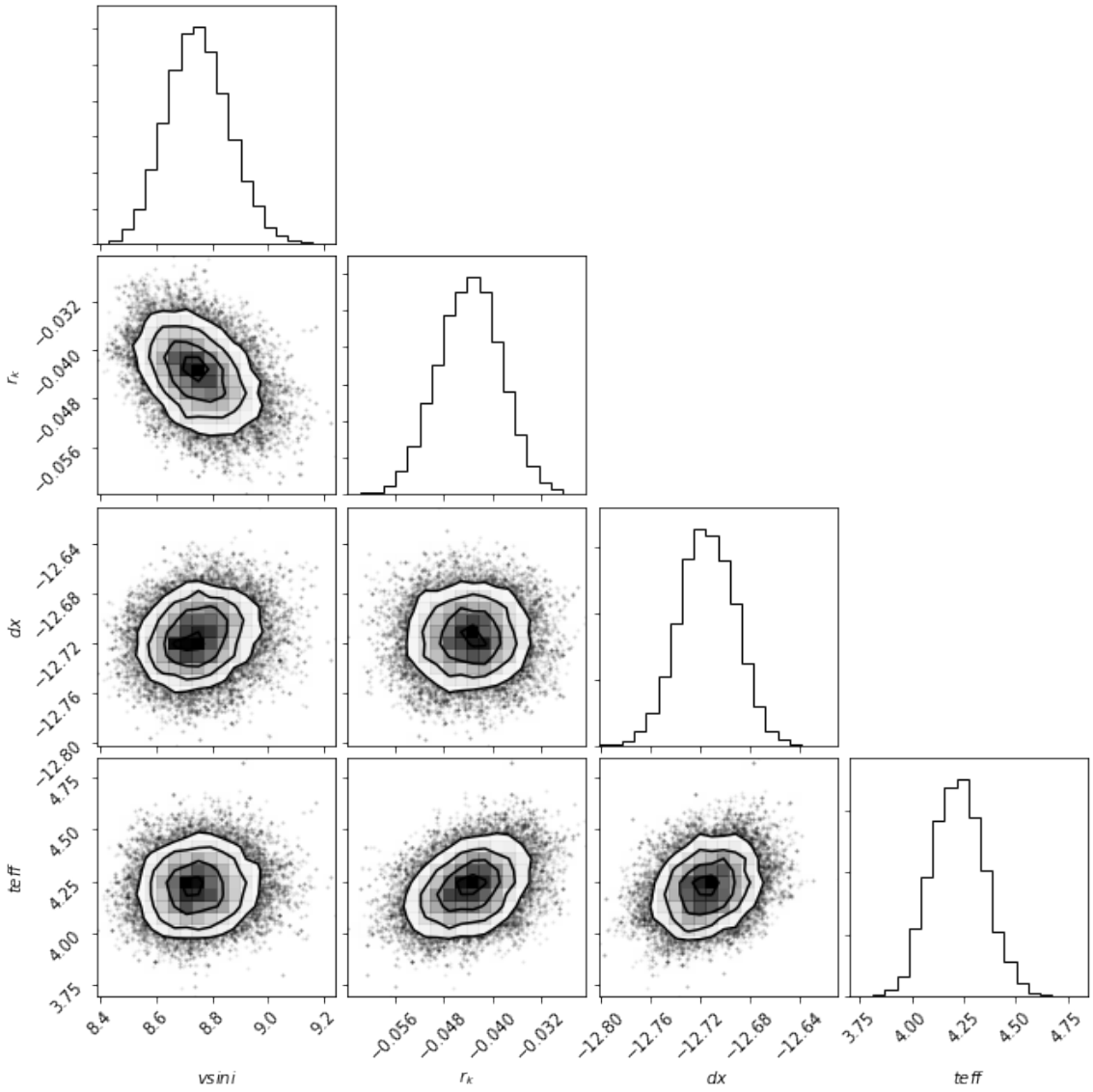

Figure 45 Relative probability distributions and correlations for the four fit parameters returned by *emcee* to best match the CSHELL spectrum of radial velocity standard HD 122120 corresponding to $T = 3940 \pm 20$ K, $vsini = 8.8 \pm 0.1$ km s^{-1}, $r_k = 0.00 \pm 0.01$, and $dx = -12.72 \pm 0.02$.

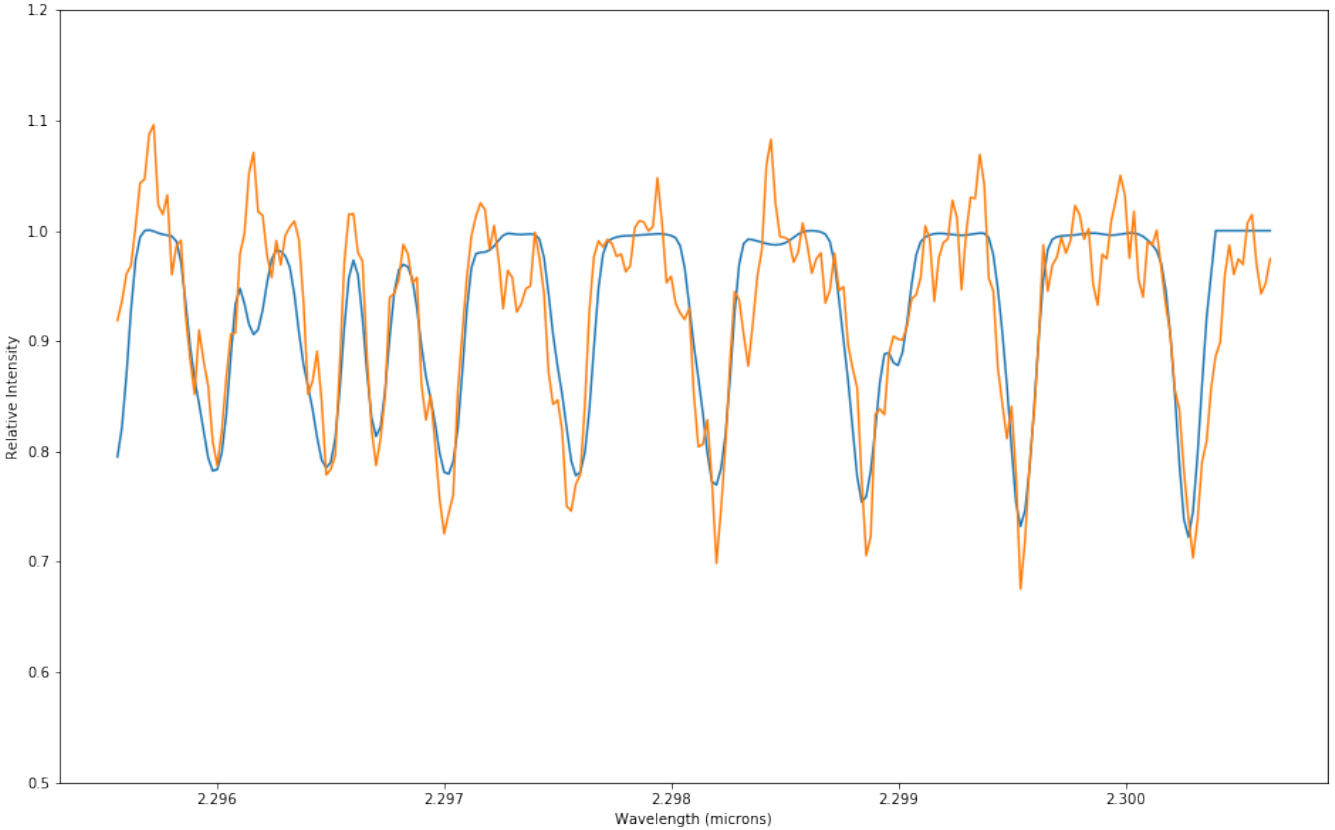

Figure 46 Synthetic overlay (blue) on top of the data (orange) for the four fit parameters returned by *emcee* to best match the CSHELL spectrum of radial velocity standard HD 122120 corresponding to $T = 3940 \pm 20$ K, $vsini = 8.8 \pm 0.1$ km s^{-1}, $r_k = 0.00 \pm 0.01$, and $dx = -12.72 \pm 0.02$.

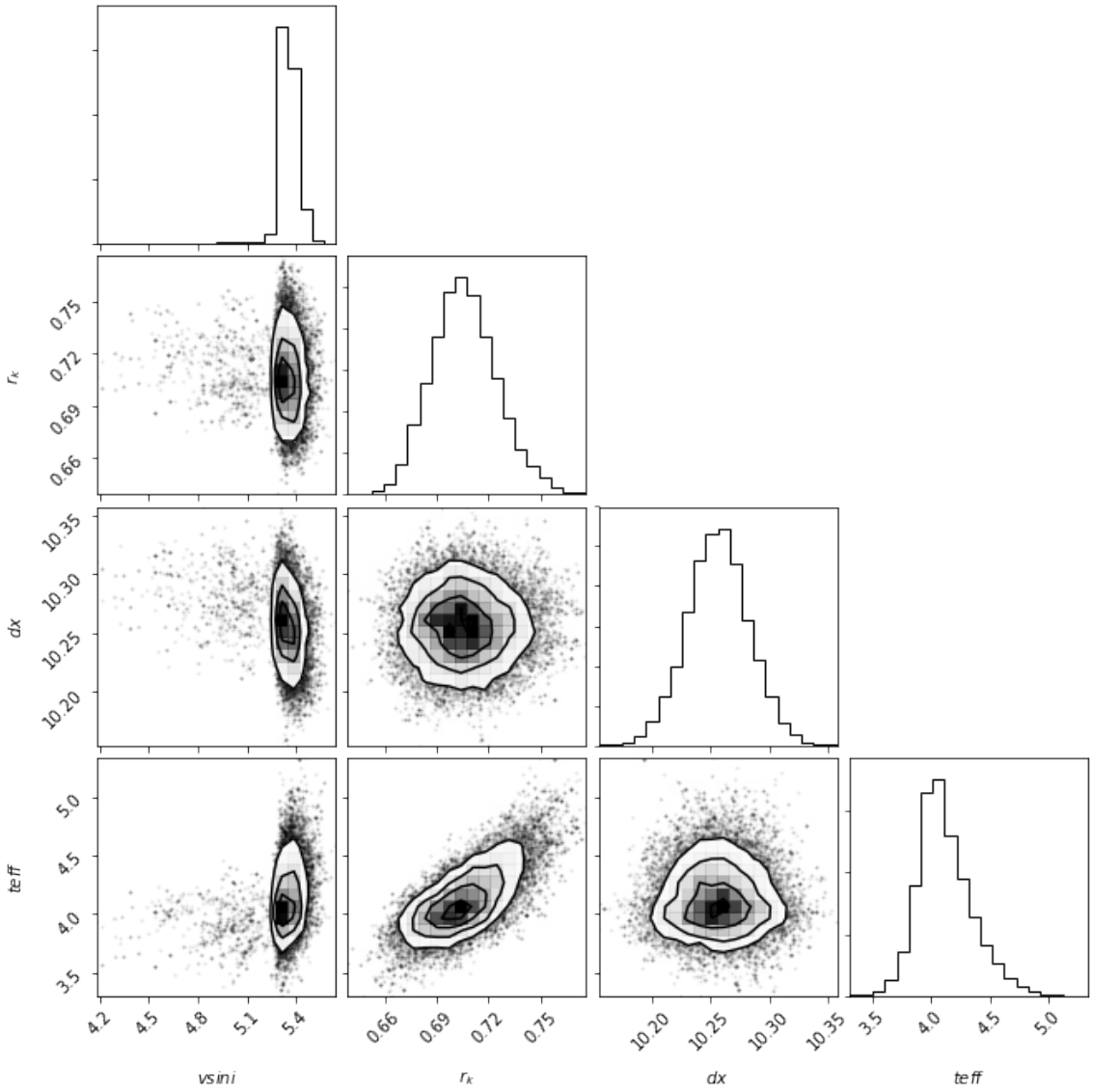

Figure 47 Relative probability distributions and correlations for the four fit parameters returned by *emcee* to best match the CSHELL spectrum of radial velocity standard HD 147776 corresponding to $T = 3920 \pm 50$ K, $vsini = 5.4 \pm 0.1$ km s^{-1}, $r_k = 0.71 \pm 0.02$, and $dx = 10.62 \pm 0.03$.

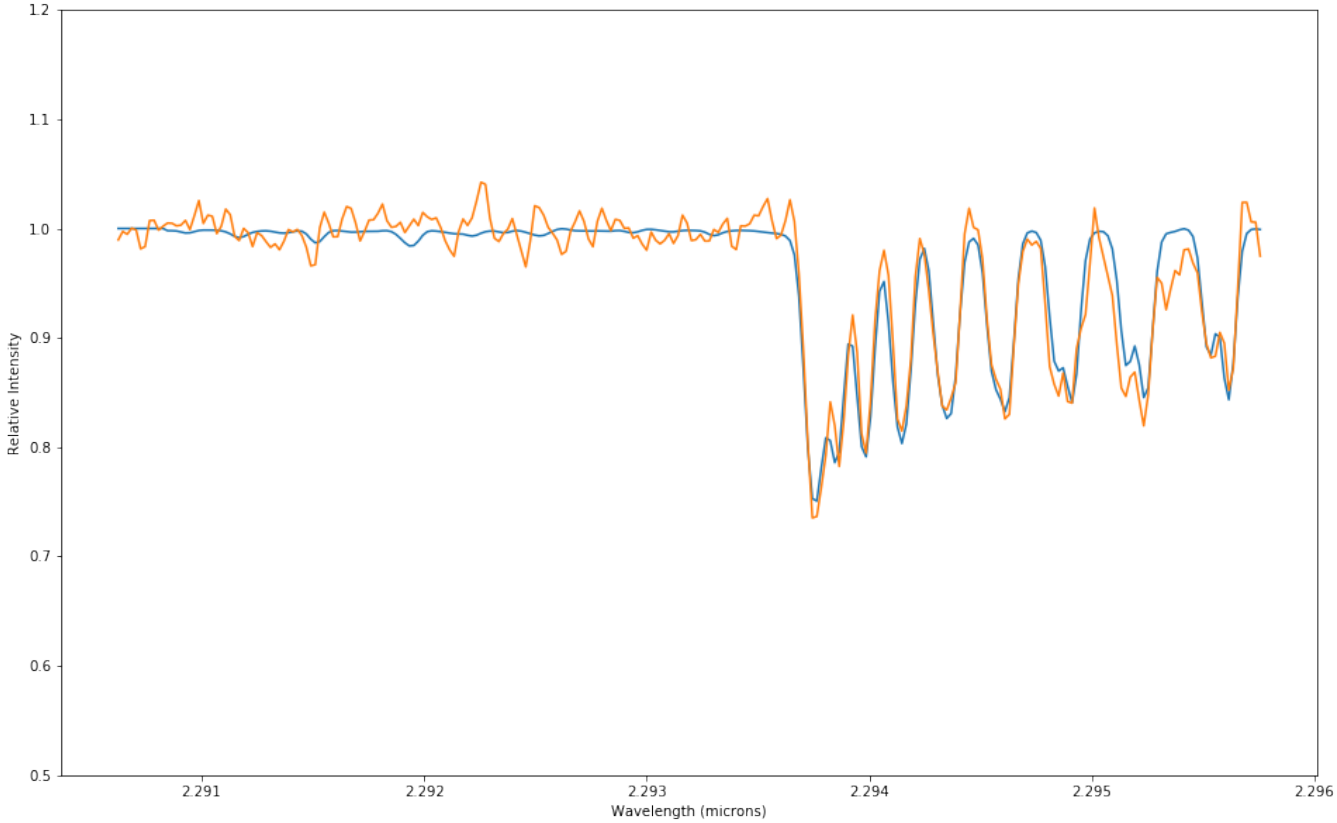

Figure 48 Synthetic overlay (blue) on top of the data (orange) for the four fit parameters returned by *emcee* to best match the CSHELL spectrum of radial velocity standard HD 147776 corresponding to $T = 3920 \pm 50$ K, $vsini = 5.4 \pm 0.1$ km s^{-1}, $r_k = 0.71 \pm 0.02$, and $dx = 10.62 \pm 0.03$.

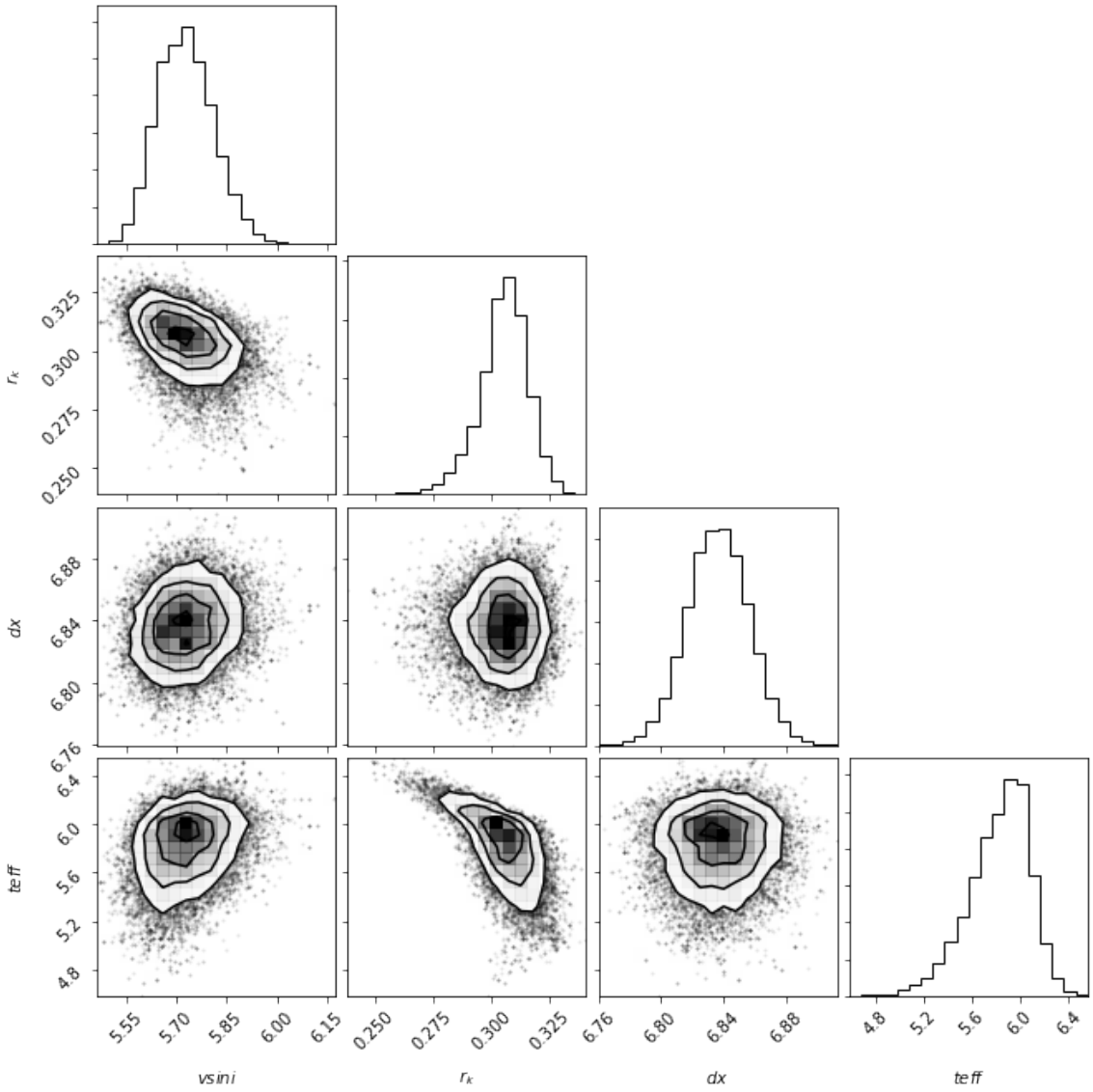

Figure 49 Relative probability distributions and correlations for the four fit parameters returned by *emcee* to best match the CSHELL spectrum of radial velocity standard HD 156026 corresponding to $T = 4280 \pm 50$ K, $vsini = 5.7 \pm 0.1$ km s^{-1}, $r_k = 0.31 \pm 0.01$, and $dx = 6.84 \pm 0.02$.

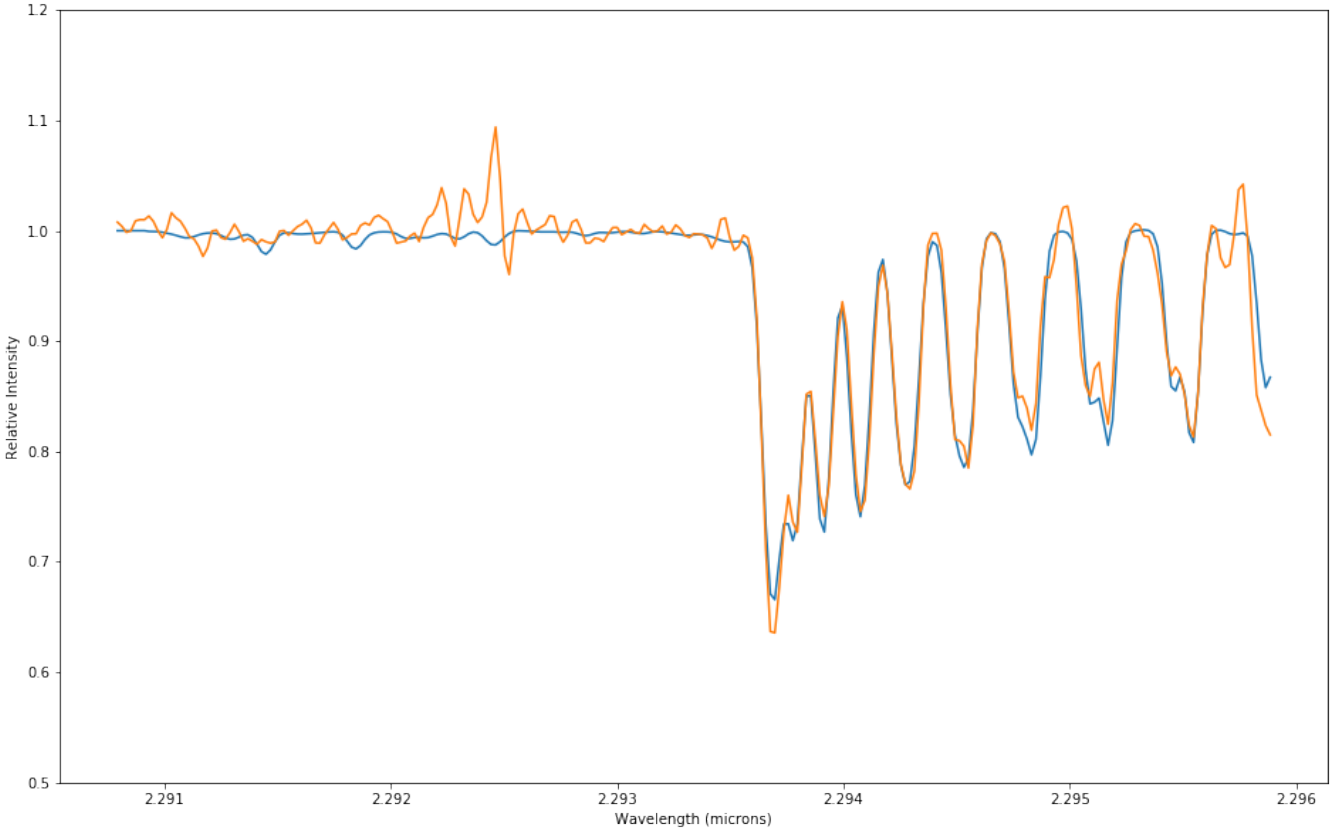

Figure 50 Synthetic overlay (blue) on top of the data (orange) for the four fit parameters returned by *emcee* to best match the CSHELL spectrum of radial velocity standard HD 156026 corresponding to $T = 4280 \pm 50$ K, $vsini = 5.7 \pm 0.1$ km s^{-1}, $r_k = 0.31 \pm 0.01$, and $dx = 6.84 \pm 0.02$.

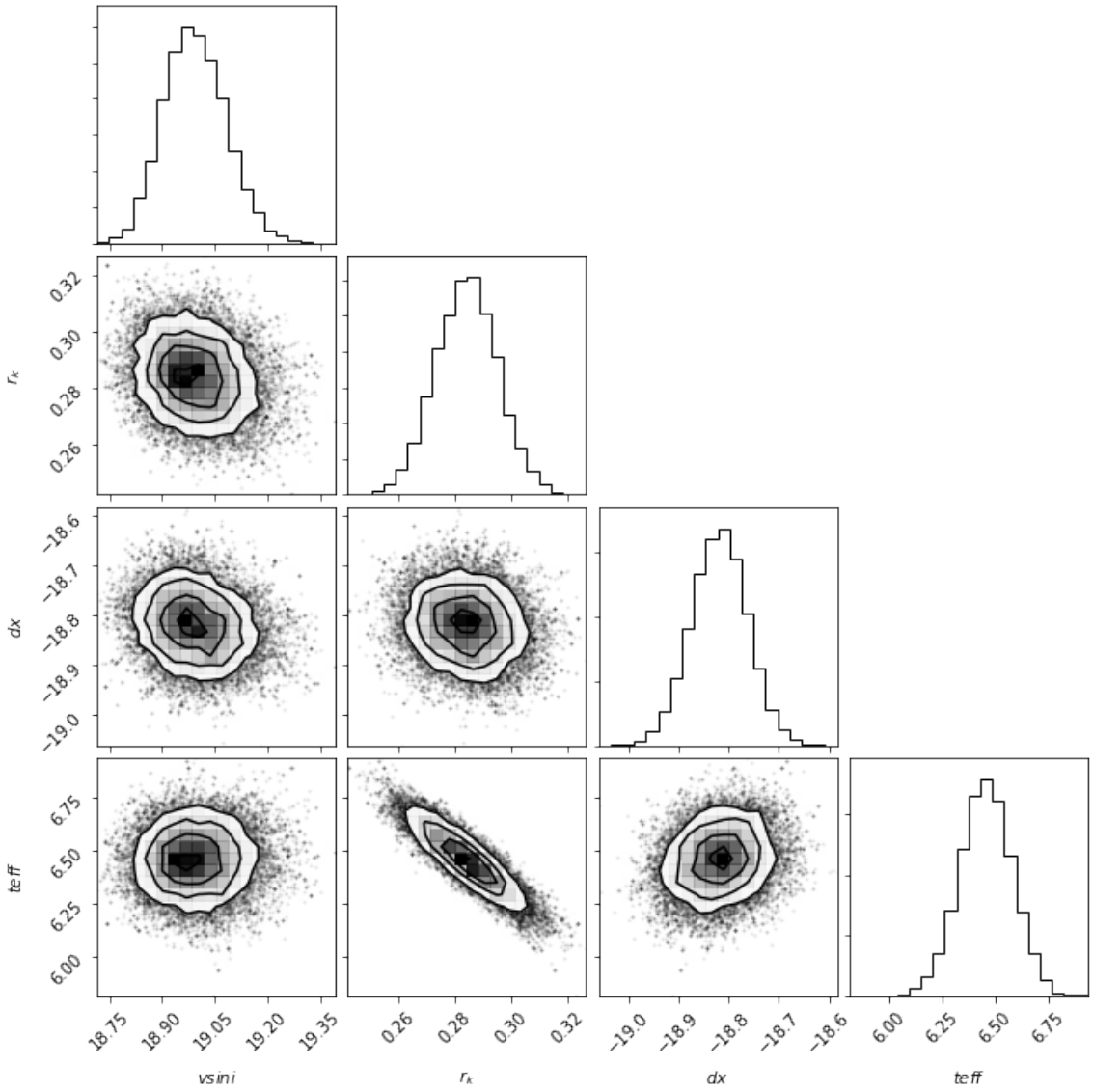

Figure 51 Relative probability distributions and correlations for the four fit parameters returned by *emcee* to best match the CRIRES spectrum of object GSS 26 corresponding to $T = 4400 \pm 20$ K, $vsini = 19.0 \pm 0.1$ km s^{-1}, $r_k = 0.28 \pm 0.01$, and $dx = -18.82 \pm 0.06$.

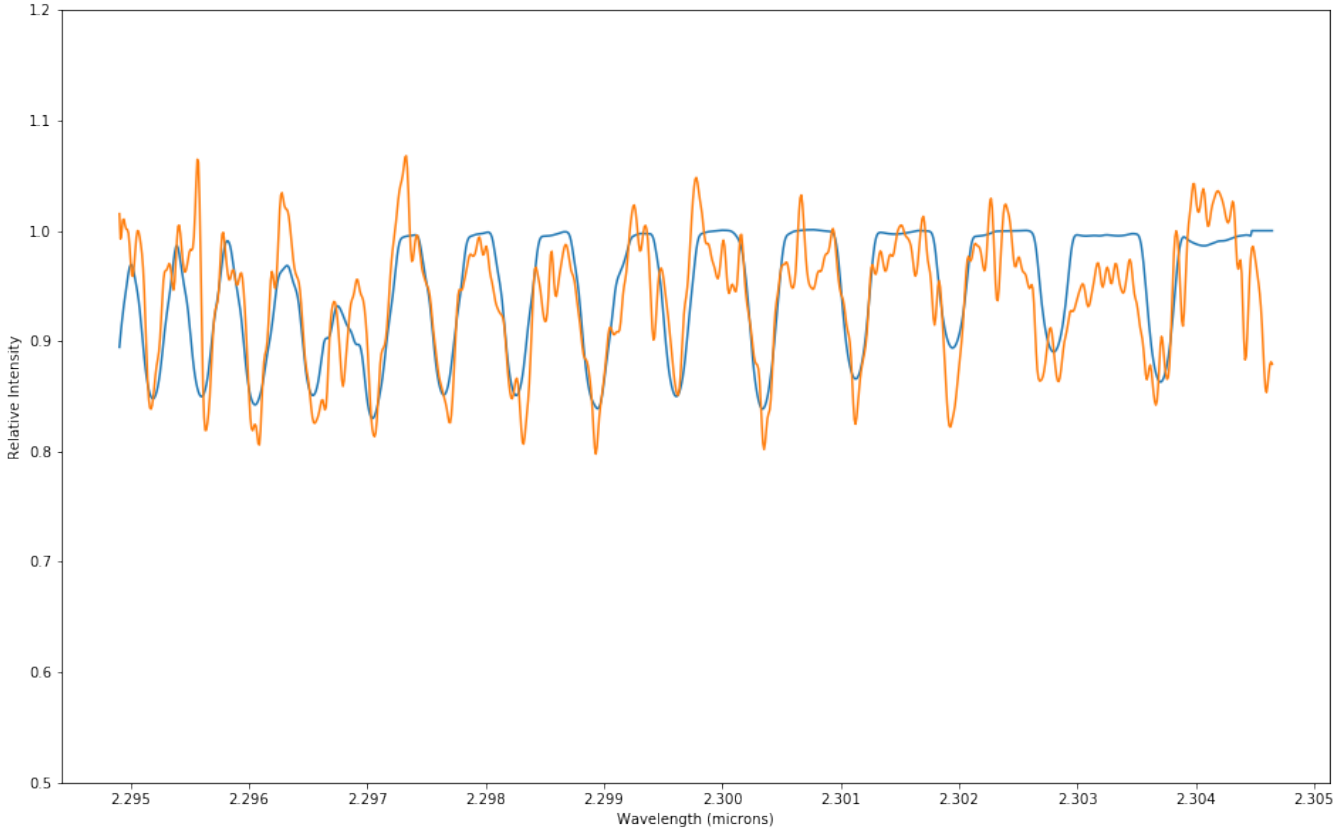

Figure 52 Synthetic overlay (blue) on top of the data (orange) for the four fit parameters returned by *emcee* to best match the CRIRES spectrum of object GSS 26 corresponding to $T = 4400 \pm 20$ K, $vsini = 19.0 \pm 0.1$ km s^{-1}, $r_k = 0.28 \pm 0.01$, and $dx = -18.82 \pm 0.06$.

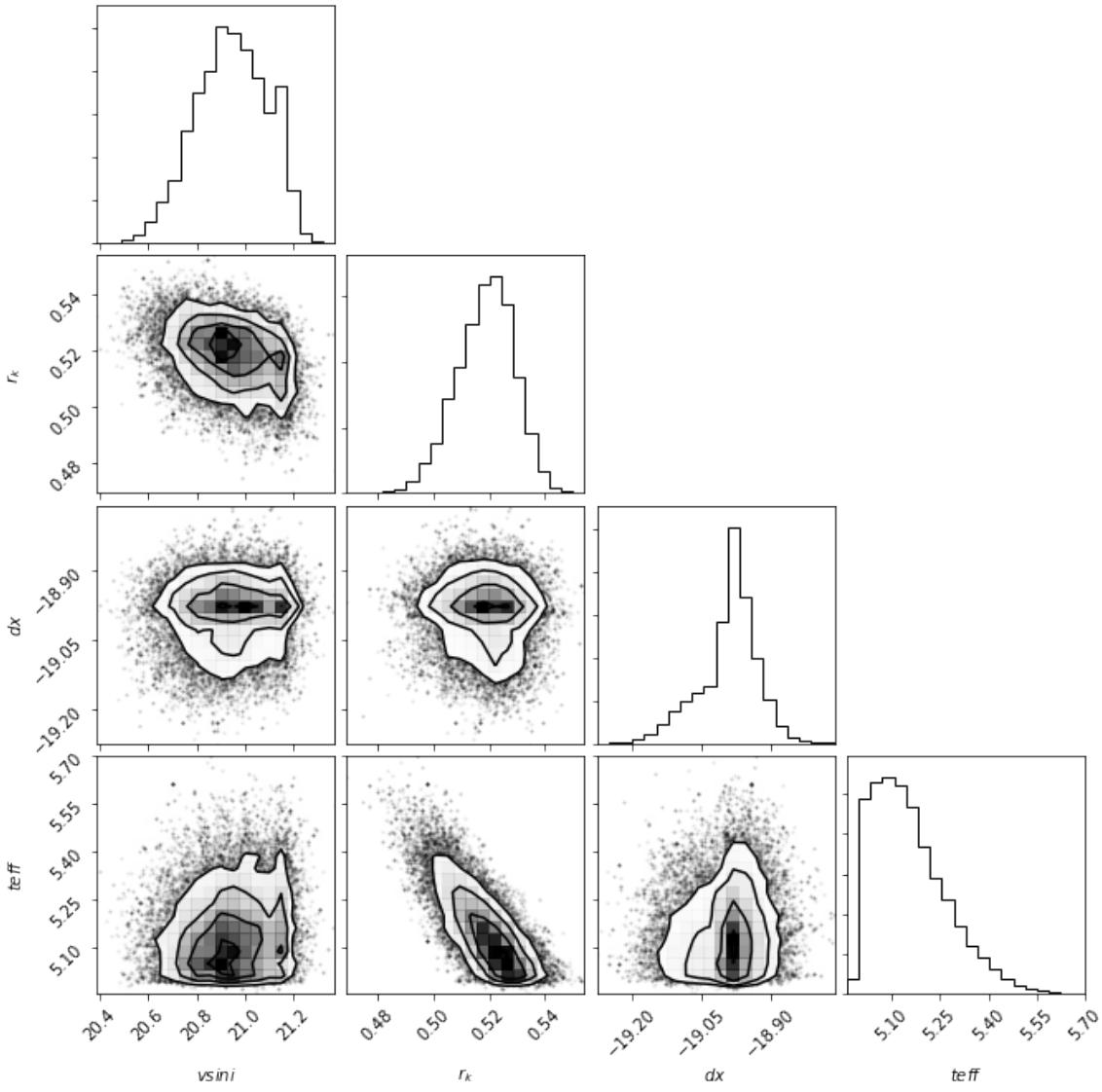

Figure 53 Relative probability distributions and correlations for the four fit parameters returned by *emcee* to best match the CRIRES spectrum of object GY 23 corresponding to $T = 4120 \pm 20$ K, $vsini = 20.9 \pm 0.2$ km s^{-1}, $r_k = 0.52 \pm 0.01$, and $dx = -18.98 \pm 0.06$.

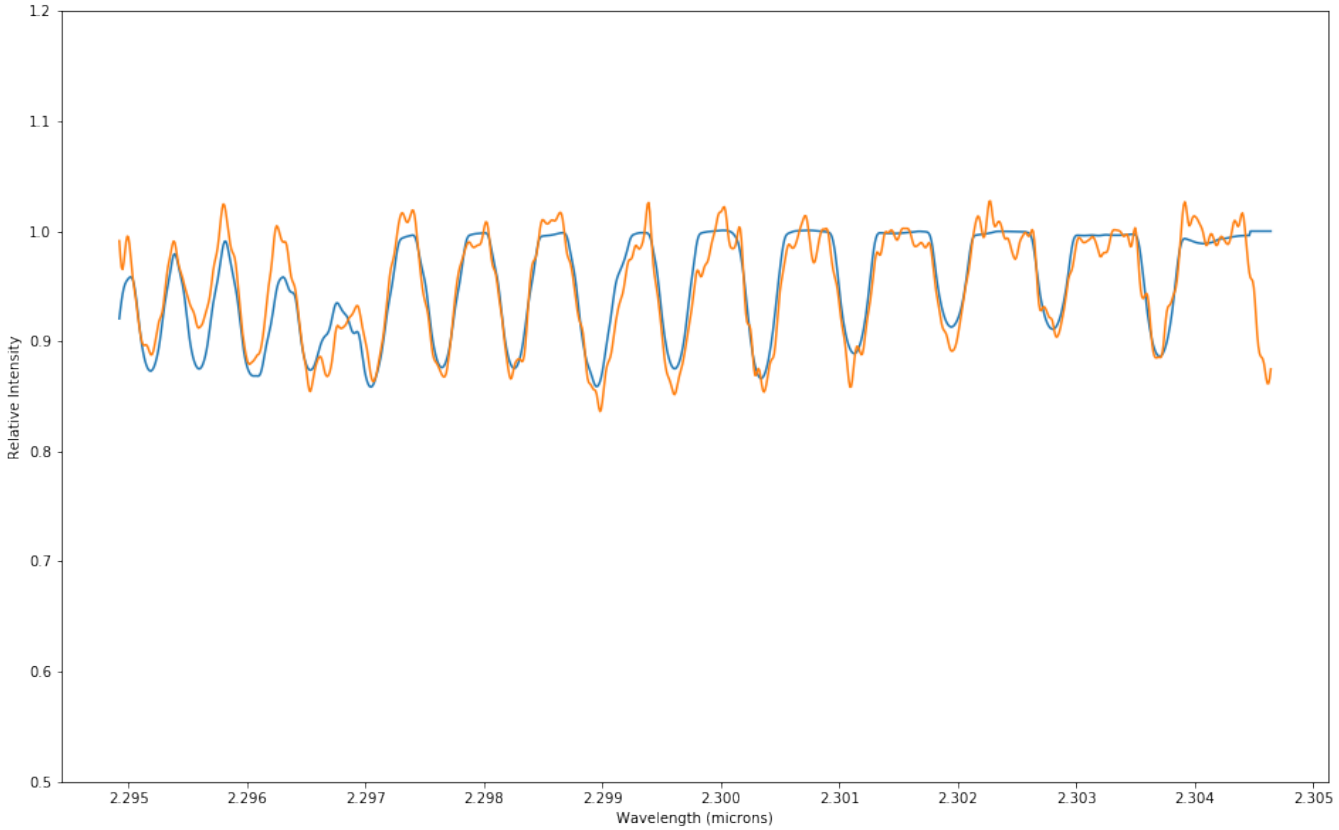

Figure 54 Synthetic overlay (blue) on top of the data (orange) for the four fit parameters returned by *emcee* to best match the CRIRES spectrum of object GY 23 corresponding to $T = 4120 \pm 20$ K, $vsini = 20.9 \pm 0.2$ km s^{-1}, $r_k = 0.52 \pm 0.01$, and $dx = -18.98 \pm 0.06$.

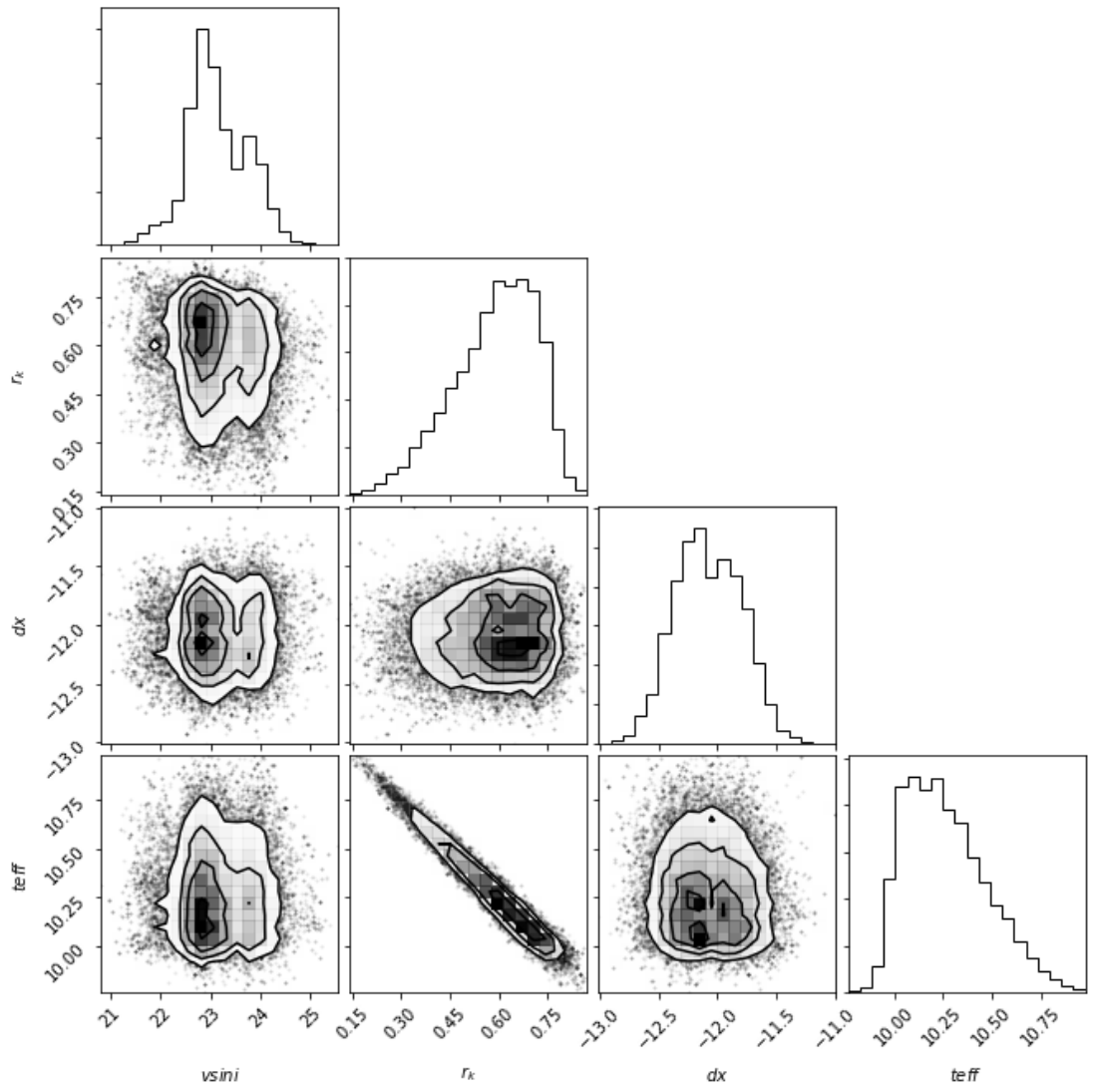

Figure 55 Relative probability distributions and correlations for the four fit parameters returned by *emcee* to best match the CRIRES spectrum of object GY 224 corresponding to $T = 5240 \pm 50$ K, $vsini = 23.0 \pm 0.8$ km s^{-1}, $r_k = 0.6 \pm 0.13$, and $dx = -12.10 \pm 0.29$.

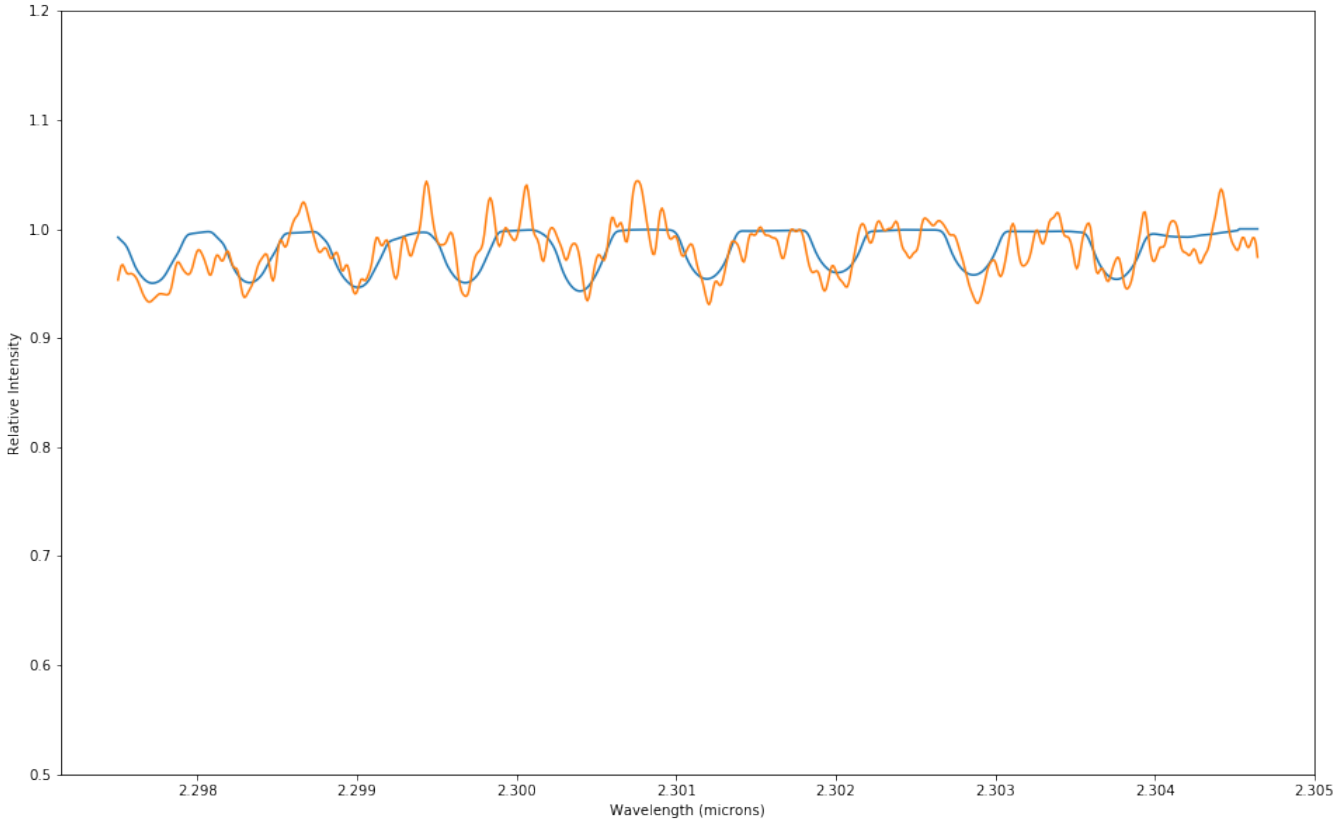

Figure 56 Synthetic overlay (blue) on top of the data (orange) for the four fit parameters returned by *emcee* to best match the CRIRES spectrum of object GY 224 corresponding to $T = 5240 \pm 50$ K, $vsini = 23.0 \pm 0.8$ km s^{-1}, $r_k = 0.6 \pm 0.13$, and $dx = -12.10 \pm 0.29$.

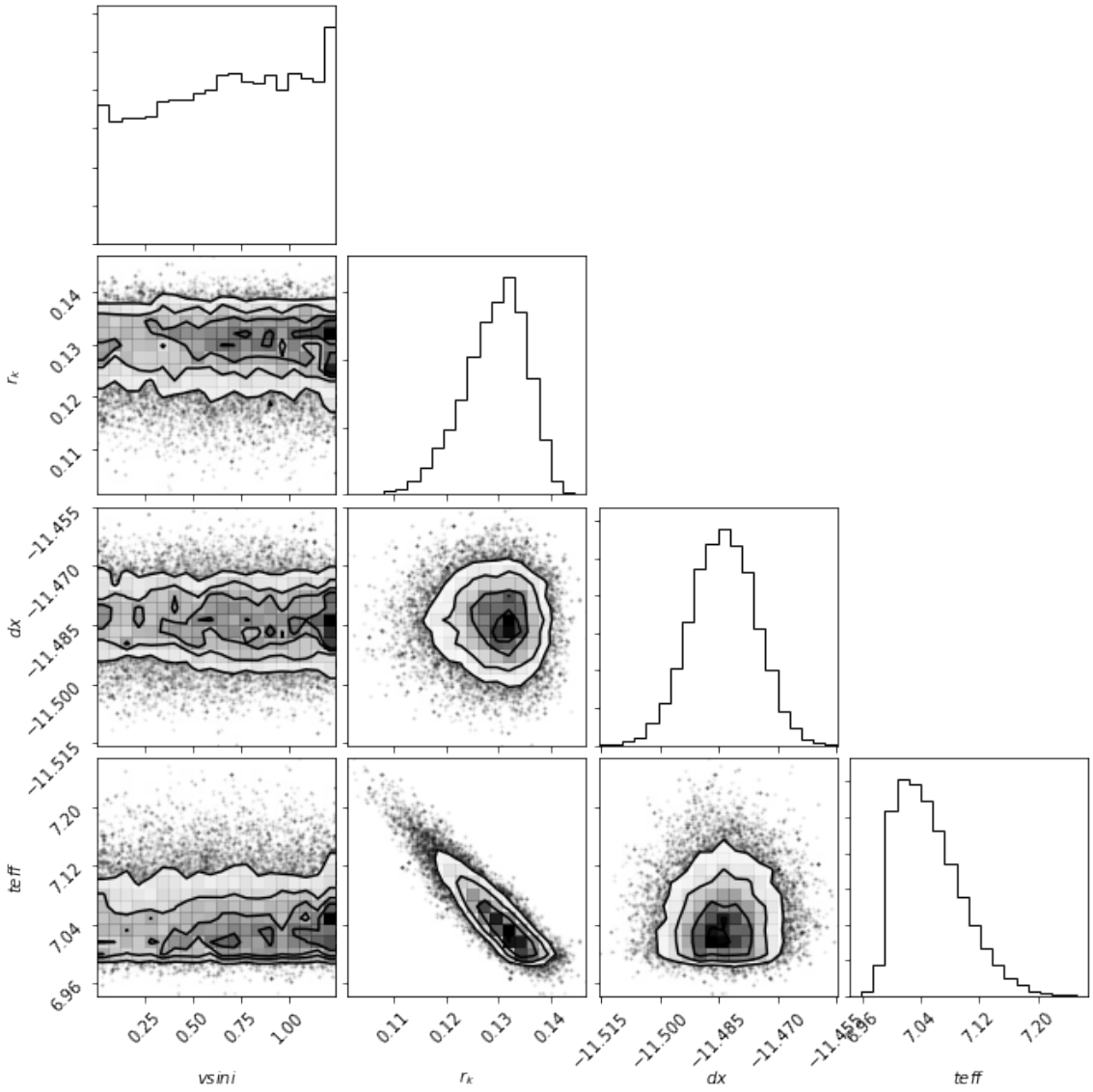

Figure 57 Relative probability distributions and correlations for the four fit parameters returned by *emcee* to best match the CRIRES spectrum of radial velocity standard HD 129642 corresponding to $T = 4600 \pm 20$ K, $vsini = 0.7 \pm 0.3$ km s^{-1}, $r_k = 0.13 \pm 0.01$, and $dx = -11.48 \pm 0.01$.

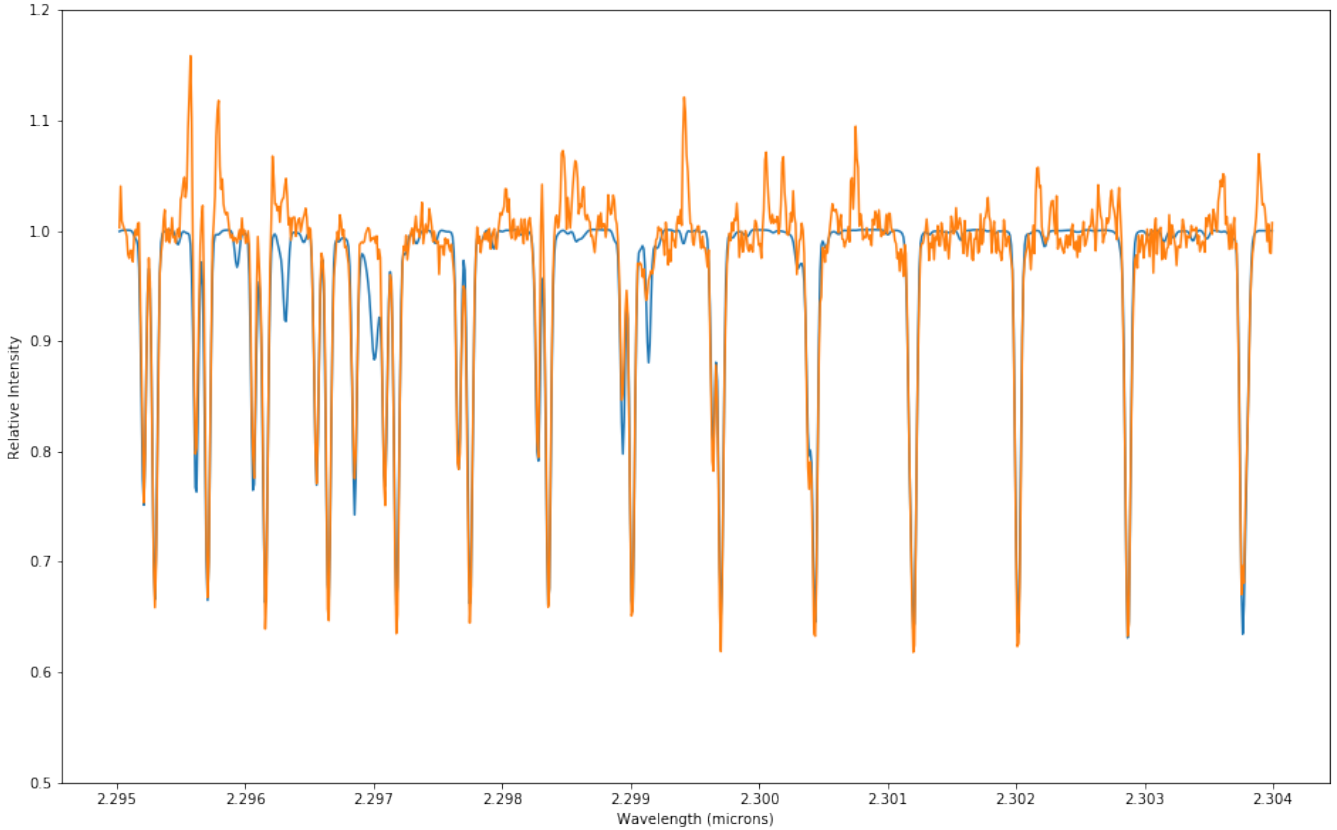

Figure 58 Synthetic overlay (blue) on top of the data (orange) for the four fit parameters returned by *emcee* to best match the CRIRES spectrum of radial velocity standard HD 129642 corresponding to $T = 4600 \pm 20$ K, $vsini = 0.7 \pm 0.3$ km s^{-1}, $r_k = 0.13 \pm 0.01$, and $dx = -11.48 \pm 0.01$.

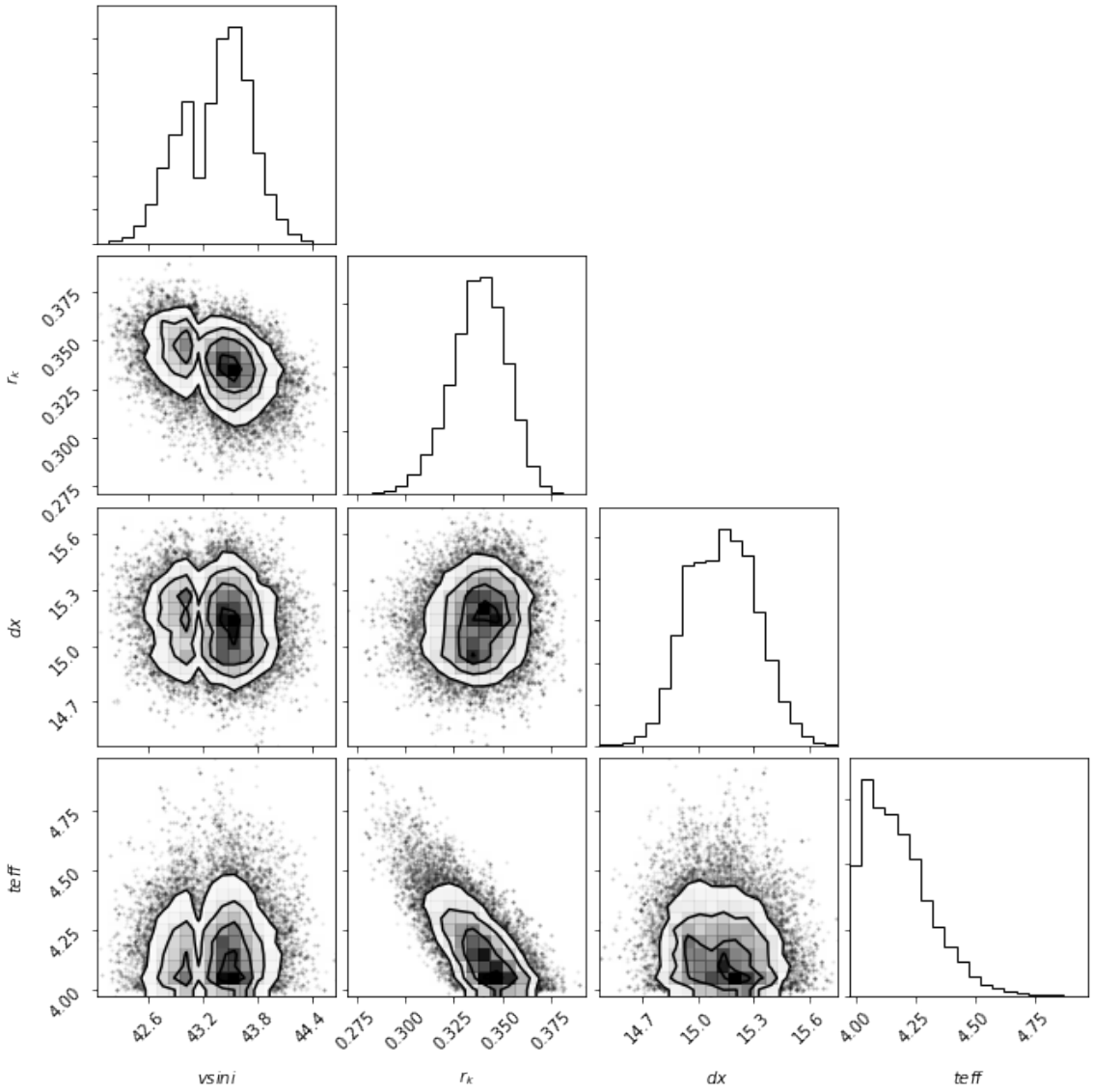

Figure 59 Relative probability distributions and correlations for the four fit parameters returned by *emcee* to best match the CRIRES spectrum of object VSSG 17 corresponding to $T = 4040 \pm 40$ K, $vsini = 43.4 \pm 0.5$ km s^{-1}, $r_k = 0.34 \pm 0.01$, and $dx = 15.13 \pm 0.20$.

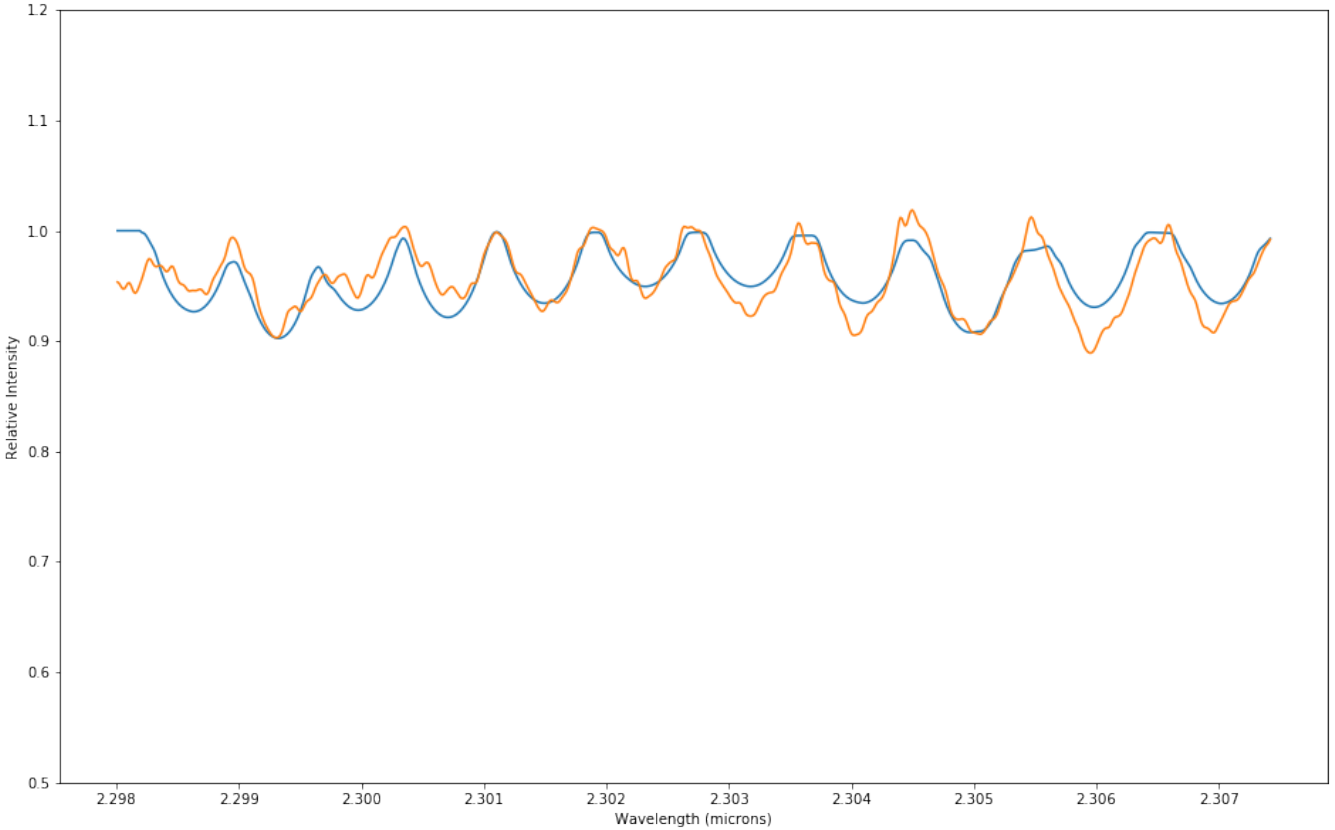

Figure 60 Synthetic overlay (blue) on top of the data (orange) for the four fit parameters returned by *emcee* to best match the CRIRES spectrum of object VSSG 17 corresponding to $T = 4040 \pm 40$ K, $vsini = 43.4 \pm 0.5$ km s^{-1}, $r_k = 0.34 \pm 0.01$, and $dx = 15.13 \pm 0.20$.

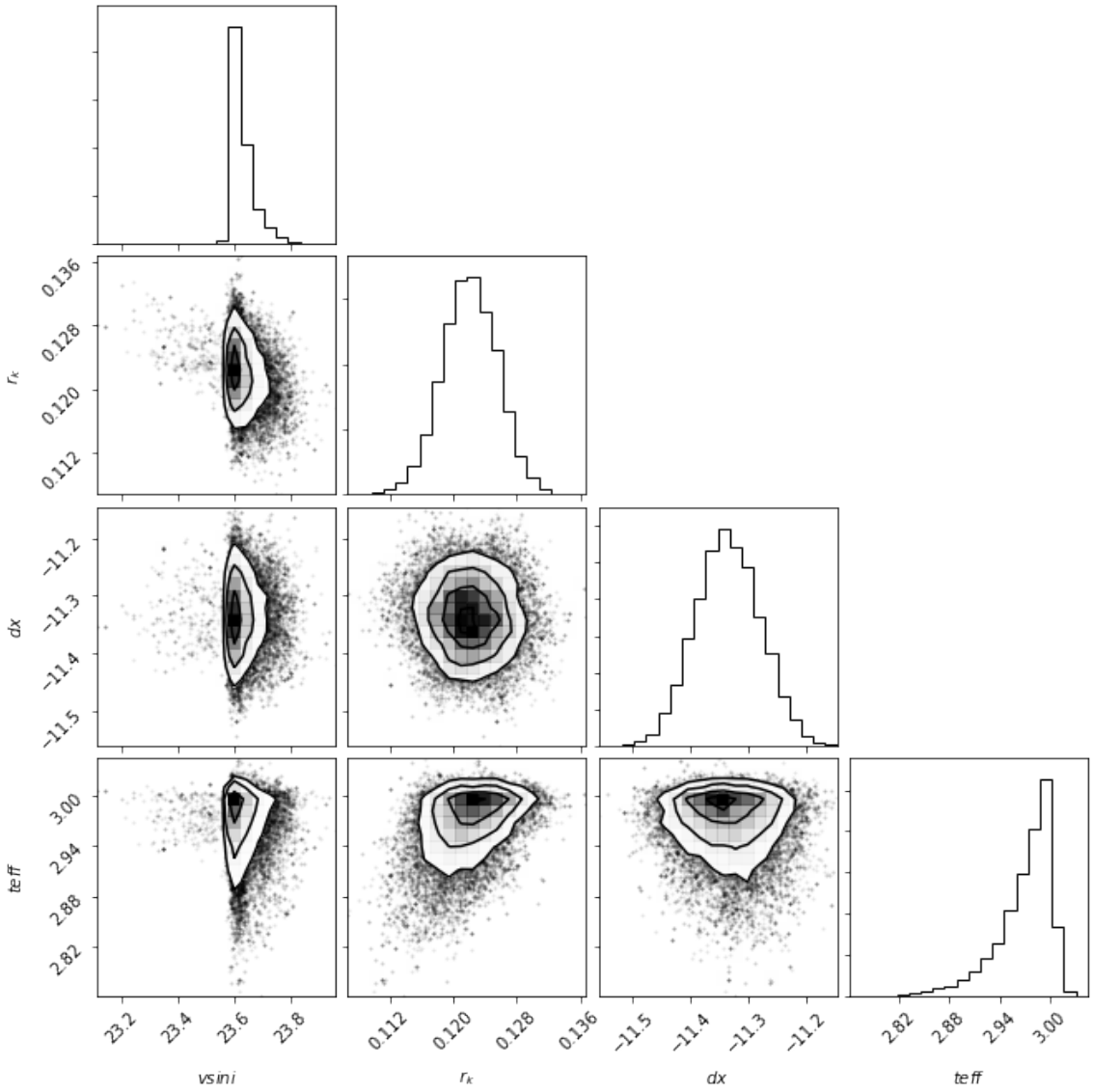

Figure 61 Relative probability distributions and correlations for the four fit parameters returned by *emcee* to best match the CRIRES spectrum of object VSSG 18 from 2008 corresponding to $T = 3800 \pm 20$ K, $vsini = 23.61 \pm 0.05$ km s^{-1}, $r_k = 0.12 \pm 0.01$, and $dx = -11.34 \pm 0.06$.

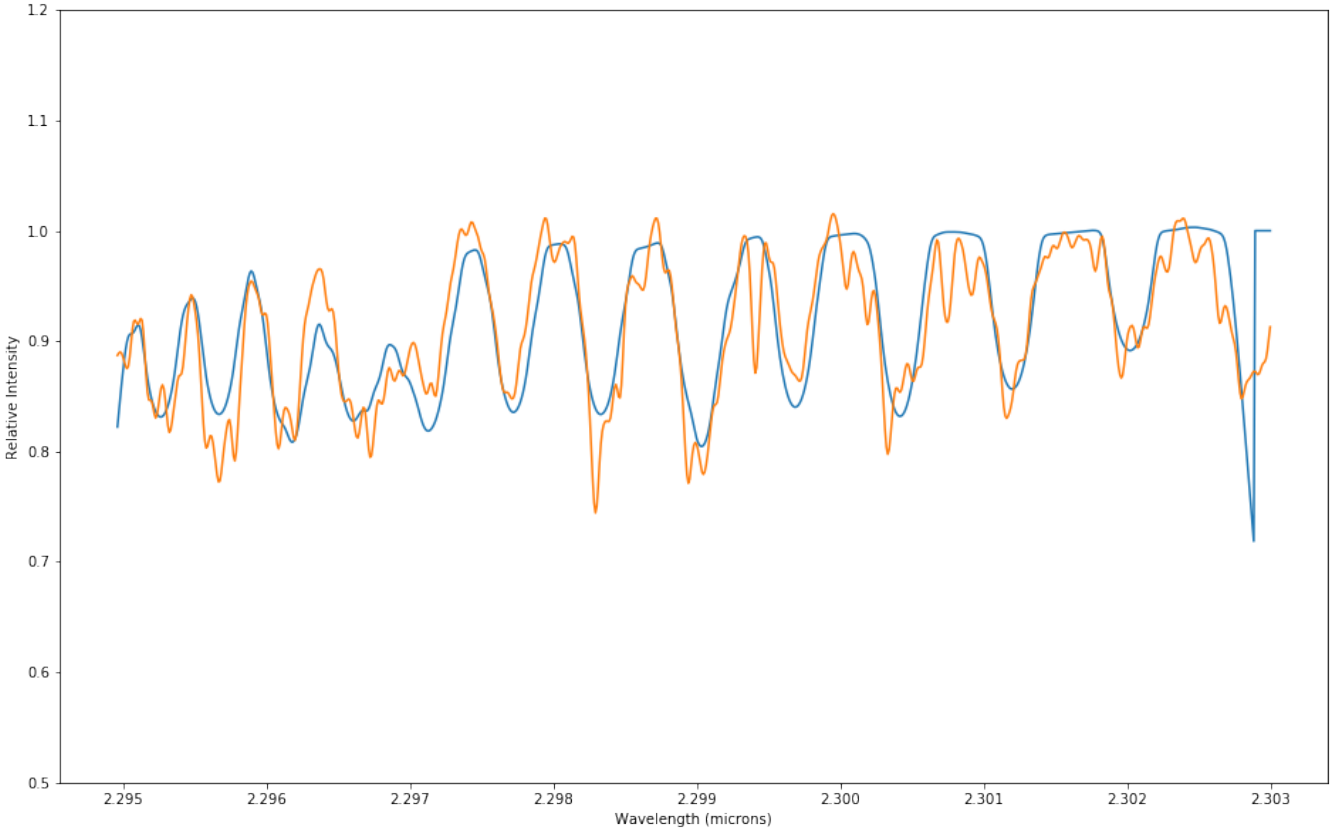

Figure 62 Synthetic overlay (blue) on top of the data (orange) for the four fit parameters returned by *emcee* to best match the CRIRES spectrum of object VSSG 18 from 2008 corresponding to $T = 3800 \pm 20$ K, $vsini = 23.61 \pm 0.05$ km s^{-1}, $r_k = 0.12 \pm 0.01$, and $dx = -11.34 \pm 0.06$.

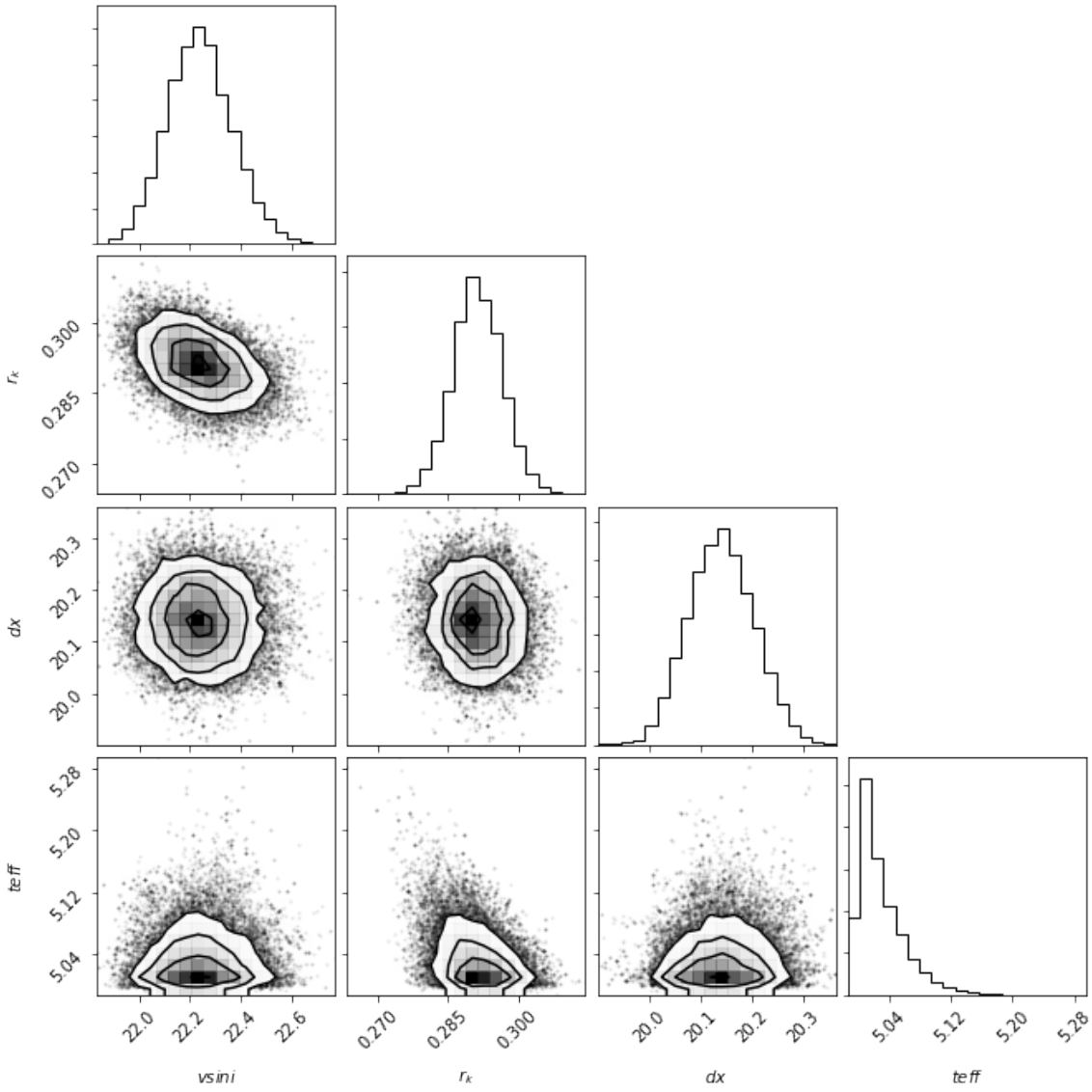

Figure 63 Relative probability distributions and correlations for the four fit parameters returned by *emcee* to best match the CRIRES spectrum of object VSSG 18 from 2012 corresponding to $T = 4100 \pm 20$ K, $vsini = 22.2 \pm 0.1$ km s^{-1}, $r_k = 0.29 \pm 0.01$, and $dx = 20.40 \pm 0.06$.

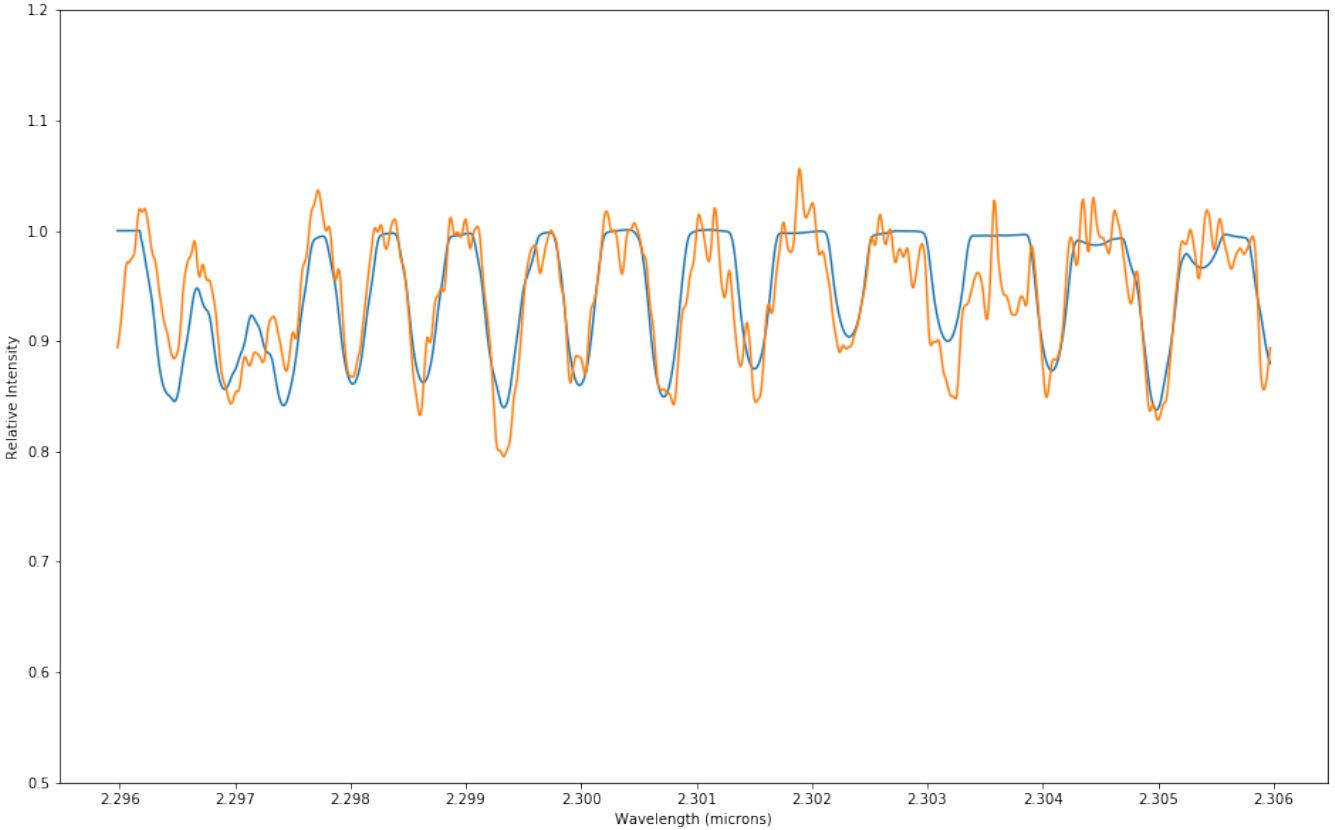

Figure 64 Synthetic overlay (blue) on top of the data (orange) for the four fit parameters returned by *emcee* to best match the CRIRES spectrum of object VSSG 18 from 2012 corresponding to $T = 4100 \pm 20$ K, $vsini = 22.2 \pm 0.1$ km s^{-1}, $r_k = 0.29 \pm 0.01$, and $dx = 20.40 \pm 0.06$.

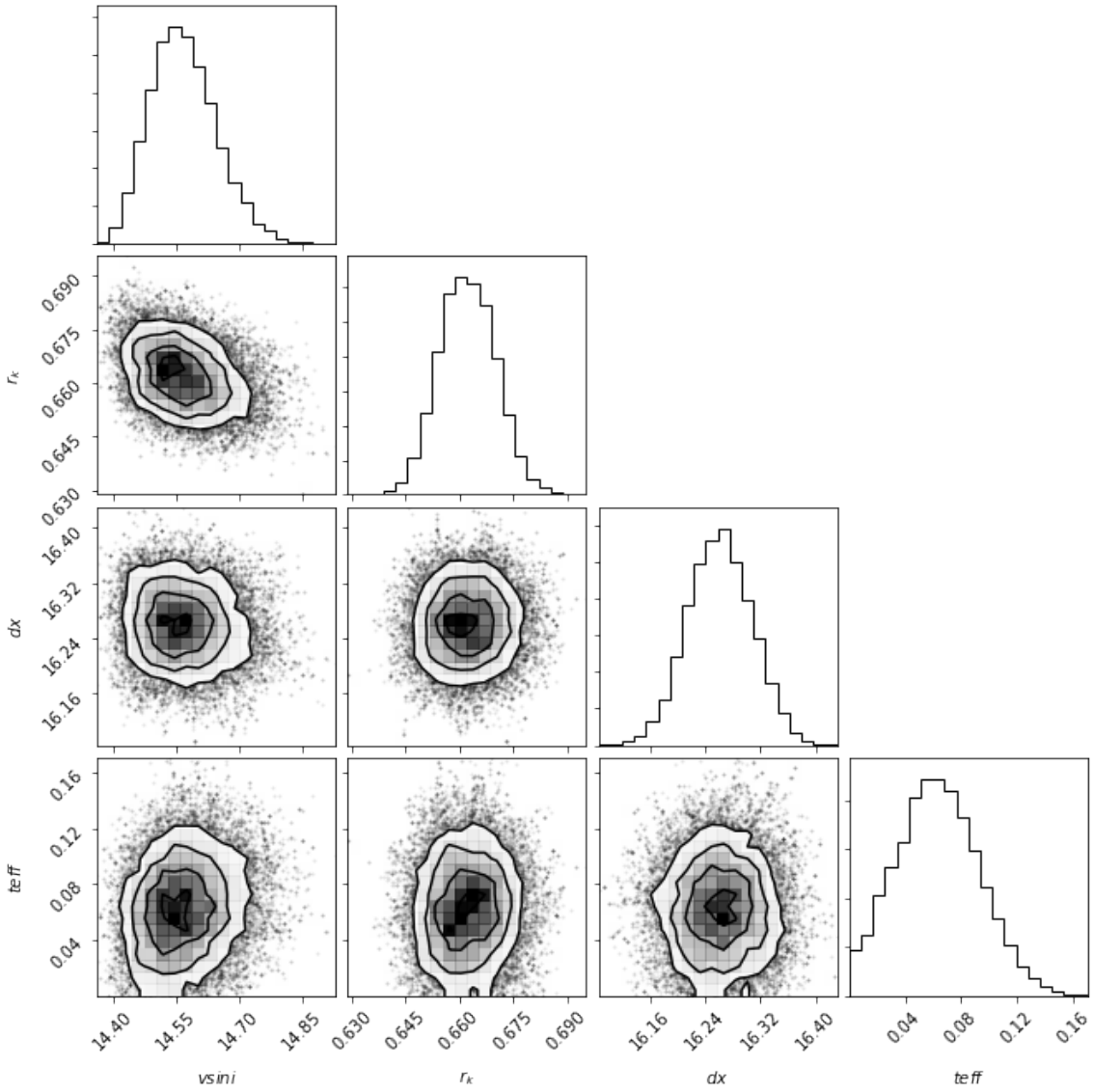

Figure 65 Relative probability distributions and correlations for the four fit parameters returned by *emcee* to best match the CRIRES spectrum of object WL 17 corresponding to $T = 3120 \pm 20$ K, $vsini = 14.56 \pm 0.08$ km s^{-1}, $r_k = 0.66 \pm 0.01$, and $dx = 16.26 \pm 0.05$.

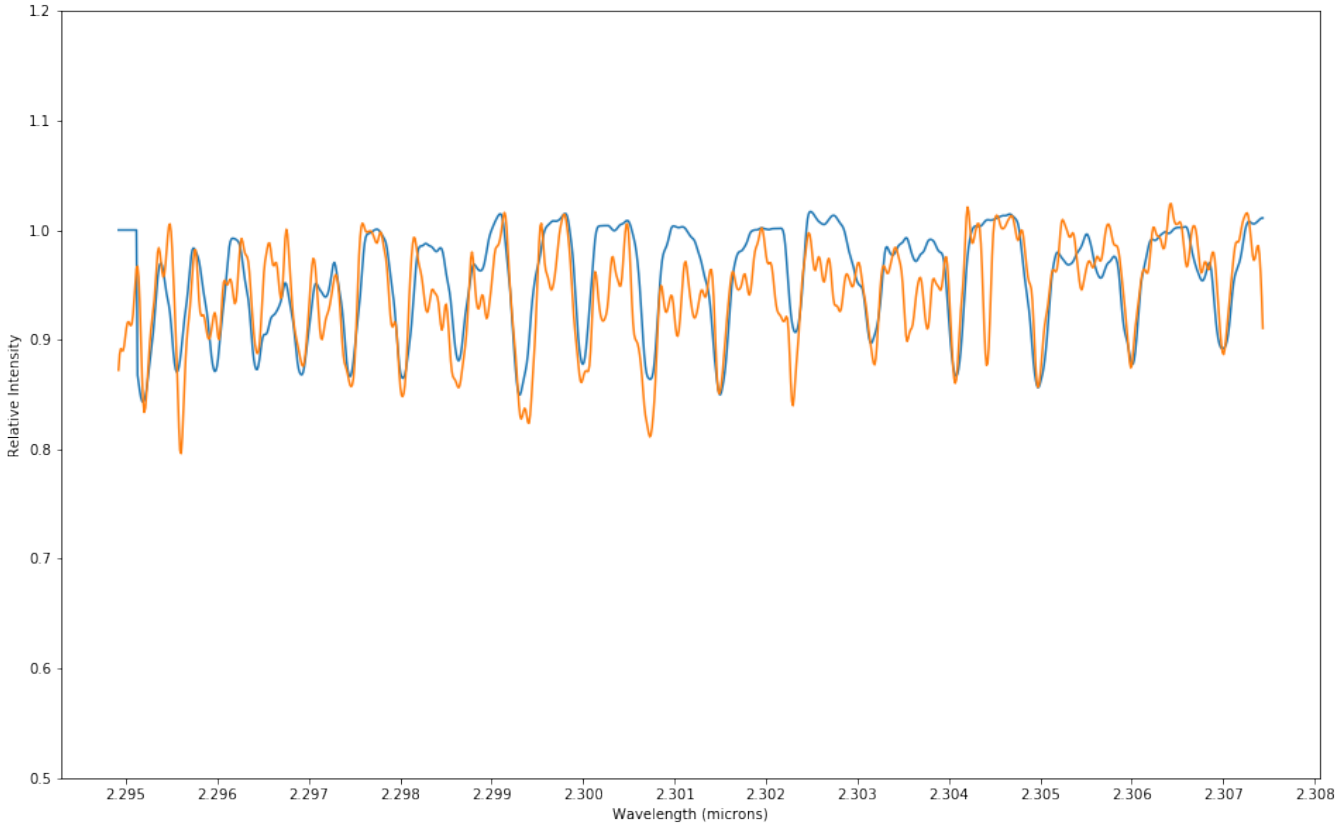

Figure 66 Synthetic overlay (blue) on top of the data (orange) for the four fit parameters returned by *emcee* to best match the CRIRES spectrum of object WL 17 corresponding to $T = 3120 \pm 20$ K, $vsini = 14.56 \pm 0.08$ km s^{-1}, $r_k = 0.66 \pm 0.01$, and $dx = 16.26 \pm 0.05$.

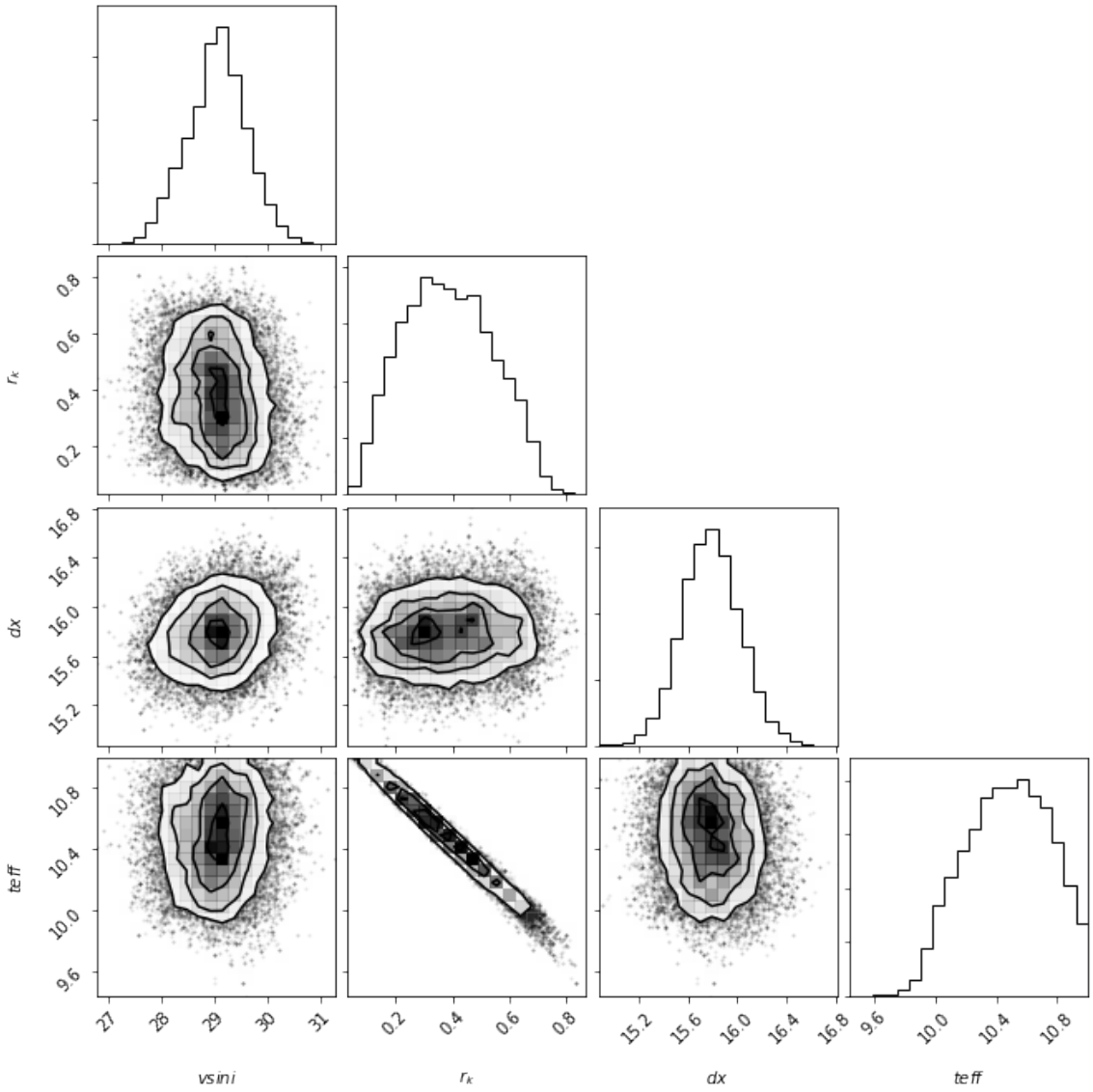

Figure 67 Relative probability distributions and correlations for the four fit parameters returned by *emcee* to best match the CRIRES spectrum of object WLY 2-44 corresponding to $T = 5300 \pm 60$ K, $vsini = 29.1 \pm 0.6$ km s^{-1}, $r_k = 0.38 \pm 0.17$, and $dx = 15.78 \pm 0.24$.

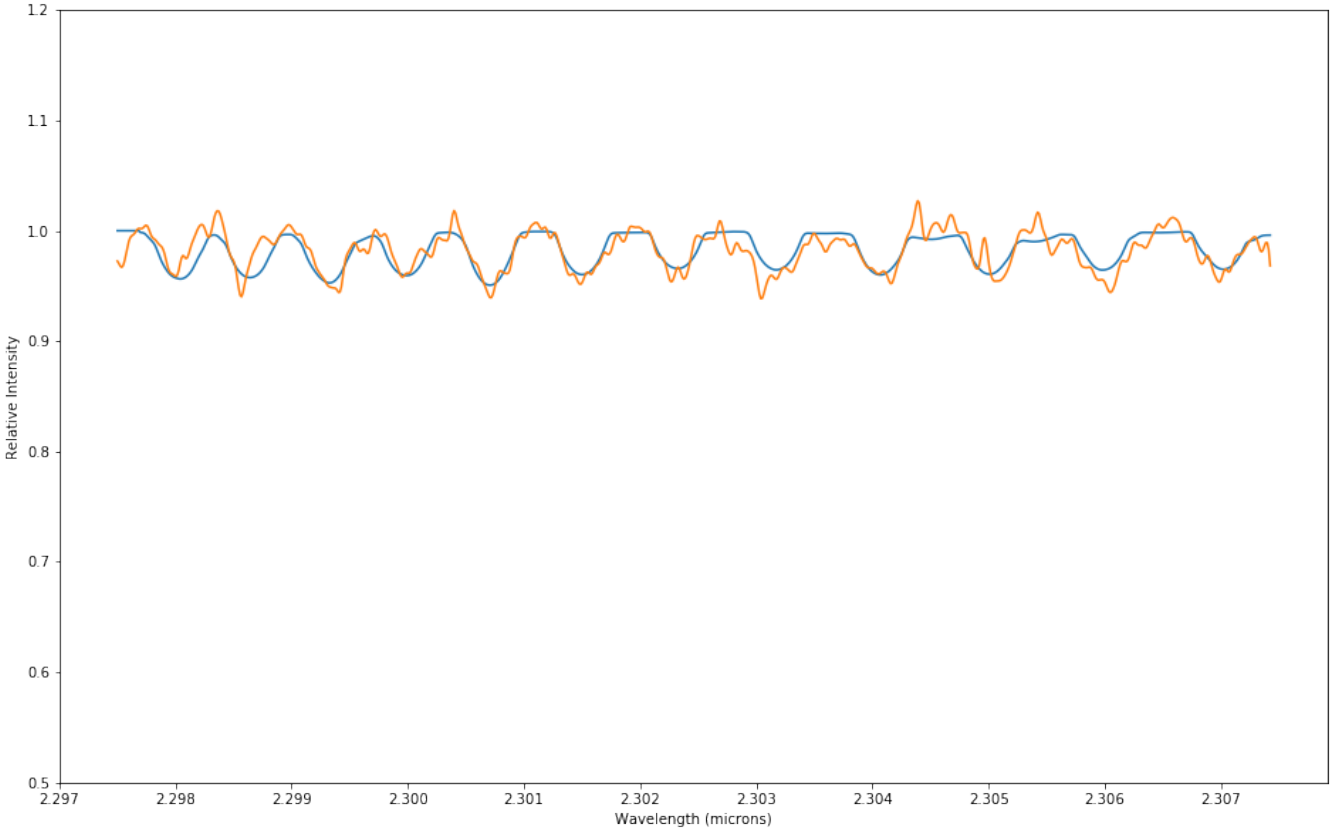

Figure 68 Synthetic overlay (blue) on top of the data (orange) for the four fit parameters returned by *emcee* to best match the CRIRES spectrum of object WLY 2-44 corresponding to $T = 5300 \pm 60$ K, $vsini = 29.1 \pm 0.6$ km s^{-1}, $r_k = 0.38 \pm 0.17$, and $dx = 15.78 \pm 0.24$.

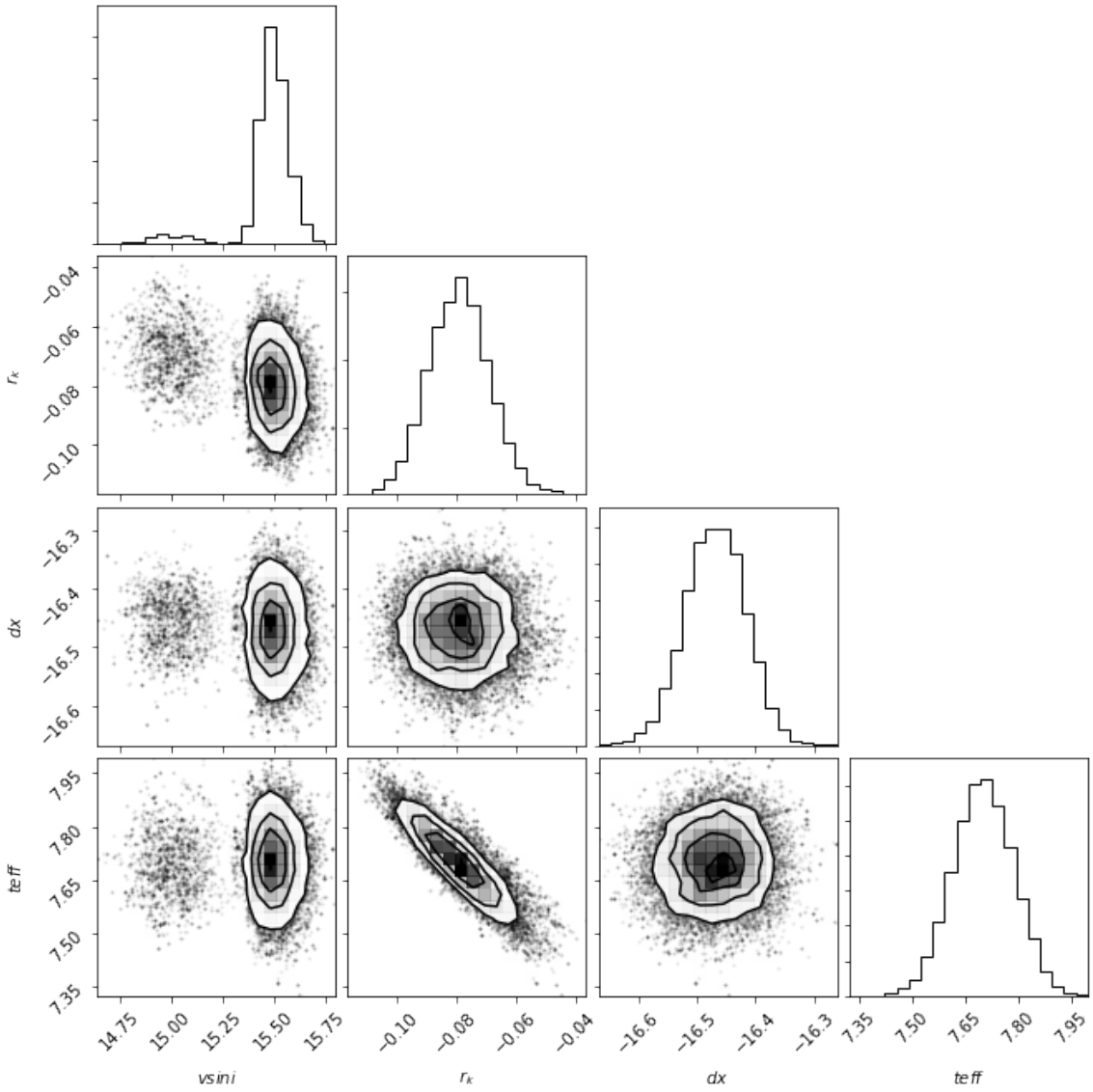

Figure 69 Relative probability distributions and correlations for the four fit parameters returned by *emcee* to best match the iSHELL spectrum of order 224 of object GY 33 corresponding to $T = 4640 \pm 20$ K, $vsini = 15.49 \pm 0.07$ km s^{-1}, $r_k = 0.00 \pm 0.01$, and $dx = -16.47 \pm 0.05$.

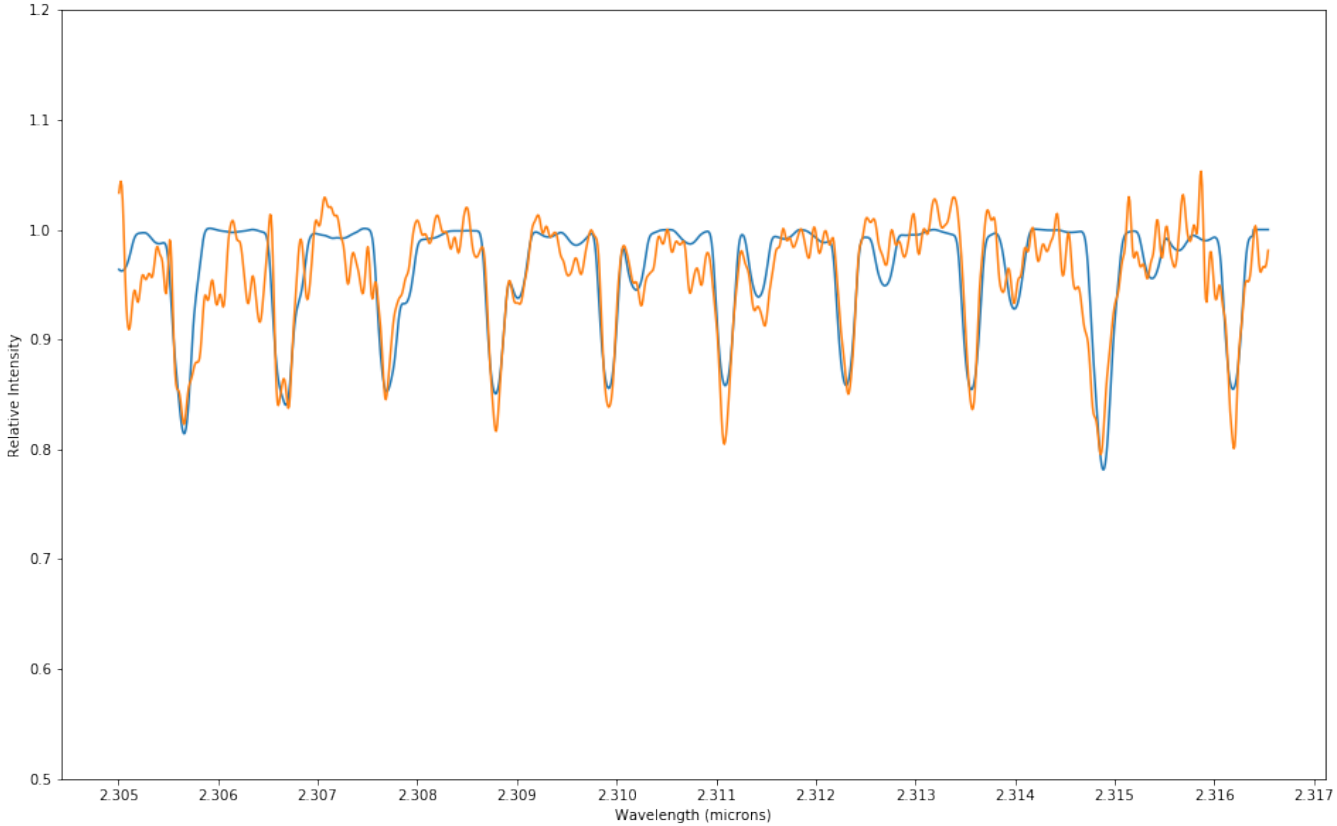

Figure 70 Synthetic overlay (blue) on top of the data (orange) for the four fit parameters returned by *emcee* to best match the iSHELL spectrum of order 224 of object GY 33 corresponding to $T = 4640 \pm 20$ K, $vsini = 15.49 \pm 0.07$ km s^{-1}, $r_k = 0.00 \pm 0.01$, and $dx = -16.47 \pm 0.05$.

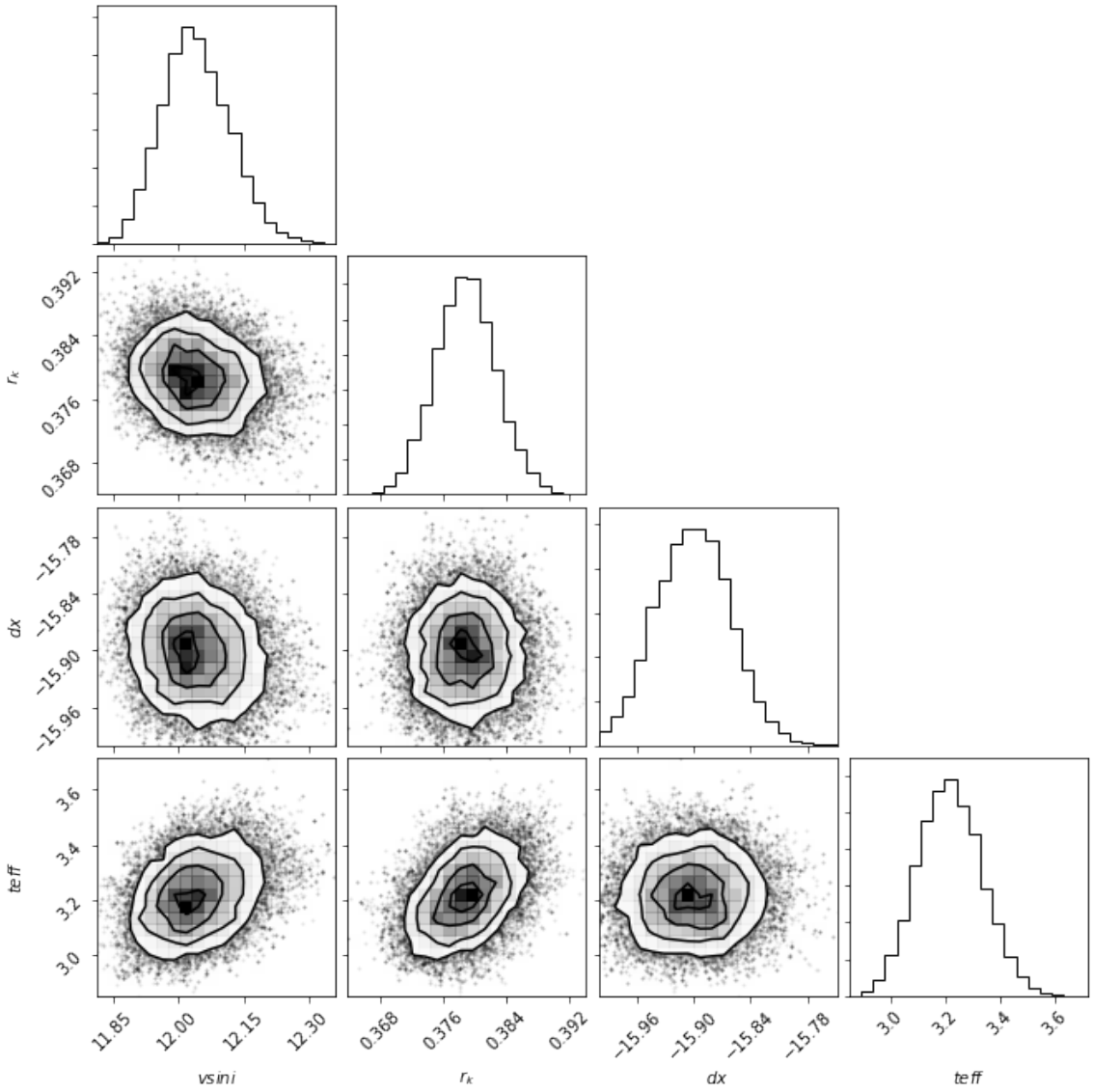

Figure 71 Relative probability distributions and correlations for the four fit parameters returned by *emcee* to best match the iSHELL spectrum of order 226 of object GY 33 corresponding to $T = 3640 \pm 20$ K, $vsini = 12.04 \pm 0.08$ km s^{-1}, $r_k = 0.04 \pm 0.01$, and $dx = -15.90 \pm 0.04$.

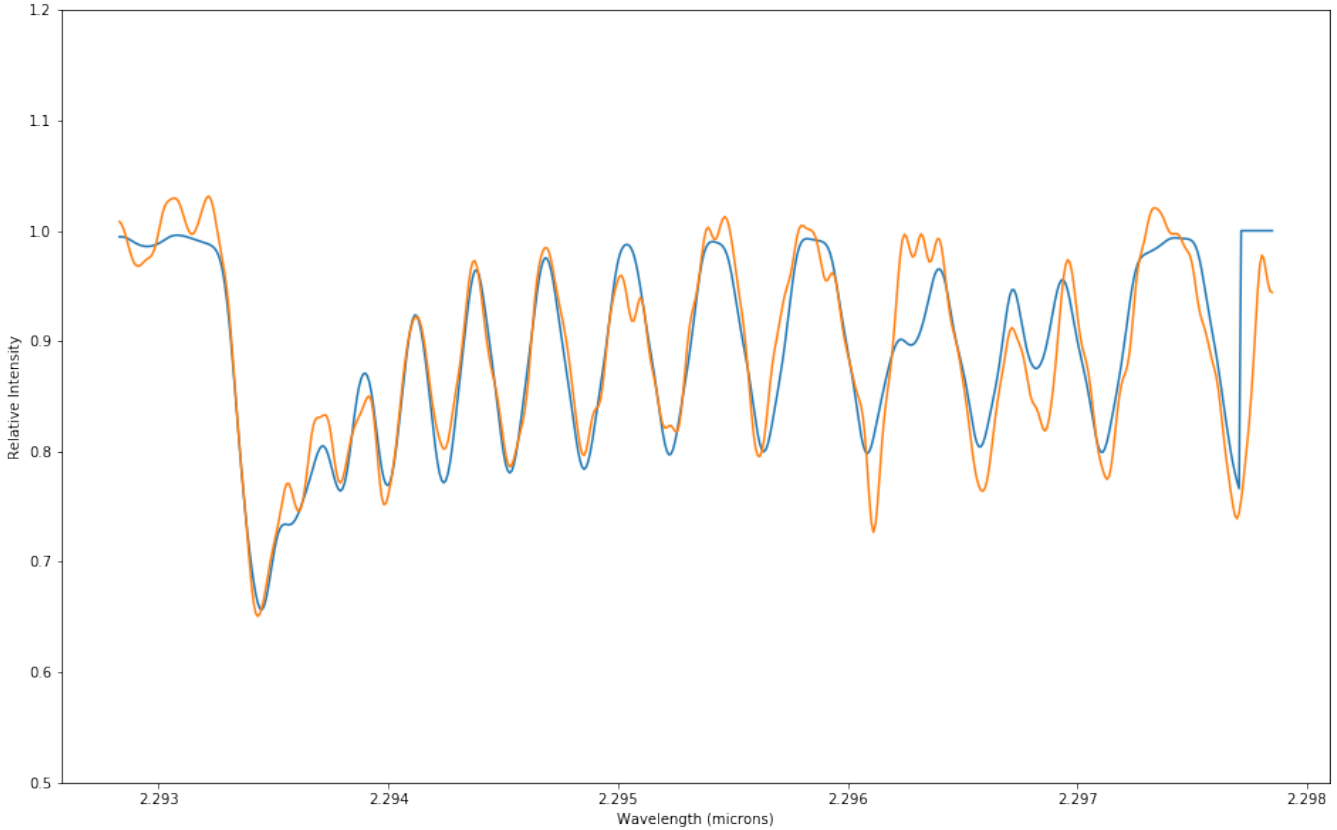

Figure 72 Synthetic overlay (blue) on top of the data (orange) for the four fit parameters returned by *emcee* to best match the iSHELL spectrum of order 226 of object GY 33 corresponding to $T = 3640 \pm 20$ K, $vsini = 12.04 \pm 0.08$ km s^{-1}, $r_k = 0.04 \pm 0.01$, and $dx = -15.90 \pm 0.04$.

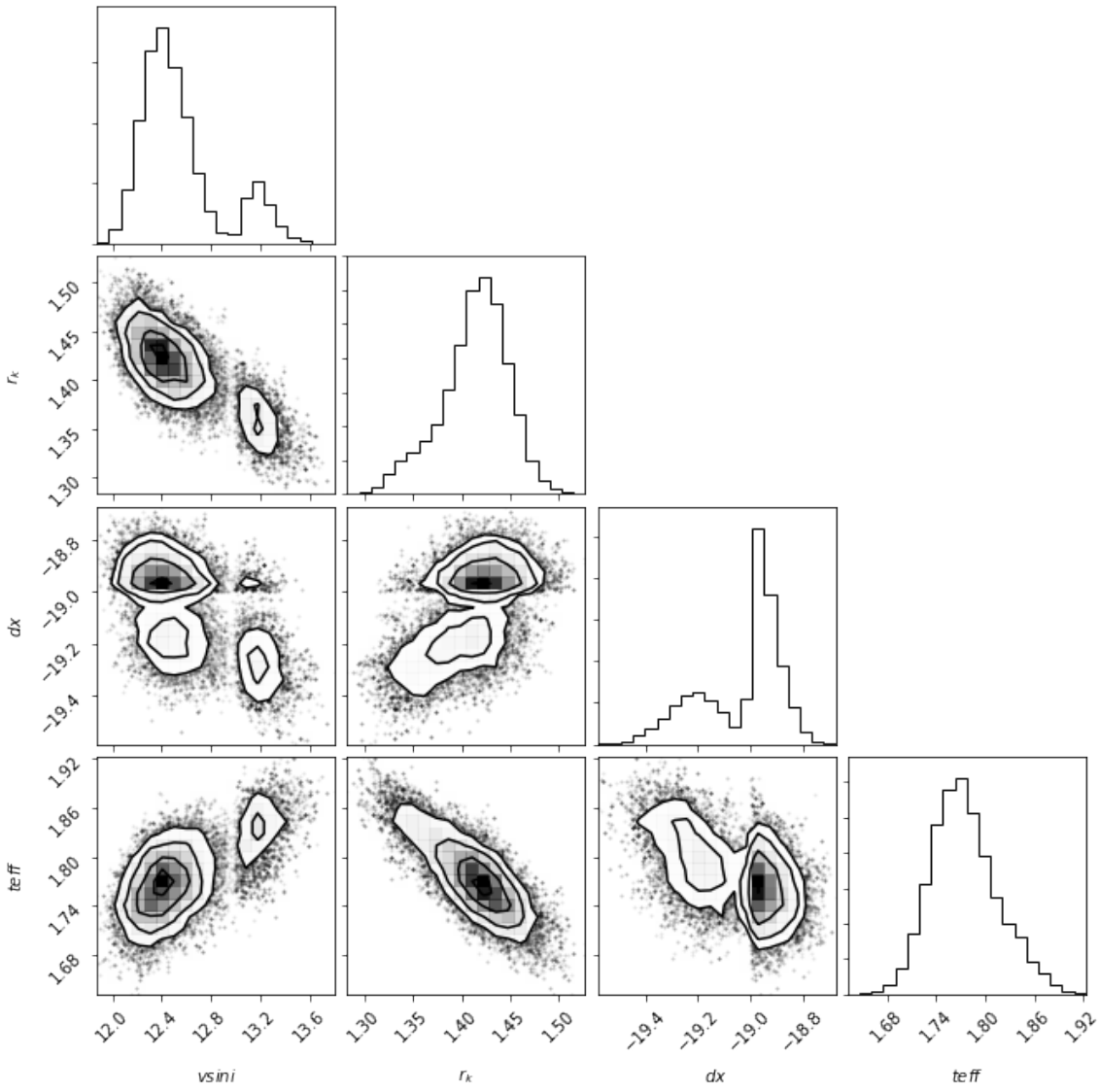

Figure 73 Relative probability distributions and correlations for the four fit parameters returned by *emcee* to best match the iSHELL spectrum of order 224 of object GY 235 corresponding to $T = 3460 \pm 20$ K, $vsini = 12.45 \pm 0.32$ km s^{-1}, $r_k = 1.42 \pm 0.04$, and $dx = -19.00 \pm 0.50$.

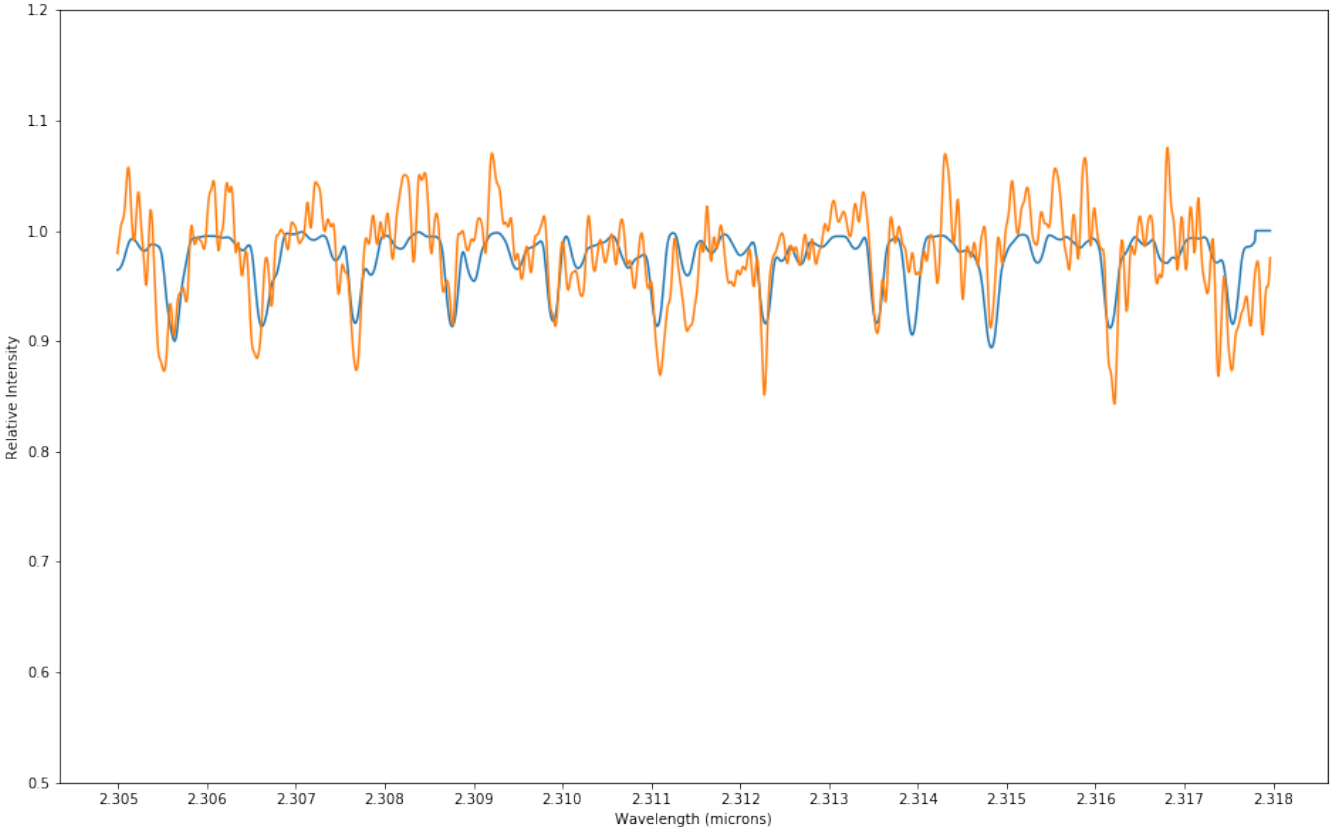

Figure 74 Synthetic overlay (blue) on top of the data (orange) for the four fit parameters returned by *emcee* to best match the iSHELL spectrum of order 224 of object GY 235 corresponding to $T = 3460 \pm 20$ K, $vsini = 12.45 \pm 0.32$ km s^{-1}, $r_k = 1.42 \pm 0.04$, and $dx = -19.00 \pm 0.50$.

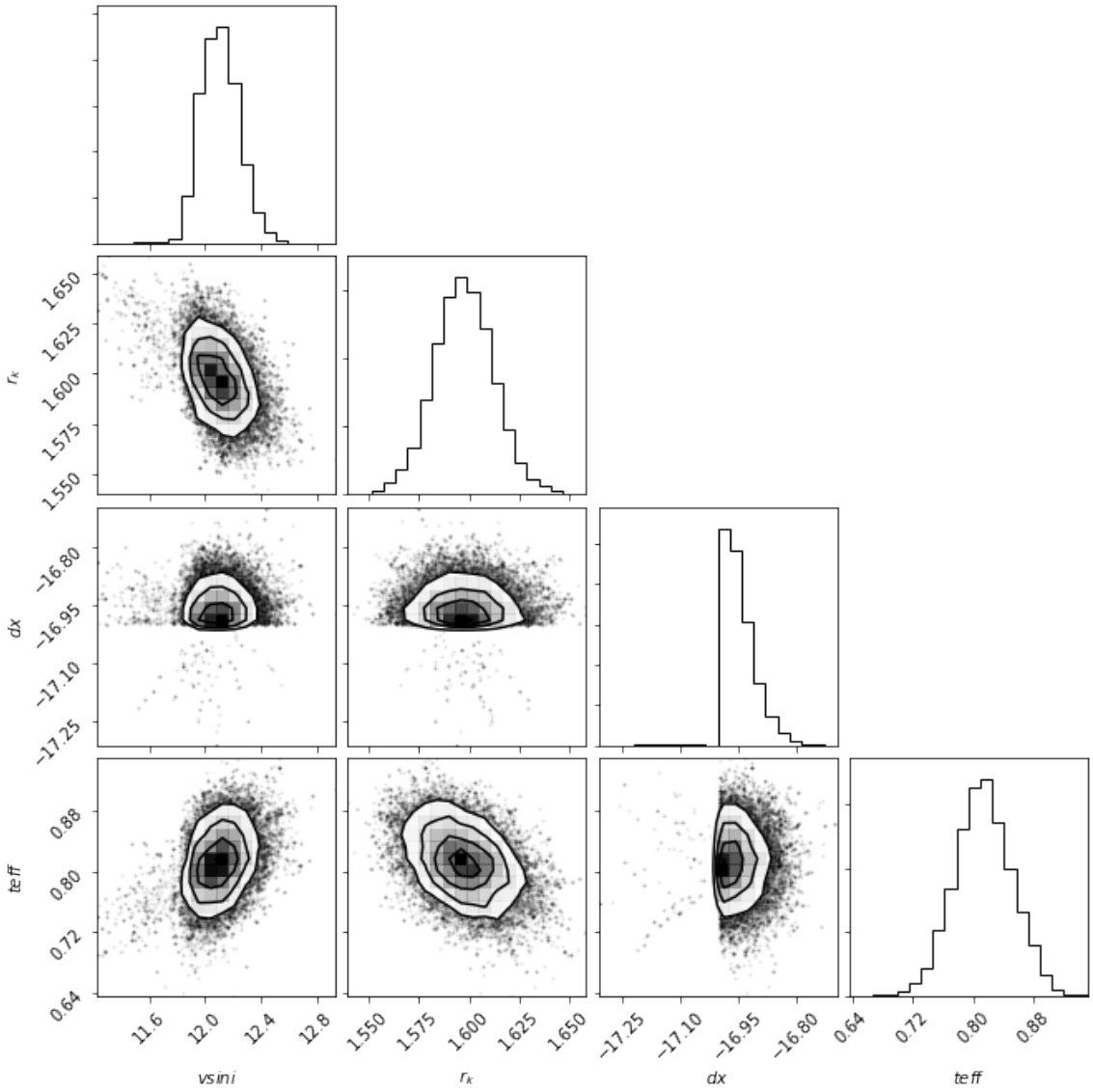

Figure 75 Relative probability distributions and correlations for the four fit parameters returned by *emcee* to best match the iSHELL spectrum of order 225 of object GY 235 corresponding to $T = 3260 \pm 20$ K, $vsini = 12.09 \pm 0.14$ km s^{-1}, $r_k = 1.60 \pm 0.01$, and $dx = -17.00 \pm 0.50$.

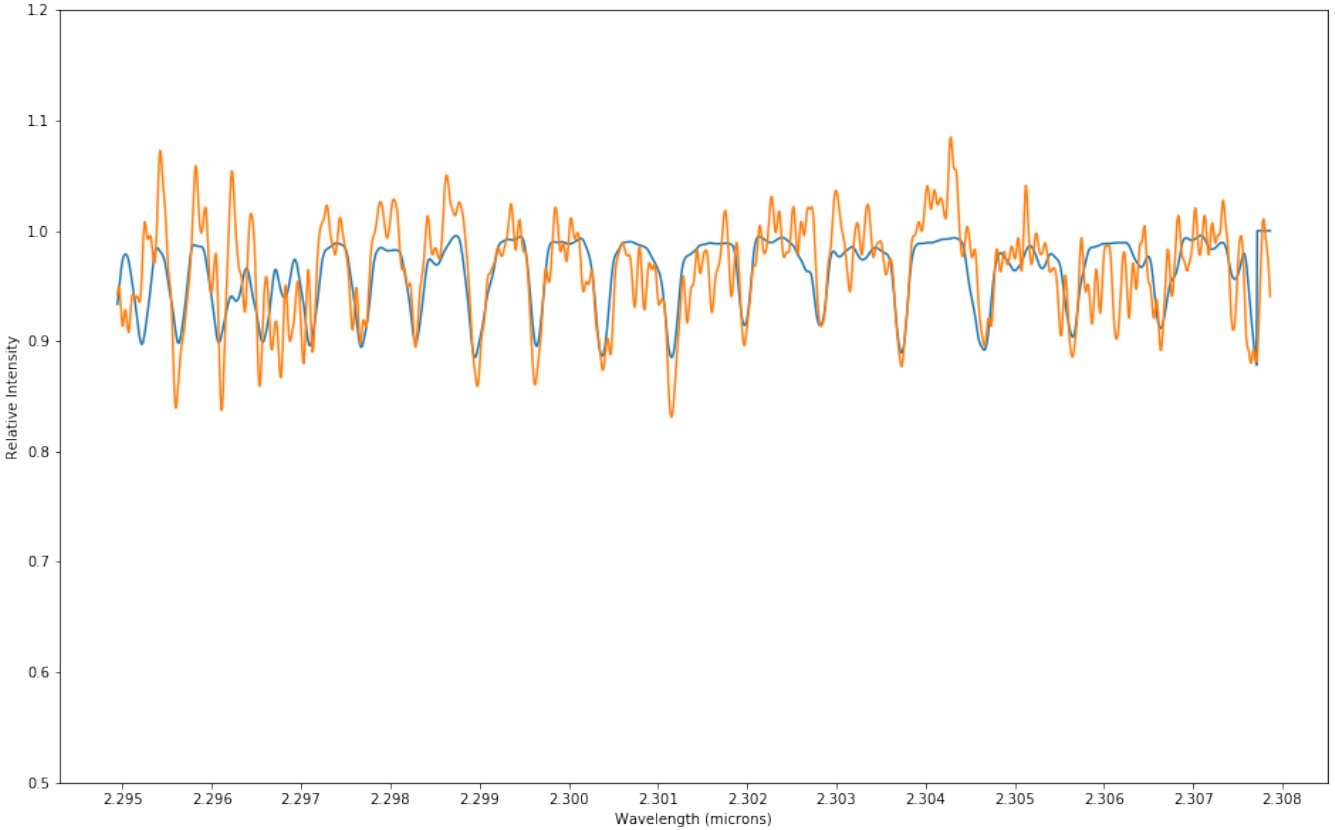

Figure 76 Synthetic overlay (blue) on top of the data (orange) for the four fit parameters returned by *emcee* to best match the iSHELL spectrum of order 225 of object GY 235 corresponding to $T = 3260 \pm 20$ K, $vsini = 12.09 \pm 0.14$ km s^{-1}, $r_k = 1.60 \pm 0.01$, and $dx = -17.00 \pm 0.50$.

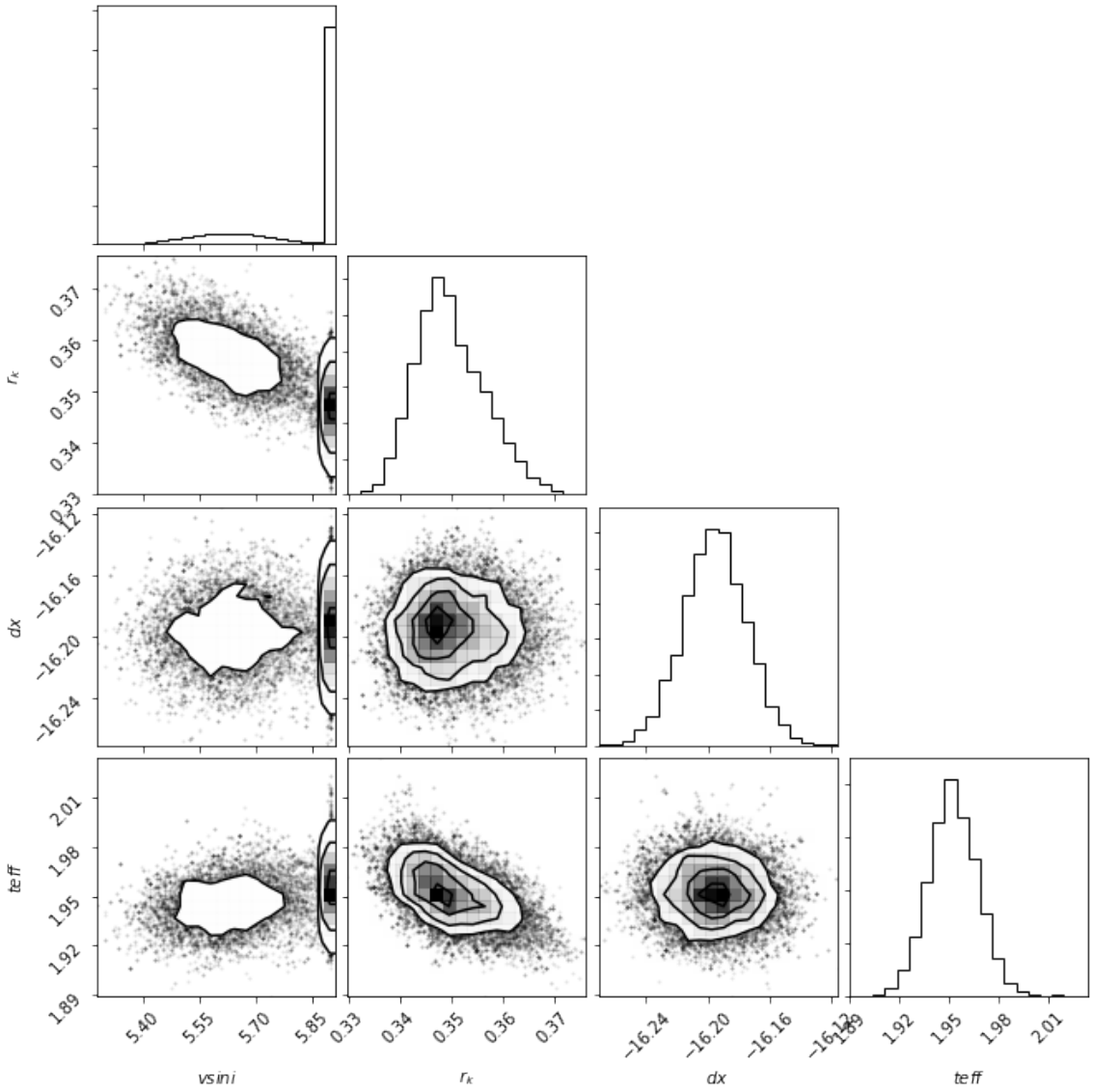

Figure 77 Relative probability distributions and correlations for the four fit parameters returned by *emcee* to best match the iSHELL spectrum of order 224 of object GY 284 corresponding to $T = 3500 \pm 20$ K, $vsini = 5.90 \pm 0.14$ km s^{-1}, $r_k = 35 \pm 0.01$, and $dx = -16.20 \pm 0.02$.

Figure 78 Synthetic overlay (blue) on top of the data (orange) for the four fit parameters returned by *emcee* to best match the iSHELL spectrum of order 224 of object GY 284 corresponding to $T = 3500 \pm 20$ K, $vsini = 5.90 \pm 0.14$ km s^{-1}, $r_k = 35 \pm 0.01$, and $dx = -16.20 \pm 0.02$.

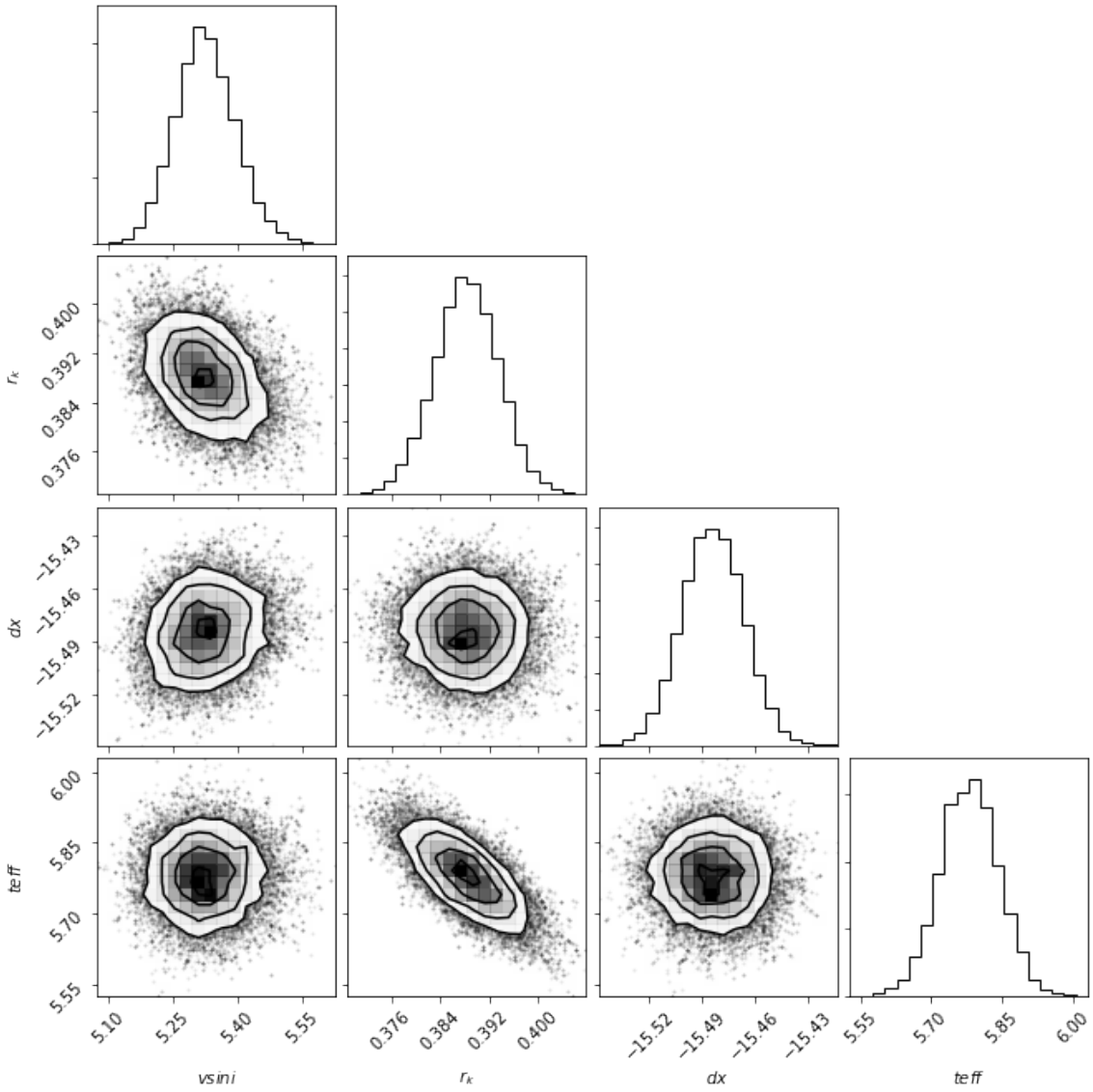

Figure 79 Relative probability distributions and correlations for the four fit parameters returned by *emcee* to best match the iSHELL spectrum of order 225 of object GY 284 corresponding to $T = 4260 \pm 20$ K, $vsini = 5.32 \pm 0.07$ km s^{-1}, $r_k = 0.39 \pm 0.02$, and $dx = -15.48 \pm 0.02$.

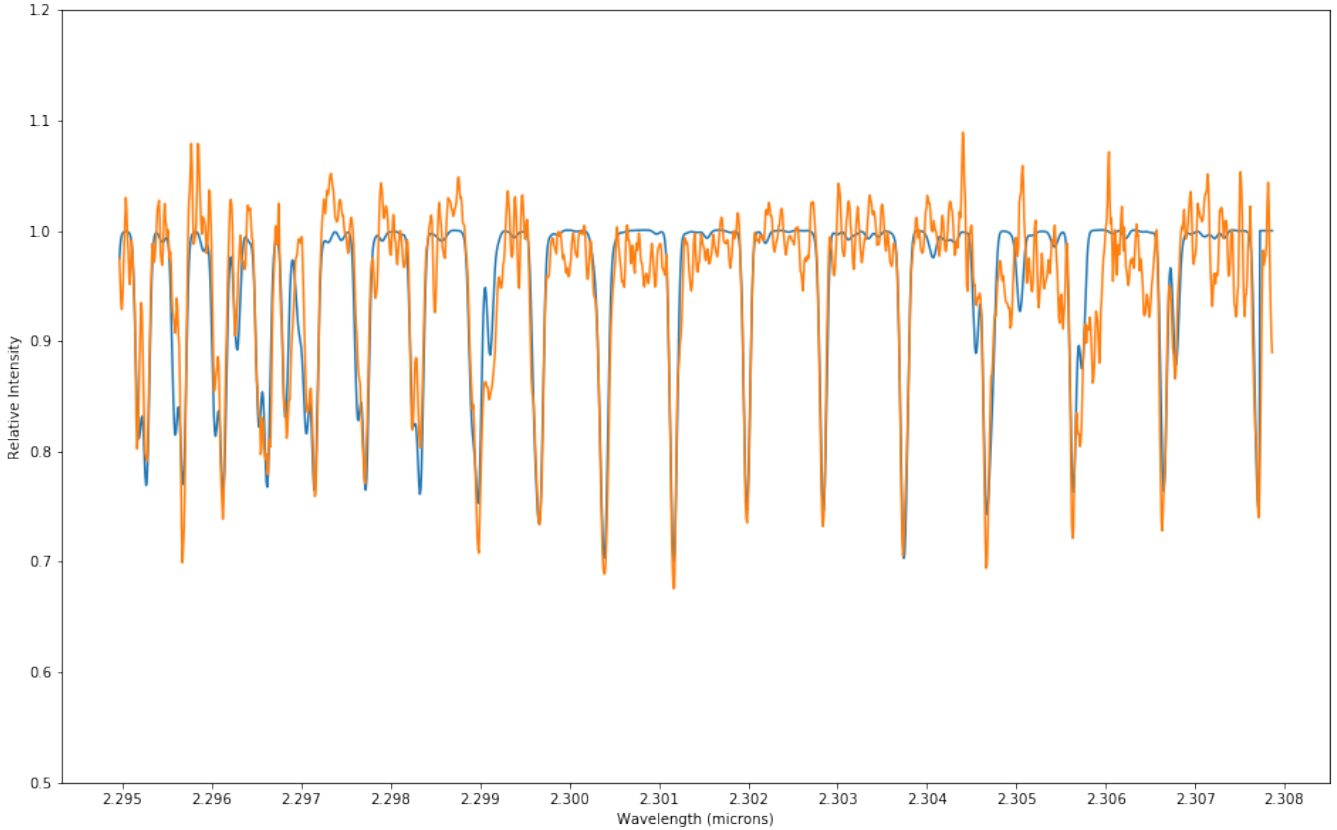

Figure 80 Synthetic overlay (blue) on top of the data (orange) for the four fit parameters returned by *emcee* to best match the iSHELL spectrum of order 225 of object GY 284 corresponding to $T = 4260 \pm 20$ K, $vsini = 5.32 \pm 0.07$ km s^{-1}, $r_k = 0.39 \pm 0.02$, and $dx = -15.48 \pm 0.02$.

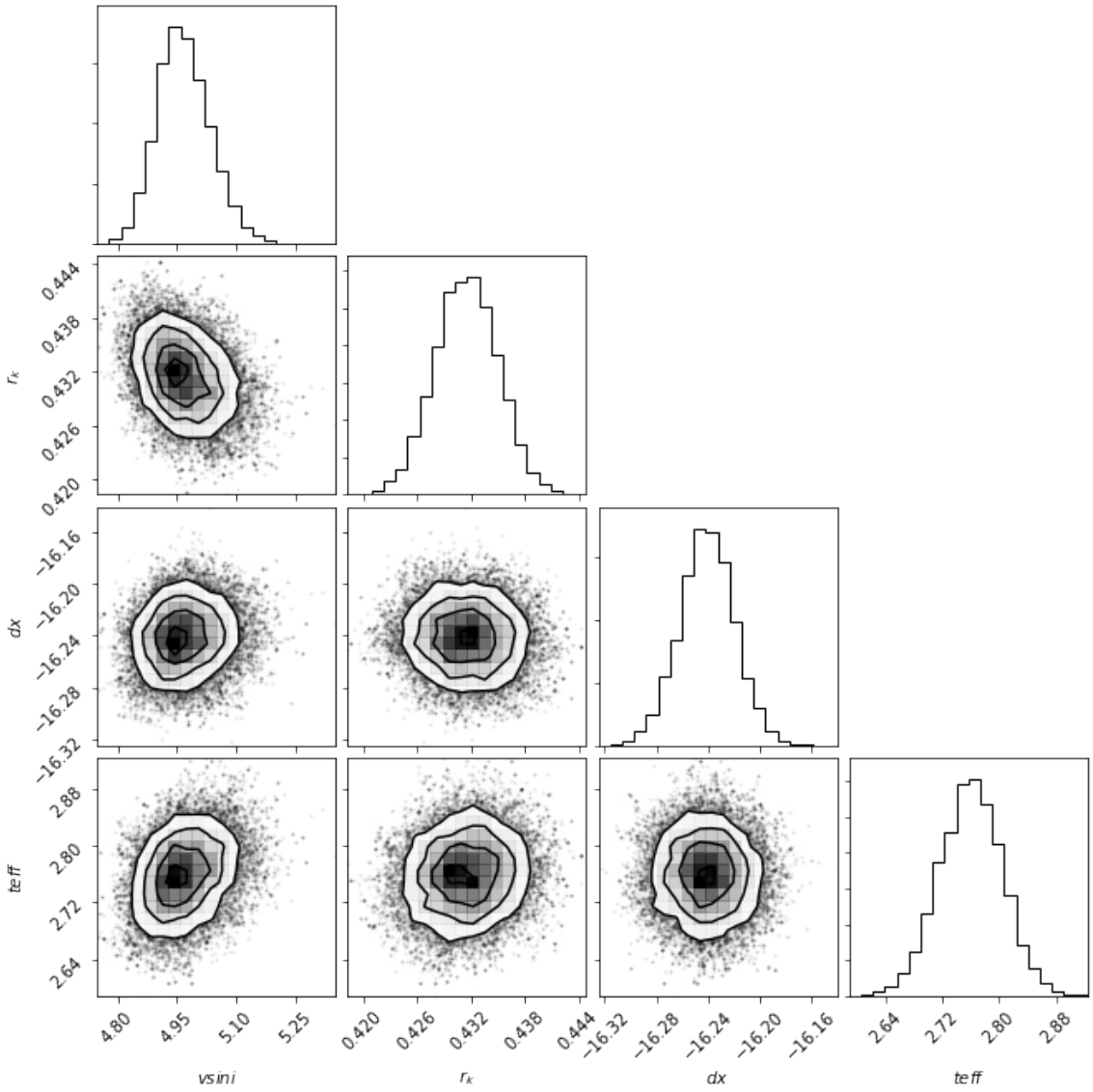

Figure 81 Relative probability distributions and correlations for the four fit parameters returned by *emcee* to best match the iSHELL spectrum of order 226 of object GY 284 corresponding to $T = 3560 \pm 20$ K, $vsini = 4.96 \pm 0.07$ km s^{-1}, $r_k = 0.43 \pm 0.01$, and $dx = -16.24 \pm 0.02$.

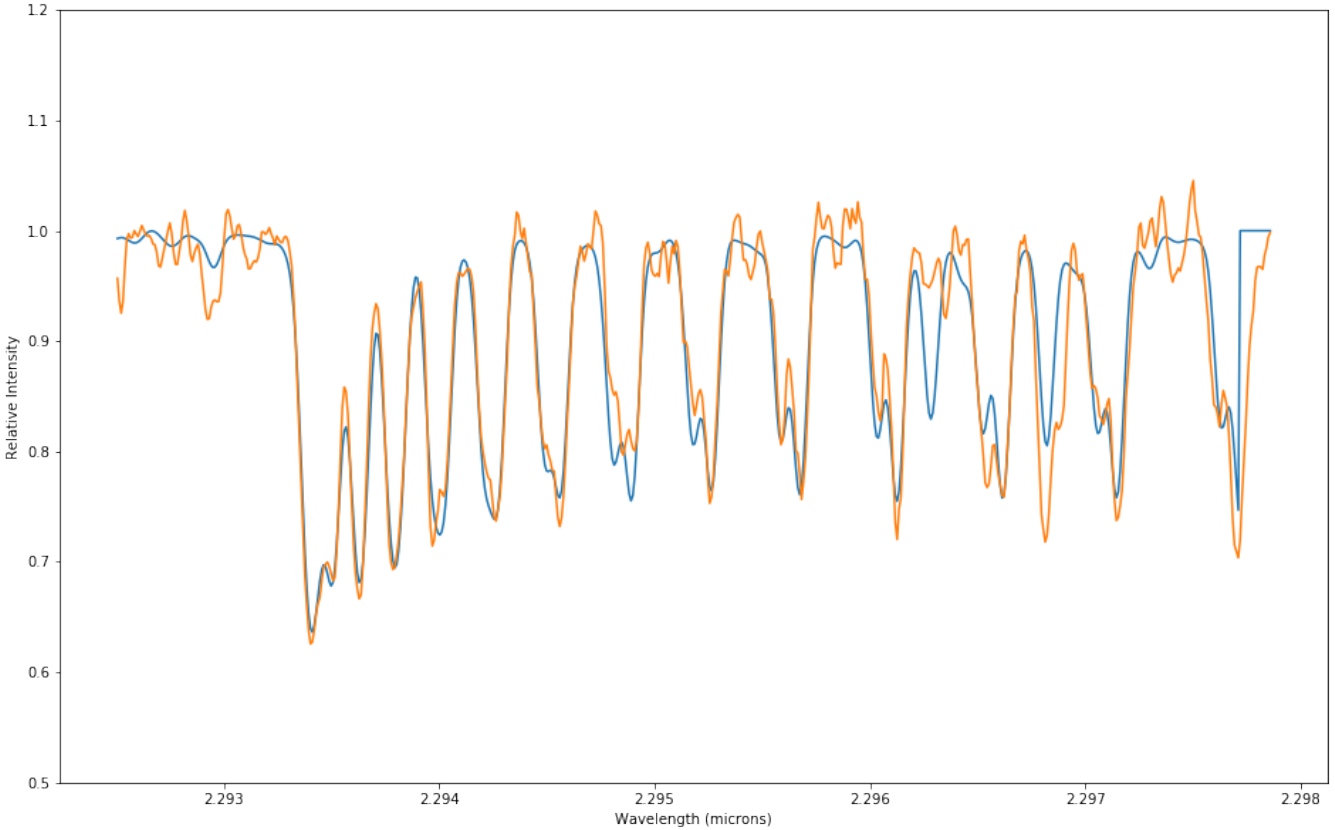

Figure 82 Synthetic overlay (blue) on top of the data (orange) for the four fit parameters returned by *emcee* to best match the iSHELL spectrum of order 226 of object GY 284 corresponding to $T = 3560 \pm 20$ K, $vsini = 4.96 \pm 0.07$ km s^{-1}, $r_k = 0.43 \pm 0.01$, and $dx = -16.24 \pm 0.02$.

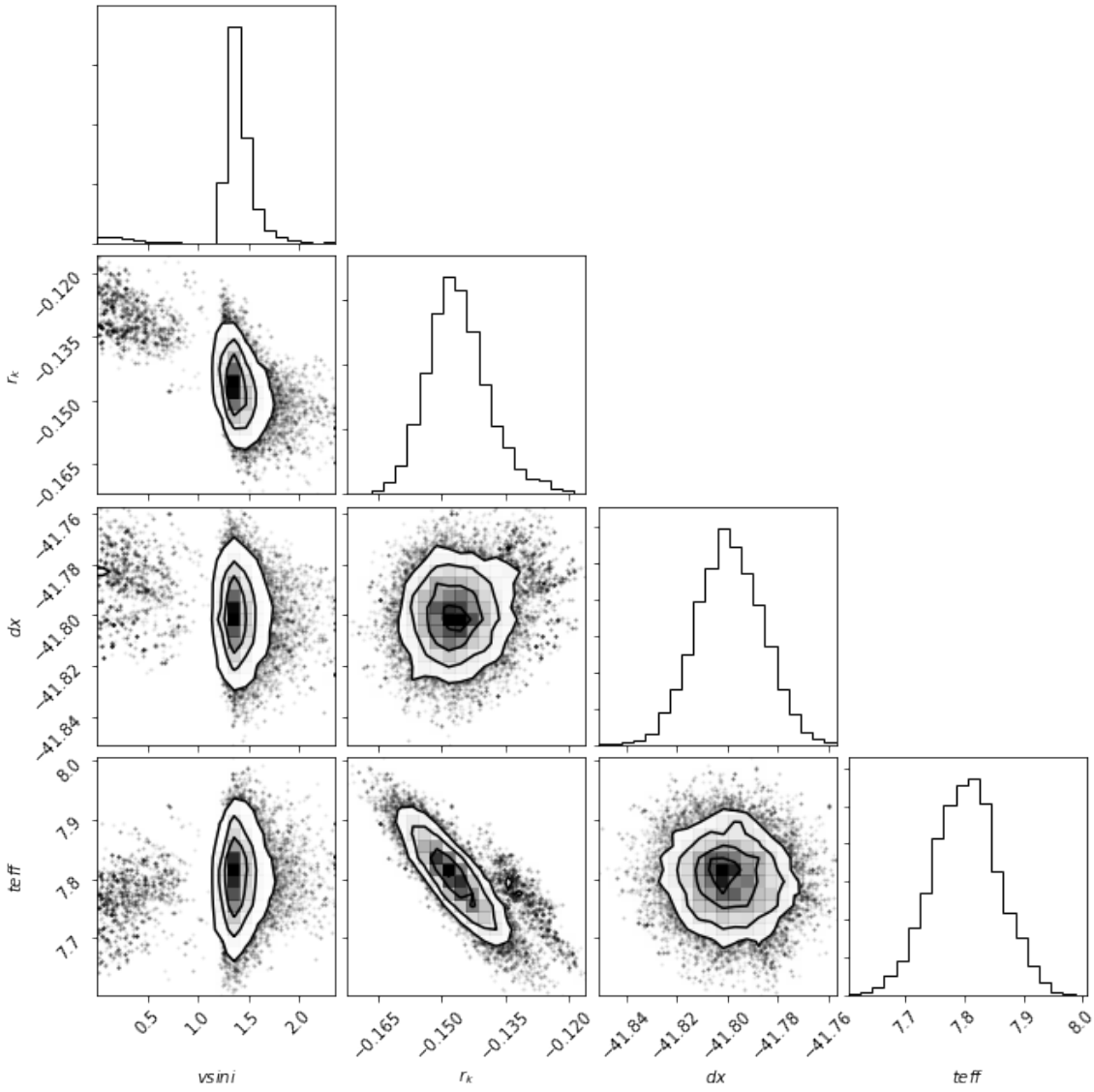

Figure 83 Relative probability distributions and correlations for the four fit parameters returned by *emcee* to best match the iSHELL spectrum of order 224 of radial velocity standard HD 122120 corresponding to $T = 4660 \pm 20$ K, $vsini = 1.38 \pm 0.11$ km s^{-1}, $r_k = 0.00 \pm 0.01$, and $dx = -41.80 \pm 0.01$.

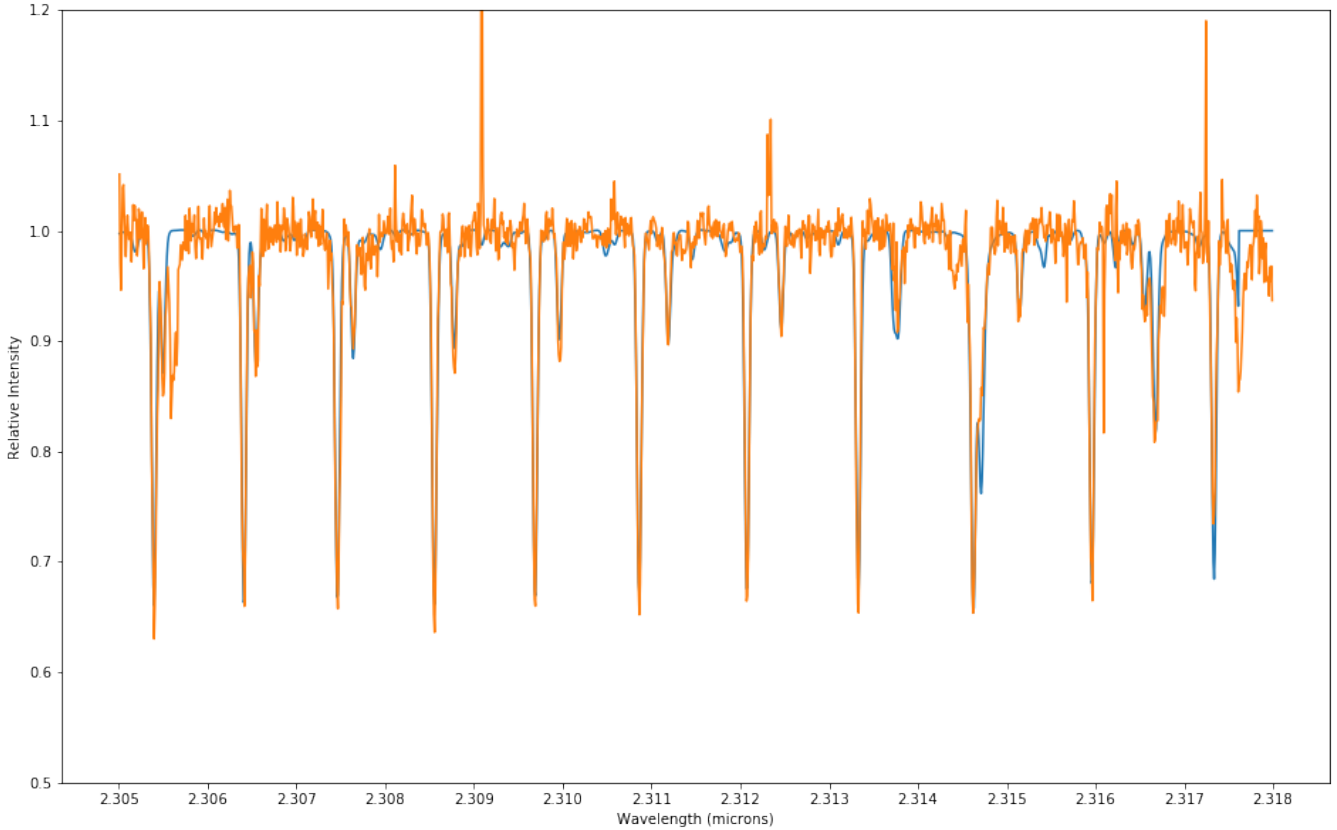

Figure 84 Synthetic overlay (blue) on top of the data (orange) for the four fit parameters returned by *emcee* to best match the iSHELL spectrum of order 224 of radial velocity standard HD 122120 corresponding to $T = 4660 \pm 20$ K, $vsini = 1.38 \pm 0.11$ km s^{-1}, $r_k = 0.00 \pm 0.01$, and $dx = -41.80 \pm 0.01$.

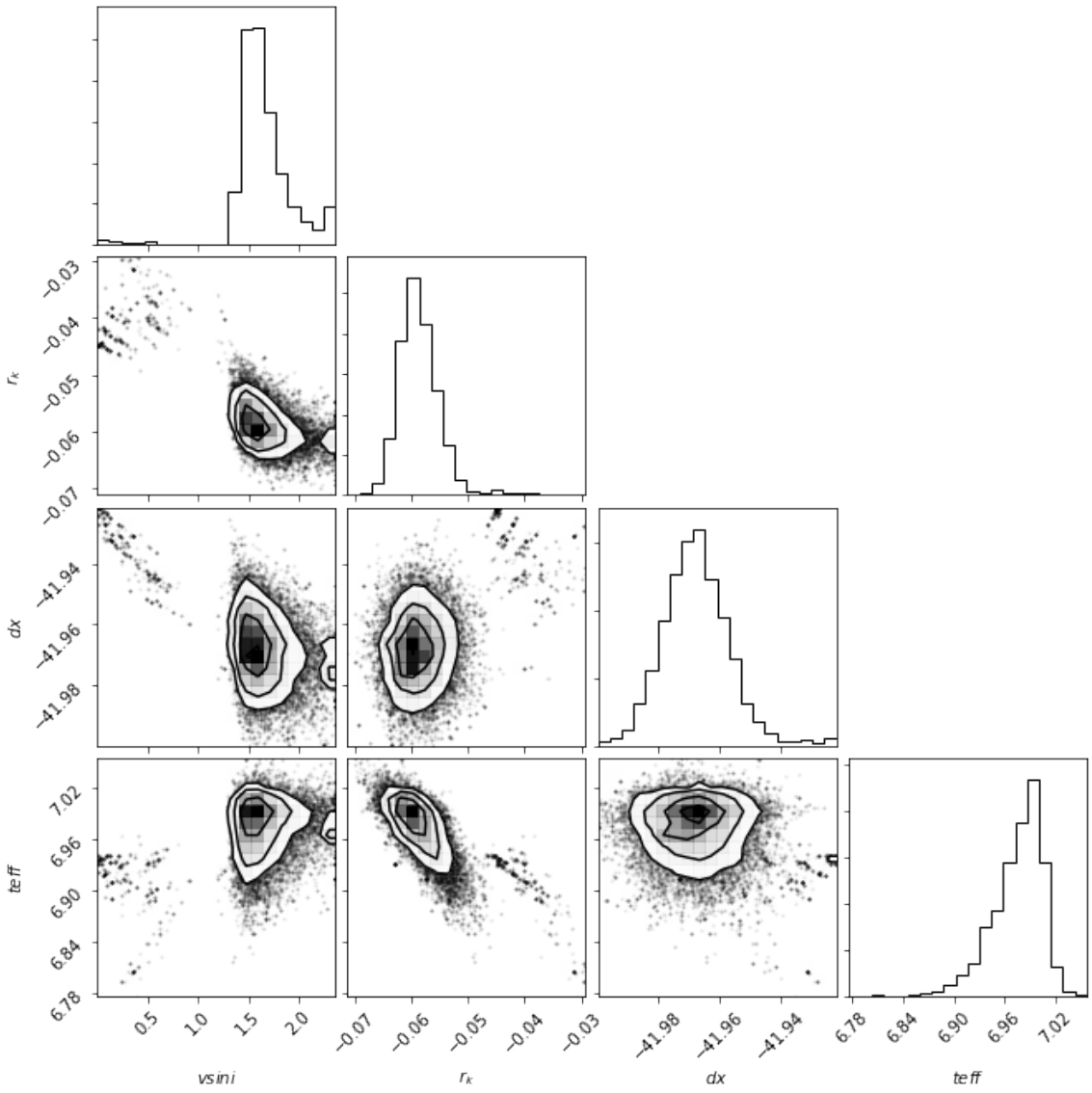

Figure 85 Relative probability distributions and correlations for the four fit parameters returned by *emcee* to best match the iSHELL spectrum of order 225 of radial velocity standard HD 122120 corresponding to $T = 4500 \pm 20$ K, $vsini = 1.60 \pm 0.20$ km s^{-1}, $r_k = 0.00 \pm 0.01$, and $dx = -41.97 \pm 0.01$.

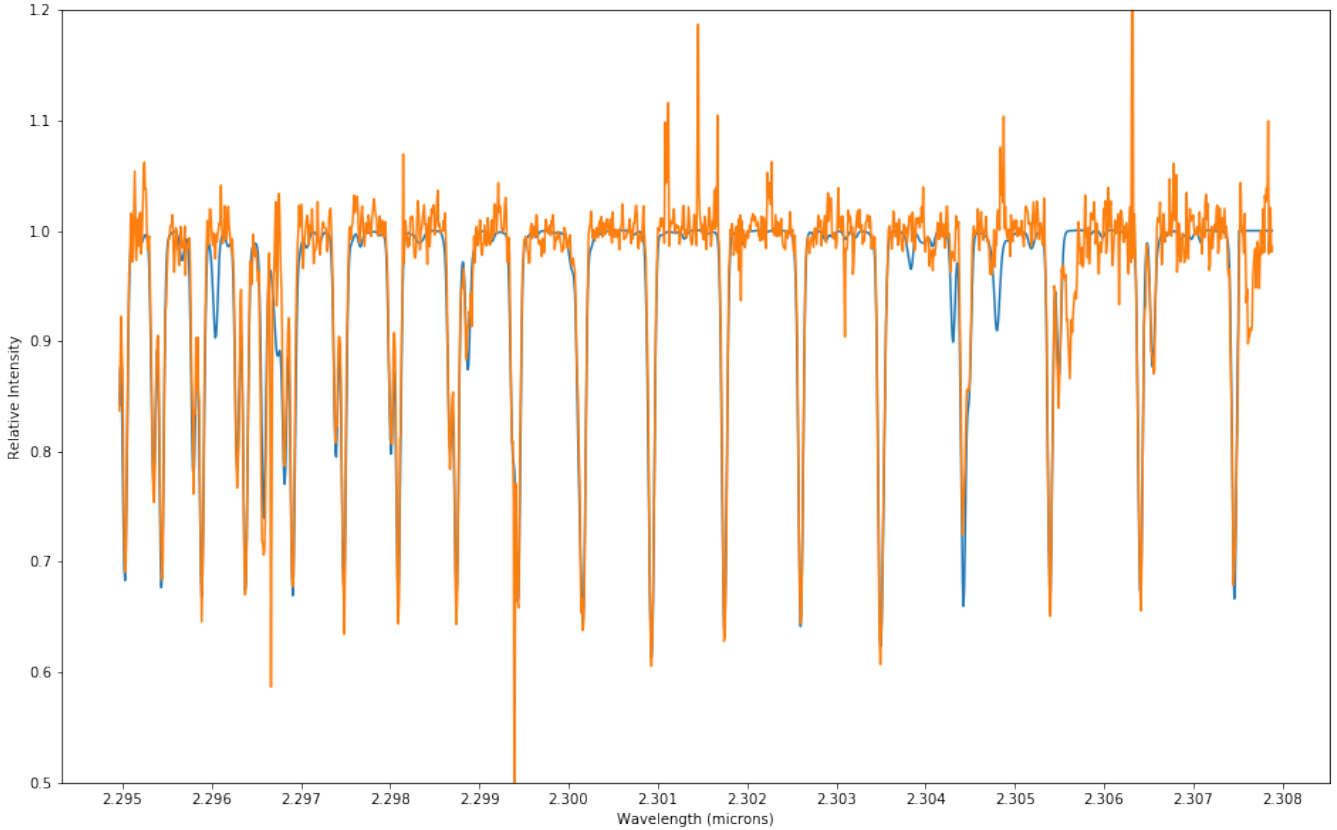

Figure 86 Synthetic overlay (blue) on top of the data (orange) for the four fit parameters returned by *emcee* to best match the iSHELL spectrum of order 225 of radial velocity standard HD 122120 corresponding to $T = 4500 \pm 20$ K, $vsini = 1.60 \pm 0.20$ km s^{-1}, $r_k = 0.00 \pm 0.01$, and $dx = -41.97 \pm 0.01$.

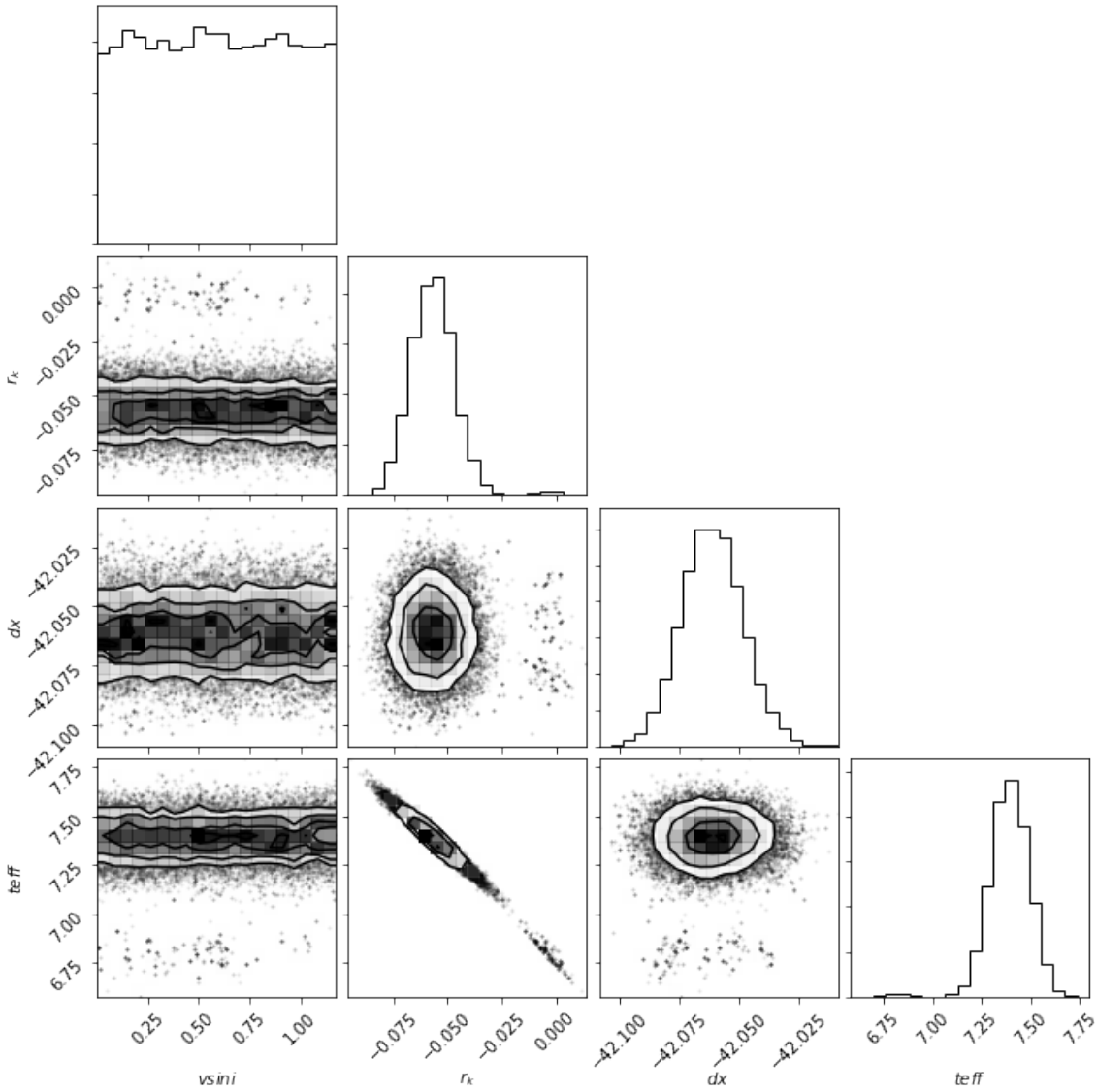

Figure 87 Relative probability distributions and correlations for the four fit parameters returned by *emcee* to best match the iSHELL spectrum of order 226 of radial velocity standard HD 122120 corresponding to $T = 4480 \pm 20$ K, $vsini = 0.59 \pm 0.40$ km s^{-1}, $r_k = 0.00 \pm 0.01$, and $dx = -42.06 \pm 0.01$.

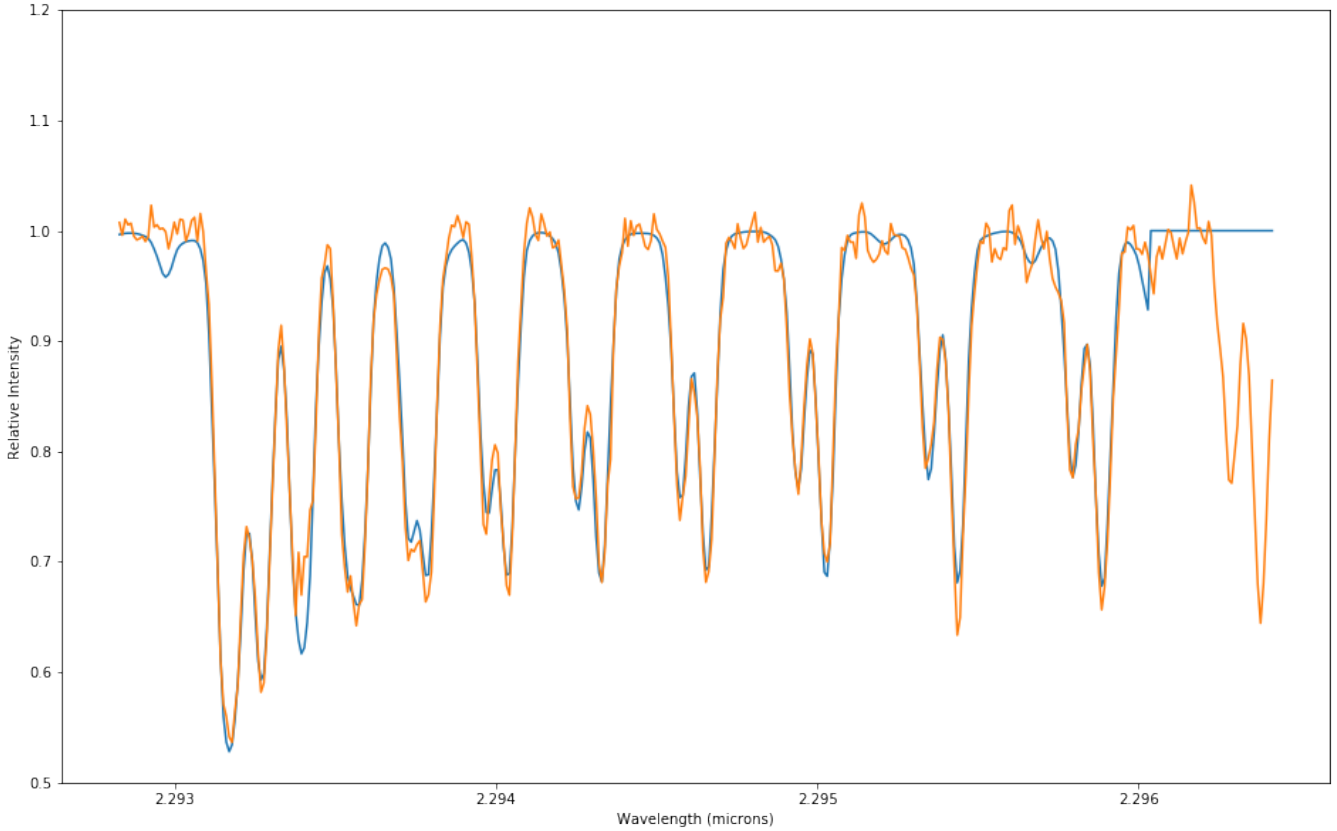

Figure 88 Synthetic overlay (blue) on top of the data (orange) for the four fit parameters returned by *emcee* to best match the iSHELL spectrum of order 226 of radial velocity standard HD 122120 corresponding to $T = 4480 \pm 20$ K, $vsini = 0.59 \pm 0.40$ km s^{-1}, $r_k = 0.00 \pm 0.01$, and $dx = -42.06 \pm 0.01$.

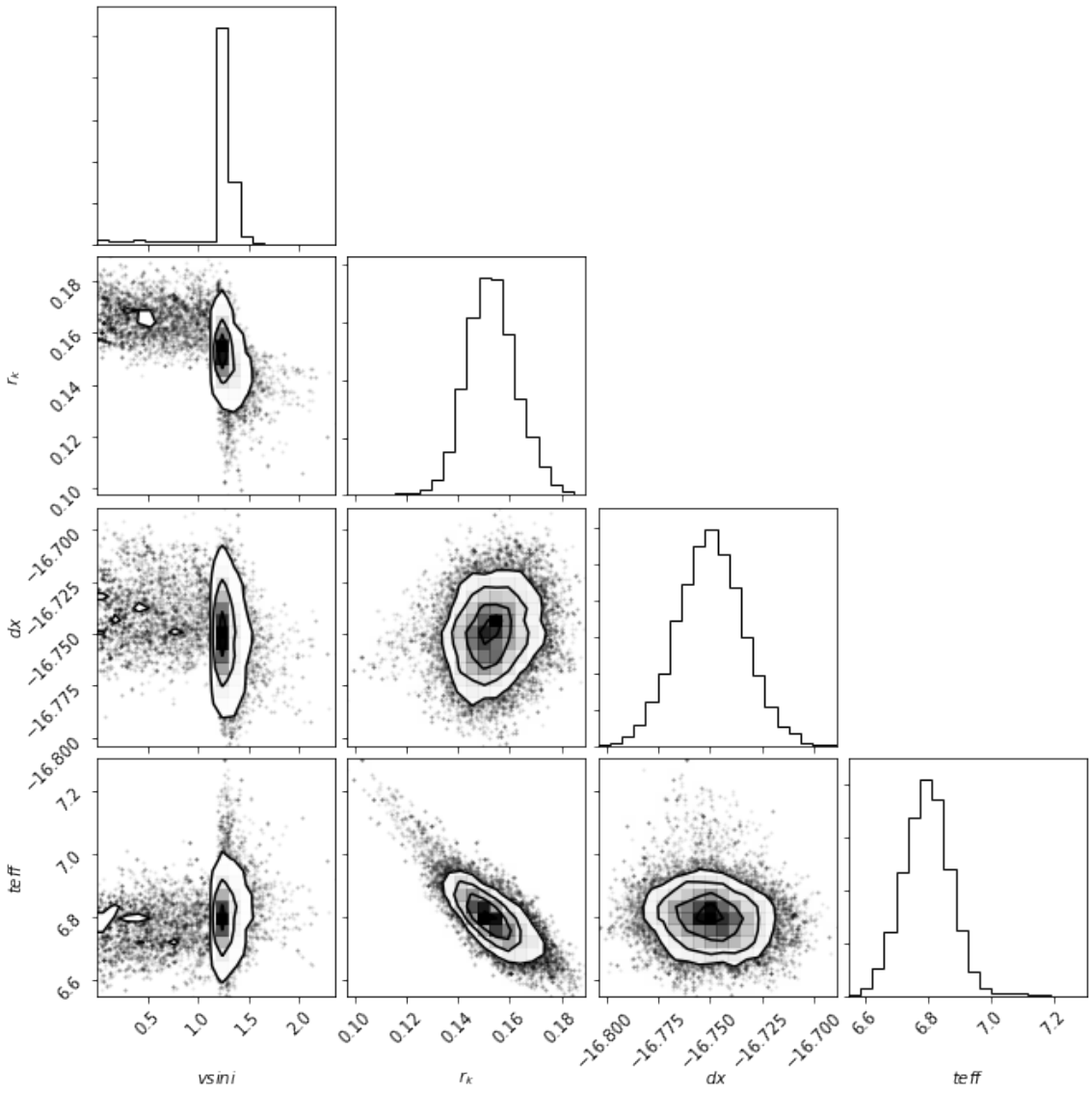

Figure 89 Relative probability distributions and correlations for the four fit parameters returned by *emcee* to best match the iSHELL spectrum of order 224 of radial velocity standard HD 156026 corresponding to T = 4460 ± 20 K, $vsini$ = 1.25 ± 0.06 km s^{-1}, r_k = 0.15 ± 0.01, and dx = −16.75 ± 0.02.

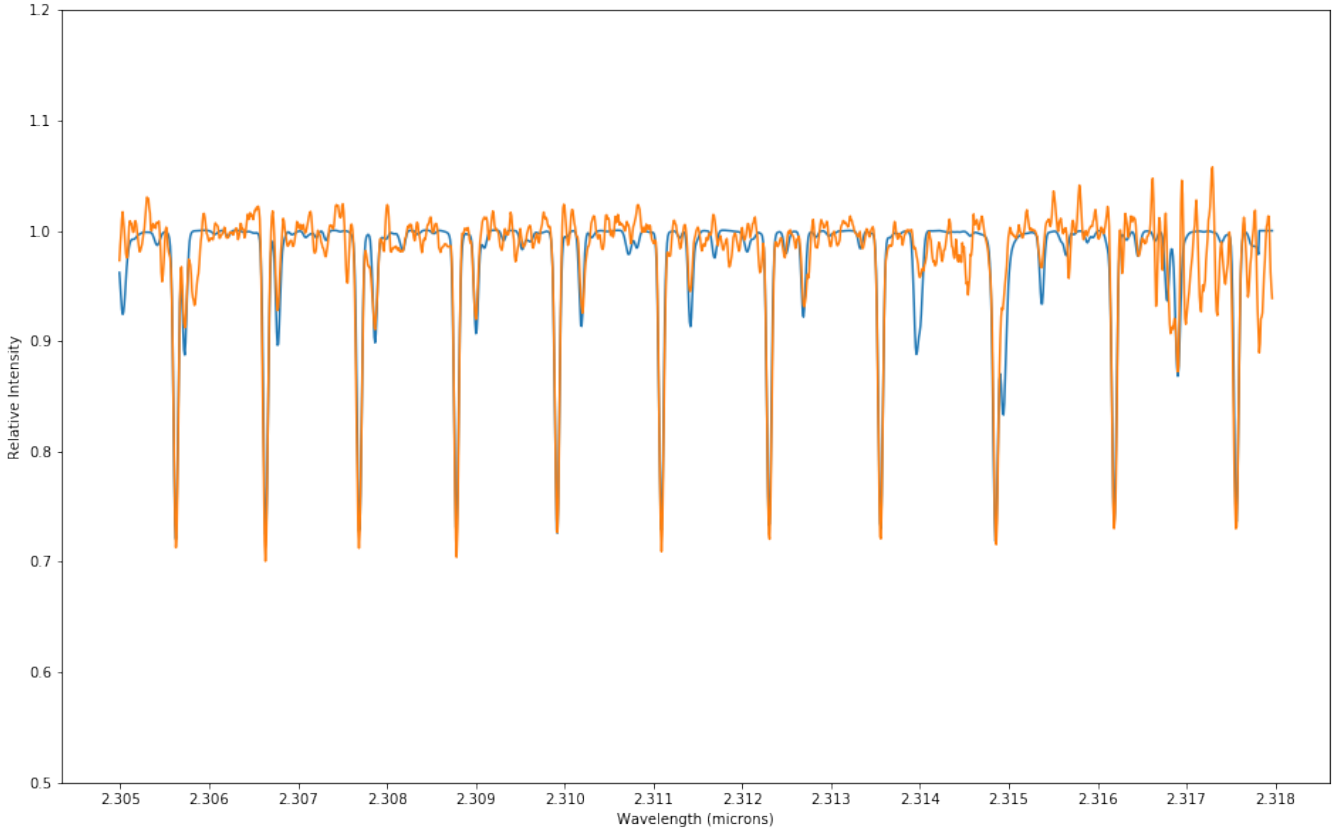

Figure 90 Synthetic overlay (blue) on top of the data (orange) for the four fit parameters returned by *emcee* to best match the iSHELL spectrum of order 224 of radial velocity standard HD 156026 corresponding to $T = 4460 \pm 20$ K, $vsini = 1.25 \pm 0.06$ km s^{-1}, $r_k = 0.15 \pm 0.01$, and $dx = -16.75 \pm 0.02$.

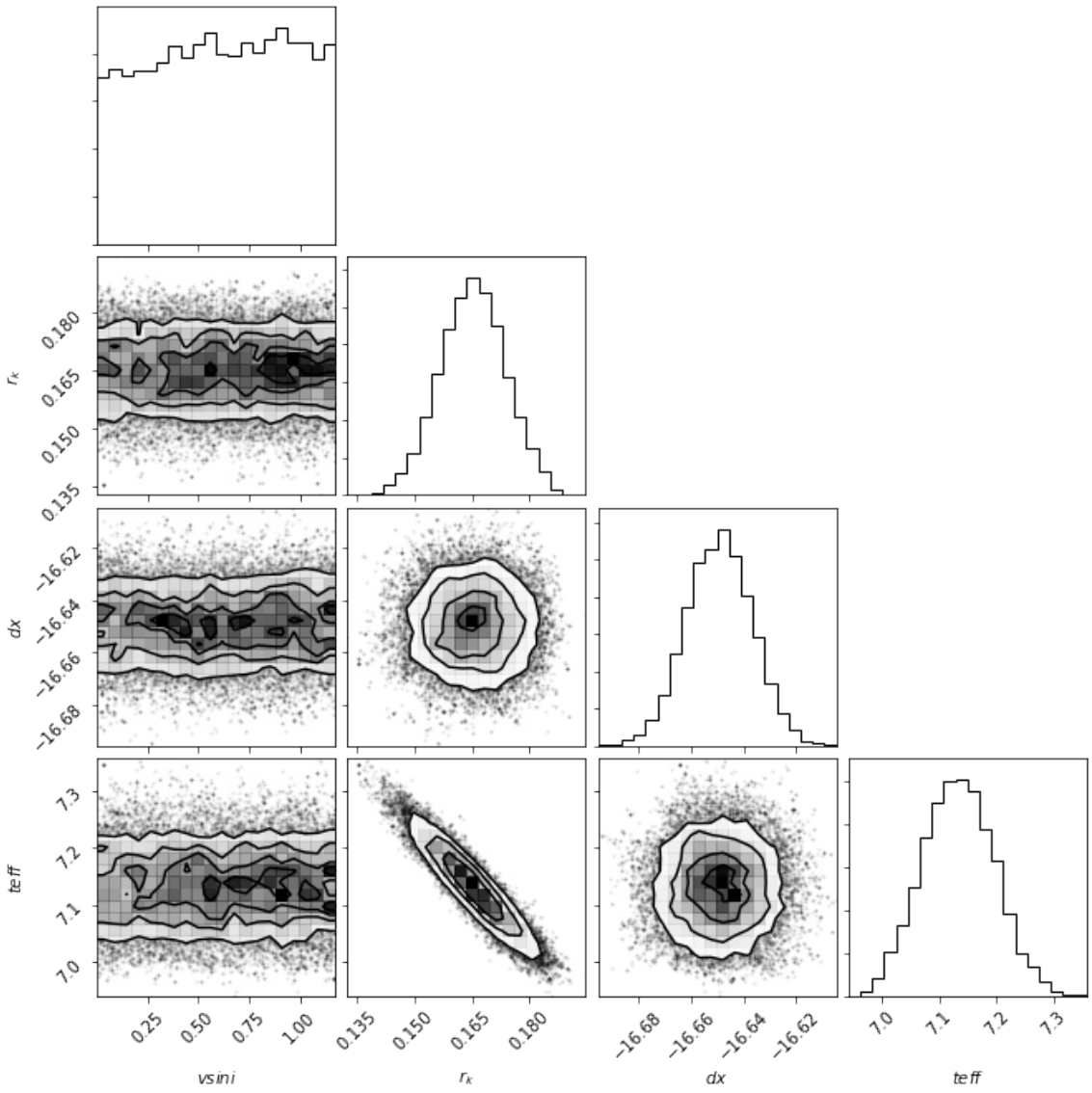

Figure 91 Relative probability distributions and correlations for the four fit parameters returned by *emcee* to best match the iSHELL spectrum of order 225 of radial velocity standard HD 156026 corresponding to $T = 4520 \pm 20$ K, $vsini = 0.61 \pm 0..9$ km s^{-1}, $r_k = 0.17 \pm 0.01$, and $dx = -16.65 \pm 0.01$.

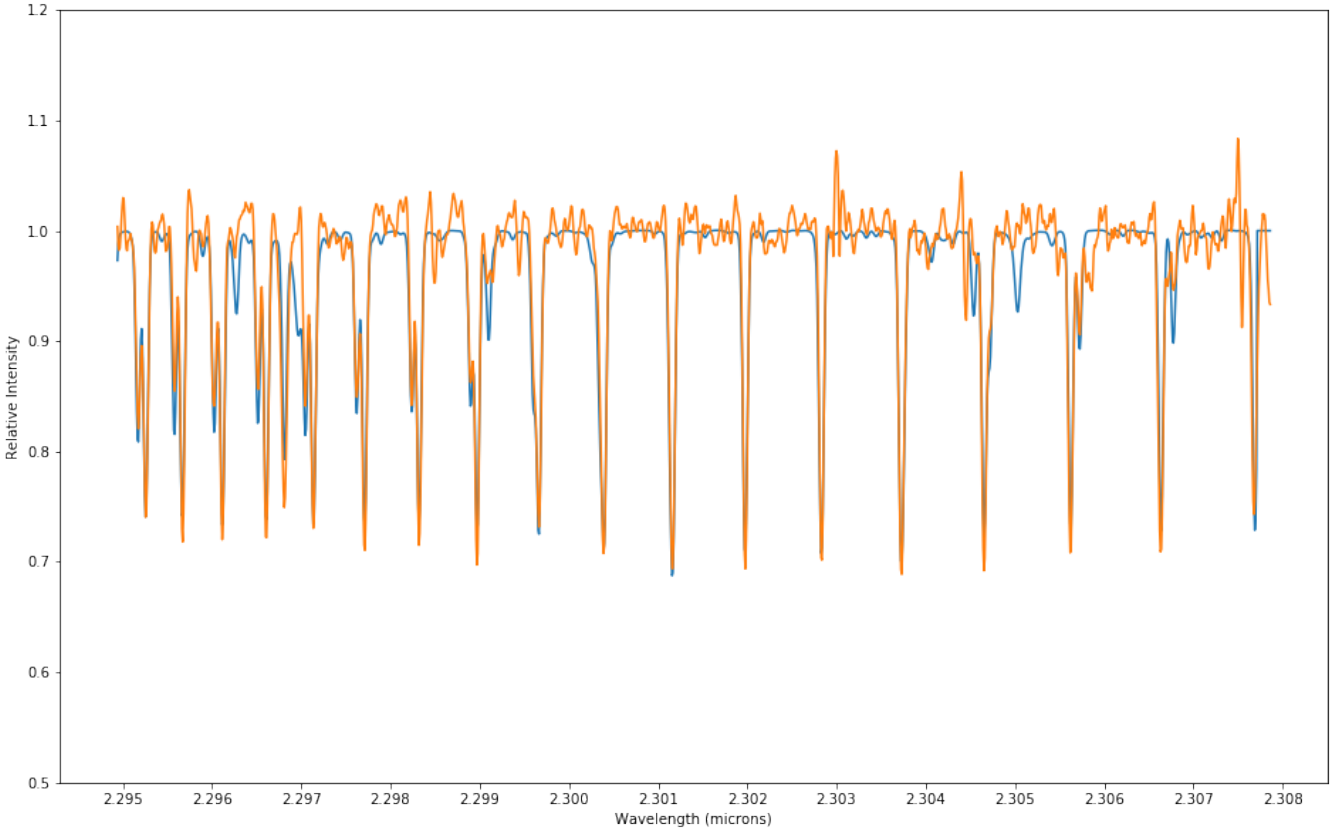

Figure 92 Synthetic overlay (blue) on top of the data (orange) for the four fit parameters returned by *emcee* to best match the iSHELL spectrum of order 225 of radial velocity standard HD 156026 corresponding to $T = 4520 \pm 20$ K, $vsini = 0.61 \pm 0..9$ km s^{-1}, $r_k = 0.17 \pm 0.01$, and $dx = -16.65 \pm 0.01$.

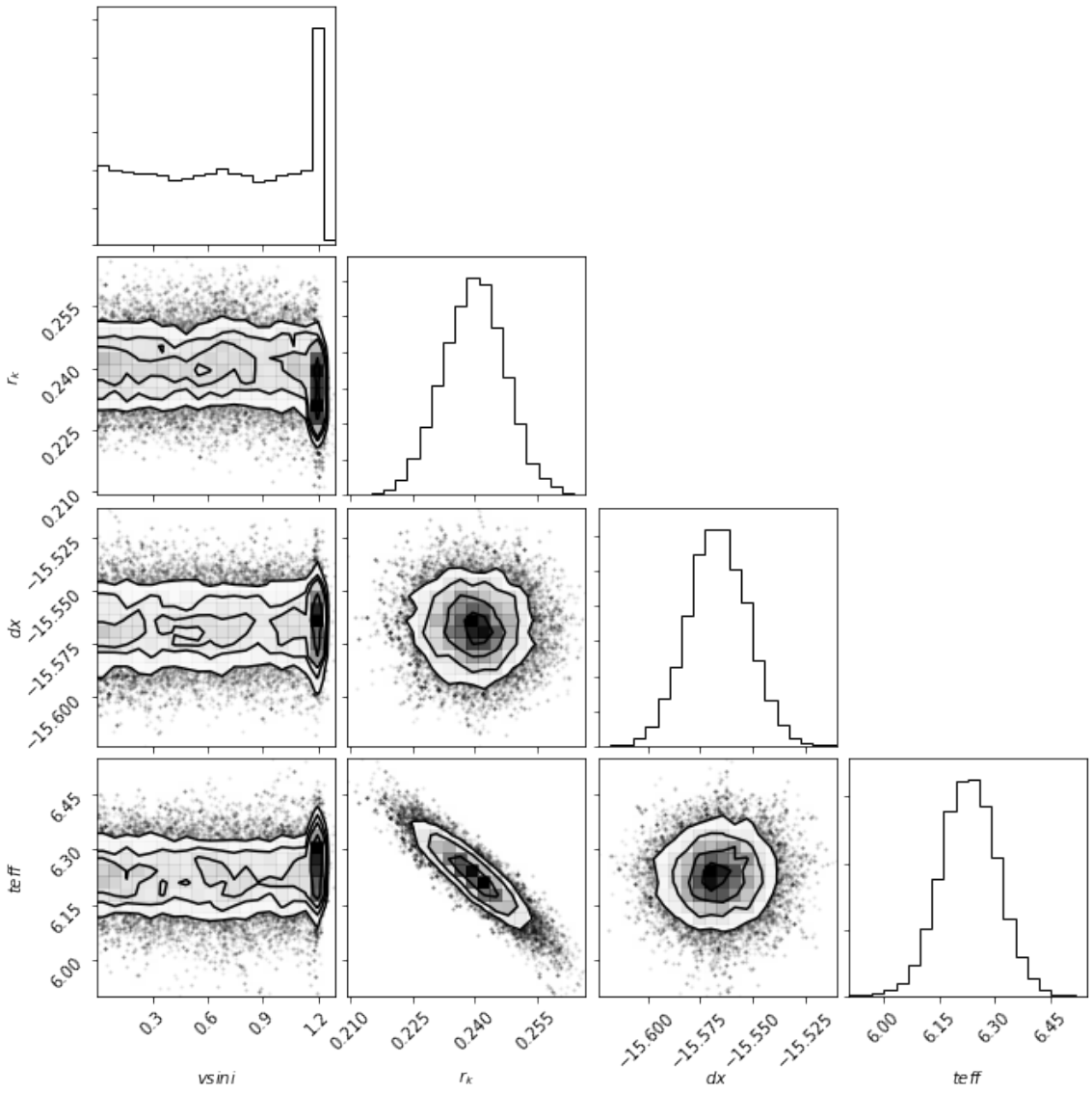

Figure 93 Relative probability distributions and correlations for the four fit parameters returned by *emcee* to best match the iSHELL spectrum of order 226 of radial velocity standard HD 1560262 corresponding to $T = 4340 \pm 20$ K, $vsini = 0.68 \pm 0.48$ km s^{-1}, $r_k = 0.24 \pm 0.01$, and $dx = -15.57 \pm 0.01$.

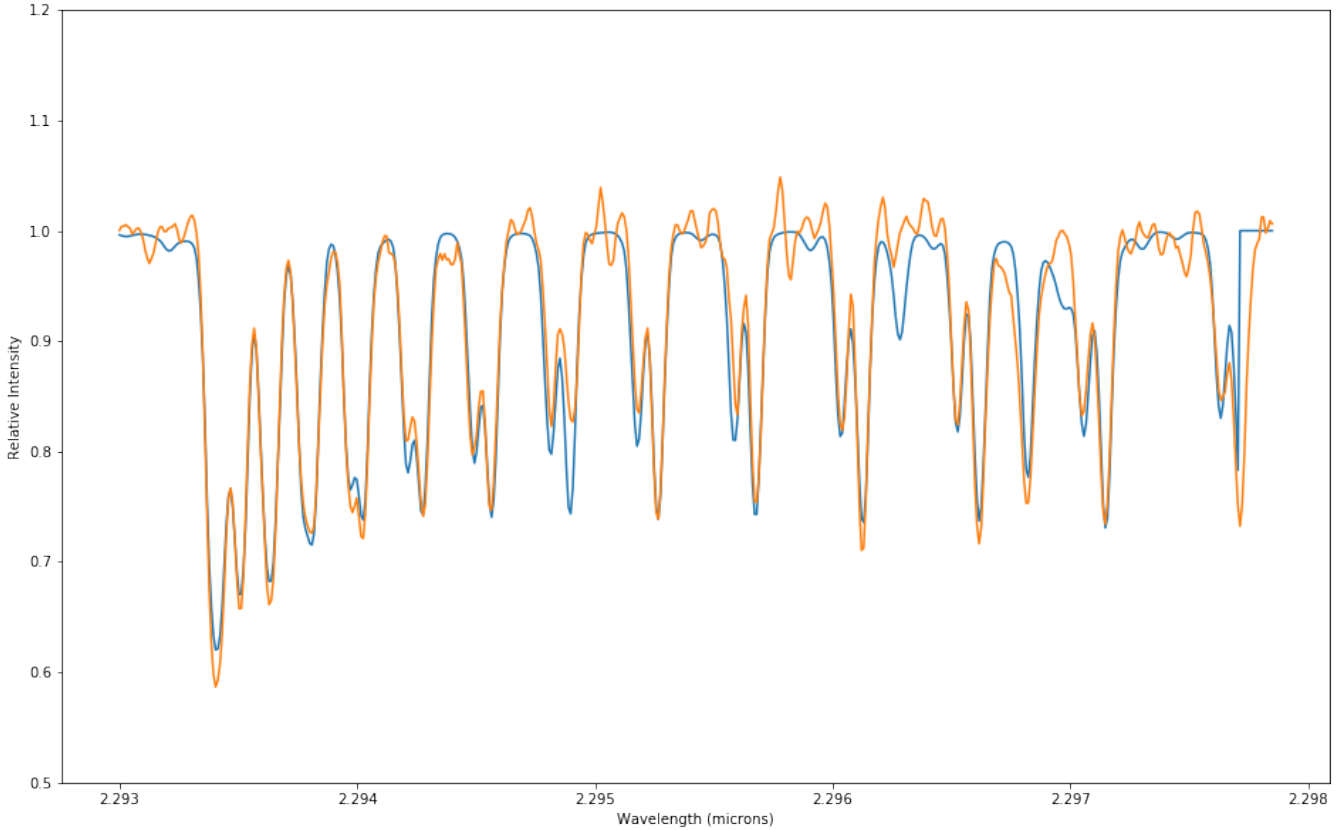

Figure 94 Synthetic overlay (blue) on top of the data (orange) for the four fit parameters returned by *emcee* to best match the iSHELL spectrum of order 226 of radial velocity standard HD 156026 corresponding to $T = 4340 \pm 20$ K, $vsini = 0.68 \pm 0.48$ km s^{-1}, $r_k = 0.24 \pm 0.01$, and $dx = -15.57 \pm 0.01$.

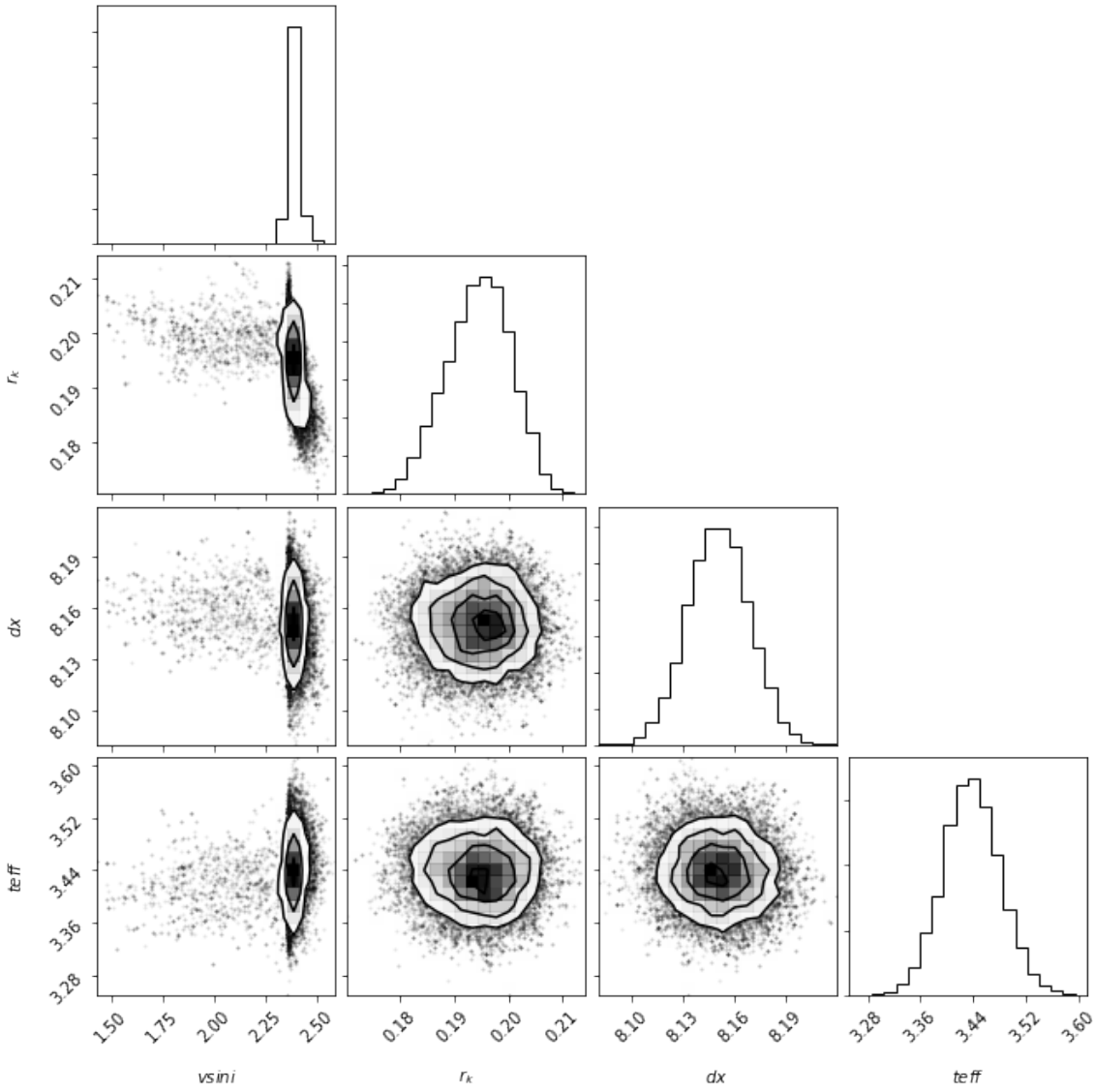

Figure 95 Relative probability distributions and correlations for the four fit parameters returned by *emcee* to best match the iSHELL spectrum of order 224 of radial velocity standard HD 165222 corresponding to $T = 3780 \pm 20$ K, $vsini = 2.37 \pm 0.03$ km s^{-1}, $r_k = 0.19 \pm 0.01$, and $dx = 8.15 \pm 0.02$.

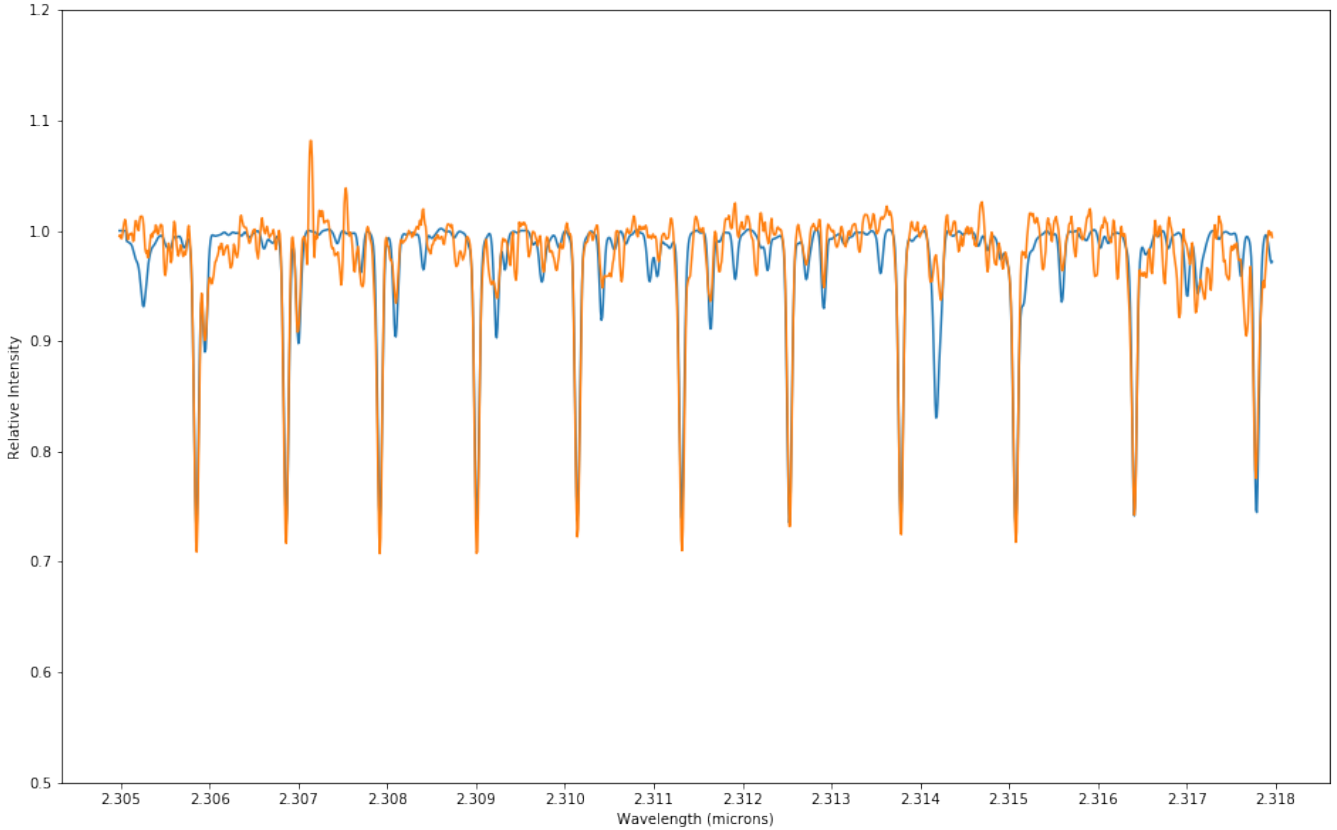

Figure 96 Synthetic overlay (blue) on top of the data (orange) for the four fit parameters returned by *emcee* to best match the iSHELL spectrum of order 224 of radial velocity standard HD 165222 corresponding to $T = 3780 \pm 20$ K, $vsini = 2.37 \pm 0.03$ km s^{-1}, $r_k = 0.19 \pm 0.01$, and $dx = 8.15 \pm 0.02$.

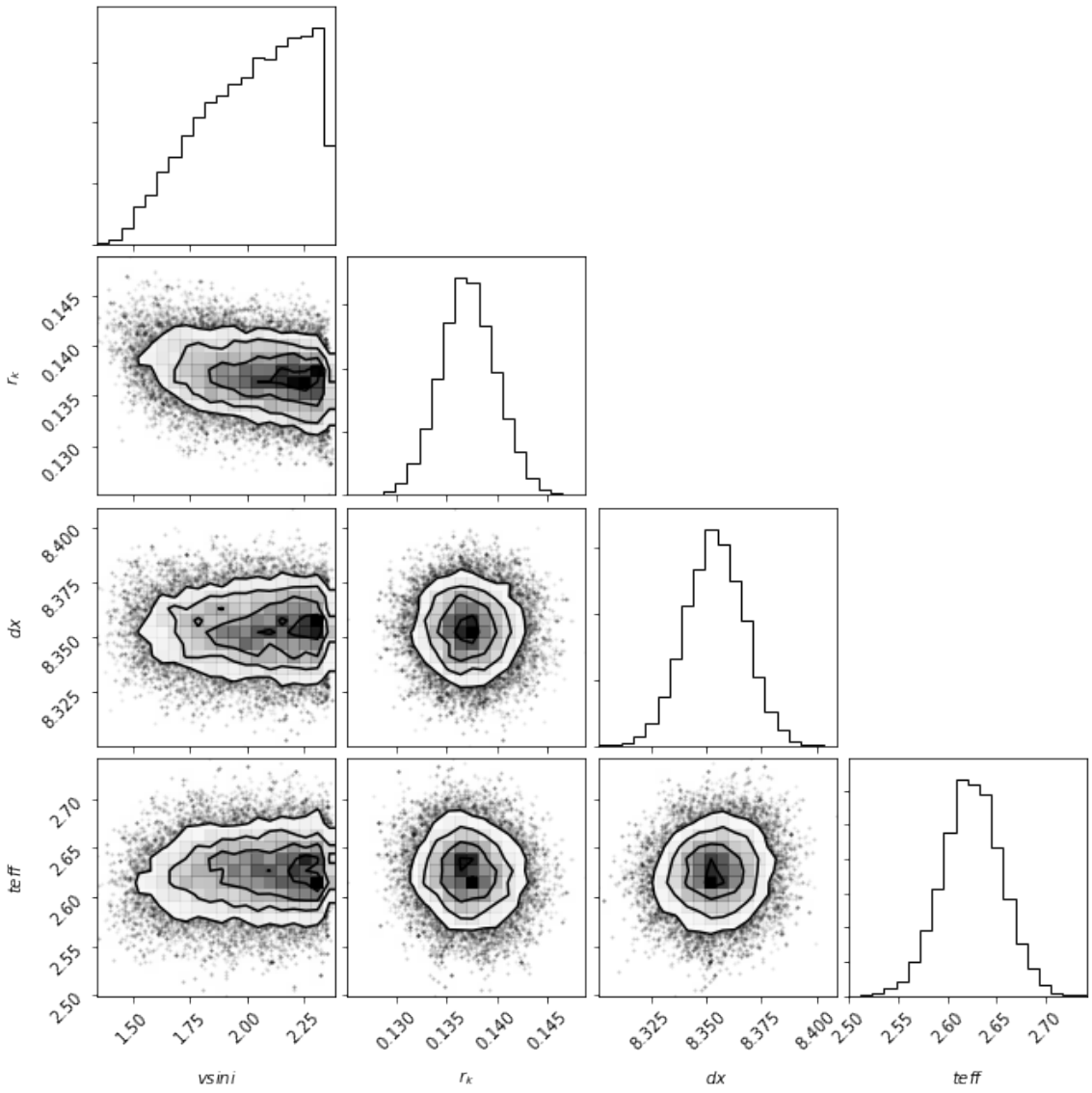

Figure 97 Relative probability distributions and correlations for the four fit parameters returned by *emcee* to best match the iSHELL spectrum of order 225 of radial velocity standard HD 165222 corresponding to T = 3620 ± 20 K, $vsini$ = 2.05 ± 0.25 km s^{-1}, r_k = 0.14 ± 0.01, and dx = 8.35 ± 0.01.

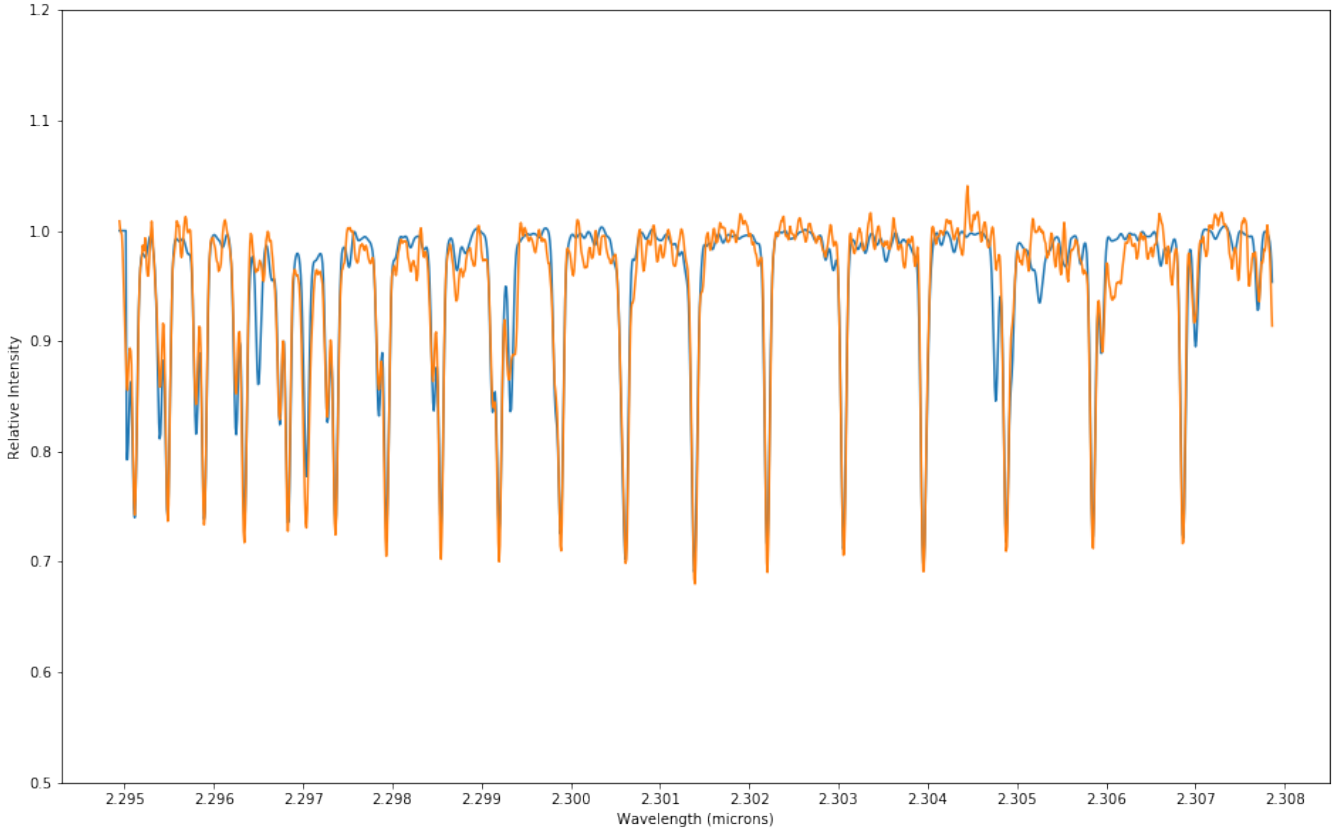

Figure 98 Synthetic overlay (blue) on top of the data (orange) for the four fit parameters returned by *emcee* to best match the iSHELL spectrum of order 225 of radial velocity standard HD 165222 corresponding to $T = 3620 \pm 20$ K, $vsini = 2.05 \pm 0.25$ km s^{-1}, $r_k = 0.14 \pm 0.01$, and $dx = 8.35 \pm 0.01$.

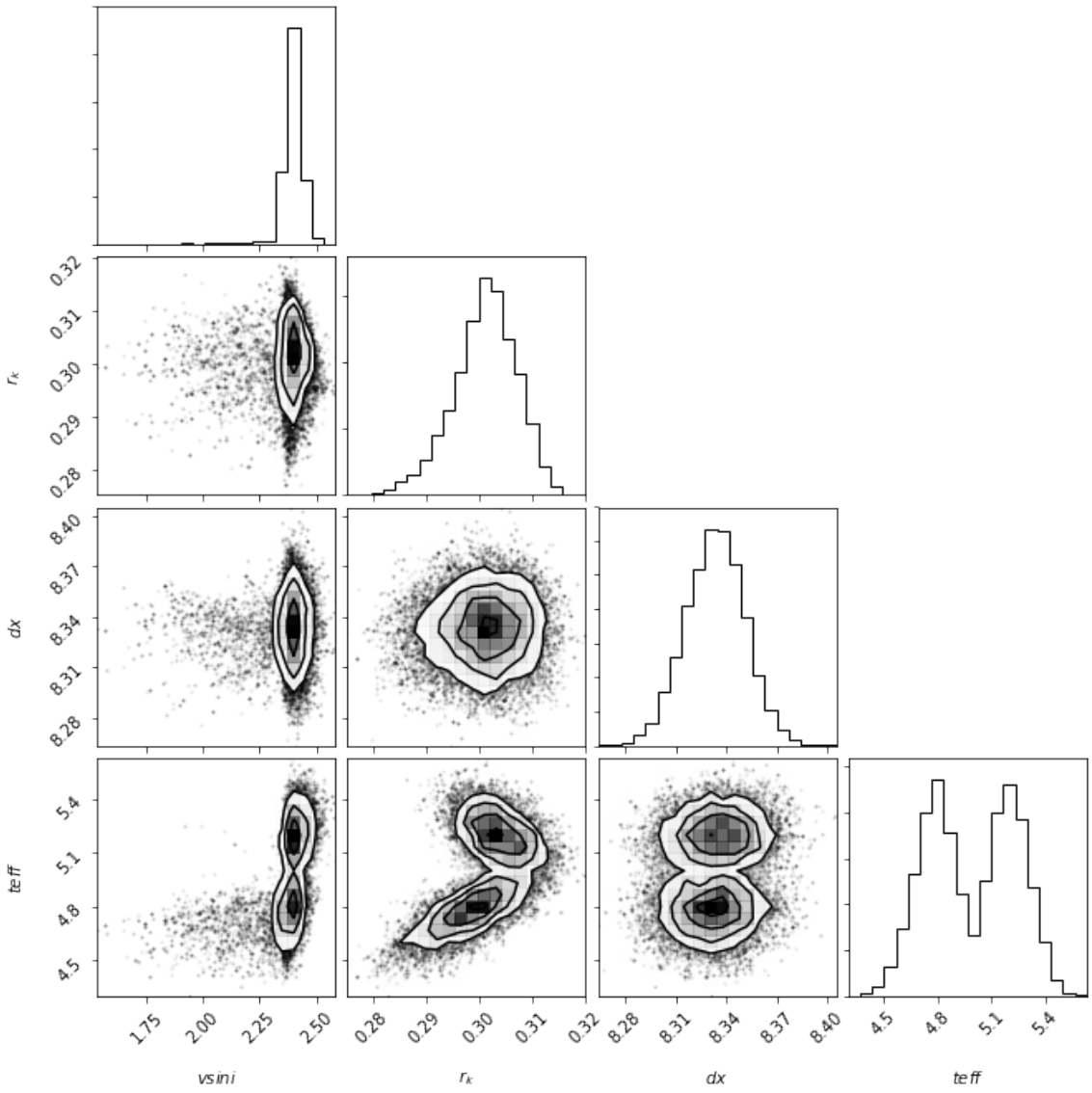

Figure 99 Relative probability distributions and correlations for the four fit parameters returned by *emcee* to best match the iSHELL spectrum of order 226 of radial velocity standard HD 165222 corresponding to $T = 4100 \pm 60$ K, $vsini = 2.39 \pm 0.04$ km s^{-1}, $r_k = 0.30 \pm 0.01$, and $dx = 8.33 \pm 0.02$.

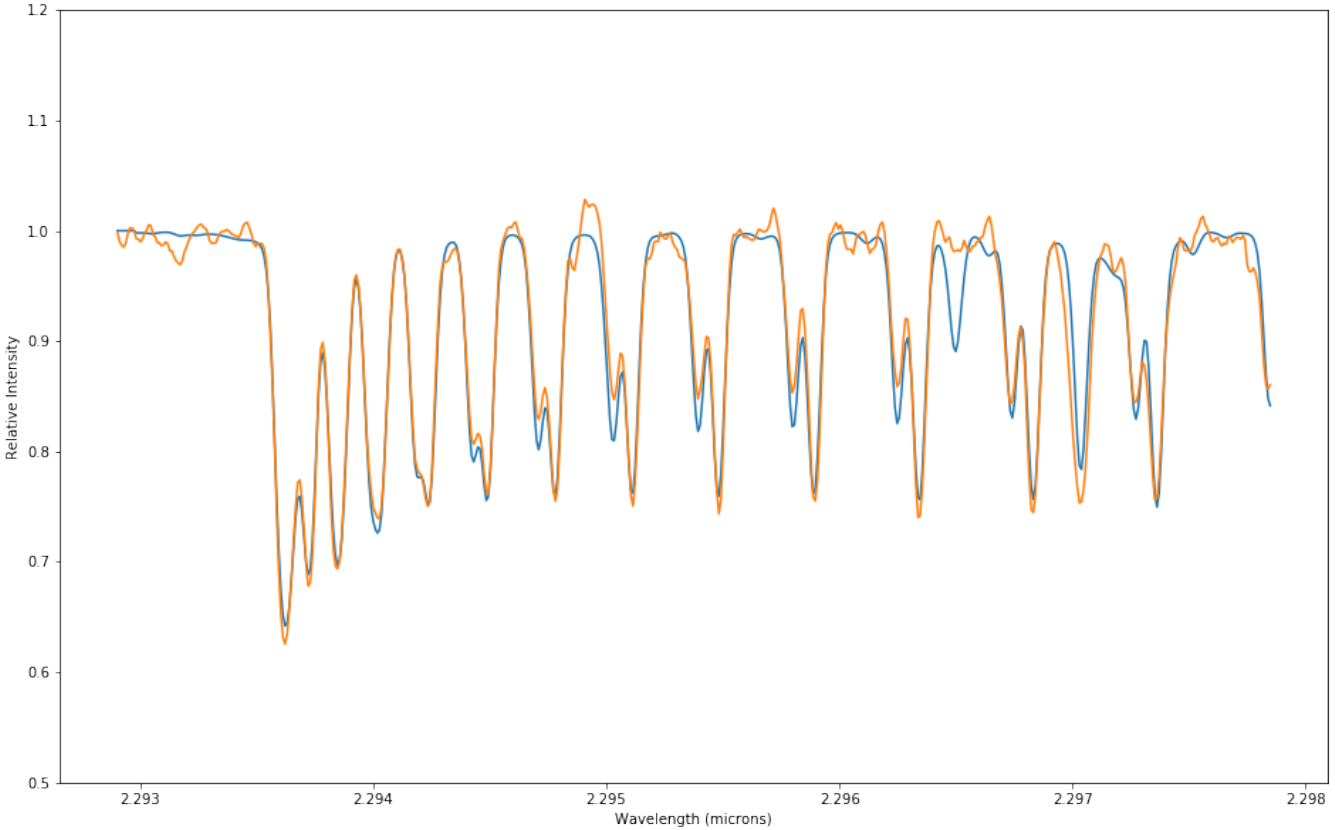

Figure 100 Synthetic overlay (blue) on top of the data (orange) for the four fit parameters returned by *emcee* to best match the iSHELL spectrum of order 226 of radial velocity standard HD 165222 corresponding to $T = 4100 \pm 60$ K, $vsini = 2.39 \pm 0.04$ km s^{-1}, $r_k = 0.30 \pm 0.01$, and $dx = 8.33 \pm 0.02$.

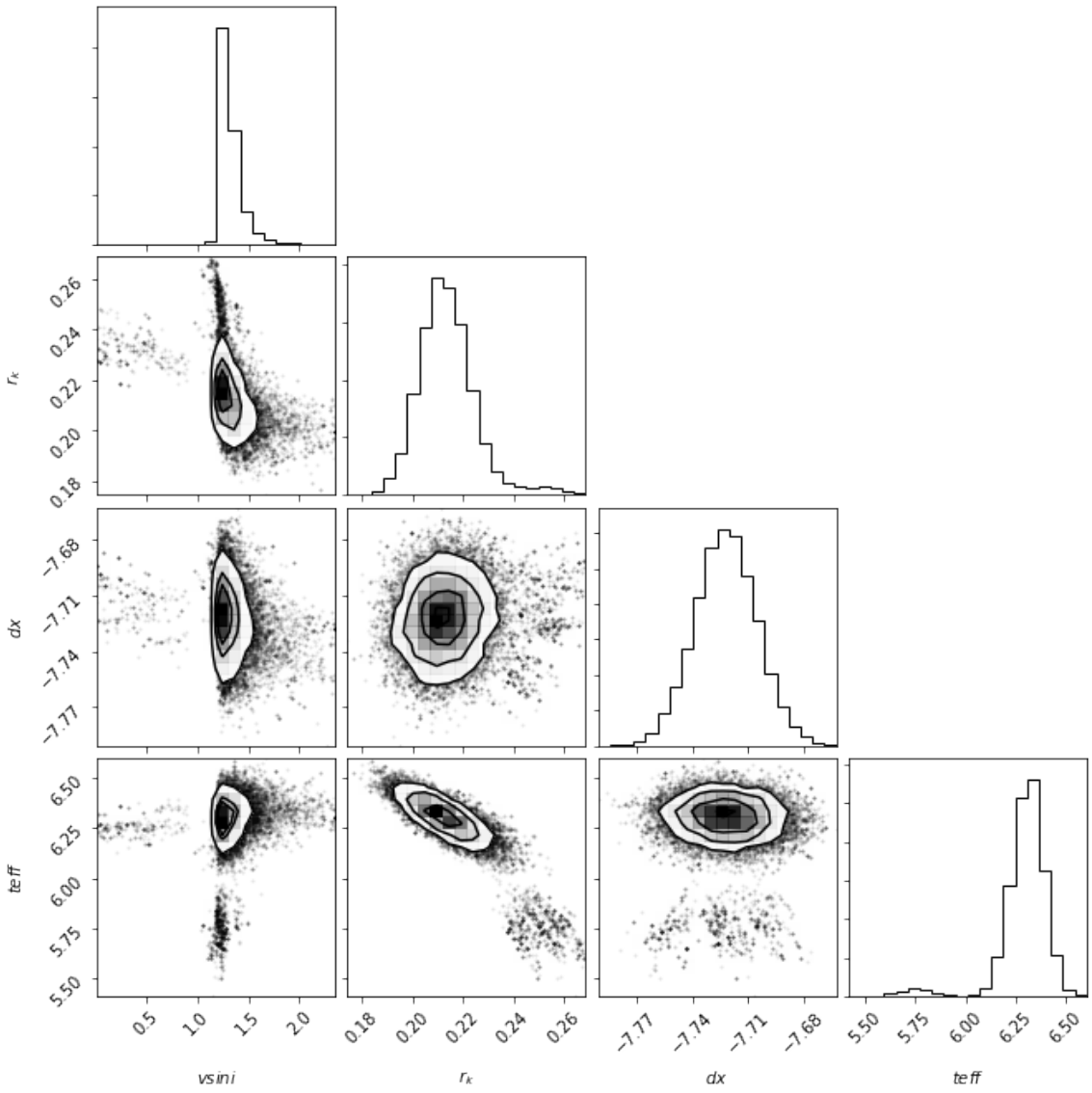

Figure 101 Relative probability distributions and correlations for the four fit parameters returned by *emcee* to best match the iSHELL spectrum of order 224 of radial velocity standard HD 173818 corresponding to $T = 4360 \pm 20$ K, $vsini = 1.29 \pm 0.09$ km s^{-1}, $r_k = 0.21 \pm 0.01$, and $dx = -7.72 \pm 0.02$.

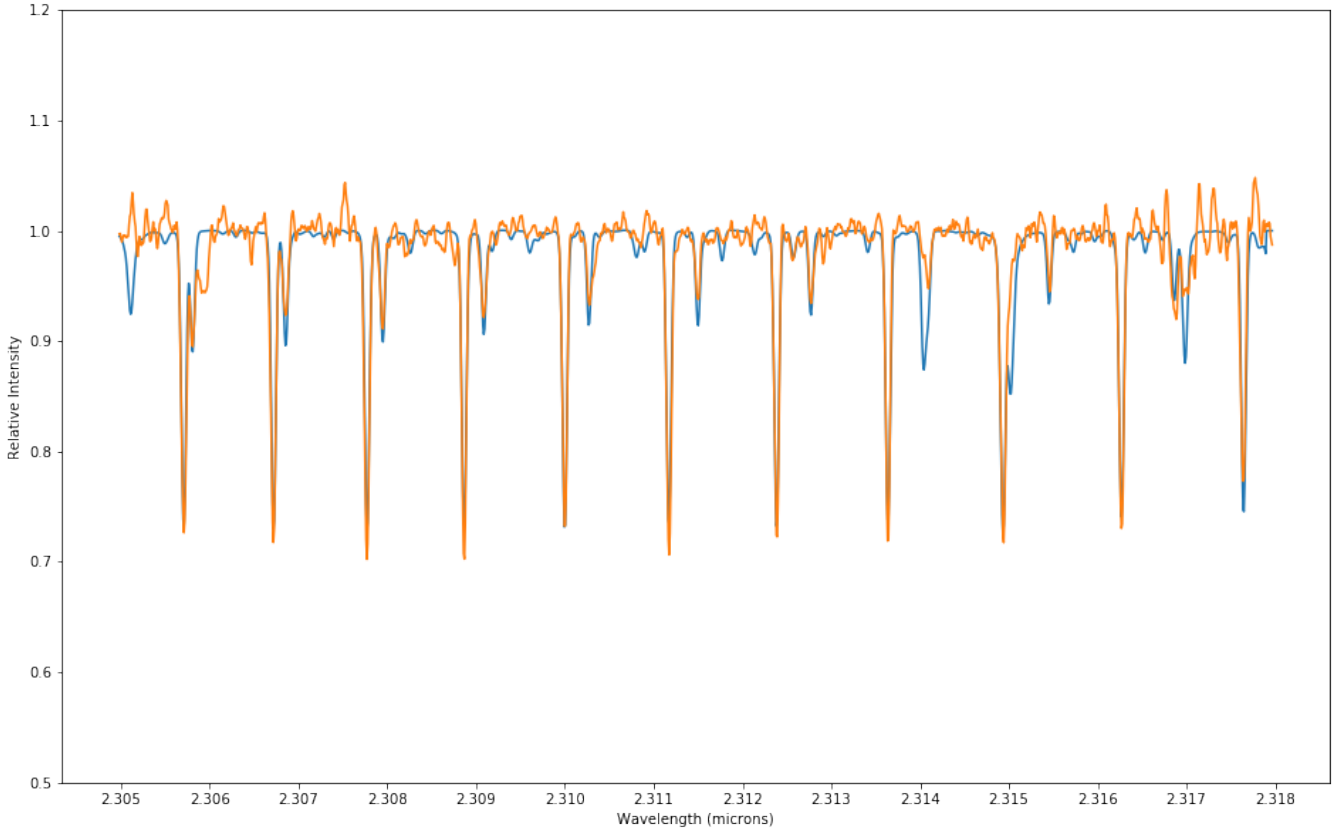

Figure 102 Synthetic overlay (blue) on top of the data (orange) for the four fit parameters returned by *emcee* to best match the iSHELL spectrum of order 224 of radial velocity standard HD 173818 corresponding to $T = 4360 \pm 20$ K, $vsini = 1.29 \pm 0.09$ km s^{-1}, $r_k = 0.21 \pm 0.01$, and $dx = -7.72 \pm 0.02$.

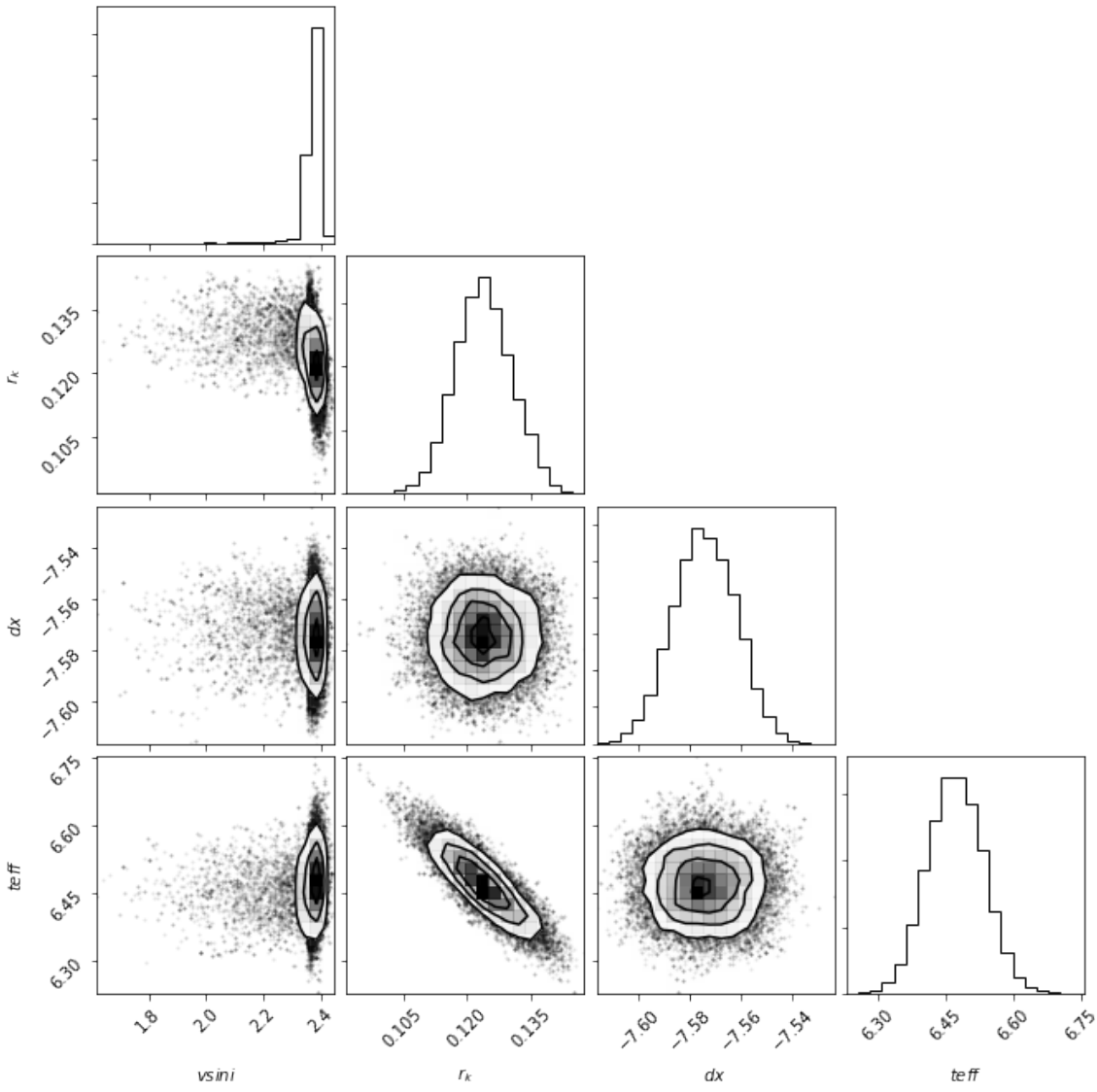

Figure 103 Relative probability distributions and correlations for the four fit parameters returned by *emcee* to best match the iSHELL spectrum of order 225 of radial velocity standard HD 173818 corresponding to $T = 4400 \pm 20$ K, $vsini = 2.37 \pm 0.02$ km s^{-1}, $r_k = 0.12 \pm 0.01$, and $dx = -7.57 \pm 0.01$.

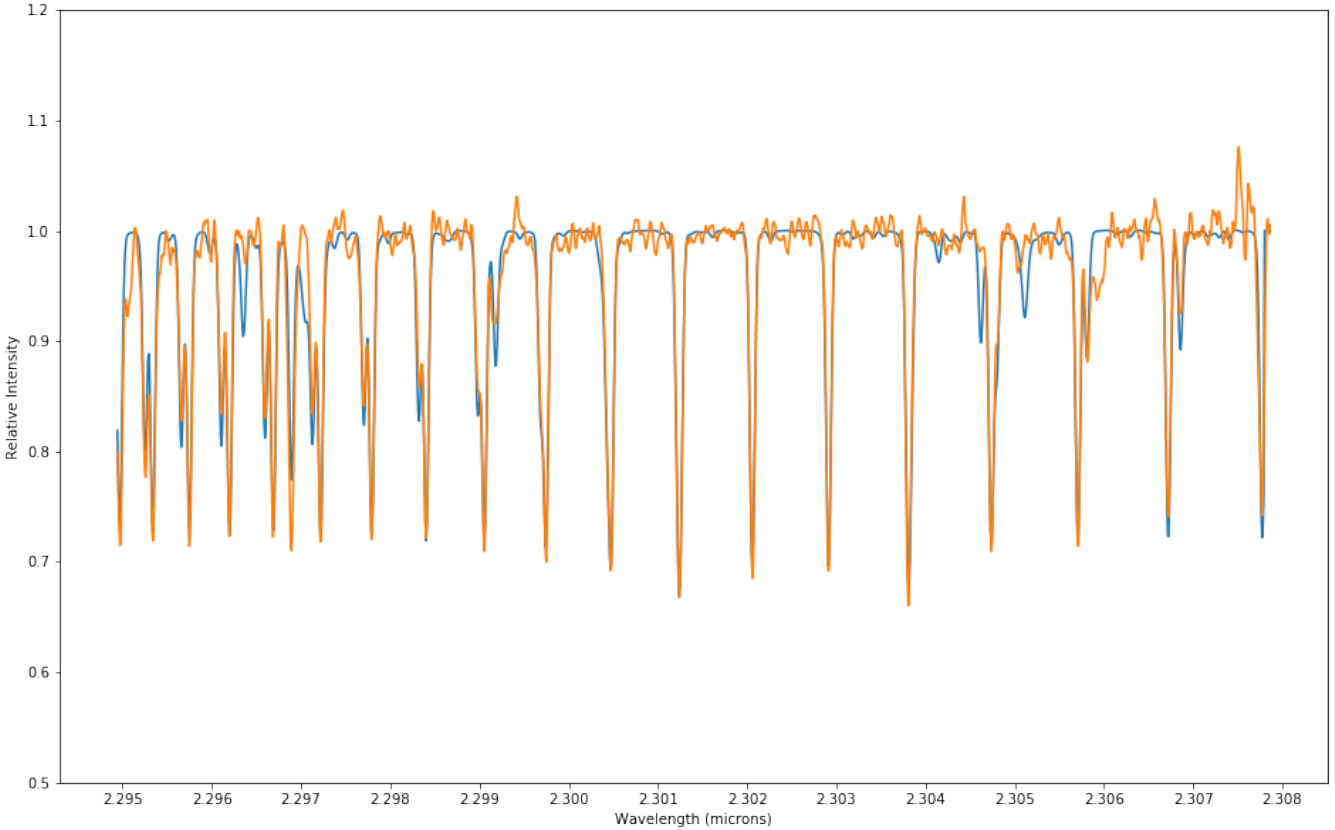

Figure 104 Synthetic overlay (blue) on top of the data (orange) for the four fit parameters returned by *emcee* to best match the iSHELL spectrum of order 225 of radial velocity standard HD 173818 corresponding to $T = 4400 \pm 20$ K, $vsini = 2.37 \pm 0.02$ km s^{-1}, $r_k = 0.12 \pm 0.01$, and $dx = -7.57 \pm 0.01$.

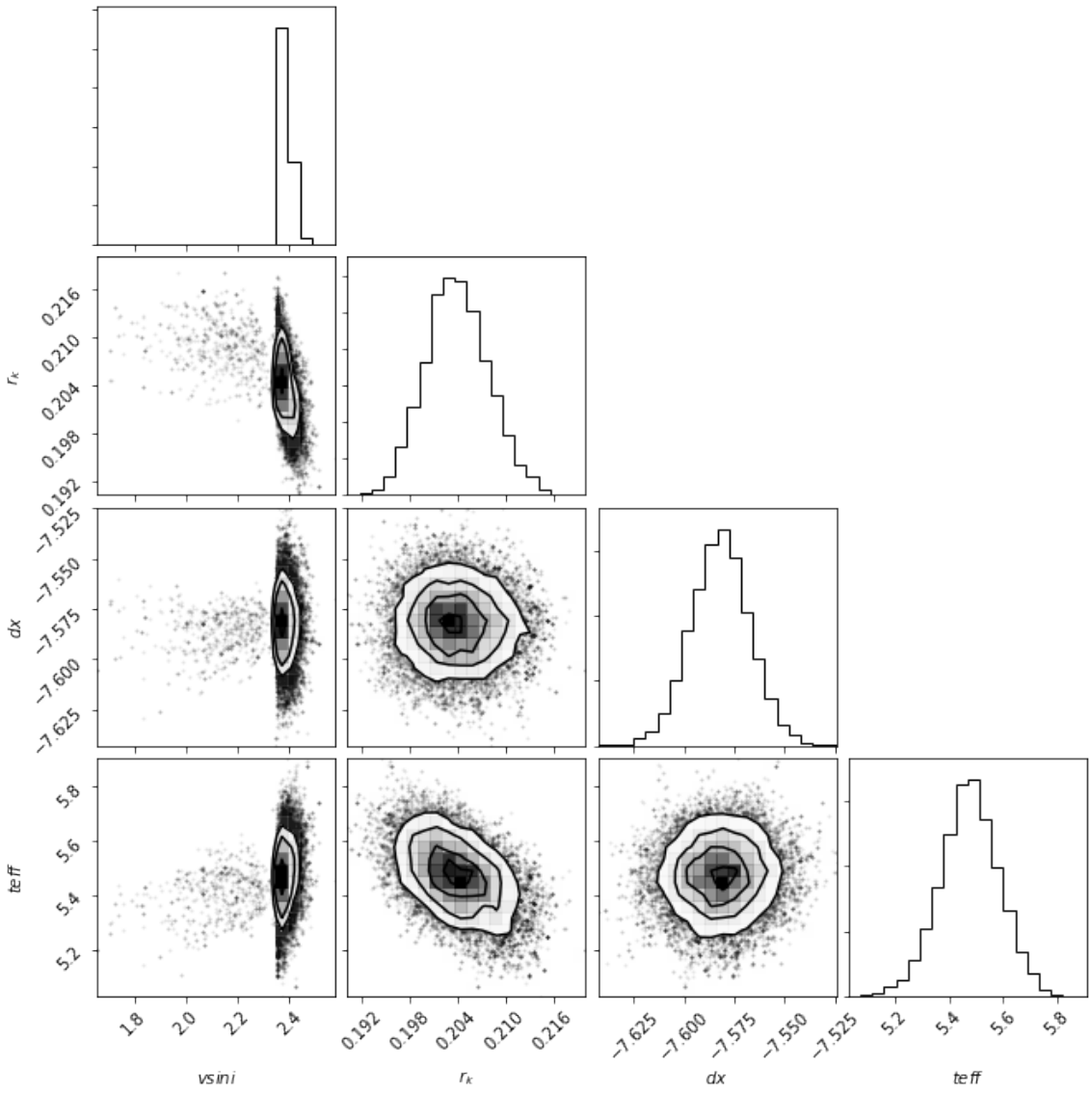

Figure 105 Relative probability distributions and correlations for the four fit parameters returned by *emcee* to best match the iSHELL spectrum of order 226 of radial velocity standard HD 173818 corresponding to $T = 4200 \pm 20$ K, $vsini = 2.38 \pm 0.03$ km s^{-1}, $r_k = 0.20 \pm 0.01$, and $dx = -7.58 \pm 0.01$.

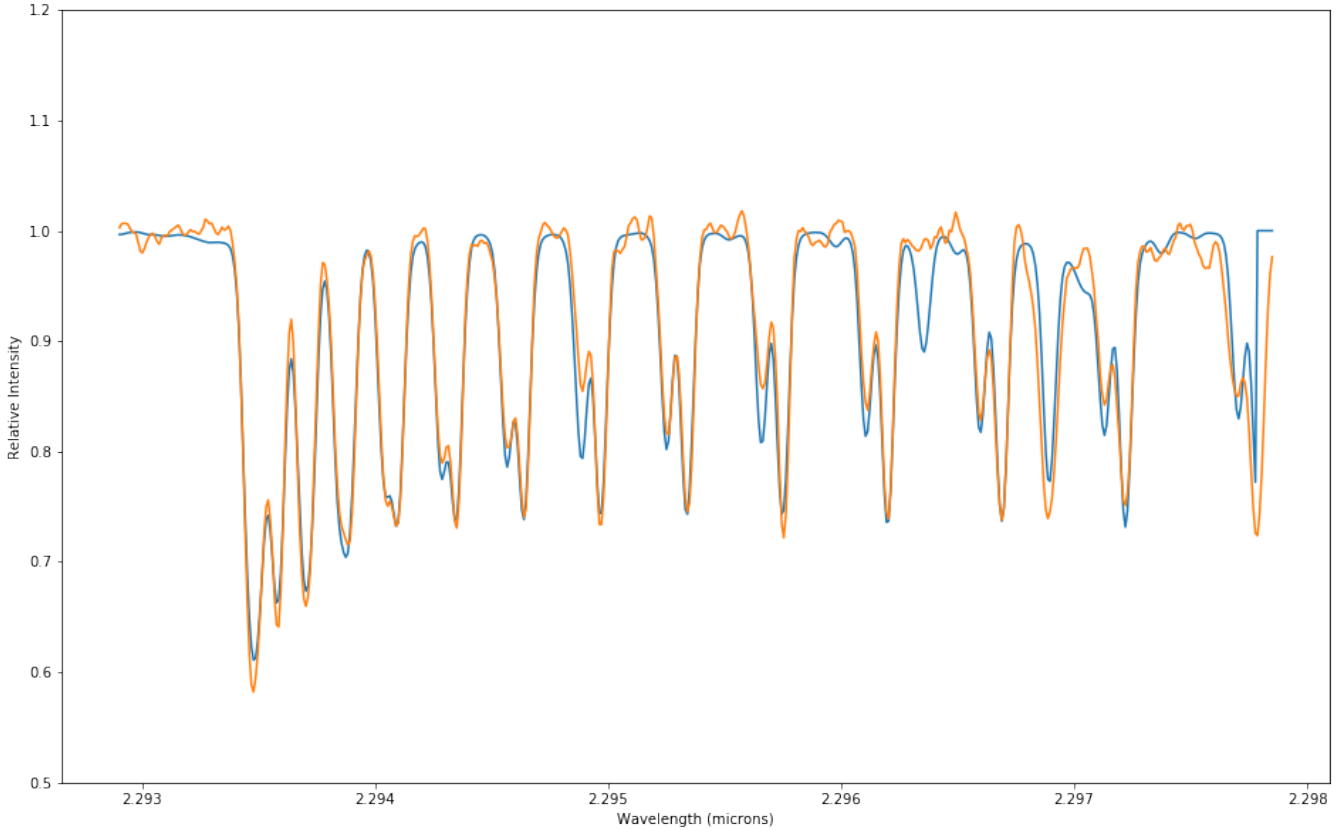

Figure 106 Synthetic overlay (blue) on top of the data (orange) for the four fit parameters returned by *emcee* to best match the iSHELL spectrum of order 226 of radial velocity standard HD 173818 corresponding to $T = 4200 \pm 20$ K, $vsini = 2.38 \pm 0.03$ km s^{-1}, $r_k = 0.20 \pm 0.01$, and $dx = -7.58 \pm 0.01$.

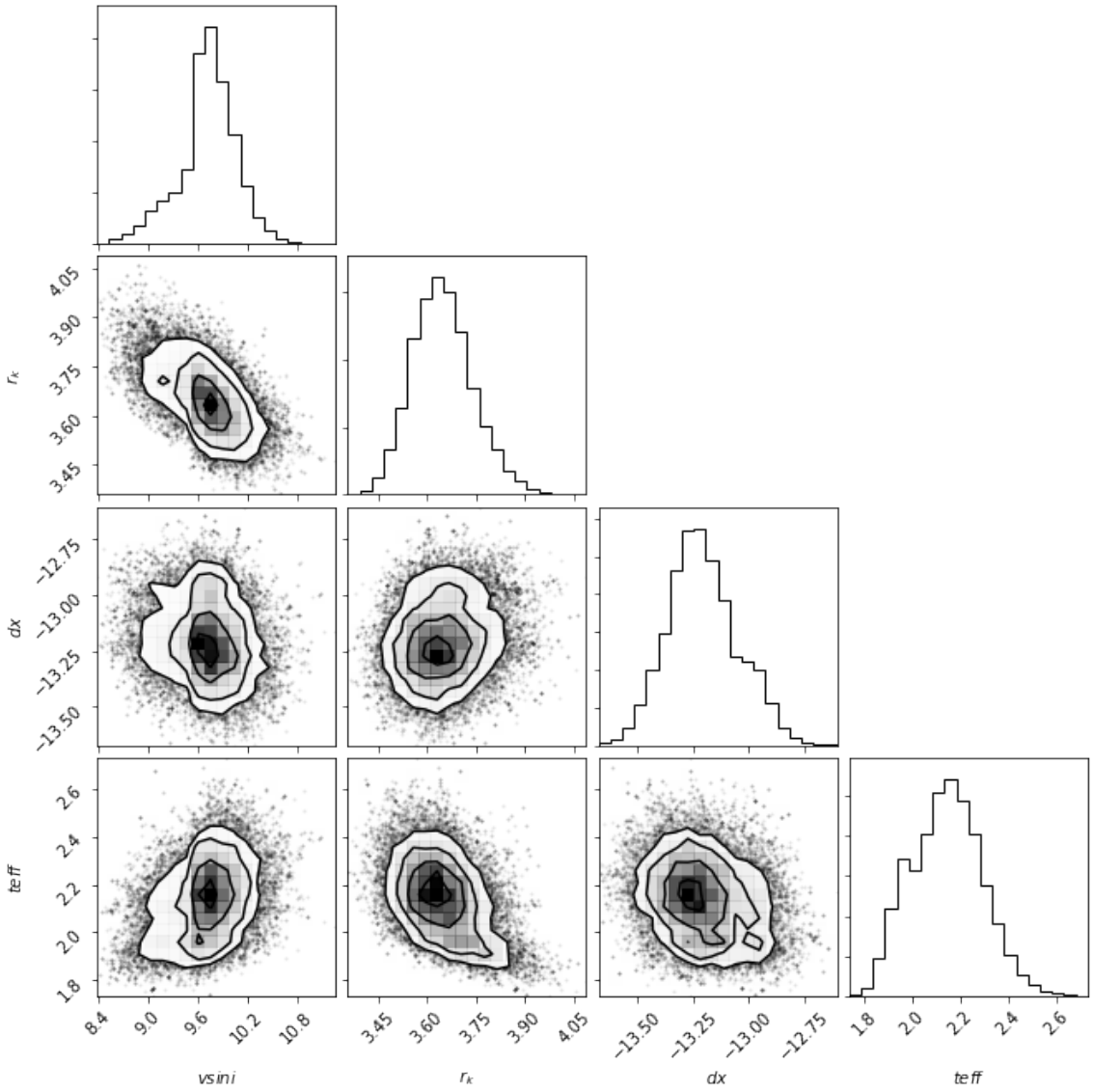

Figure 107 Relative probability distributions and correlations for the four fit parameters returned by *emcee* to best match the iSHELL spectrum of order 224 of object SR 24N corresponding to $T = 3520 \pm 40$ K, $vsini = 9.74 \pm 0.32$ km s^{-1}, $r_k = 3.64 \pm 0.09$, and $dx = -13.22 \pm 0.16$.

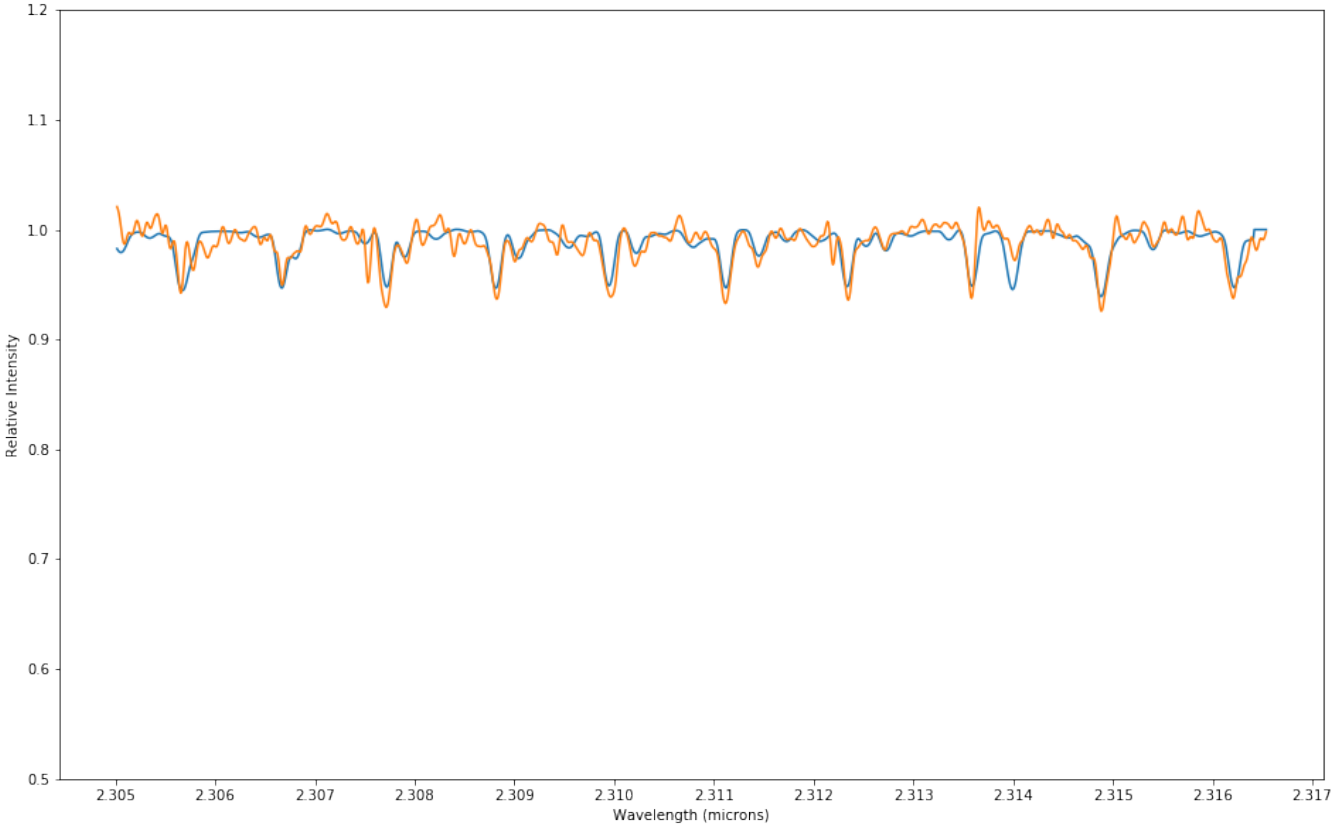

Figure 108 Synthetic overlay (blue) on top of the data (orange) for the four fit parameters returned by *emcee* to best match the iSHELL spectrum of order 224 of object SR 24N corresponding to $T = 3520 \pm 40$ K, $vsini = 9.74 \pm 0.32$ km s^{-1}, $r_k = 3.64 \pm 0.09$, and $dx = -13.22 \pm 0.16$.

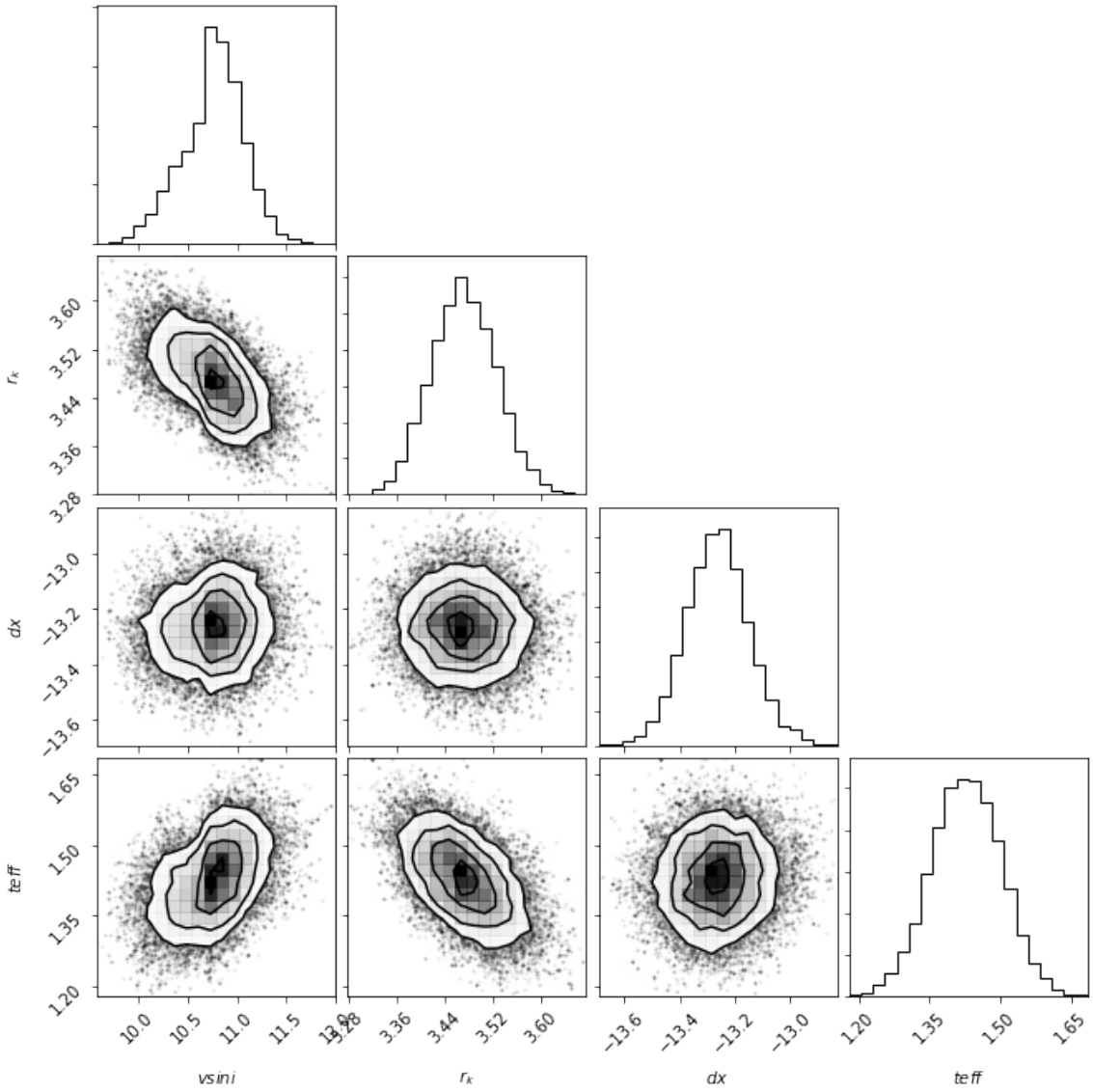

Figure 109 Relative probability distributions and correlations for the four fit parameters returned by *emcee* to best match the iSHELL spectrum of order 225 of object SR 24N corresponding to $T = 3380 \pm 20$ K, $vsini = 10.78 \pm 0.31$ km s^{-1}, $r_k = 3.47 \pm 0.05$, and $dx = -13.26 \pm 0.11$.

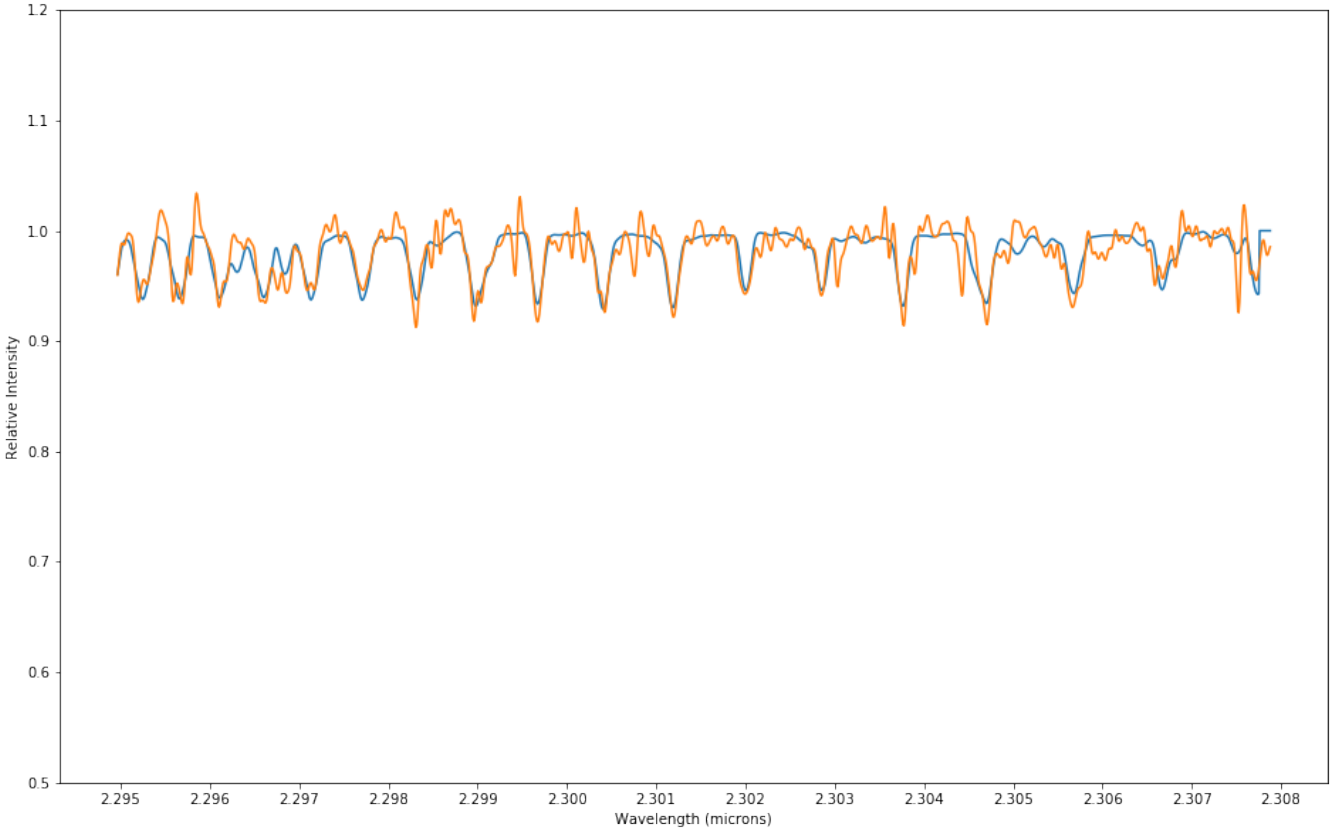

Figure 110 Synthetic overlay (blue) on top of the data (orange) for the four fit parameters returned by *emcee* to best match the iSHELL spectrum of order 225 of object SR 24N corresponding to $T = 3380 \pm 20$ K, $vsini = 10.78 \pm 0.31$ km s^{-1}, $r_k = 3.47 \pm 0.05$, and $dx = -13.26 \pm 0.11$.

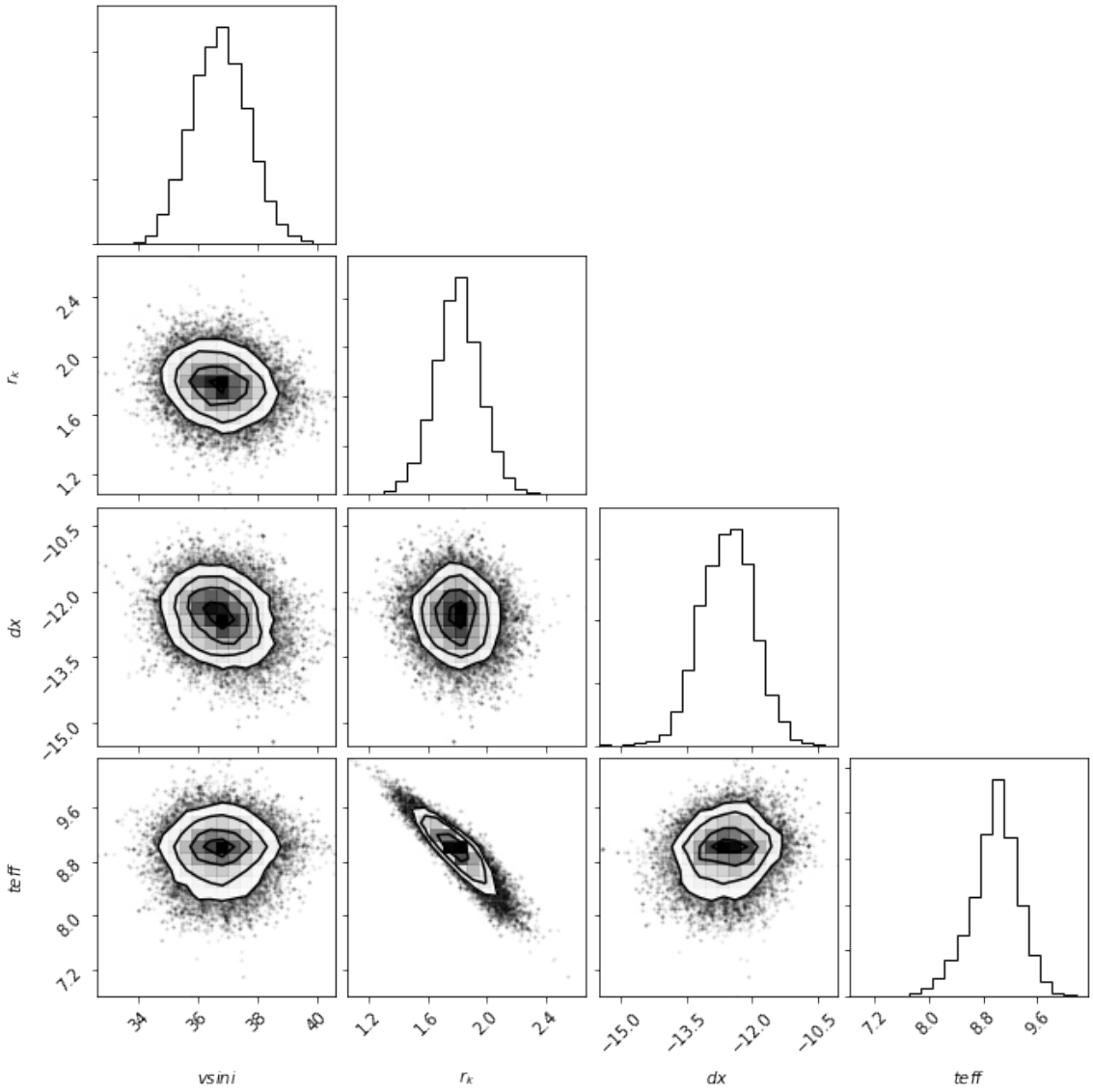

Figure 111 Relative probability distributions and correlations for the four fit parameters returned by *emcee* to best match the iSHELL spectrum of order 224 of object SR 24S corresponding to $T = 4900 \pm 70$ K, $vsini = 36.73 \pm 0.95$ km s^{-1}, $r_k = 1.80 \pm 0.15$, and $dx = -12.56 \pm 0.60$.

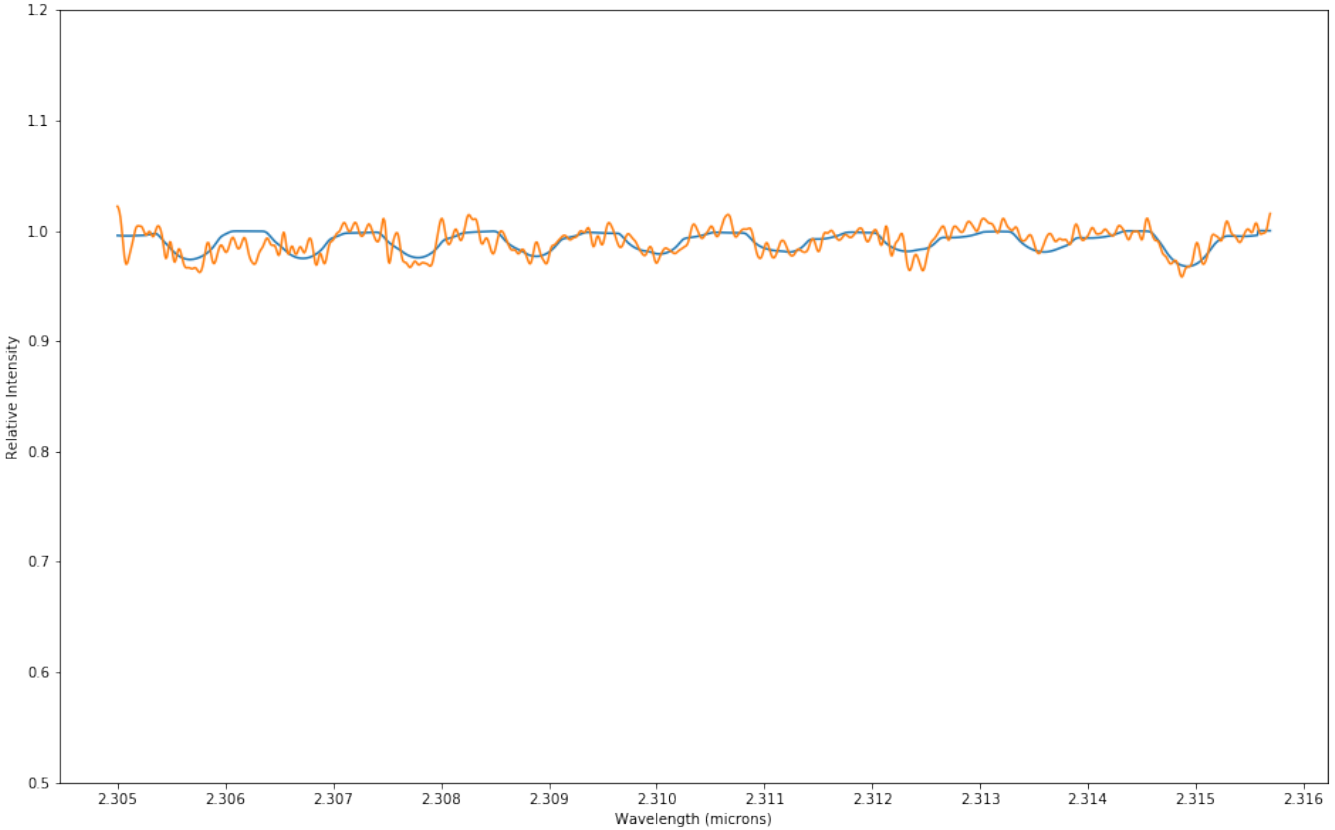

Figure 112 Synthetic overlay (blue) on top of the data (orange) for the four fit parameters returned by *emcee* to best match the iSHELL spectrum of order 224 of object SR 24S corresponding to $T = 4900 \pm 70$ K, $vsini = 36.73 \pm 0.95$ km s^{-1}, $r_k = 1.80 \pm 0.15$, and $dx = -12.56 \pm 0.60$.

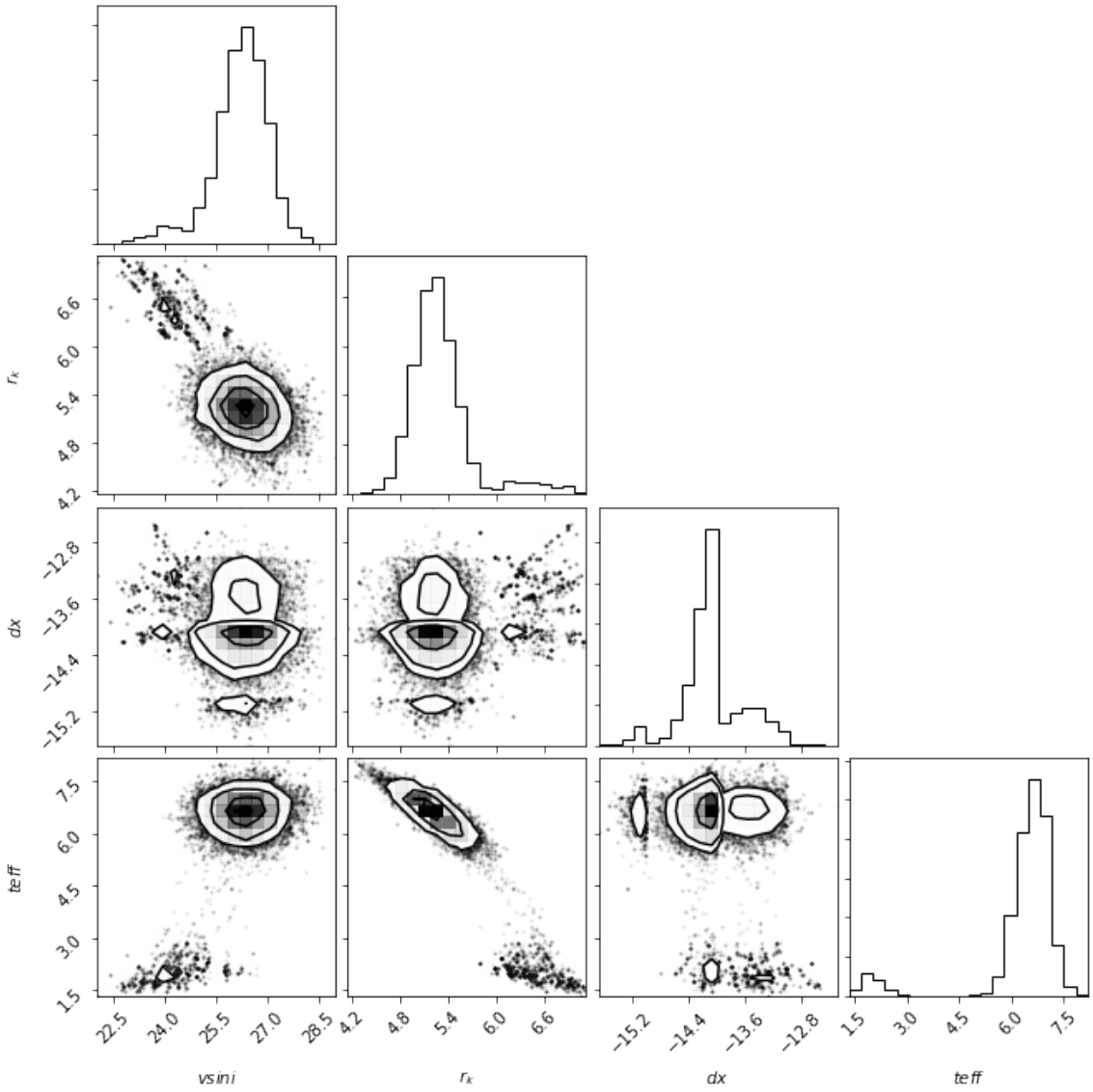

Figure 113 Relative probability distributions and correlations for the four fit parameters returned by *emcee* to best match the iSHELL spectrum of order 225 of object SR 24S corresponding to $T = 4420 \pm 100$ K, $vsini = 26.29 \pm 0.71$ km s^{-1}, $r_k = 5.24 \pm 0.28$, and $dx = -14.10 \pm 0.39$.

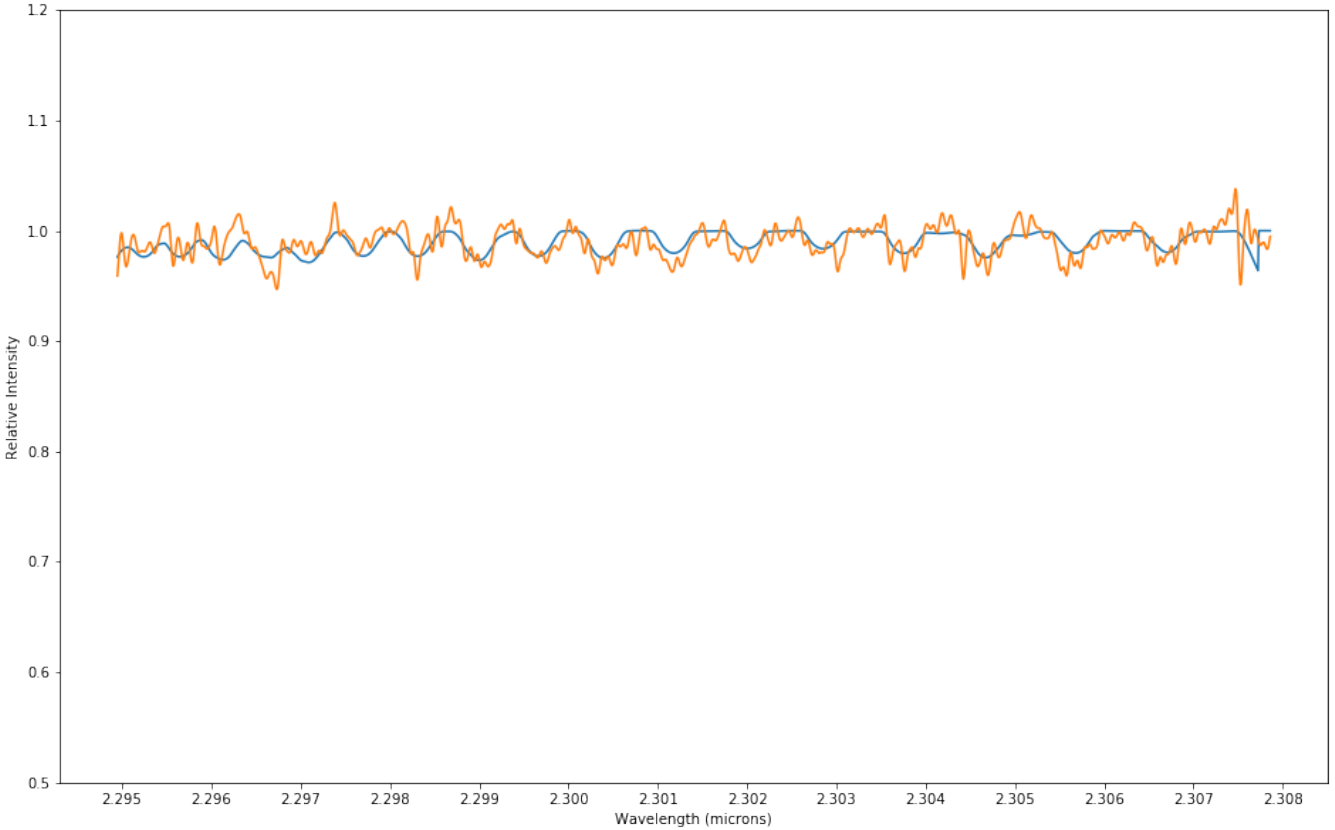

Figure 114 Synthetic overlay (blue) on top of the data (orange) for the four fit parameters returned by *emcee* to best match the iSHELL spectrum of order 225 of object SR 24S corresponding to $T = 4420 \pm 100$ K, $vsini = 26.29 \pm 0.71$ km s^{-1}, $r_k = 5.24 \pm 0.28$, and $dx = -14.10 \pm 0.39$.

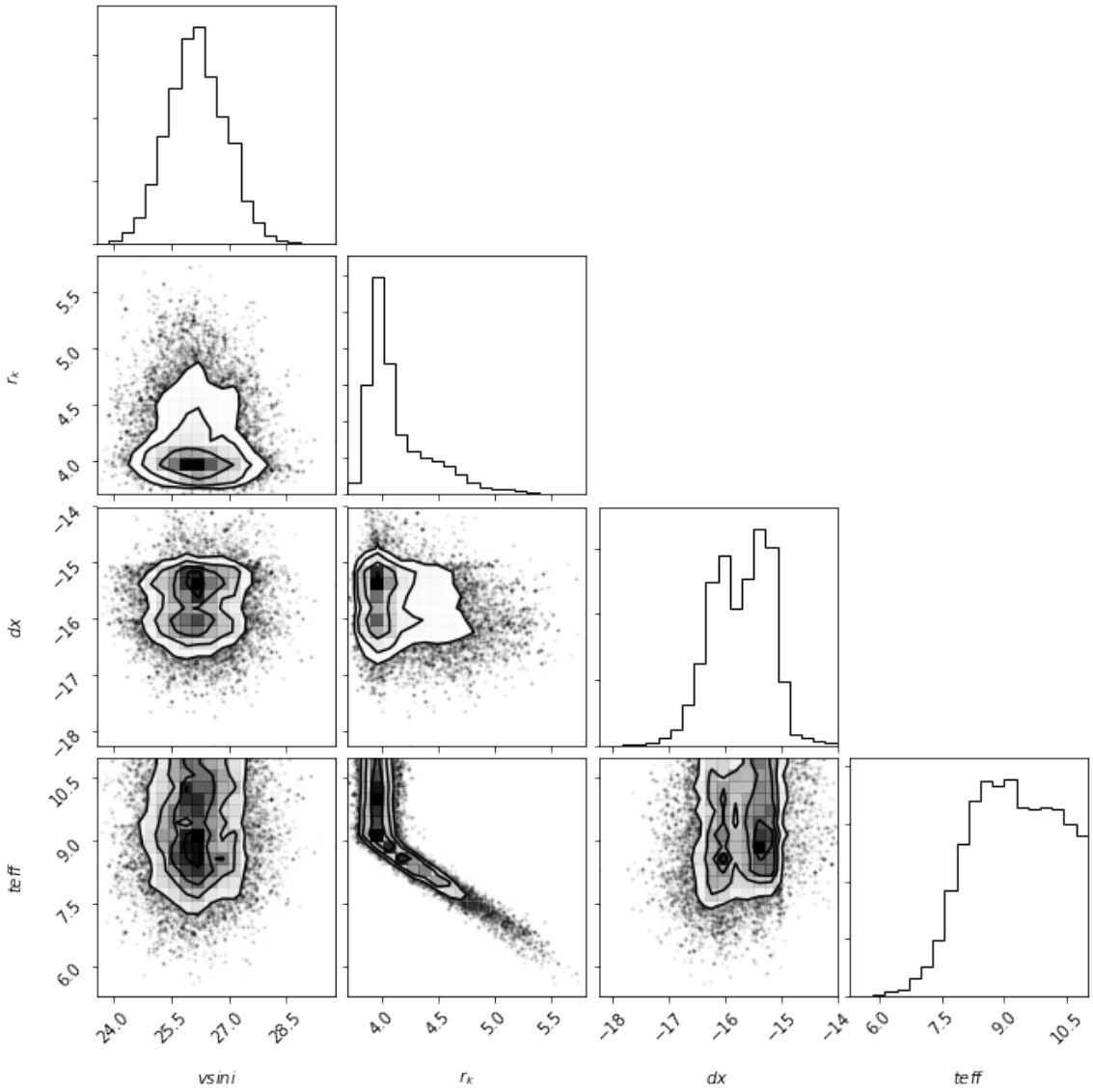

Figure 115 Relative probability distributions and correlations for the four fit parameters returned by *emcee* to best match the iSHELL spectrum of order 226 of object SR 24S corresponding to $T = 4940 \pm 230$ K, $vsini = 26.13 \pm 0.76$ km s^{-1}, $r_k = 4.04 \pm 0.27$, and $dx = -15.68 \pm 0.53$.

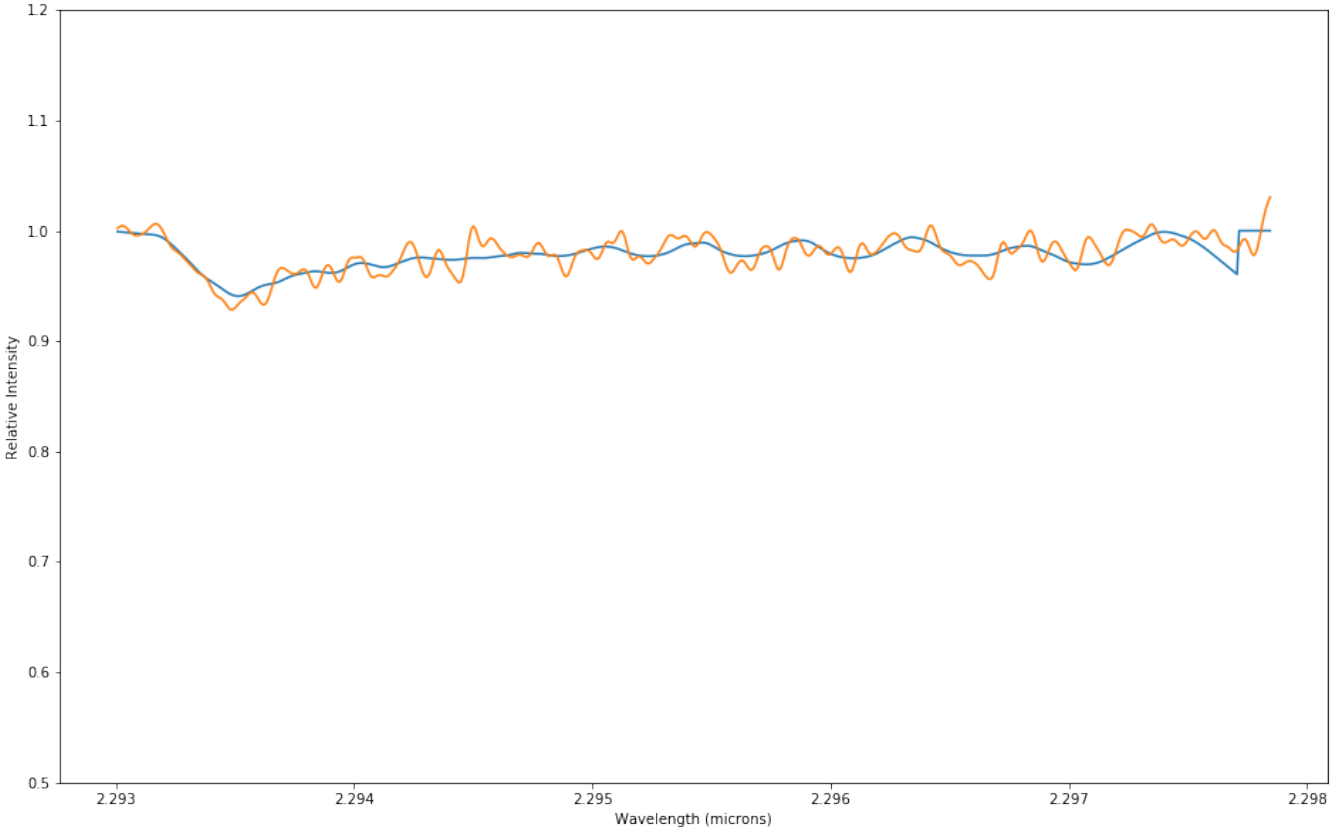

Figure 116 Synthetic overlay (blue) on top of the data (orange) for the four fit parameters returned by *emcee* to best match the iSHELL spectrum of order 226 of object SR 24S corresponding to $T = 4940 \pm 230$ K, $vsini = 26.13 \pm 0.76$ km s^{-1}, $r_k = 4.04 \pm 0.27$, and $dx = -15.68 \pm 0.53$.

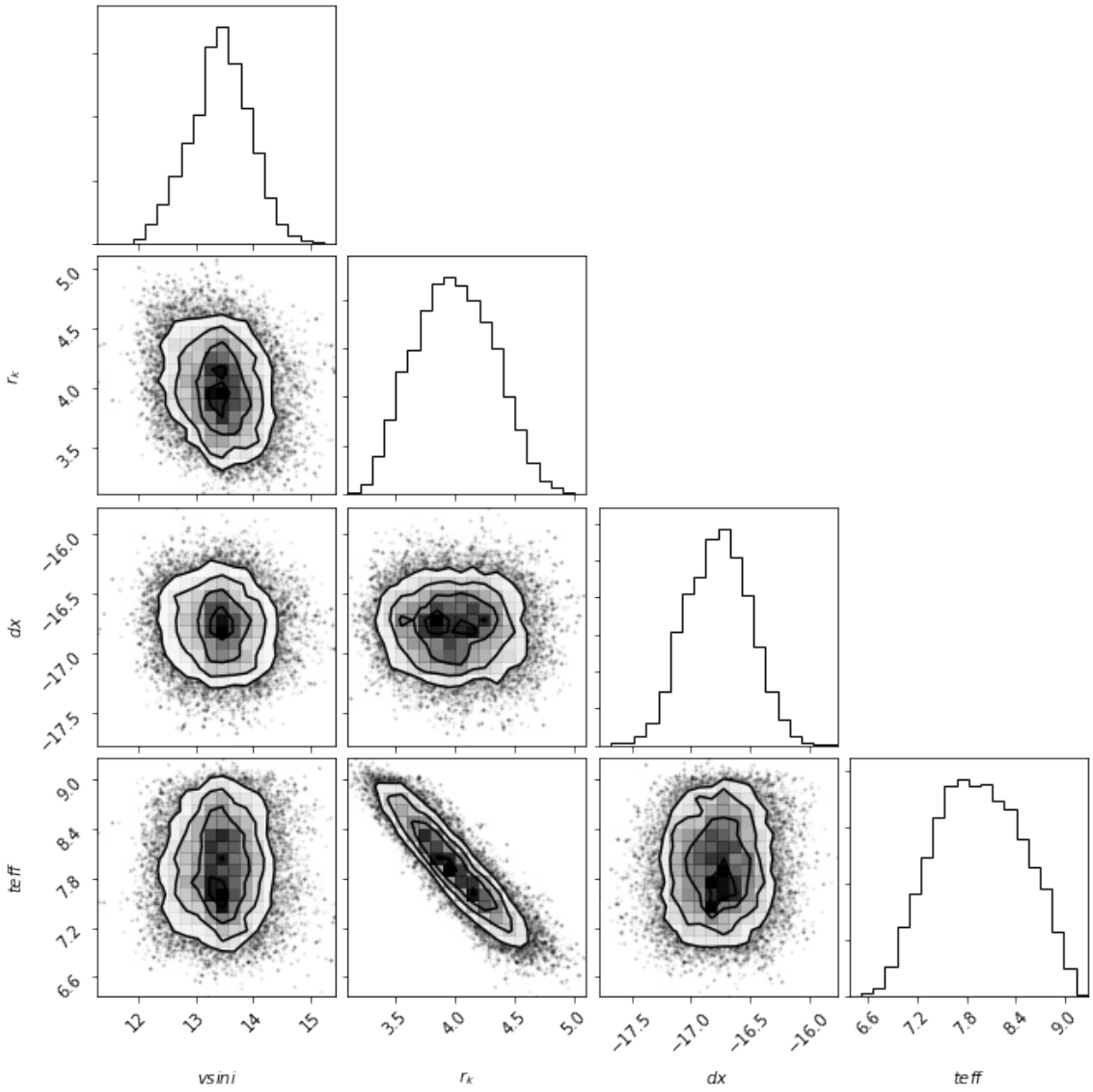

Figure 117 Relative probability distributions and correlations for the four fit parameters returned by *emcee* to best match the iSHELL spectrum of order 224 of object VSSG 1 corresponding to $T = 4680 \pm 100$ K, $vsini = 13.43 \pm 0.7$ km s^{-1}, $r_k = 3.99 \pm 0.35$, and $dx = -16.77 \pm 0.27$.

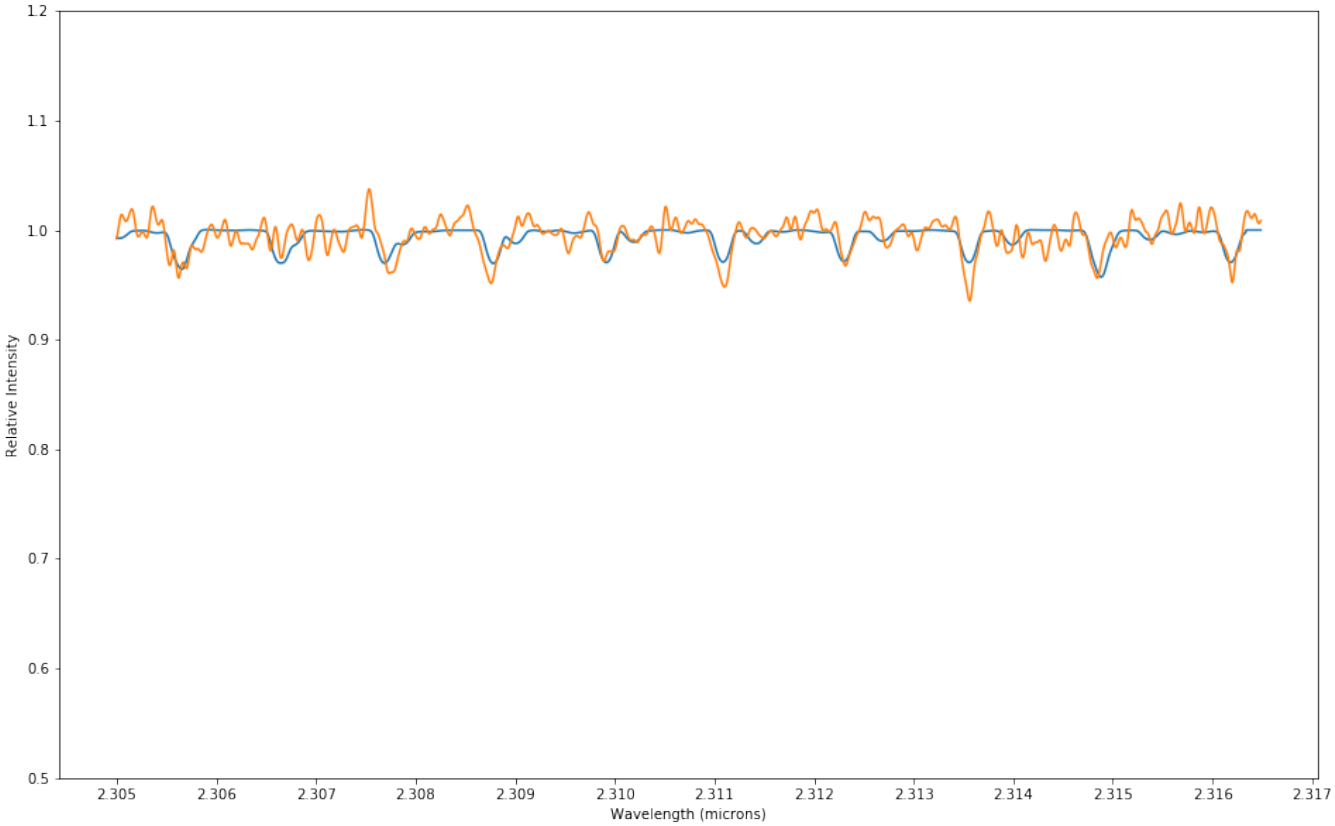

Figure 118 Synthetic overlay (blue) on top of the data (orange) for the four fit parameters returned by *emcee* to best match the iSHELL spectrum of order 224 of object VSSG 1 corresponding to $T = 4680 \pm 100$ K, $vsini = 13.43 \pm 0.7$ km s^{-1}, $r_k = 3.99 \pm 0.35$, and $dx = -16.77 \pm 0.27$.

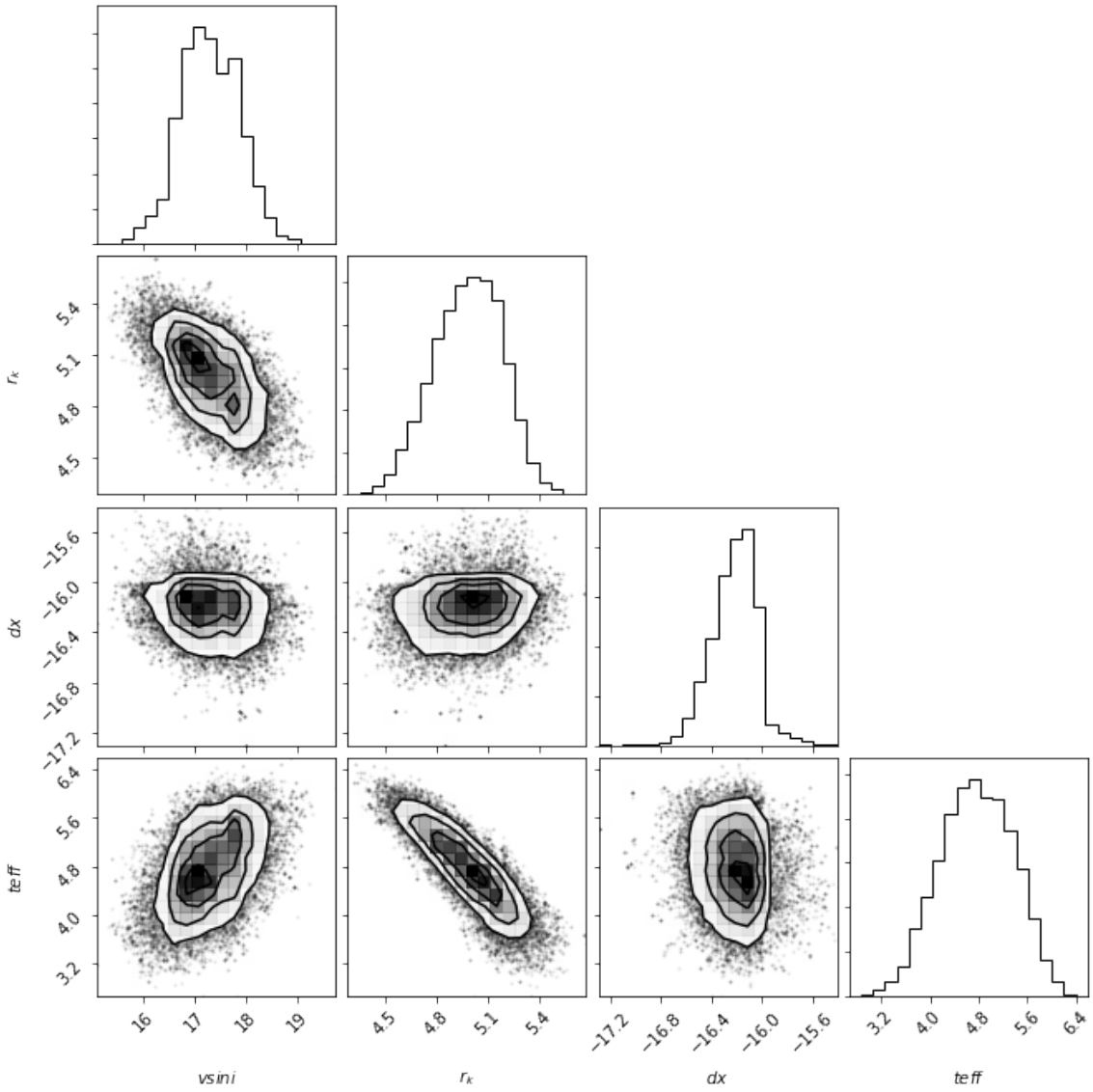

Figure 119 Relative probability distributions and correlations for the four fit parameters returned by *emcee* to best match the iSHELL spectrum of order 225 of object VSSG 1 corresponding to $T = 4060 \pm 120$ K, $vsini = 17.26 \pm 0.57$ km s^{-1}, $r_k = 4.99 \pm 0.21$, and $dx = -16.20 \pm 0.17$.

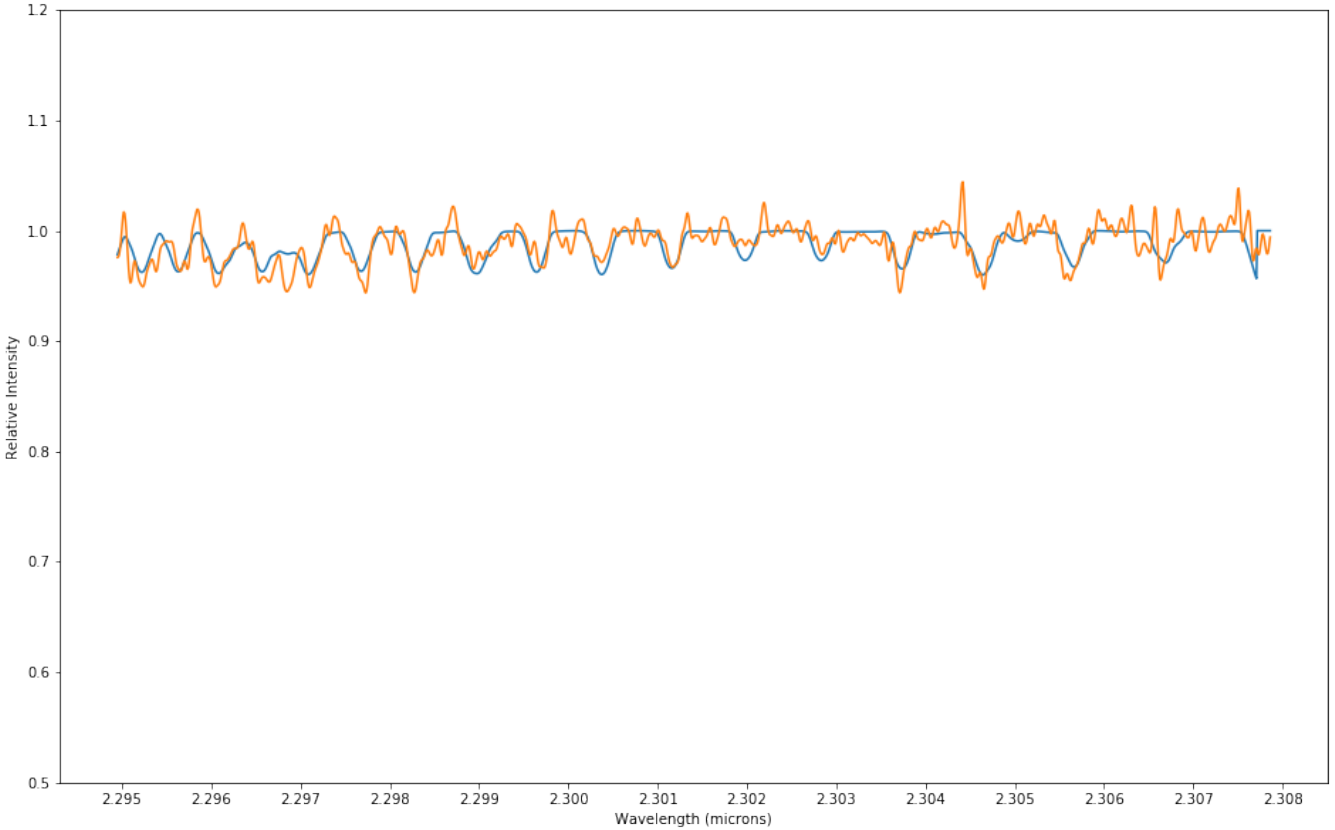

Figure 120 Synthetic overlay (blue) on top of the data (orange) for the four fit parameters returned by *emcee* to best match the iSHELL spectrum of order 225 of object VSSG 1 corresponding to $T = 4060 \pm 120$ K, $vsini = 17.26 \pm 0.57$ km s^{-1}, $r_k = 4.99 \pm 0.21$, and $dx = -16.20 \pm 0.17$.

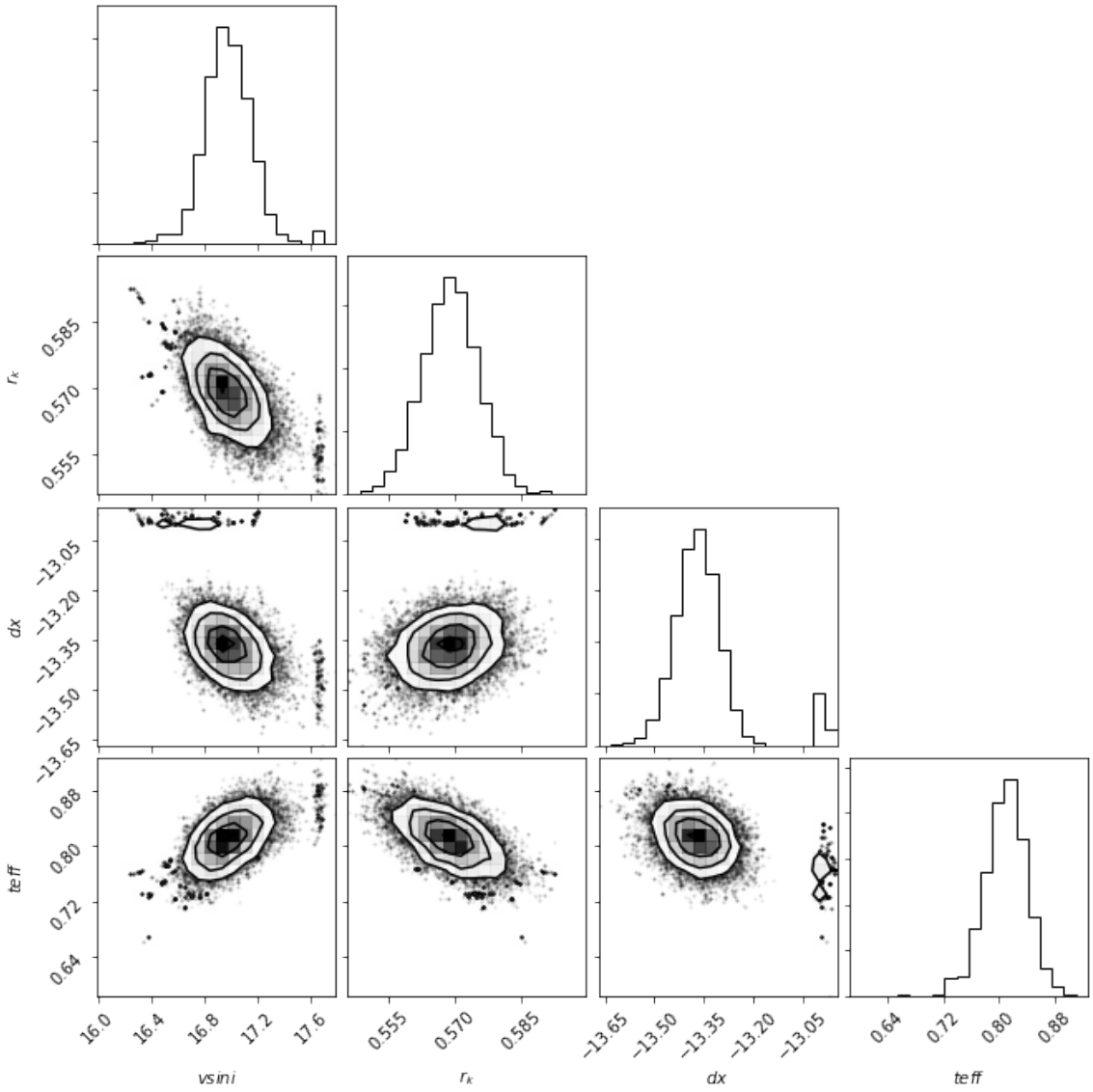

Figure 121 Relative probability distributions and correlations for the four fit parameters returned by *emcee* to best match the iSHELL spectrum of order 225 of object WL 4 corresponding to $T = 3260 \pm 20$ K, $vsini = 16.97 \pm 0.17$ km s^{-1}, $r_k = 0.57 \pm 0.01$, and $dx = -13.37 \pm 0.07$.

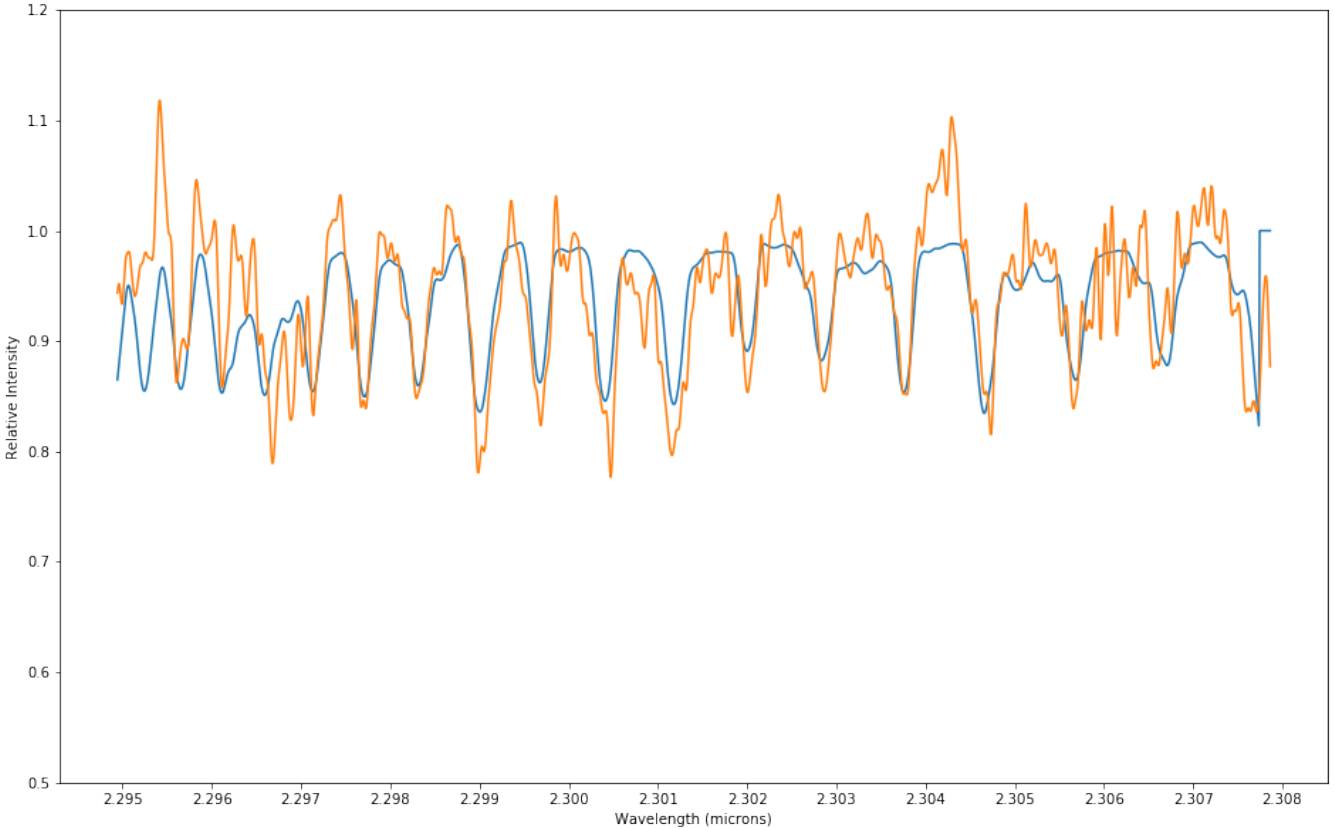

Figure 122 Synthetic overlay (blue) on top of the data (orange) for the four fit parameters returned by *emcee* to best match the iSHELL spectrum of order 225 of object WL 4 corresponding to $T = 3260 \pm 20$ K, $vsini = 16.97 \pm 0.17$ km s^{-1}, $r_k = 0.57 \pm 0.01$, and $dx = -13.37 \pm 0.07$.

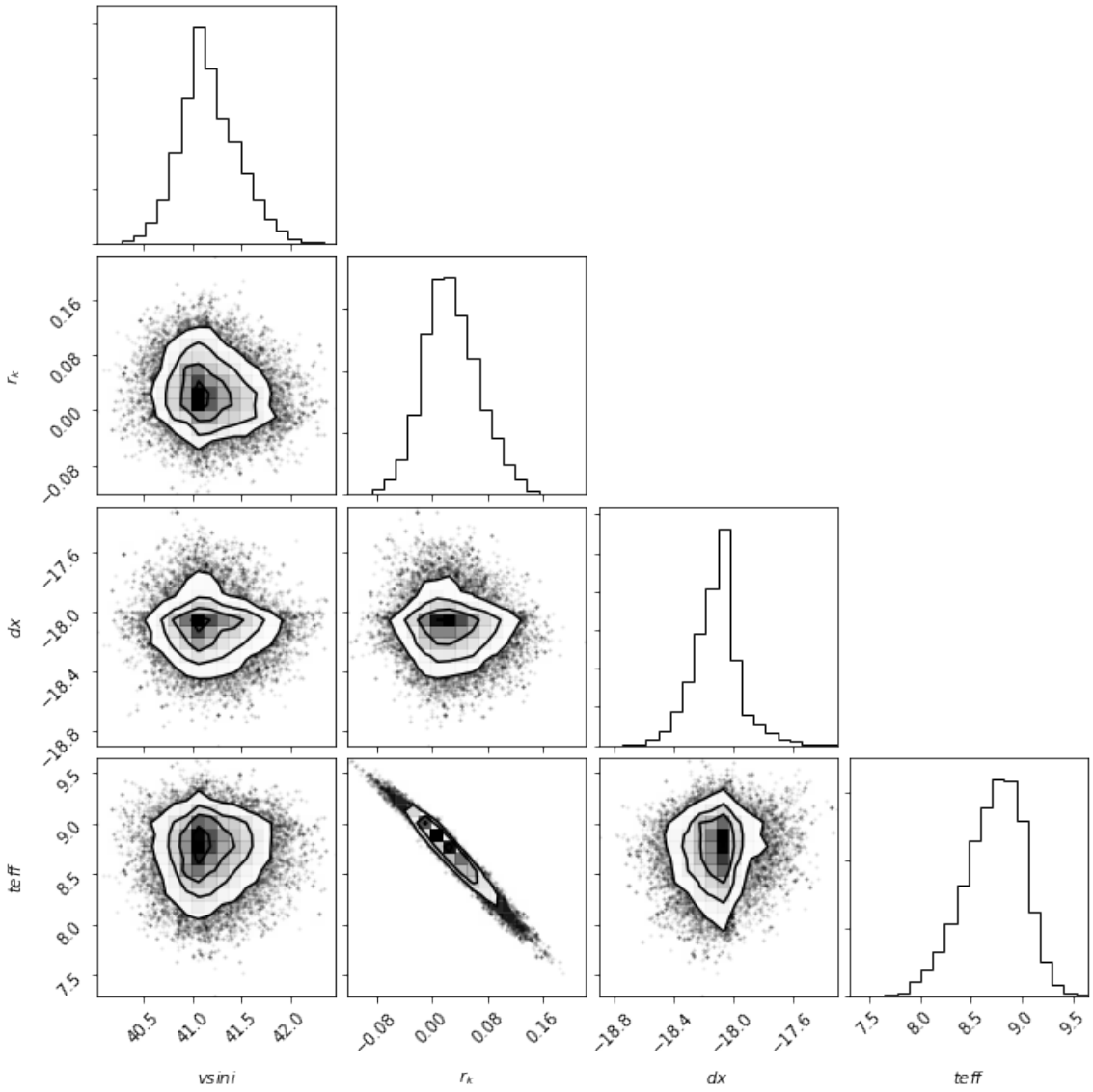

Figure 123 Relative probability distributions and correlations for the four fit parameters returned by *emcee* to best match the iSHELL spectrum of order 225 of object WL 20E corresponding to $T = 4840 \pm 60$ K, $vsini = 41.1 \pm 0.3$ km s^{-1}, $r_k = 0.02 \pm 0.04$, and $dx = -18.10 \pm 0.20$.

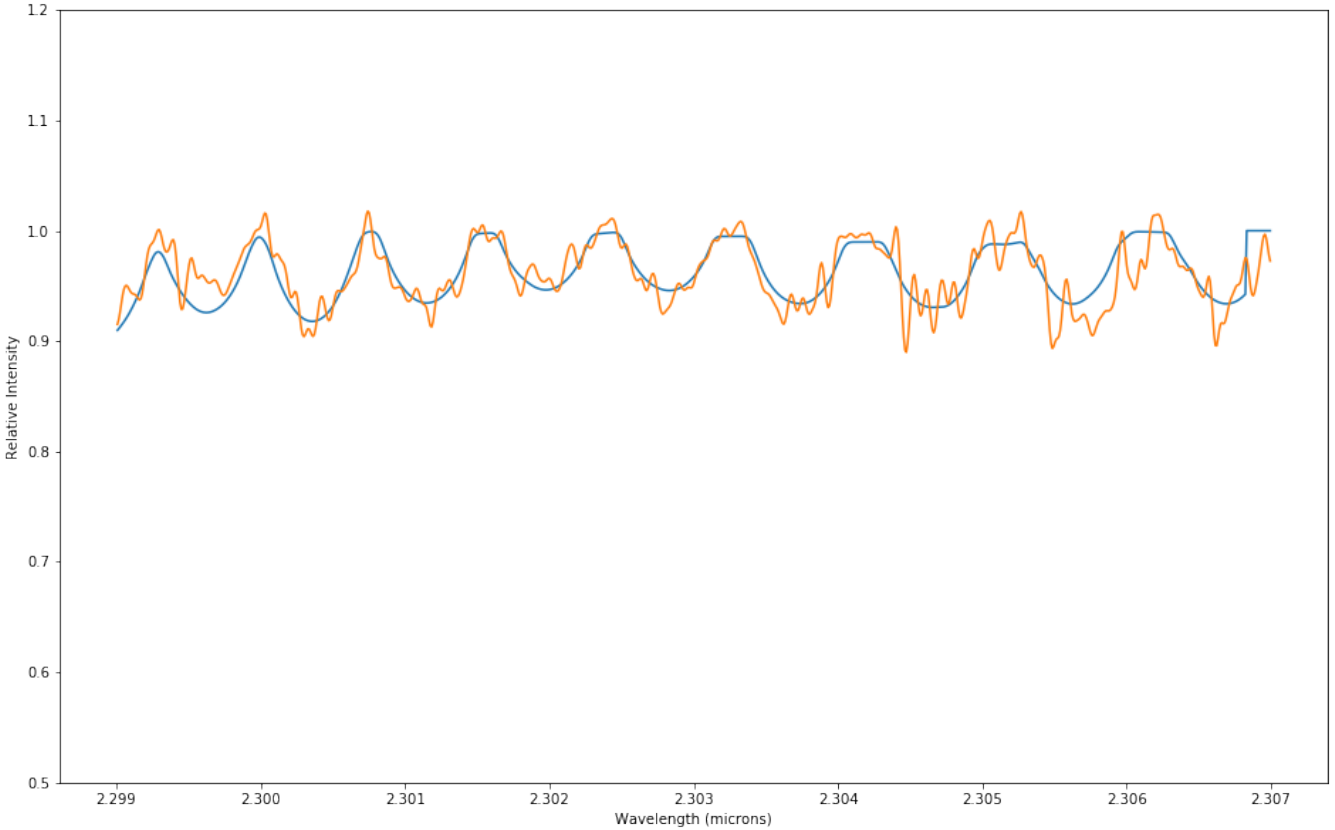

Figure 124 Synthetic overlay (blue) on top of the data (orange) for the four fit parameters returned by *emcee* to best match the iSHELL spectrum of order 225 of object WL 20E corresponding to $T = 4840 \pm 60$ K, $vsini = 41.1 \pm 0.3$ km s^{-1}, $r_k = 0.02 \pm 0.04$, and $dx = -18.10 \pm 0.20$.

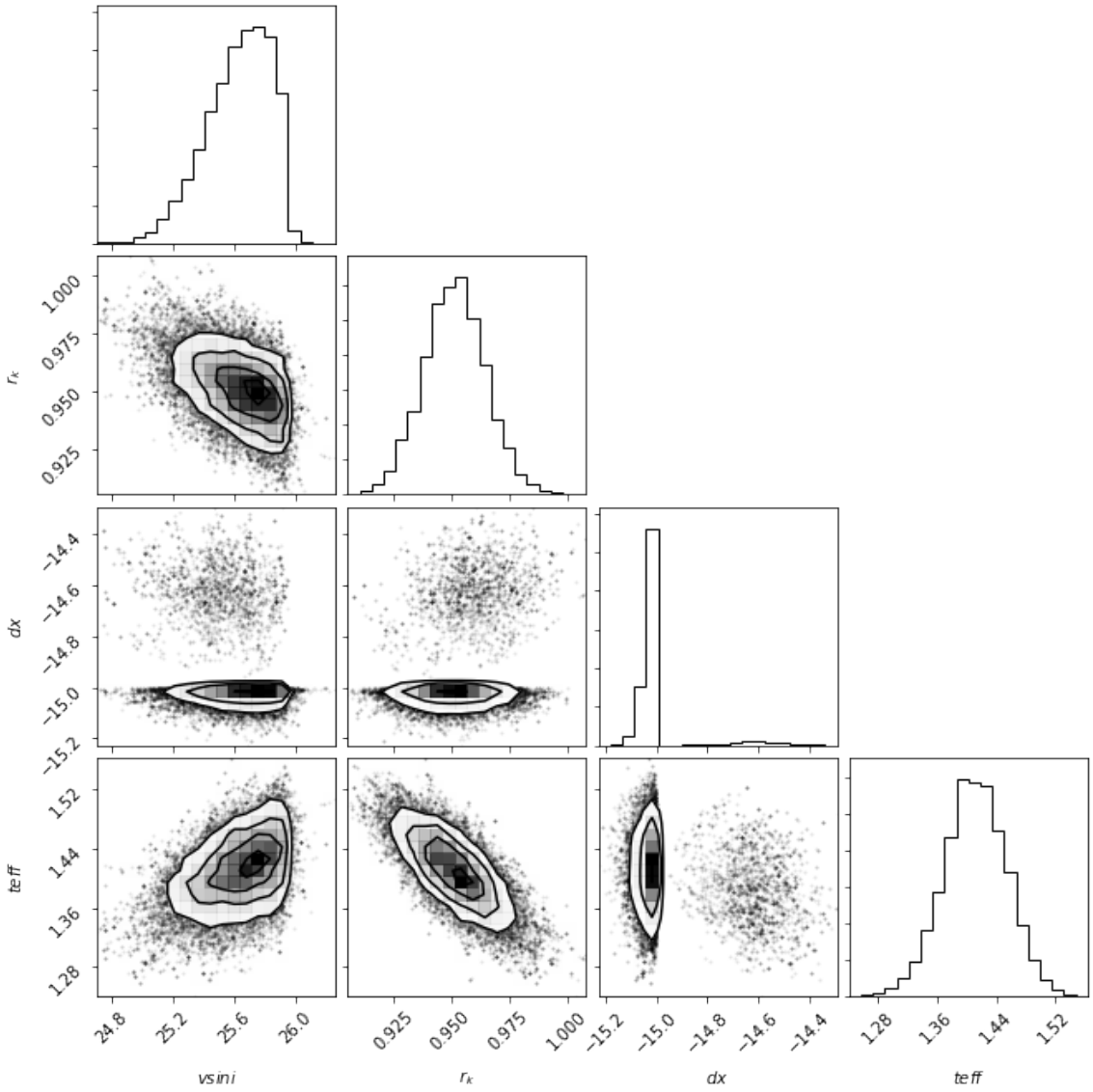

Figure 125 Relative probability distributions and correlations for the four fit parameters returned by *emcee* to best match the iSHELL spectrum of order 225 of object WL 20W corresponding to $T = 3380 \pm 20$ K, $vsini = 25.6 \pm 0.2$ km s^{-1}, $r_k = 0.95 \pm 0.01$, and $dx = -15.00 \pm 0.05$.

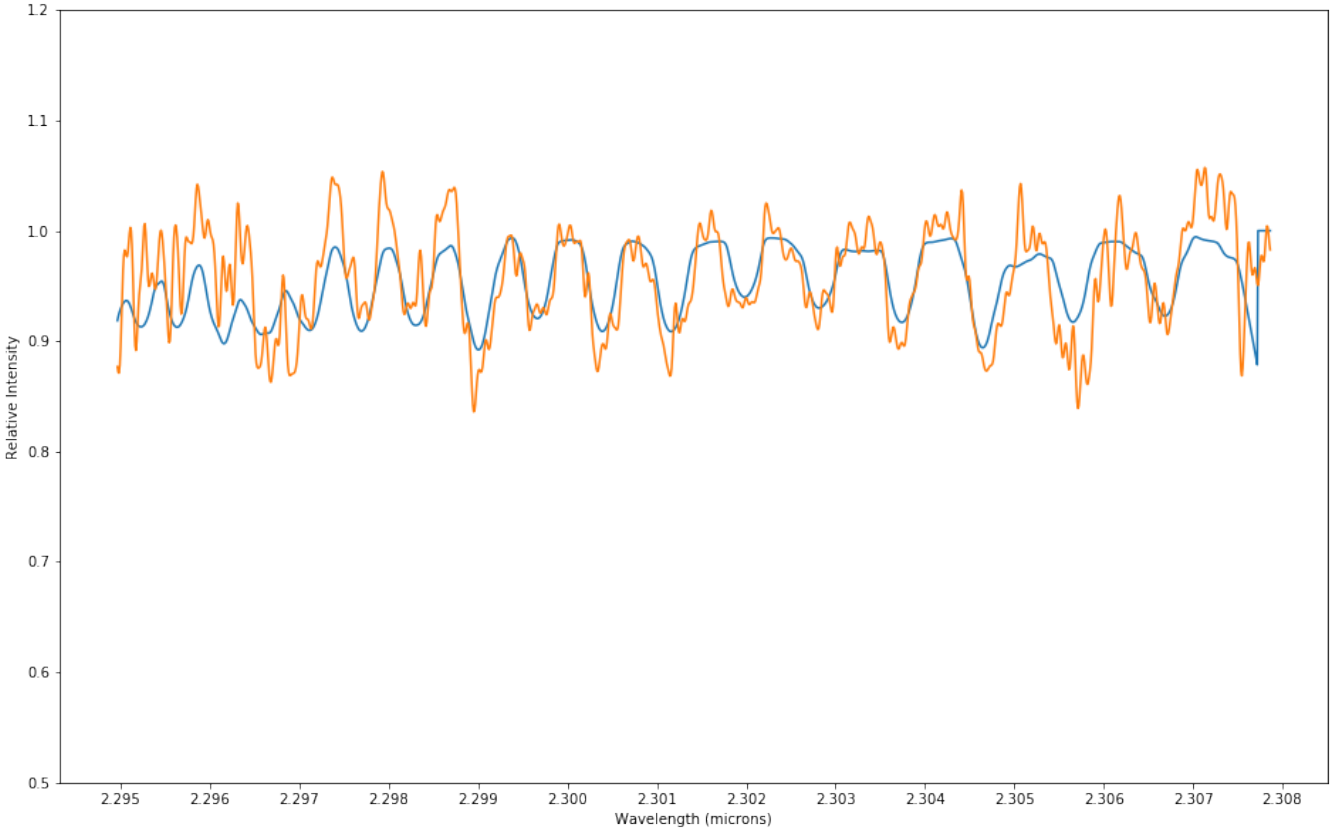

Figure 126 Synthetic overlay (blue) on top of the data (orange) for the four fit parameters returned by *emcee* to best match the iSHELL spectrum of order 225 of object WL 20W corresponding to $T = 3380 \pm 20$ K, $vsini = 25.6 \pm 0.2$ km s^{-1}, $r_k = 0.95 \pm 0.01$, and $dx = -15.00 \pm 0.05$.

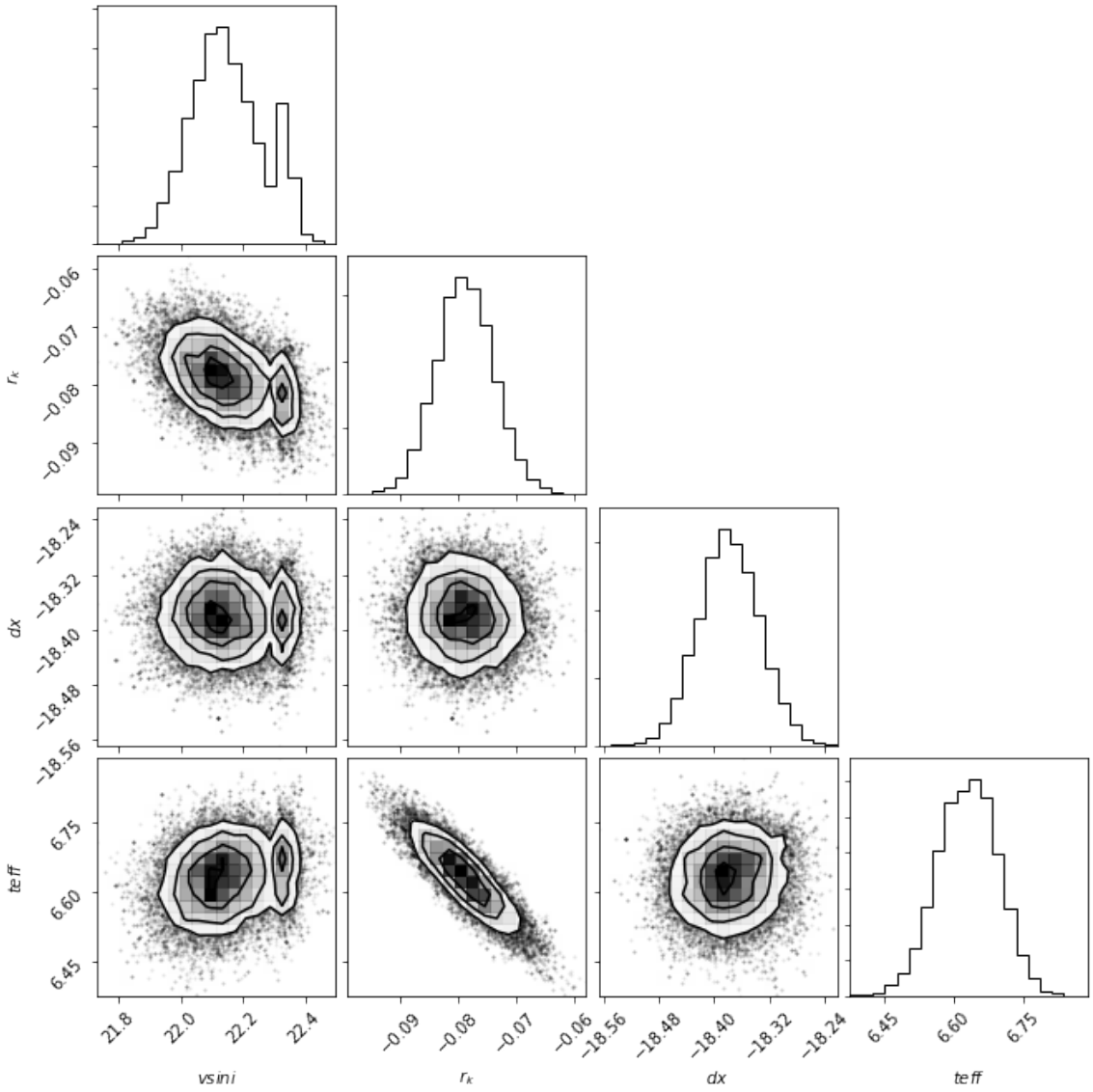

Figure 127 Relative probability distributions and correlations for the four fit parameters returned by *emcee* to best match the iSHELL spectrum of order 225 of object WLY 2-42 corresponding to $T = 4420 \pm 20$ K, $vsini = 22.1 \pm 0.2$ km s^{-1}, $r_k = 0.00 \pm 0.01$, and $dx - 18.38 \pm 0.04$.

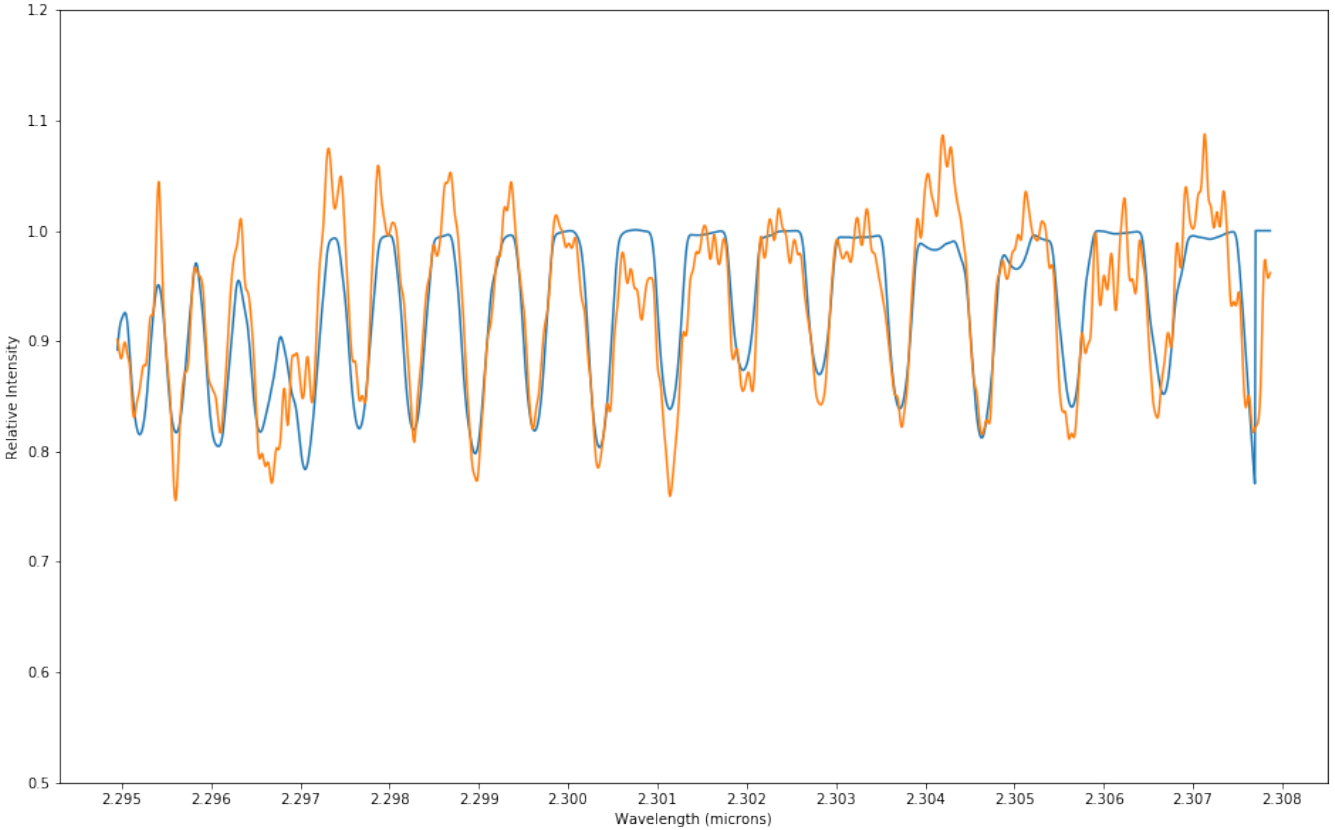

Figure 128 Synthetic overlay (blue) on top of the data (orange) for the four fit parameters returned by *emcee* to best match the iSHELL spectrum of order 225 of object WLY 2-42 corresponding to T = 4420 ± 20 K, $vsini$ = 22.1 ± 0.2 km s^{-1}, r_k = 0.00 ± 0.01, and dx − 18.38 ± 0.04.

APPENDIX C.

NOTES ON INDIVIDUAL SOURCES

- GSS 26 – Our radial velocity of -7.58±0.14 km s^{-1}, derived from a reanalysis of 2008 August CRIRES data obtained by Viana Almeida *et al.* (2012), is more negative than their published value -6.95±0.03 km s^{-1}. A dynamical mass of 1.5 $M_{\odot}$ and a radial velocity of -6.44 km s^{-1} were derived based on observations of its disk (Simon *et al.*, 2017). Our derived temperature, suggesting a K5 spectral type with low veiling, is counter to previous estimates but consistent with its observed variability in veiling and brightness (Greene and Lada, 2000; Luhman and Rieke, 1999).

- VSSG 1 – Our best fit temperature of 4430 K suggests a mid-K spectral type. In addition to the photospheric absorption lines, the iSHELL spectrum shows Brackett gamma in emission.

- GY 21 – Best fit temperature is warmer and *vsini* smaller than derived from the CSHELL spectrum of Greene and Lada (1997) but in better agreement with those derived from the same spectrum by Doppmann *et al.* (2005).

- GY 23/Source 2 - Spectral classifications vary from K5-M0 (Doppmann *et al.*, 2005; Erickson *et al.*, 2011; Greene and Lada, 1997; Luhman and Rieke, 1999). Temperature and *vsini* are in good agreement with Greene and Lada (1997). Our best fit temperature and low veiling favor the mid-K classification of Erickson *et al.* (2011). Our modeling of the 2008 April CRIRES spectrum obtained by Viana Almeida *et al.* (2012) yields a radial velocity that is not in agreement with theirs and calls into question their identification of this source as a radial velocity variable.

- GY 30 – The Class I source is associated with a fan-shaped near-infrared nebula and a molecular outflow (Kamazaki *et al.*, 2003).

- ISO-Oph 51 – The resolved circumstellar disk displays an asymmetry indicative of planet formation (Cox *et al.*, 2017).

- GY 91 – Millimeter continuum observations exhibit a disk/envelope structure characteristic of an embedded source and have resolved an $r = 80$ AU disk with three dark lanes suggestive of planet formation (Sheehan and Eisner, 2018).

- SR 24 – SR 24N (SR 24B) and SR 24S (SR 24A) form a wide binary with a separation of $\sim 6''$ within a circumbinary disk (Fernández-López *et al.*, 2017; Mayama *et al.*, 2010; Struve and Rudkjobing, 1949). SR 24N itself is a close binary with a projected separation of 100 mas with an orbital period of 78 to 216 years and a total mass of 1.24±0.24 $M_\odot$ (Correia *et al.*, 2006; Schaefer *et al.*, 2018; Simon *et al.*, 1995).

- SR 24S – Our radial velocity from 2017 of -0.27±0.32 km s^{-1} is significantly different than that derived from optical spectra in 2012 of -8.19±0.33 by Rigliaco *et al.* (2016), suggesting a binary companion. This velocity variation is much larger than would be expected to arise from interactions with SR 24N. In addition to the photospheric absorption lines, the iSHELL spectrum shows both Brackett gamma and molecular hydrogen (2.12 μm) in emission.

- SR 24N - In addition to the photospheric absorption lines, the iSHELL spectrum shows molecular hydrogen in emission at 2.12 μm.

- WL 1- A binary with a $0.8''$ projected separation (Haisch *et al.*, 2002). The primary (WL 1S), which is 0.1 mag brighter at K, was presumably centered in the $0.58''$ NIRSPEC slit. The radial velocity of -25 km s-1 is far from the median value for our sample.

- GY 197 – Deep near-infrared images reveal a bipolar outflow cavity centered on the source (Hsieh *et al.*, 2017).

- WL 17 – The radial velocities we derive from spectra obtained in 2001 and 2012 are in good agreement but not consistent with the values reported by Viana Almeida *et al.* (2012). High spatial resolution ALMA images reveal a transition disk in

a disk/envelope system suggesting planets can form at an early embedded stage (Sheehan and Eisner, 2017). Dynamical clearing by a close companion seems to be ruled out by the lack of variability in the radial velocity.

- GY 224 – The radial velocities from spectra obtained in 2001 and 2008 are consistent.

- WL 19- The radial velocity of -27 km s^{-1} is far from the median value for our sample. The weak mid-infrared emission and lack of compact dust and gas emission has led to the suggestion it is not an embedded source but a heavily reddened Class III object behind the molecular cloud (Bontemps *et al.*, 2001; Van Kempen *et al.*, 2009). It is, however, an X-ray source (Imanishi *et al.*, 2001) suggesting it is a cluster member.

- GY 235 – Our best fit temperature agrees very well with that derived from moderate resolution infrared spectra (Manara *et al.*, 2015)(Manara et al. 2015). In addition to the photospheric absorption lines, the iSHELL spectrum shows both Brackett gamma and molecular hydrogen (2.12 μm) in emission.

- WL 20 – Two components of this triple system, WL 20E and WL 20W, were observed. They were easily resolved with a projected separation of 3.2″(Ressler and Barsony, 2001). Our best fit for WL 20E is warmer than reported by Barsony *et al.* (2002).

- WL 4 – A periodic variable has been modeled as an equal brightness triple system (Plavchan *et al.*, 2008) with a heretofore unobserved close binary (WL 4a/4b, 0.47 AU) and a known 0.176″ companion WL 4C at 120 AU, Ratzka *et al.* (2005).

- WL 3 – Our derived value for *vsini* of 41 km $s^{-1}$is higher than that of Greene and Lada (1997) but consistent with that derived from the same spectrum by Doppmann *et al.* (2005).

- WLY 2-43/YLW 15 – VLA observations show this to be a 0.6 ″ binary also observed in the mid-infrared (Curiel *et al.*, 2003). Our fits suggest a K3 spectral type.

- WLY 2-44/YLW 16a – Infrared imaging reveals two components of equal brightness at 3.8 μm with a projected separation of 0.3″ (Plavchan *et al.*, 2013; Terebey *et al.*, 2001). A possible third component is suggested from the periodic photometric variability. Radial velocities derived from spectra in 2001 and 2012 show evidence for variability.

- VSSG 18/WLY 2-35 – Radial velocities derived in 2008 and 2012 suggest it is a radial velocity variable, however, our velocity from 2008 does not agree with Viana Almeida *et al.* (2012). Luhman and Rieke (1999) assigned a spectral classification of K6.5 which is consistent with our best fit temperature.

- VSSG 17/WLY 2-47 - This source is a subarcsecond binary with a projected separation of 0.25″ (Costa *et al.*, 2000). Radial velocities derived from spectra in 2001 and 2012 do not show evidence of variability. Spectral classifications vary from K8-M2 (Greene and Lada, 1997; Luhman and Rieke, 1999). Our MCMC results favor the late K classification. Our *vsini* of 41 km s^{-1} agrees well with previous estimates of 43-47 km s^{-1} (Doppmann *et al.*, 2005; Greene and Lada, 1997).

- GY 314/WSB 52 – Spectral classifications vary from K5-M3 (Doppmann *et al.*, 2005; Greene and Lada, 1997; Luhman and Rieke, 1999). Our MCMC results favor the later spectral classification.

- WLY 2-51 –A faint companion (ΔK = 3.5 mag) with a projected separation of 1.6″ has been reported by Ratzka *et al.* (2005). The iSHELL spectrum suggests weak Brackett gamma emission.

- WLY 2-54 – The iSHELL spectrum is devoid of photospheric absorption lines but does show Brackett gamma and molecular hydrogen (2.12 μm) in emission. The spectrum also displays narrow interstellar absorption lines from low R and P branch lines from the CO $v = 0 - 2$ transitions.

APPENDIX D.

PERMISSIONS FOR FIGURES

1. PERMISSION FOR FIGURE 1.1 FROM PHILIPPE ANDRÉ

Dear Tim Sullivan,

Thank you for your e-mail. You did not specify where you intend to reproduce the figure but, yes, you have my permission to use this figure (provided a reference to "The Cold Universe" paper is included).

[Incidentally, you may possibly be interested in this version of the figure, including prestellar cores: http://cdsads.u-strasbg.fr/abs/2002EAS.....3....1A]

With best wishes,

Philippe André

2. PERMISSIONS FOR FIGURE 2.1 FROM VOLKER OSSENKOPF-OKADA AND FREDERIQUE MOTTE

Dear Tim Sullivan,

For this particular case, I am the wrong person to ask, because for that figure I got the data from Frederique Motte. I am fine with using my particular version, but you should rather get permission from her.

Best regards

Volker Ossenkopf-Okada

Dear Timothy,

Sorry for the delay in answering. . . I hereby give you permission to reproduce the Fig. 1 of my 1998 paper (such an old paper!). One question about your rho Oph study: do you study the dynamical state of the cloud? of protostars? or even of stars?

Cheers,

Fred

REFERENCES

Adams, F., Bodenheimer, P., and Laughlin, G., 'M dwarfs: Planet formation and long term evolution,' AN, 2005, **326**, pp. 913–919.

André, P., 'Observations of protostars and protostellar stages,' in 'The Cold Universe,' pp. 179–192, Editions Frontiéres, B.P.33 91192 Gif-sur-Yvette Cedex - France, 1994.

André, P., Belloche, A., and Peretto, N., 'The initial conditions of star formation in the ophiuchus main cloud: Kinematics of the protocluster condensations,' A&A, 2007, **472**, pp. 519–535.

André, P. and Montmerle, T., 'From t tauri stars to protostars: Circumstellar material and young stellar objects in the rho ophiuchi cloud,' ApJ, 1994, **420**, pp. 837–862.

André, P., Ward-Thompson, D., and Barsony, M., 'Submillimeter continuum observations of rho ophuchi a: The candidate protostar vla 1623 and prestellar clumps,' ApJ, 1993, **406**, pp. 122–141.

André, P., Ward-Thompson, D., and M., B., 'From prestellar cores to protostars: the initial conditions of star formation,' in 'Protostars and Planets IV,' pp. 179–192, The University of Arizona Press, Tucson, Arizona, 2000.

Barsony, M., Greene, T., and Blake, G., 'A tidally interacting disk in the young triple system wl 20?' ApJL, 2002, **572**, pp. L75–L78.

Barsony, M. and Kenyon, S. J., 'On the origin of submillimeter emission from young stars in taurus-auriga,' ApJ, 1992, **348**, pp. L53–L57.

Bate, M., 'The dependence of star formation on initial conditions and molecular cloud structure,' MNRAS, 2009, **397**, pp. 232–248.

Bate, M., Bonnell, I., and Bromm, V., 'The formation of a star cluster: predicting the properties of stars and brown dwarfs,' MNRAS, 2003, **339**, pp. 577–599.

Binney, J. and Merrifield, M., *Galactic Astronomy*, Princeton University Press, Princeton, N.J., 1998.

Bok, B., 'The stability of moving clusters.' Harvard College Obs., 1934, **384**.

Bonnell, I. and Davies, M., 'Mass segregation in young stellar clusters,' MNRAS, 1998, **295**, p. 691.

Bonnell, I., Larson, R., and Zinnecker, H., 'The origin of the initial mass function,' in 'Protostars and Planets V,' pp. 149–164, The University of Arizona Press, Tucson, Arizona, 2007.

Bontemps, S., André, P., Kaas, A., Nordh, L., Olofsson, G., Huldtgren, M., Abergel, A., Blommaert, J., Boulanger, F., Burgdorf, M., Cesarsky, D., Copet, E., Davies, J., Falgarone, E., Lagache, G., Montmerle, T., Pérault, M., Persi, P., Prusti, T., Puget, J., and Sibille, F., 'Isocam observations of the rho ophiuchi cloud: Luminosity and mass functions of the pre-main sequence embedded cluster,' A&A, 2001, **372**, pp. 173–194.

Carpenter, J., Meyer, M., Dougados, C., Strom, S., and Hillenbrand, L., 'Properties of the monoceros r2 stellar cluster,' AJ, 1997, **114**, pp. 198–221.

Clarke, C. and Pringle, J., 'Accretion disc response to a stellar fly-by,' MNRAS, 1993, **261**, pp. 190–202.

Comeron, F., Rieke, G., Burrows, A., and Rieke, M., 'The stellar population in the rho ophuchi cluster,' ApJ, 1993, **416**, p. 185.

Correia, S., Zinnecker, H., Ratzka, T., and Sterzik, M., 'A vlt/naco survey for triple and quadruple systems among visual pre-main sequence binaries,' A&A, 2006, **459**, pp. 909–926.

Costa, A., Jessop, N., Yun, J., Santos, C., Ward-Thompson, D., and Casali, M., 'Yso binaries in rho ophiuchi,' in 'Birth and Evolution of Binary Stars, Poster Proceedings of IAU Symposium No. 200 on The Formation of Binary Stars,' p. 48, IAU, Potsdam, Germany, 2000.

Cottaar, M., Meyer, M., and Parker, R., 'Characterizing a cluster's dynamic state using a single epoch of radial velocities,' A&A, 2012, **547**, p. 35.

Covey, K., Greene, T., Doppmann, G., and Lada, C., 'The radial velocity distribution of class i and flat-spectrum protostars,' AJ, 2006, **131**, pp. 512–519.

Cox, E., Harris, R., Looney, L., Chiang, H.-F., Chandler, C., Kratter, K., Li, Z.-Y., Perez, L., and Tobin, J., 'Protoplanetary disks in rho ophiuchus as seen from alma,' ApJ, 2017, **851**, p. 83.

Cox, R., 'Probability, frequency and reasonable expectation,' American Journal of Physics, 1946, **14**, pp. 1–13.

Curiel, S., Girat, J., Rodriguez, L., and Canto, J., 'Very large array observations of proper motions in ylw 15,' ApJ, 2003, **582**, p. L109.

Cushing, M., W.D., V., and Rayner, J., 'Spextool: A spectral extraction package for spex, a 0.8-5.5 micron cross-dispersed spectrograph,' PASP, 2004, **116**.

Cutri, R., Skrutskie, M., van Dyk, S., Beichman, C., Carpenter, J., Chester, T., Cambresey, L., Evans, T., Fowler, J., Gizis, J., Howard, E., Huchra, J., Jarrett, T., Kopan, E., Kirkpatrick, J., Light, R., Marsh, K., McCallon, H., Schneider, S., Stiening, R., Sykes, M., Weinberg, M., Wheaton, W., Wheelock, S., and Zacarias, N., 'Vizier online data catalog: 2mass all-sky catalog of point sources,' yCat, 2003, **2246**.

D'Antona, F. and Mazzitelli, I., 'Evolution of low mass stars,' MmSAI, 1997, **68**, p. 807.

De Geus, E., 'Interactions of stars and interstellar matter in scorpio centaurus,' A&A, 1992, **262**, pp. 258–270.

Doppmann, G., Greene, T., Covey, K., and Lada, C., 'The physical natures of class i and flat-spectrum protostellar photospheres: A near-infrared spectroscopic study,' AJ, 2005, **130**, pp. 1145–1170.

Dunham, M., Stutz, A., Allen, L., Evans, N. I., Fischer, W., Megeath, S., Myers, P., Offner, C., S.S.R. andpoteet, Tobin, J., and Vorobyov, E., 'The evolution of protostars: Insights from ten years of infrared surveys with spitzer and herschel,' in 'Protostars and Planets VI,' pp. 195–218, The University of Arizona Press, Tucson, Arizona, 2014.

Elias, J., 'An infrared study of the ophiuchus dark cloud,' ApJ, 1978, **224**, pp. 453–472.

Elmegreen, B., Efremov, Y., Pudritz, R., and Zinnecker, H., 'Observations and theory of star cluster formation,' in 'Protostars and Planets IV,' p. 179, The University of Arizona Press, Tucson, Arizona, 2000.

Elmegreen, B. and Lada, C., 'Sequential formation of subgroups in ob associations,' ApJ, 1977, **214**, pp. 725–741.

Erickson, K., Wilking, B., Meyer, M., Robinson, J., and Stephenson, L., 'The initial mass function and disk frequency of the rho ophiuchi cloud: An extinction-limited sample,' AJ, 2011, **142**, p. 140.

Fernández-López, M., Zapata, L. A., and Gabbasov, R., 'Strongly misaligned triple system in sr 24 revealed by alma,' ApJ, 2017, **845**, p. 10.

Foreman-Mackey, D., 'emcee: The mcmc hammer: User guide,' http://dfm.io/emcee/current/, 2013.

Foreman-Mackey, D., Hogg, D., Lang, D., and Goodman, J., 'emcee: The mcmc hammer,' PASP, 2013, **125**, p. 306.

Foster, J., Cottaar, M., Covey, K., Arce, H., Meyer, M., Nidever, D., Stassun, K., Tan, J., Chojnowski, S., da Rio, N., Flaherty, K., Rebull, L., Frinchaboy, P., Majewski, S., Skrutskie, M., Wlison, J., and Zasowski, G., 'In-sync. ii. virial stars from subvirial cores—the velocity dispersion of embedded pre-main-sequence stars in ngc 1333,' ApJ, 2015, **799**, p. 136.

Gieles, M., Sana, H., and Portegies Zwart, S., 'On the velocity dispersion of young star clusters: super-virial or binaries?' MNRAS, 2010, **402**, pp. 1750–1757.

Goodman, J. and Weare, J., 'Ensemble samplers with affine invariance,' Commun. Appl. Math. Comput. Sci, 2010, **5**, pp. 65–80.

Gordon, I., Rothman, L., Tan, Y., Kochanov, R., and Hill, C., 'Near-infrared observations of young stellar objects in the rho ophiuchi dark cloud,' ApJ, 1992, **395**, pp. 516–528.

Grasdalen, G., Strom, K., and Strom, S., 'A 2-micron map of the ophiuchus dark-cloud region,' ApJL, 1973, **184**, p. L53.

Greene, T. and Lada, C., 'Near-infrared spectra of flat-spectrum protostars: Extremely young photospheres revealed,' AJ, 1997, **114**, p. 2157.

Greene, T. and Lada, C., 'High-resolution near-infrared spectra of protostars,' ApJ, 2000, **120**, p. 430.

Greene, T., Tokunaga, A., Toomey, D., and Carr, J., 'Cshell: a high spectral resolution 1-5 um cryogenic echelle spectrograph for the irtf,' SPIE, 1993, **1946**, pp. 313–324.

Greene, T., Wilking, B., André, P., Young, E., and Lada, C., 'Further mid-infrared study of the rho ophiuchi cloud young stellar population: Luminosities and masses of pre-main-sequence stars,' ApJ, 1994, **434**, pp. 614–626.

Greene, T. and Young, E., 'Near-infrared observations of young stellar objects in the rho ophiuchi dark cloud,' ApJ, 1992, **395**, pp. 516–528.

Haisch, K. J., Barsony, M., Greene, T., and Ressler, M., 'An infrared multiplicity survey of class i/flat-spectrum systems in the rho ophiuchi and serpens molecular clouds,' AJ, 2002, **124**, pp. 2841–2852.

Heger, A., Fryer, C., Woosley, S., Langer, N., and Hartmann, D., 'Hitran2016: Part i. line lists for h2o, co2, o3, n2o, co, ch4, and o2,' 72nd International Symposium on Molecular Spectroscopy, 2017.

Herbig, G. and Dahm, S., 'The young cluster ic 5146,' AJ, 2002, **123**, pp. 304–327.

Herczeg, G. and Hillenbrand, L., 'Empirical isochrones for low mass stars in nearby young associations,' ApJ, 2015, **808**, pp. 23–40.

Hillenbrand, L. and Hartmann, L., 'A preliminary study of the orion nebula cluster structure and dynamics,' ApJ, 1998, **492**, pp. 540–553.

Hogg, D., Bovy, J., and Lang, D., 'Data analysis recipes: Fitting a model to data*,' arXiv:1008.4686, 2010.

Hsieh, T.-H., Lai, S.-P., and Belloche, A., 'Widening of protostellar outflows: An infrared outflow survey in low-luminosity objects,' AJ, 2017, **153**, p. 173.

Husser, T.-O., Wende-von Berg, S., Dreizler, S., Homeier, D., Reiners, T., A .and Barman, , and Hauschildt, P., 'A new extensive library of phoenix stellar atmospheres and synthetic spectra,' A&A, 2013, **553**, p. 6.

Iben, I. J., 'Post main sequence evolution of single stars,' ARA&A, 2013, **12**, pp. 215–256.

Imanishi, K., Koyama, K., and Tsuboi, Y., 'Chandra observation of the rho ophiuchi cloud,' ApJ, 2001, **557**, pp. 747–760.

Jeans, J., 'The stability of a spherical nebula,' Philosophical Transactions, 1902, **199**, pp. 1–53.

Kamazaki, T., Saito, M., Hirano, N., Umemoto, T., and Tomofumi, K., 'Molecular outflow search in the rho ophiuchi a and b2 regions,' ApJ, 2003, **584**, pp. 357–367.

Kirk, H., Pineda, J., Johnstone, D., and Goodman, A., 'The dynamics of dense cores in the perseus molecular cloud. ii. the relationship between dense cores and the cloud,' ApJ, 2010, **723**, pp. 457–475.

Klessen, R., Heitsch, F., and Mac Low, M.-M., 'Gravitational collapse in turbulent molecular clouds. i. gasdynamical turbulence,' ApJ, 2000, **535**, pp. 887–906.

Kobayashi, H. and Ida, S., 'The effects of a stellar encounter on a planetesimal disk,' Icarus, 2001, **153**, pp. 416–429.

Kouwenhoven, M. and de Grijs, R., 'The effect of binaries on the dynamical mass determination of star clusters,' A&A, 2008, **480**, pp. 103–114.

Kouwenhoven, M. and de Grijs, R., 'How do binaries affect the derived dynamical mass of a star cluster?' Ap&SS, 2009, **324**, pp. 171–176.

Krebs, J. and Hillenbrandt, W., 'The interaction of supernova shockfronts and nearby interstellar clouds,' A&A, 1983, **128**, pp. 411–419.

Kuhn, M., Hillenbrand, L., Sills, A., Feigelson, E., and Getman, K., 'Kinematics in young star clusters and associations with gaia dr2,' arXiv:1807.02115, 2018.

Käufl, H., Ballester, P., Biereichel, P., Delabre, B., Donaldson, R., Dorn, R., Fedrigo, E., Finger, G., Fischer, G., Franza, F., Gojak, D., Huster, G., Jung, Y., Lizon, J.-L., Mehrgan, L., Meyer, M., Moorwood, A., Pirar, J.-F., Paufique, J., Pozna, E., Siebenmorgen, R., Silber, A., Stegmeier, J., and Wegerer, S., 'Crires: a high-resolution infrared spectrograph for eso's vlt,' SPIE, 2004, **5492**, pp. 1281–1227.

Lada, C., 'Star formation: From ob associations to protostars,' in 'Star Forming Regions,' pp. 1–17, Dordrecht, D. Reidel Publishing Co., Dordrecht, Holland, 1987.

Lada, C. and Lada, E., 'The nature, origin and evolution of embedded star clusters,' in 'The formation and evolution of star clusters,' pp. 3–22, ASP, 1991.

Lada, C. and Lada, E., 'Embedded clusters in molecular clouds,' ARA&A, 2003, **41**, pp. 57–115.

Laughlin, G., Bodenheimer, P., and Adams, F., 'The end of the main sequence,' ApJ, 1997, **482**, pp. 420–432.

Loinard, L., Torres, R., Mioduszewski, A., and Rodríguez, L., 'Very long baseline array astrometry of low-mass young stellar objects,' RMx, 2008, **34**, pp. 14–21.

Lombardi, M., Lada, C., and Alves, J., 'Hipparcos distance estimates of the ophiuchus and the lupus cloud complexes,' A&A, 2008, **480**, pp. 785–792.

Loren, R., 'The cobwebs of ophiuchus. ii - (c-13)o filament kinematics,' ApJ, 1989, **338**, pp. 925–944.

Luhman, K. and Rieke, G., 'Low-mass star formation and the initial mass function in the rho ophiuchi cloud core,' ApJ, 1999, **525**, p. 440.

Maciel, W., Costa, R., and Idiart, T., 'Chemical composition of planetary nebulae: The galaxy and the magellanic clouds,' in 'Planetary nebulae beyond the Milky Way,' p. 209, Proceedings of the ESO workshop held in Garching, Germany, 19-21 May 2004 ESO astrophysics symposia, 1991.

Mamajek, E., 'On the distance to the ophiuchus star-forming region,' AN, 2008, **329**, p. 10.

Manara, C., Testi, L., Natta, A., and Alcalá, J., 'X-shooter study of accretion in rho-ophiucus: very low-mass stars and brown dwarfs,' A&A, 2015, **579**, p. A66.

Matzner, C. and McKee, C., 'Efficiencies of low-mass star and star cluster formation,' ApJ, 2000, **545**, pp. 364–378.

Mayama, S., Tamura, M., Hanawa, T., Matsumoto, T., Ishii, M., Pyo, T.-S., Suto, H., Naoi, T., Kudo, T., Hashimoto, J., Nishiyama, S., Kuzuhara, M., and Hayashi, M., 'Direct imaging of bridged twin protoplanetary disks in a young multiple star,' Sci, 2010, **327**, p. 306.

McConnachie, A. and Côté, P., 'Revisiting the influence of unidentified binaries on velocity dispersion measurements in ultra-faint stellar systems,' ApJL, 2010, **722**, pp. L209–L214.

McLean, I., Becklin, E., Bendiksen, O., Brims, G., Canfield, J., Figer, D., Graham, J., Hare, J., Lacayanga, F., Larkin, J., Larson, S., Levenson, N., Magnone, N., Teplitz, H., and Wong, W., 'Design and development of nirspec: a near-infrared echelle spectrograph for the keck ii telescope,' SPIE, 1998, **3354**, pp. 566–578.

Muench, A., Lada, E., and Lada, C., 'Modeling the near-infrared luminosity functions of young stellar clusters,' ApJ, 2000, **533**, pp. 358–371.

Muzerolle, J., Hartmann, L., and Calvet, N., 'A brgamma probe of disk accretion in t tauri stars and embedded young stellar objects,' AJ, 1998, **116**, pp. 2965–2974.

Ortiz-León, G., Loinard, L., Kounkel, M., Dzib, S., Mioduszewski, A., Rodrígues, L., Torres, R., González-Lópzlira, R., Pech, G., Rivera, J., Hartmann, L., Boden, A., Evans, N. I., Briceño, C., Tobin, J., Galli, P., and Gudehus, D., 'The gould's belt distances survey (gobelins). i. trigonometric parallax distances and depth of the ophiuchus complex,' ApJ, 2017, **843**, p. 141.

Ossenkopf, V., Krips, M., and Stutzki, J., 'Structure analysis of interstellar clouds. ii. applying the δ-variance method to interstellar turbulence,' A&A, 2008, **485**, pp. 719–727.

Palla, F. and Stahler, S., 'Star formation in the orion nebula cluster,' ApJ, 1999, **525**, pp. 772–783.

Pecaut, M. and Mamajek, E., 'Intrinsic colors, temperatures, and bolometric corrections of pre-main-sequence stars,' ApJS, 2013, **208**, p. 9.

Peretto, N., André, P., and Belloche, A., 'Probing the formation of intermediate- to high-mass stars in protoclusters. a detailed millimeter study of the ngc 2264 clumps,' A&A, 2006, **445**, pp. 979–998.

Plavchan, P., Gee, A., Stapelfeldt, K., and Becker, A., 'The peculiar periodic yso wl 4 in rho ophiuchus,' ApJ, 2008, **684**, p. L37.

Plavchan, P., Güth, T., Laohakunakorn, N., and Parks, J., 'The identification of 93 day periodic photometric variability for yso ylw 16a,' A&A, 2013, **554**, p. 110.

Prato, L., 'A survey for young spectroscopic binary k7 - m4 stars in ophiuchus,' ApJ, 2007, **657**, pp. 338–346.

Proszkow, E.-M. and Adams, F., 'Dynamical evolution of young embedded clusters: A parameter space survey,' ApJS, 2009, **185**, pp. 486–510.

Raghavan, D., McAlister, H., Henry, T., Latham, D., Marcy, G., Mason, B., Gies, D., White, R., and ten Brummelaar, T., 'A survey of stellar families: Multiplicity of solar-type stars,' ApJS, 2010, **190**, p. 1.

Ratzka, I., Kohler, R., and Leinert, C., 'A multiplicity survey of the rho ophiuchi molecular clouds,' A&A, 2005, **437**, pp. 611–626.

Rayner, J., *iSHELL Observing Manual*, University of Hawaii, Honolulu, Hawaii, 2017.

Rayner, J., Tokunaga, A., Jaffe, D., Bonnet, M., Ching, G., Connelley, M., Kokubun, D., Lockhart, C., and Warmbier, E., 'ishell: Construction, assembly, and testing,' SPIE, 2016, **9908**, p. 84.

Reggiani, M. and Meyer, M., 'Binary formation mechanisms: Constraints from the companion mass ratio distribution,' ApJ, 2011, **783**, p. 60.

Reipurth, B., Clarke, C., Boss, A., Goodwin, S., Rodríguez, L., Stassun, K., Tokovinin, A., and Zinnecker, H., 'Multiplicity in early stellar evolution,' in 'Protostars and Planets VI,' pp. 267–290, The University of Arizona Press, Tucson, Arizona, 2014.

Ressler, M. and Barsony, M., 'A luminous infrared companion in the young triple system wl 20,' AJ, 2001, **121**, pp. 1098–1110.

Rigliaco, E., Wilking, B., and Meyer, M., 'The gaia-eso survey: Dynamical analysis of the l1688 region in ophiuchus,' A&A, 2016, **588**, p. 123.

Salpeter, E., 'The luminosity function and stellar evolution.' ApJ, 1955, **121**, p. 161.

Schaefer, G., Prato, L., and Simon, M., 'Orbital motion of young binaries in ophiuchus and upper centaurus-lupus,' AJ, 2018, **155**, p. 109.

Sharma, S., 'Markov chain monte carlo methods for bayesian data analysis in astronomy,' ARA&A, 2017, **55**, pp. 213–256.

Sheehan, P. and Eisner, J., 'Wl 17: A young embedded transition disk,' ApJL, 2017, **840**, p. L12.

Sheehan, P. and Eisner, J., 'Multiple gaps in the disk of the class i protostar gy 91,' ApJ, 2018, **857**, p. 18.

Shklovskii, I., *Stars: Their Birth, Life, and Death*, W.H. Freeman and Company, New York, New York, 1978.

Siess, L., Dufour, E., and Forestini, M., 'An internet server for pre-main sequence tracks of low- and intermediate-mass stars,' A&A, 2000, **358**, pp. 593–599.

Sills, A., Rieder, S., Scora, J., McCloskey, J., and Jaffa, S., 'Dynamical evolution of stars and gas of young embedded stellar sub-clusters,' MNRAS, 2018, **477**, pp. 1903–1912.

Simon, M., Ghez, A., Leinert, C., Cassar, L., Chen, W., Howell, R., Jameson, R., Matthews, K., Neugebauer, G., and Richichi, A., 'A lunar occultation and direct imaging survey of multiplicity in the ophiuchus and taurus star-forming regions,' ApJ, 1995, **443**, pp. 625–637.

Simon, M., Guilloteau, S., Di Folco, E., Dutrey, A., Grosso, N., Piétu, V., Chapillon, E., Prato, L., Schaefer, G., Rice, R., and Boehler, Y., 'Dynamical masses of low-mass stars in the taurus and ophiuchus star-forming regions,' ApJ, 2017, **844**, p. 158.

Soubiran, C., Jasniewicz, G., Chemin, L., Zurbach, C., Brouillet, N., Panuzzo, P., Sartoretti, P., Katz, D., Le Campion, J.-F., Marchal, O., Hestroffer, D., Thévenin, F., Crifo, F., Udry, S., Cropper, M., Seabroke, G., Viala, Y., Benson, K., Blomme, R., Jean-Antoine, A., Huckle, H., Smith, M., Baker, S., Damerdji, Y., Dolding, C., Frémat, Y., Gosset, E., Guerrier, A., Guy, L., Haigron, R., Janssen, K., Plum, G., Fabre, C., Lasne, Y., Pailler, F., Panem, C., Riclet, F., Royer, F., Tauran, G., Zwitter, T., Gueguen, A., and Turon, C., 'Gaia data release 2. the catalogue of radial velocity standard stars,' A&A, 2018, **616**, p. 7.

Spitzer, L. J., 'Disruption of galactic clusters.' ApJ, 1958, **127**, p. 17.

Stahler, S. and Palla, F., *The Formation of Stars*, WILEY-VCH Verlag GmbH & Co. KGaA, Weinheim, Germany, 2004.

Stassun, K., Feiden, G., and Torres, G., 'Empirical tests of pre-main-sequence stellar evolution models with eclipsing binaries,' NewAR, 2014, **60**, pp. 1–28.

Struve, O. and Rudkjobing, M., 'Stellar spectra with emission lines in the obscuring clouds of ophiuchus and scorpius.' ApJ, 1949, **109**, p. 92.

Terebey, S., van Buren, D., Hancock, T., Padgett, D., Brundage, M., and Hancock, T., 'Dynamical structure in hst/nicmos images of nearby protostars,' in 'From Darkness to Light: Origin and Evolution of Young Stellar Clusters, ASP Conference Proceedings,' volume 243, p. 243, Astronomical Society of the Pacific, San Francisco, California, 2001.

Van Kempen, T., van Dishoeck, E., Salter, D., Hogerheijde, M., Jorgensen, J., and Boogert, A., 'The nature of the class i population in ophiuchus as revealed through gas and dust mapping,' A&A, 2009, **498**, pp. 167–194.

Viana Almeida, P., Melo, C., Santos, N., Figueira, P., Sterzik, M., and Gameiro, J., 'Finding proto-spectroscopic binaries. precise multi-epoch radial velocities of seven protostars in rho ophiuchus,' A&A, 2012, **539**, p. 62.

Vrba, F., Strom, K., Strom, S., and Grasdalen, G., 'Further study of the stellar cluster embedded in the ophiuchus dark cloud complex,' ApJ, 1975, **197**, pp. 77–84.

Ward-Thompson, D., André, P., Crutcher, R., Johnstone, D., Onishi, T., and Wilson, C., 'An observational perspective of low-mass dense cores ii: Evolution toward the initial mass function,' in 'Protostars and Planets V,' pp. 33–46, The University of Arizona Press, Tucson, Arizona, 2007.

White, R., Greene, T., Doppmann, G., Covey, K., and Hillenbrand, L., 'An observational perspective of low-mass dense cores ii: Evolution toward the initial mass function,' in 'Protostars and Planets V,' pp. 117–132, The University of Arizona Press, Tucson, Arizona, 2007.

Whitworth, A., 'The erosion and dispersal of massive molecular clouds by young stars,' MNRAS, 1979, **186**, pp. 59–67.

Wilking, B., Gagné, M., and Allen, L., 'Star formation in the rho ophiuchi molecular cloud,' in 'Handbook of Star Forming Regions, Volume II: The Southern Sky,' volume 5, p. 351, ASP Monograph Publications, 2008.

Wilking, B. and Lada, C., 'The discovery of new embedded sources in the centrally condensed core of the rho ophiuchi dark cloud - the formation of a bound cluster,' ApJ, 1983, **274**, pp. 698–716.

Wilking, B., Lada, C., and Young, E., 'Iras observations of the rho ophiuchi infrared cluster - spectral energy distributions and luminosity function,' ApJ, 1989, **340**, pp. 826–852.

Wilking, B., Schwartz, R., and Blackwell, J., 'An h-alpha emission-line survey of the rho ophiuchi dark cloud complex,' AJ, 1987, **94**, pp. 106–110.

Wilking, B., Vrba, F., and Sullivan, T., 'Relative proper motions in the rho ophiuchi cluster,' ApJ, 2015, **815**, p. 2.

Young, E., Lada, C., and Wilking, B., 'High-resolution iras observations of the rho ophiuchi cloud core,' ApJL, 1986, **304**, pp. L45–L49.

Yuan, H., Liu, W., and Xiang, M., 'Empirical extinction coefficients for the galex, sdss, 2mass and wise passbands,' MNRAS, 2013, **430**, pp. 2188–2199.

VITA

Timothy Sullivan was born in Kansas City, Missouri in 1989. He finished his B.S. in Physics from Truman State University in Kirksville, Missouri in May 2012, and began working on his M.S. in Physics at the University of Missouri - St. Louis the following fall, which was completed in May 2014. He earned his Ph. D. in Physics from the University of Missouri of Science and Technology and the University of Missouri - St. Louis in May 2019.